SIMULATION OF THE PERMANENT DEFORMATION OF ASPHALT CONCRETE MIXTURES USING DISCRETE ELEMENT METHOD (DEM)

By

HABTAMU MELESE ZELELEW

A dissertation submitted in partial fulfillment of
the requirements for the degree of

DOCTOR OF PHILOSOPHY

WASHINGTON STATE UNIVERSITY
Department of Civil and Environmental Engineering

May 2008

To the Faculty of Washington State University:

The members of the Committee appointed to examine the dissertation of HABTAMU MELESE ZELELEW find it satisfactory and recommend that it be accepted.

_____
Chair

_____

_____

_____

ACKNOWLEDGEMENT

First and foremost, I would like to express my deepest gratitude to Dr. Tom Papagiannakis, my Professor, advisor, and mentor for his encouragement, advice, and financial assistance throughout the development of the thesis. Your motivations, kindness and energy made me to produce this work.

Dr. Tom, you have given me confidence, authority and most importantly the trust. During my training, we have never failed to communicate. Of course, there are times that I never even smile when I get frustrated. Your door always had a green light and you never said that you were too busy. I am really proud of you.

Special thanks to Dr. Balasingam Muhunthan who blessed me with core courses (CE 509: Numerical Modeling of Geomaterials and CE 510: Advanced Geomaterial Characterization). Dr. Muhunthan, I learned a lot from you. I owe you my gratitude for having shown me your research approach. Special thanks are also due to Dr. Adrian Rodriguez-Marek for interesting discussions on continuum and micromechanical modeling approaches. I also wish to extend my sincere thanks to Dr. Hussein M. Zbib for his cooperation and for serving as a committee member.

My special thanks are also due to Dr. Eyad Masad for the X-ray CT images and interesting discussions on watershed transformations and to Dr. Soheil Nazarian for the creep data. Special thanks to Dr. Ala Abbas for many interesting discussions on image analysis and DEM simulations.

My gratitude also goes to: Dr. Laith Tashman, Dr. Kitae Nam, Dr. David McLean, Mrs. Vicki Ruddick, Mrs. Gina Paroline, Mr. Enad Mahmoud, Dr. David

Potyondy, Mr.Thomas Gebrenegus, Mr. Yonas Keleta, Dr. Wudneh Admassu, Mr. Seyoum Gebremariam, WSU GeoTransportation group, and UTSA CEE staff members, especially Ms. Laurie De La Paz, Mr. John Strubelt, and Ms. Lisa Ramirez. In addition, financial support from Washington State University (WSU) and University of Texas at San Antonio (UTSA) is also acknowledged.

Finally, many thanks to all of my friends, faculty and staff members of WSU and the UTSA CEE department.

Thank you all.

SIMULATION OF THE PERMANENT DEFORMATION OF ASPHALT CONCRETE MIXTURES USING DISCRETE ELEMENT METHOD (DEM)

Abstract

by Habtamu Melese Zelelew, Ph.D.
Washington State University
May 2008

Chair: Tom Papagiannakis

This study describes a methodology for simulating the permanent deformation resistance behavior of asphalt concrete mixtures using the discrete element method (DEM). The microstructure of asphalt concrete cores was obtained through X-Ray CT imaging techniques. Rheological tests on asphalt binders and mastics were performed to characterize their viscoelastic properties and establish their strength.

An Automated Digital Image Processing (DIP) algorithm, called Volumetric-based Global Minima (VGM) thresholding algorithm was developed in the MATLAB® environment to process the AC X-ray CT images for DEM simulation. VGM identifies the gray scale intensity boundary thresholds between air, mastic and aggregate phases with reference to volumetric information. It involves three interdependent stages, namely image preprocessing, gray scale thresholding, and post-processing. The first stage involves image pre-processing for contrast enhancement and noise removal. The second stage is the main thresholding routine accepting as input the enhanced images of the first stage and volumetric information for the AC. It consists of two components, namely volumetrics-driven thresholding and three-dimensional representation and sectioning. The third stage further enhances particle separation through edge detection and image

segmentation techniques. It was demonstrated that the VGM processed images are suitable for inputting to a numerical simulation technique such as FEM and DEM. This algorithm was shown to be a major improvement over the largely manual techniques used in the past.

DEM simulations of unconfined uniaxial static creep tests in compression were performed to predict deformation behavior of the AC models. Moreover, the effect of contact stiffness ratio (K_n/K_s) and aggregate-to-aggregate contact friction (μ) on the deformation behavior of the AC model were investigated. Laboratory uniaxial compression static creep tests were performed on the same nine AC mixtures imaged by the VGM technique. The total axial strains and the creep compliance DEM predictions were compared with the experimental results. Overall, the slope of the secondary compression part of the creep compliance curves was satisfactorily predicted.

TABLE OF CONTENTS

Page

LIST OF TABLES

Page

LIST OF FIGURES

Page

Dedication

This dissertation is dedicated to my sister Beletu Melese Zelelew and her daughter Bsrat Ketema Woldesemayat

Chapter 1

INTRODUCTION

1.1 Problem Statement

Asphalt Concrete (AC) mixtures are uniquely complex heterogeneous materials composed of air voids, asphalt cement and aggregates. Mastics are blends of asphalt binder and fines, typically considered as particles passing sieve No. 200 (i.e., sizes finer than 75 microns). The distribution of these three phases and their interaction define the mechanical properties of ACs and contribute significantly to the load carrying capacity and durability of flexible pavements. The load carrying capacity of ACs comes primarily from aggregate-to-aggregate interlocking and contact friction. The mastic plays a cementing role in keeping the aggregate particles together. The overall performance of ACs is highly dependent on the proportions of these constituents, as well as their physical properties and distribution. The highly complex air void-mastic-aggregate interaction affects greatly the permanent deformation behavior of AC pavements. Hence, their microstructure plays a significant role in their performance.

Pavement rutting is a surface depression along wheel paths caused by the plastic deformation of the AC materials which is mainly a problem in hot climates. At higher temperature, AC pavements become softer due to a reduction in asphalt binder viscosity. This phenomenon increases the rutting potential of the AC pavements. Moreover, the physical properties of aggregate such as shape (or form), angularity (or roundness), and surface texture governs the performance of AC pavements. Several studies have shown that the permanent deformation behavior of AC mixtures is highly dependent on the aggregate characteristics (Brown et al., 1980; Hopman et al., 1992; Sousa et al., 1991; Masad et al., 2002; Tashman et al., 2005). The contribution of the AC layer to rutting is very significant when compared to the contribution of the other pavement layers (i.e., base, subbase, and compacted subgrade).

AC pavements are typically designed to provide a safe and smooth riding quality to the public. Sousa et al. (1991) mentioned two main rutting associated problems in AC

pavements: (1) vehicle steering difficulty, and (2) hydroplaning (water in the ruts), particularly for light passenger cars. Pavement distresses are usually caused by traffic and/or environmental conditions. A typical AC pavement rutting is shown in Figure 1.1. The existence of permanent deformation is one of the major problems affecting the overall performance of AC pavements. State DOT's and agencies are compelled to invest millions of dollars on pavement rehabilitation programs to correct pavement rutting problems. Proper characterization of the AC rutting assists to design a rutting resistant pavement structures and increases the pavement service life with minimal maintenance cost.

On the other hand, cracking mostly occurs during low to medium temperature seasons. Fatigue cracking is due to repeated traffic loading as shown in Figure 1.2. At a very low temperature, the asphalt binder hardens which increases rutting resistance and yet leads to thermal cracking along the transversal direction of the pavement structure. A typical AC thermal cracking is shown in Figure 1.3. Pavement cracks may initiate at top and grow towards the bottom and/or vise versa. According to a recent industry survey, rutting is the most serious pavement distress. Fatigue cracking was rated as the second most serious problem, followed by thermal cracking (Witczak et al., 2002). These distresses are affected by material properties, loading history and environment. They are further compounded by poor design procedures and/or pavement maintenance and rehabilitation practices.

Figure 1.1 A Typical AC Pavement Rutting

Figure 1.2 A Typical AC Pavement Fatigue Cracking

Figure 1.3 A Typical AC Pavement Thermal Cracking

Prediction of rutting requires proper characterization of asphalt binders, mastics, aggregates, and AC mixture using appropriate testing devices. Currently, the traditional asphalt mixtures design procedures, namely the Marshal and Hveem method have been replaced by the Superior Performing Asphalt Pavements (Superpave™) method for specifying asphalt materials. Superpave™ was developed in early 1990s under the Strategic Highway Research Program (SHRP). It utilizes a novel approach for material testing, specifying and selection of asphalt binders. The properties of asphalt binders and mastics significantly affect their rutting resistance potential, and hence proper characterization of these materials is a mandatory task. For example, the viscosity of the

binding material decreases at higher temperature that results poor rutting resistant AC mixture. In order to characterize the viscoelastic rheological properties of asphalt unaged and RTFO-aged binders, test devices that include dynamic shear rheometer (DSR), rotational viscometer (RV), bending beam rheometer (BBR), and indirect tension tester (IDT) can be used. Since the current AASHTO/ASTM specification standards fall short to document formal testing protocols for asphalt mastics, the RTFO-aged binder testing procedures may be employed for asphalt mastic materials. The performance of the asphalt concrete mixture is greatly influenced by the properties of the asphalt binders (Tunnicliff, 1962; Kallas and Puzinauskas, 1967; Puzinauskas, 1969; Andereson and Goetz, 1973; Harris and Stuart, 1995; Ishai and Craus, 1996; Chen and Peng, 1998; Shashidhar and Romero, 1998; Buttlar et al., 1999; Kim et al., 2003; Kim and Little, 2004; Abbas et al., 2005).

The permanent deformation behavior of AC mixtures is highly dependent on the testing methods, specimen preparation procedures, testing temperature, stress level, and loading time. A fundamental understanding of the AC mixture responses under any testing method is needed to fully characterize their permanent deformation behavior. The selection of suitable testing methods depends on the property being measured, the cost of the equipment and the simplicity of the testing procedures. The simple shear test (SST) is suitable for simulating AC rutting, as the shear deformation is the dominant failure mechanism of AC rutting (Long, 2001). Its main limitation is that the stress/strain state inside the sample is not uniform. Another test has been proposed involving uniaxial compression, referred to as the Simple Performance Test (SPT). Samples are subjected to unconfined creep loads and vertical strain is measured. This test is relatively easy to perform and yields parameters, such as the creep compliance, which has been successfully utilized by several researchers to predict AC rutting (Van de Loo, 1974, 1976, 1978; Khanzada, 2000). The experimentally observed rutting behavior can be used to verify the predicted values using numerical simulation schemes such as continuum and micromechanical models.

Continuum and micromechanical modeling approaches are the two commonly used numerical simulation techniques that are utilized by several researchers to model the AC behavior under different testing conditions. Moreover, researchers have attempted to

model behavior of AC mixtures using hybrid modeling schemes by combining the continuum and micromechanical modeling approaches in order to effectively predict material responses. Recently, the FEM-DEM modeling and simulation techniques have been implemented to characterize the AC mixture properties under a range of temperature and laboratory testing condition (Dai and You, 2007).

The continuum modeling approaches that include the finite element method (FEM), involve undertaking careful experiments to measuring the macroscopic stress-strain response of the AC mixtures for a given in-service traffic loading and temperature conditions using specified boundary constraints. Several researchers proposed models to study the behavior of AC mixtures utilizing this approach (Sousa et al., 1993; Sousa and Weissman, 1994; Scarpas et al., 1997; Bahia et al., 1999; Huang et al., 2002; Papagiannakis et al., 2002; Masad et al., 2002; Tashman, 2003; Abbas et al., 2004; Dessouky, 2005; Bahuguna et al., 2006). Studies to model the AC mixture permanent deformation behavior using continuum-based constitutive models applicable to the entire material volume include (Schapery, 1984; Kim et al., 1991; Judycki, 1992; Sousa et al., 1993a; Sousa et al., 1993b; Collop et al., 1995; Park et al., 1996; Lee and Kim, 1998; Bahia et al., 1999; Papagiannakis et al., 2002; Abbas et al., 2004; Dai et al., 2006). Moreover, researchers have attempted to model the permanent deformation behavior of the AC mixtures by incorporating the effects of loading, dilation, anisotropy and crack/damage (e.g., Desai and Zhang, 1987; Sepehr et al., 1994; Scarpas et al., 1997a, 1997b; Seibi et al., 2001; Si, 2001; Soares et al., 2003; Tashman, 2003; Dessouky, 2005; Panneerselvam, 2005).

Such continuum-based models have a number of limitations, namely they are not well suited to describe large strains and discontinuities, such as air voids and cracks. Furthermore, AC behavior is dominated by the interaction between distinct aggregate particles. Shashidhar et al., (2000) investigated the role of aggregate structures in asphalt pavements and demonstrated that AC mixtures behave as granular materials. An alternative approach for modeling such materials is the Discrete Element Method (DEM) pioneered by Cundall and Strack, (1979). DEM is proven successful in modeling discontinuous materials, such as rocks and soils. It is suitable to simulate the mechanical response of a granular assembly composed of discrete particles. DEM appears to be

superior to continuous methods in modeling particulate materials, capturing fairly complicated behavior with few assumptions and by utilizing few parameters Cundall, (2001). DEM allows finite displacements and rotations of particles to simulate their complex interactions within the loaded particulate assembly of the AC mixture models. These models predict the macroscopic constitutive relationship using the particle contact force-displacement relationships that are found by tracing the movements of the individual particles at a given vanishingly small contact point.

In the past, the application of DEM was restricted by the lack of sufficient memory and computational power. This is no longer a problem however, which makes DEM an attractive tool for simulating AC microstructure under large deformations. Previous studies on modeling the AC mixture behavior using micromechanical modeling approach include (Rothenburg et al., 1992; Buttlar and Roque, 1996; Chang and Meegoda, 1997; Cheung et al., 1999; Uddin, 1999; Shashidhar et al., 2000; You and Buttlar, 2001; Collop et al., 2004a; You and Buttlar, 2004; Abbas et al., 2005; Collop et al., 2006; Zelelew et al., (2007a).

Rothenburg et al., (1992) proposed a micromechanical discrete model for AC pavements to study AC rutting. In this model, AC was represented by a set of discrete elastic elements bounded by a linear viscoelastic binder, and the binder within voids was treated as a compressible Newtonian fluid. It was demonstrated that the mechanical response of asphalt concrete is highly dependent on the performance of the granular material. Simulation of the creep tests also showed that the steady-state properties were also largely controlled by the proportion of frictional inter-granular contact compared to the proportion of cohesive contact. Moreover, Chang and Meegoda, (1997) proposed an innovative DEM model, by modifying TRUBAL program, to describe interaction of aggregate-to-aggregate and asphalt-to-aggregate contacts. They utilized mechanistic models to simulate the viscoelastic behavior of asphalt binder using linear viscoelastic elements. Based on the mechanical responses and comparisons with experimental results, Burger model was found to be the most promising element for modeling the asphalt binder behavior. They showed the success of DEM simulations on AC mixtures. Recently, researchers developed simulation techniques by extending the conventional DEM analysis in order to account the mastic and aggregate phases and model the AC

microstructure using microfabric distinct element method (MDEM) (You and Buttlar 2001). They described the AC microstructure using clusters of circular particles to simulate the behavior of AC mixture using indirect tension test (IDT). The role of aggregate-to-aggregate contact was also carefully examined to investigate its effect on dynamic modulus simulation analysis results using uniaxial compression tests on mastics and coarse grained mixtures (You and Buttlar, 2002).

A highly idealized AC mixture under uniaxial creep tests in compression was simulated using a DEM software package called *Particle Flow Code in three-dimensions* (PFC^{3D}) to investigate the applicability of DEM to study the AC mixture behavior and responses (Collop et al., 2004a). In their study, effects of particle size and contact stiffnesses along normal and shear direction on material properties were assessed. They showed that the linear dependency of bulk modulus on the normal contact stiffness and the Poisson's ratio was found to be dependent only on the ratio of the shear contact stiffness to the normal contact stiffness. More interestingly, they extended the study by including the Burger viscoelastic model to investigate the time dependency contact stiffness of the model. Further, they successfully implemented DEM simulation to characterize the permanent deformation behavior of idealized AC mixtures using uniaxial and triaxial creep tests.

Abbas et al., (2005) characterized the behavior of asphalt mastics using DEM simulation to capture the micromechanical responses of mastics and AC mixtures. They demonstrated the potential application of DEM simulation for capturing the effects of the aggregate filler volume fraction on the mastic stiffnesses. They concluded that the predicted dynamic shear modulus of the mastic was found to be highly dependent on the dynamic shear modulus of the binder that is favorable with experimental testing data. Moreover, they extended the simulation process to investigate the effects of adhesive bonds along with binder films. Moreover, the viscoelastic response of AC mixtures at high temperatures and their fracture mechanism at low temperature using DEM was studied. DEM simulation studies that utilize the Burger contact model to simulate the micromechanical contact behavior of the asphalt mastics include (Collop et al., 2004a; Abbas et al., 2005; You and Buttlar, 2006; Hu et al., 2007; Yu et al., 2007).

The above mentioned studies clearly demonstrated the potential applicability of DEM simulations for studying the micromechanical behavior of AC mixtures at a large scale. In addition, they capitalized on the availability of high resolution X-ray CT scanning facilities and robust software for processing the AC or mastic X-ray CT images. The images, properly processed, can be used to characterize the AC microstructure in a form that allows its direct input into a DEM algorithm. Realistic representation of the AC microstructure (i.e., the air, mastic and aggregate phases) is needed in order to simulate their deformation behavior accurately. This can be accomplished by utilizing digital image processing techniques.

Recently, advances in characterization of the AC microstructure using imaging techniques have gained popularity with many researchers. The development of high resolution X-ray computed tomography (CT) has demonstrated considerable promise to efficiently capture and characterize the AC microstructure. A large volume of literatures deals with characterizing AC X-ray CT images using Digital Image Processing (DIP) techniques include (Synolakis et al., 1996; Kuo et al., 1998; Persson, 1998; Masad et al., 1999a,1999b; Shashidhar, 1999; Masad and Button, 2000; Masad, 2001; Masad et al., 2001; Tashman et al., 2001; Al-Omari et al., 2002; Papagiannakis et al., 2002; Saadeh et al., 2002; Tashman et al., 2002; Banta et al., 2003; Kim et al., 2003; Al-Omari and Masad, 2004; Wang et al., 2004a, 2004b). Moreover, Masad and Button, (2004) examined the AC microstructure based on volumetric and imaging techniques and studied their effect on overall performance. Aggregate orientations and their effects on engineering properties of asphalt mixtures are well investigated and characterized using imaging techniques (Masad et al., 1998; Chen et al., 2001; Chen et al., 2002; Chen et al., 2005). These techniques have been used to obtain quantitative information about the air voids, mastic and aggregate distribution, shape of the aggregate particles, aggregate orientation, aggregate gradation, aggregates contacts, aggregate segregation and so on. Despite these developments, identifying the three phases in AC X-ray CT images has been treated subjectively. This involves establishing the grey level thresholds that separate aggregate from mastic and mastic from air.

The majority of the studies highlighted above use a combination of DIP and manual/subjective techniques for processing AC images in a format suited to numerical

simulation. DIP techniques include image contrast enhancement, image noise removal, thresholding, edge detection and image segmentation. Typically, the gray level threshold that separates aggregates from mastics referred to as thresholding is selected subjectively. Additional pixel modifications are required to adjust the relative proportions of aggregate and mastic to reflect the actual volumetrics of the AC. Isolating the air phase further complicates the problem. To date, there have been few attempts to fully automate this process by solely utilizing DIP techniques (Kose et al., 2000; Yue et al., 2003; Offrell and Magnusson, 2004). Developing an algorithm for processing automatically AC X-ray CT images is inevitable in effectively capturing the microstructure of a large number of AC cores for modeling their mechanical behavior. Consequently, these processes assist to accurately predict the permanent deformation behavior of AC mixtures.

DEM can be utilized to simulate the permanent deformation behavior of AC using input from the processed X-ray CT images. In DEM, more complex physical properties of the material, example aggregate shape, size, and gradation can be similarly represented and modeled using clusters of particles forming particle clumps. This modeling technique is particularly suitable to investigate the mechanical behavior of materials and hence can effectively predict the performance properties of AC mixtures under different loading and testing conditions. At present, bulk of cutting-edge DEM simulations on AC rutting predictions are being implemented without proper characterization of air void-mastic and mastic-aggregate gray scale boundary thresholds. In this modeling approach, quantitative evaluation of AC mixture component interface is critical. For example, in material characterization context, this means that under- or over-estimation of air voids, mastics or aggregates leads to unrealistic prediction of AC rutting.

In summary, there is a pressing need to develop an approach that overcomes the shortcomings of the existing continuum-based and DEM-based simulation processes by utilizing automatically processed AC X-ray CT images to characterize the permanent deformation behavior of AC mixtures. Hence, simulation of the permanent deformation behavior of AC mixtures using a DEM software package called *Particle Flow Code in two-dimensions* (PFC^{2D}) has become the focus of this research to mitigate the problem of permanent deformation in AC pavements.

1.2 Research Objectives

The primary objectives of this research are to:

- Develop innovative techniques to process AC X-ray CT images for input into numerical simulation models, and
- Simulate AC permanent deformation behavior and validate the results with experimental observations.

1.3 Thesis Organization

The dissertation has nine chapters and is organized as follows. Chapter 2 highlights the most relevant literature related to this research work. The research methodology is described in Chapter 3. Chapter 4 presents the uniaxial static creep tests to investigate the rutting behavior of AC mixtures. Chapter 5 describes the innovative method called Volumetrics-based Global Minima (VGM) thresholding algorithm for processing AC X-ray CT images. In Chapter 6, the binder and mastic dynamic shear rheological tests to characterize the viscoelastic model parameters are presented. Chapter 7 describes the development and working frameworks of discrete/distinct element method (DEM). Implementation of the DEM software called *Particle Flow Code in two-dimensions* (PFC^{2D}) to simulate the uniaxial static creep tests and predict the permanent deformation behavior of the AC mixtures are given in Chapter 8. Moreover, validation of the predicted values to the experimentally observed values is also given in this chapter. The conclusions of the study and recommendations for future research work are given in Chapter 9.

Chapter 2

LITERATURE REVIEW

2.1 Introduction

Rutting is a surface depression along wheel paths caused by the plastic deformation of the AC materials. Rutting is considered to be one of the most serious distresses in AC pavements. It usually occurs in their early life. This chapter begins by summarizing the permanent deformation behavior of AC pavements. The causes and mechanisms of permanent deformation and its laboratory testing methods are briefly reviewed. Relevant literature on the numerical modeling and simulation of the permanent deformation behavior of AC pavements using continuum, micromechanical and continuum-micromechanical approaches are also reviewed.

2.2 Permanent Deformation Behavior of AC Pavements

The properties of the AC mixture components, namely air voids, asphalt cement (mastics), and aggregates significantly influence the rutting resistance behavior of AC mixtures. Their volumeterics and aggregate gradation has a direct effect on their performances. Prediction of rutting requires proper characterization of these components. For example, over-estimation of the air voids leads to aggregate segregation that result higher permanent deformation. The properties of the asphalt mastic/binder (i.e., binder grade, mixing and compaction viscosities, and aging process) are also among the major contributors to rutting problems. At higher pavement temperature, the viscosity of the binder tends to decrease, yielding less rutting resistant AC pavement. The physical properties of aggregate such as shape (or form), angularity (or roundness), and surface texture governs the rutting resistance of AC pavements. Moreover, the highly complex air void-mastic-aggregate interaction affects greatly the permanent deformation behavior of AC pavements.

2.2.1 Causes and Mechanisms of Permanent Deformation

AC pavement rutting is considered as one of the main traffic-related distress in AC pavements. Studies have indicated that the behavior of AC rutting can be modeled using viscoplastic constitutive models by considering the non-linear AC mixture responses (Tashman, 2003; Dessouky, 2005). The total viscoplastic strain response of a ACs can be decomposed into four components: (1) elastic where the time independent deformation is fully recoverable; (2) viscoelastic where the time dependent deformation is recoverable and it is time dependent; (3) viscoplastic where the time dependent deformation is irrecoverable; and (4) plastic where the time independent deformation is irrecoverable. When the constant load is removed, the permanent deformation can be obtained using the irrecoverable strain components. Figure 2.1 illustrates the idealized strain response of an AC mixture to an applied constant creep load or stress.

The contribution of the AC layer to rutting is significant compared to the contribution of the other pavement layers (i.e., base, subbase and compacted subgrade). Densification of mixtures and shear deformation are the two mechanisms, so far identified, causing permanent deformation in AC pavements. The former is due to the action of wheel loads along the wheel paths. Its effect is small for well-compacted AC mixtures. The later is caused by the shear stresses along the edges of the wheel paths or “humps” and is considered to be the dominant rutting mechanism (Sousa et al., 1991; Sousa et al., 1994; Weissman, 1997) as illustrated in Figure 2.2.

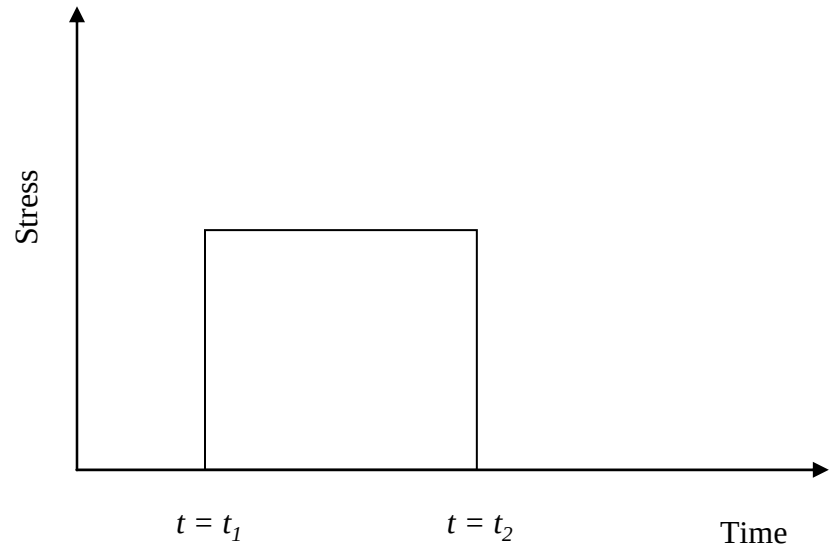

(a)

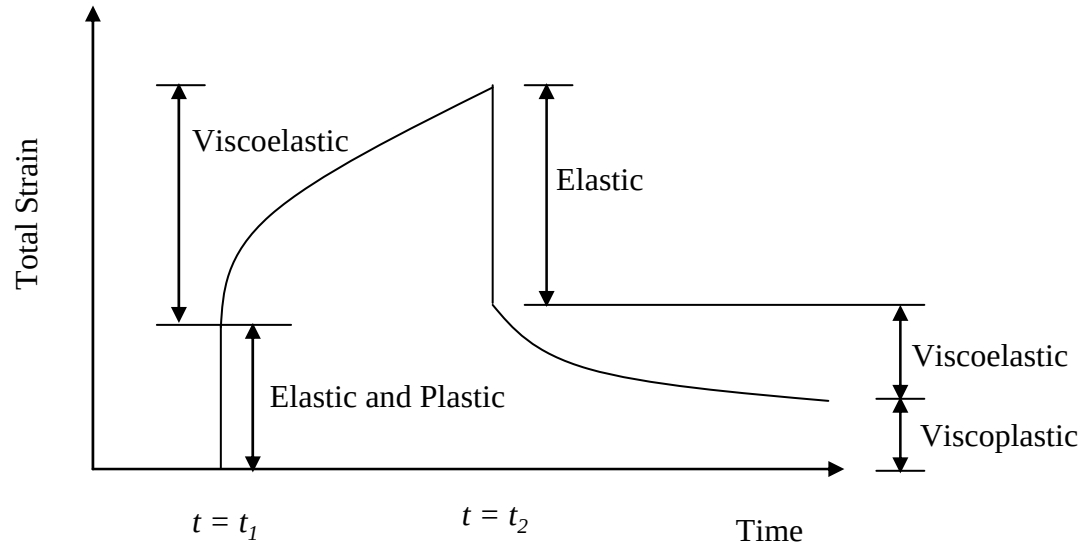

(b)

Figure 2.1 Typical Strain Decomposition of a Viscoelastic AC Material; (a) Stress Level (b) Response Strain

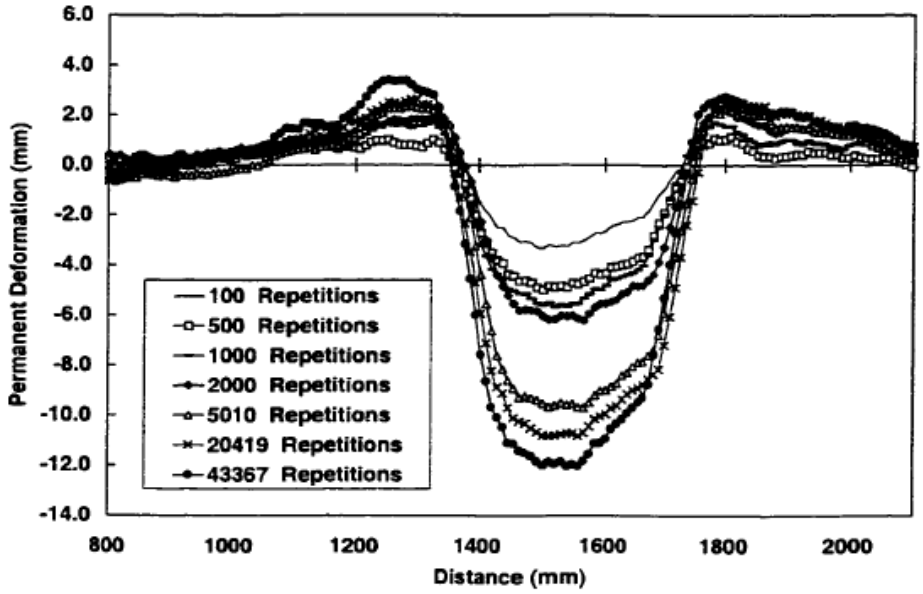

Figure 2.2 Heavy Vehicle Simulator (HVS) Rutting Test Profile (Harvery and Popescu, 2000)

2.2.2 Permanent Deformation Laboratory Testing

A number of laboratory tests are performed to characterize the permanent deformation behavior of AC mixtures. These include: (1) uniaxial creep and repeated tests (2) triaxial creep and repeated tests (3) hollow cylinder tests, and (4) simple shear tests. The permanent deformation of AC mixtures is highly dependent on the testing methods, specimen preparation procedures, testing temperature, stress level, and loading time. Selection of a particular testing method to characterize AC permanent deformation depends on the cost of the equipment, the simplicity of the testing procedures, and the material response. Simple shear tests are realistically suitable to simulate AC rutting as the shear deformation is the dominant cause and failure mechanism of AC rutting Long (2001). Unconfined creep tests are easy to perform and have been successfully utilized by several researchers to predict AC rutting (Van de Loo, 1974, 1976, 1978; Khanzada, 2000). Therefore, the unconfined static uniaxial creep tests are recommended to characterize AC mixture permanent deformation behavior (Alvarado et al., 2007).

2.2.2.1 Unconfined Static Uniaxial Creep Tests

The unconfined uniaxial compressive creep testing the AC mixtures consists of imposing a static axial load to a cylindrical specimen for a given loading time. The applied stress is computed from the load and the geometry of the specimen and the resulting total axial strain response of the specimen is measured. Creep compliance is the reciprocal of the modulus of elasticity of the material. It is a customary practice to plot the log creep compliance in ordinate axis and the log time in abscissa. As illustrated in Figure 2.3, it contains three distinct regions: a primary region where the strain rate decreases; a secondary region where the strain rate is constant; and a tertiary region where the strain rate increases. The change in volume of the specimen is increasing when primary and secondary creep stages are considered, however, the tertiary region is predominantly associated with pure plastic shear deformation where no volume change occurs. The beginning of the shear deformation under constant volume corresponds to the flow time. In static uniaxial creep testing, the tertiary response may not be appreciably present. However, the log compliance with log time captures the tertiary behavior. In addition, the intercept and slope of the secondary region can be used to characterize the rutting behavior of AC mixtures.

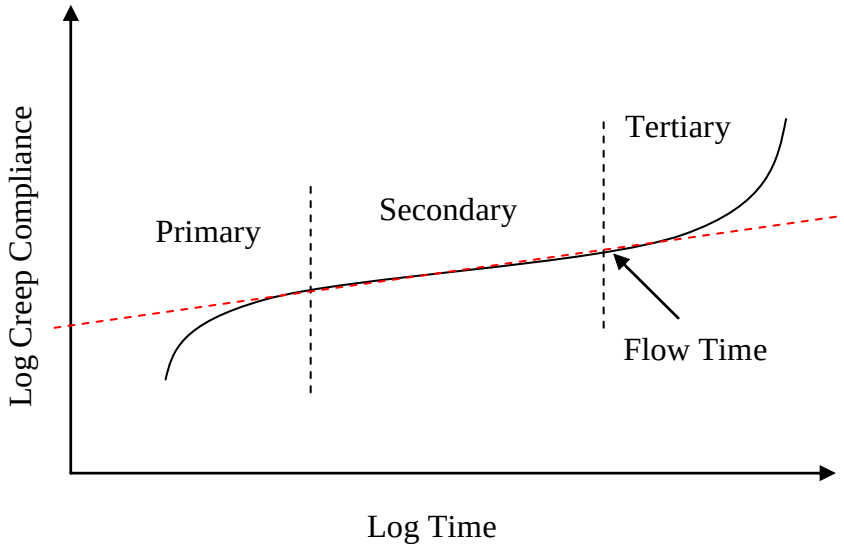

Figure 2.3 Schematic Illustration of Uniaxial Creep Permanent Deformation Test

The creep compliance parameters, namely the intercept and slope of the steady-state (i.e., secondary) region allow to distinguish the time-dependent and time-independent components of the strain response (Witczak et al., 2002). Higher intercept value indicates lower modulus of elasticity (i.e., higher creep compliance) and yields higher permanent deformation and vise versa. Furthermore, the slope of the steady-state region explains the progressive rate of deformation behavior of the AC mixtures.

2.3 Numerical Simulation Techniques for AC Mixtures

The three numerical simulation models used to simulate AC behavior include continuum, micromechanical, and continuum-micromechanical models. These modeling schemes have been utilized by several researchers to effectively characterize the mechanical behavior of AC materials under different loading and testing conditions. The continuum-based numerical models include the Finite Element Method (FEM), finite volume method (FVM), and Boundary Element Method (BEM). These models predict the macroscopic stress-strain response of the material, assuming continuity in displacements. On the other hand, the micromechanical models such as the DEM allow finite displacements and rotations of circular particles (disks) to simulate their complex interactions within the stressed granular assembly. DEM is a numerical simulation model pioneered by Cundall and Strack, (1979) has been proven to be a successful numerical simulation technique for modeling discontinuous materials such as rocks and granular materials. The future trend in numerical modeling of particulate materials is the replacement of continuum models by discrete models. The reason is that the later capture the complicated behavior of actual material with simple assumptions and by utilizing few parameters (Cundall, 2001). Moreover, researchers have attempted to model behavior of AC mixtures using hybrid modeling schemes by combining the continuum and micromechanical modeling approaches in order to effectively predict material responses. Recently, the FEM-DEM modeling and simulation techniques have been implemented to characterize the AC mixture properties under range of temperature and laboratory testing conditions (Dai and You, 2007).

2.3.1 Continuum Approach

Several researchers have been modeling the AC mixture permanent deformation behavior using continuum-based constitutive models (e.g., viscoelastic, viscoplastic and viscoelastoplastic models) applicable to the entire material volume. A common trend in modeling AC is to decompose the total strain into reversible and irreversible strain components and model them using appropriate constitutive models that adequately describes material response.

Modeling AC permanent deformation using viscoelastic modeling approaches include combinations of the different mechanical elements such as: Kelvin element, Maxwell element, and Burger element. Research efforts concentrated on developing various viscoelastic models for AC mixtures include (Schapery, 1984; Kim et al., 1991; Judycki, 1992; Sousa et al., 1993a, 1993b; Callop et al., 1995; Park et al., 1996; Lee and Kim, 1998; Bahia et al., 1999; Papagiannakis et al., 2002; Abbas et al., 2004; Dai et al., 2006). However, the viscoelastic models are not sufficient to capture AC permanent deformation due to the complexity of nonlinear response of AC mixtures. Viscoplasticity modeling is usually implemented by adding a frictional slider component to the viscoelastic or viscous element that accounts for the effects of permanent strain. Several researchers utilized the viscoelastic/viscoplastic constitutive models to characterize AC permanent deformation by including the effects of rate of loading, dilation, anisotropy and damage (Desai and Zhang, 1987; Sepehr et al., 1994; Scarpas et al., 1997a, 1997b; Seibi et al., 2001; Si, 2001; Soares et al., 2003; Tashman, 2003; Dessouky, 2005; Panneerselvam, 2005).

The above mentioned continuum-based models simulate the bulk material complex responses. However, it is difficult for these models to adequately account for the internal structures of the uniquely heterogeneous and granulate materials such as AC mixtures and predict the material response. AC materials are dominated by aggregate particles with complex physical properties, and hence it is logically meaningful to treat them as assemblages of particles and model them using micromechanical approach rather than using continuum approach.

2.3.2 Micromechanical Approach

The continuum constitutive modeling approaches relate the stress tensor to the strain tensor using material constants such as for example the isotropic modulus of elasticity and Poisson's ratio of the material. On the other hand, the micromechanical approach predicts the macroscopic constitutive relationship using the particle contact force-displacement relationships that are found by tracing the movements of the individual particles at a given vanishingly small contact point. The forces acting on any particle are determined by its interaction with the neighborhood particles.

DEM is suitable to simulate the mechanical response of a granular assembly composed of discrete particles. A vanishingly small time-stepping and explicit numerical scheme is utilized to efficiently simulate the complex interaction of particulate dynamic processes and can be used to easily understand the micromechanical behavior of the material at any stage of the simulation process. The use of an explicit numerical scheme makes it possible to simulate the non-linear interaction of large assembly of particles that exhibit physical instability without excessive memory requirements. The interaction among particles is monitored contact by contact and the motion of particles is traced particle by particle (Cundall and Strack, 1979).

The simulation processes in DEM involves two dependent schemes: first application of Newton's second law (equation of motion) to the particles and second application of a force-displacement law at the particle contacts. Unlike in continuum models, DEM predicts the stresses of the average quantities over a representative measurement volume. This procedure allows estimating the micro-stresses for the assembly considered. On the other hand, strain rates are computed using a velocity-gradient tensor based on a best-fit procedure that minimizes the error between the predicted and measured velocities within the measurement volume.

In DEM, more complex physical properties of the material, example aggregate shape, size, and gradation can be similarly represented and modeled using clusters of particles forming particle clumps. Therefore, this modeling technique is particularly suitable to investigate the mechanical behavior of materials and hence can effectively predict the performance properties of AC mixtures under different loading and testing conditions.

Due to the recent advancement in cutting-edge computing technology, the application of DEM has been growing to a variety of engineering fields. *Particle Flow Code in two-dimensions*, abbreviated as PFC^{2D}, is a commercial DEM model implementing the Cundall and Hart, (1992) algorithm. It is available commercially by Itasca Consulting Group, Inc. PFC^{2D} has the following advantages in modeling ACs:

- Aggregate particles in AC mixtures can be effectively represented using clusters or clumps of circular particles and their physical properties can be easily characterized.
- The asphalt binder or mastics can be treated as a viscoelastic material cementing the aggregate particles which can be treated as elastic material.
- The target percent air void can be used as a limiting value for compaction process of the granular assembly.
- The aggregate-to-aggregate friction and interlocking behavior can be handled.

In the last few decades, the application of DEM has been increasing to study the micromechanical behavior of AC materials. AC mixture permanent deformation tests can be realistically simulated using DEM to evaluate their rutting resistance potential. Several researchers have used the DEM simulation technique to characterize different behavior aspects of ACs. The following section briefly reviews the micromechanical approaches that have been developed for characterization different behavior of AC mixtures in a chronological order.

Rothenburg et al., (1992)

Rothenburg et al., (1992) proposed a micromechanical discrete model to investigate the behavior of AC rutting. In this model, AC was represented by a set of discrete elastic elements bounded by a linearly viscoelastic binder, and the binder within voids was treated as a compressible Newtonian fluid as shown in Figure 2.4. It was demonstrated that the mechanical response of asphalt concrete is highly dependent on the performance of the granular material. Simulation of the creep tests also showed that the steady-state properties were also largely controlled by the proportion of frictional inter-granular contact compared to the proportion of cohesive contact. The peak unconfined

compressive strength was obtained when the proportion of cohesive and frictional contacts was approximately 60% and 40%, respectively.

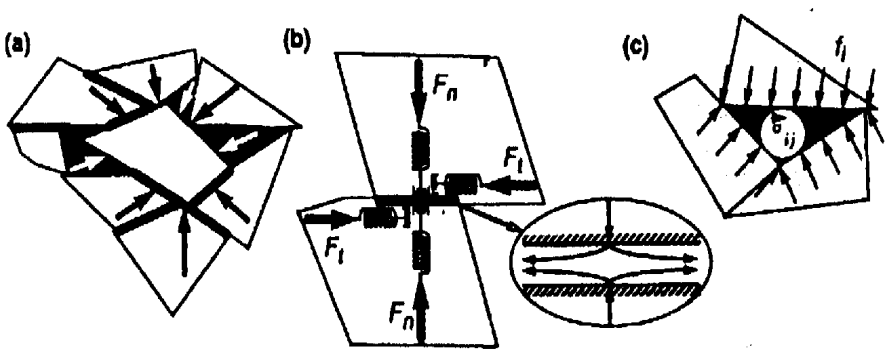

Figure 2.4 Forces Acting on Aggregate and Binder; (a) Forces Acting on Particles, (b) Aggregate-Aggregate Interaction, and (c) Aggregate-Binder Interaction (Rothenburg et al., 1992)

Buttlar and Roque, (1996)

Buttlar and Roque, (1996) showed the superiority of the micromechanical models to predict the viscoelastic properties of mastics. However, they concluded that the existed micromechanical models were found to underestimate the asphalt mixture stiffnesses at low temperatures due to a lack of proper characterization of binder and aggregate interaction in AC mixtures.

Chang and Meegoda, (1997)

Chang and Meegoda, (1997) proposed an innovative DEM model by modifying the TRUBAL program to describe different types of aggregate-aggregate and asphalt-aggregate contacts. They utilized mechanistic models to simulate the viscoelastic behavior of asphalt binder using linear viscoelastic elements, namely Maxwell, Kelvin-Voigt, and Burger's elements as illustrated in Figure 2.5. Based on the mechanical responses and comparisons with experimental results, the Burger's element was found to be the most promising for modeling asphalt binder behavior. They incorporated a Mohr-Coulomb failure criterion for the sliding of asphalt-coated particles. During the

simulation processes, both macroscopic and microscopic behavior was monitored. They concluded the simulation of AC mixtures using DEM was successful compared to experimental results.

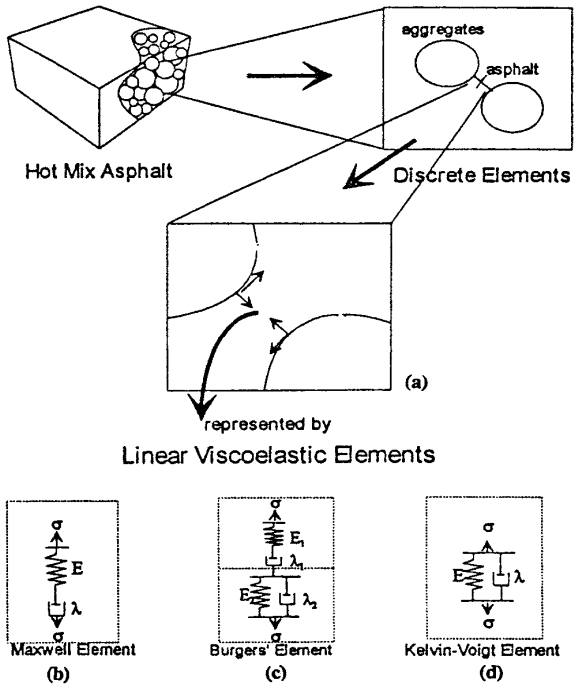

Figure 2.5 Micromechanical Systems of Hot-mix Asphalt (HMA) (Chang and Meegoda, 1997)

Cheung et al., (1999)

Cheung et al., (1999) studied the deformation behavior of an idealized AC mixture with an isotropic and anisotropic microstructure using an isolated contact model first developed for the analysis of powder compaction as shown in Figure 2.6. The model showed promise in predicting the deformation behavior of the idealized AC mixture. Moreover, it was concluded that the distribution of thin films of bitumen was very sensitive to the stress path. They concluded that the deformation behavior of an idealized AC mixture, which is different in tension and compression, depends on the deformation behavior of the mixture constituents, the structural arrangement of the particulate materials, and the stress levels.

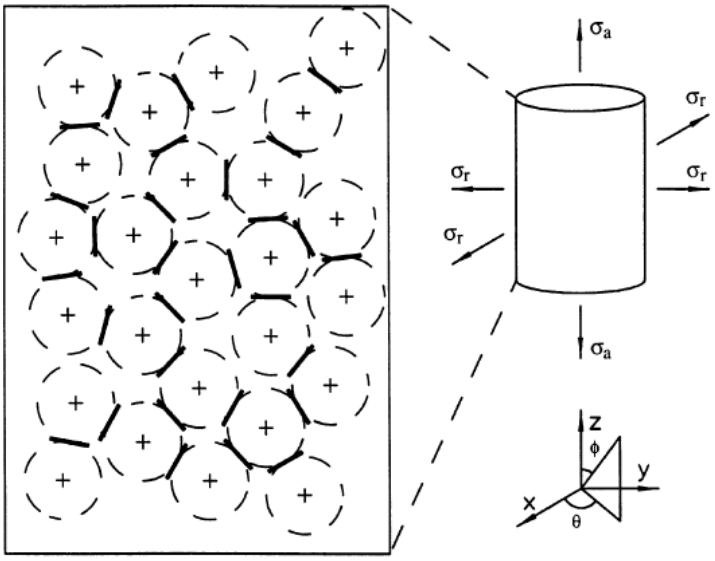

Figure 2.6 Two-dimensional Schematic Representation of an Idealized AC Mixture Subjected to Axisymmetric State of Stress (Cheung et al., 1999)

Uddin, (1999)

Uddin, (1999) presented a micromechanical analysis method for calculating the creep compliance of AC mixtures on a microscopic level using the laboratory viscoelastic characterization of the binder and elastic material properties of the aggregate at a given temperature. The micromechanical model is based upon the "method of cells" (MOC) developed by Aboudi, (1991) to predict viscoelastic response of resin matrix composites. In their models, the properties of the aggregate are assumed to be linear elastic. A time-stepping algorithm was developed for the viscoelastic material with a Prony series representation of the time-dependent properties.

Shashidhar et al., (2000)

Shashidhar et al., (2000) investigated the role of aggregate structures in asphalt pavements and demonstrated that AC mixture even with the presence of asphalt binder behaves as a granular material. They also concluded that the stress patterns within the AC material differ from the assumptions made in continuum-based models. It is also evident

that asphalt pavements constructed with gap-graded mixture exhibit typical granular materials with discontinuous aggregate gradation.

You and Buttlar, (2001)

You and Buttlar, (2001) presented a two-dimensional Microfabric Distinct Element Method (MDEM) to model the AC microstructure by extending the traditional DEM analysis that accounts for aggregate and mastic phases in AC mixtures. They described the AC microstructure using clusters of circular particles to simulate the behavior of asphalt mixture in the Indirect Tension Test (IDT). A linear contact model with bonding and sliding capabilities was used to define particles interaction. It was concluded that the aggregate-to-aggregate interaction and their physical properties have significant effects on the simulated stiffnesses of AC mixtures. Further, You and Buttlar, (2002) extended the approach to model the uniaxial compression tests on coarse grained mixtures and mastics. It was found that the DEM dynamic modulus simulation results were in good agreement with the experimental observations for coarse grained mixtures, while the DEM predicted dynamic modulus of the mastic mixtures were not favorable with experimental results. They also pointed out that insufficient aggregate-to-aggregate contact affects the dynamic modulus simulation results.

Collop et al., (2004a)

Collop et al., (2004a) investigated the use of DEM using the *Particle Flow Code in three-dimensions* (PFC^{3D}). Simulation processes were carried out on a highly idealized bituminous mixture using uniaxial creep tests in compression. In this study, the effects of particle size and contact stiffnesses along the normal and shear direction on material properties were assessed. The minimum number of particles needed to predict AC elastic modulus and Poisson's ratio parameters within certain degree of accuracy were quantified. Moreover, the bulk modulus of the idealized mixture showed a linear dependency on the normal contact stiffness and the Poisson's ratio was found to be dependent on only the ratio of the shear contact stiffness to the normal contact stiffness. They also extended the study to include the Burger viscoelastic model to account time dependency contact stiffnesses.

You and Buttlar, (2004)

You and Buttlar, (2004) further extended the prediction of the dynamic modulus of AC mixtures using different testing temperatures and loading frequencies to account for aggregate-to-aggregate contacts. To do this, they proposed a method to increase the aggregate sizes so as to create additional aggregate contacts and found an apparent sensitivity of the AC dynamic modulus to high temperatures.

Abbas et al., (2005)

Abbas et al., (2005) studied the behavior of asphalt mastics using DEM and micromechanics-based models, namely the lower-bound Hashin model, the generalized self-consistent scheme model, and the inverse rule of mixtures. They found that the micromechanics-based models underestimate the stiffening effect of the mineral fillers and are not sensitive to the change in dynamic shear moduli of the asphalt binder. Moreover, they demonstrated the potential application of DEM model to capture the effect of the aggregate filler volume fraction on the mastic stiffness. In their simulation, the binder stiffness value was multiplied by a factor of 30 in order to obtain reasonable prediction of the dynamic shear modulus of the AC mixture. They concluded that the predicted dynamic shear modulus of the mastic was shown to be highly dependent on the dynamic shear modulus of the binder, which is in agreement with experimental data. Moreover, the effects of adhesive bonds along with thin and thick films of the binders were analyzed and found that the models containing thin films of binder were more sensitive to the adhesive bond strength than those containing thick films of the binder.

AC mixtures exhibited dilation under shearing load. There are many studies in the literature on modeling AC mixture dilation behavior using continuum-based models (Lytton et al., 1993; Tashman, 2003; Dessouky, 2005). However, only few studies were found addressing this phenomenon using the DEM simulation techniques (Collop et al., 2006; Zelelew et al., 2007a).

Collop et al., (2006)

Collop et al., (2006) simulated the dilation behavior of an idealized AC mixture using PFC^{3D} under uniaxial and triaxial creep tests in compression. They found that

dilation behavior is observed when the ratio of compressive to tensile contact stiffness increases as a function of loading time. Further, viscoelastic simulations were performed to investigate the effects of stress ratio on the rate of dilation and found that dilation increases when the stress ratio decreases.

Zelelew et al., (2007a)

Zelelew et al., (2007a) developed a user-defined viscoplastic contact model implemented in PFC^{2D} to simulate the confined static creep tests on idealized AC mixtures under biaxial compression conditions. In their model, the asphalt binder was treated as a viscoplastic material cementing the aggregate particles which were considered to be elastic materials. It was found that the volumetric strain behavior in AC mixtures due to the imposed shear was initially contractive followed by a dilative. A significant observation in this simulation was that the time at which the dilation begins corresponds to the flow time of the AC mixtures. Moreover, the dependency of dilation level on the confining stress levels was also clearly demonstrated.

2.3.3 Continuum-Micromechanical Approach

Recently, researchers have attempted to model behavior of geomaterials using hybrid modeling schemes combining the continuum and micromechanical modeling approaches. Several researchers implemented Finite Element Method (FEM) and discrete element method (DEM) to model/simulate the different material behavior, such as soils (e.g., Onate and Rojek, 2004; Bierawski and Maeno, 2006; Rojek, 2006), rocks (e.g., Zhang et al., 2004; Morris et al., 2006), and concretes (e.g., Bangash and Munjiza, 2002a, 2002b).

Recently, FEM-DEM modeling and simulation techniques were implemented to characterize the AC mixture properties under range of temperature and laboratory testing conditions. Dai and You, (2007) predicted the viscoelastic creep stiffness of AC mixture using FEM and DEM models. The FE model utilized an equivalent lattice network structure whereby inter-granular load transfer is simulated through an effective asphalt mastic zone. These models significantly over-predicted the creep stiffnesses at initial loading stage. On the other hand, the DE models used the two-dimensional

microstructure of asphalt mixtures, which was obtained by optically scanning the smoothly sawn surface of asphalt specimens. This approach under-predicted the creep stiffnesses, especially at higher test temperature and longer loading time as illustrated in Figure 2.7. It was found that the aggregate stiffness values affect the simulation results significantly. In their model, a regression fitting method was employed to evaluate mastic viscoelastic properties with a generalized Maxwell model.

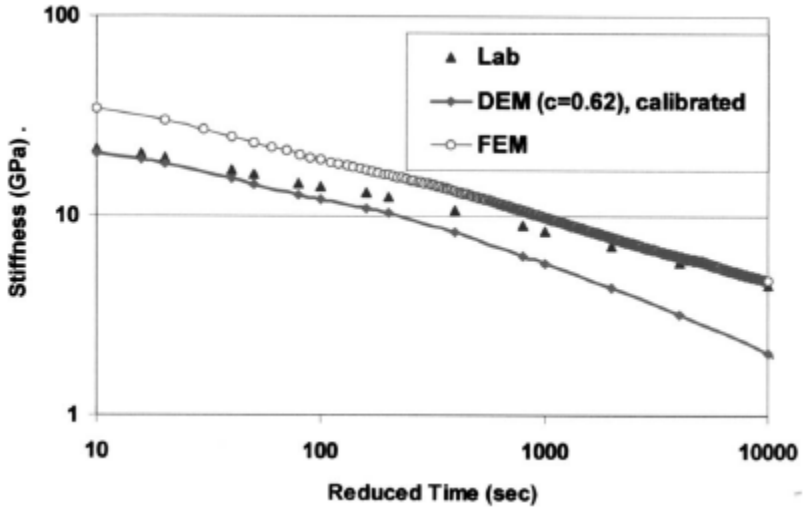

Figure 2.7 FEM and DEM Predictions and Measurements of AC Mixture Creep Stiffness Versus Reduced Time (Dai and You, 2007)

2.4 Summary and Conclusions

In this chapter, the causes and mechanism of AC pavement rutting and the laboratory testing methods involved to characterize rutting were presented. Relevant studies in relation to modeling the permanent deformation behavior of ACs using the numerical modeling approaches, namely continuum, micromechanical, and continuum-micromechanical were briefly reviewed. The efforts to characterize the different behavior of AC mixtures using DEM simulation techniques are presented. In addition, the potential applicability of DEM to simulate the permanent deformation behavior of the AC mixtures is demonstrated.

Chapter 3

RESEARCH METHODOLOGY

3.1 Background

In Chapters 1 and 2, the problem statement was briefly stated and the most relevant literature on addressing the AC permanent deformation challenges were described. As clearly mentioned in these chapters, ACs are uniquely heterogenous materials composed of air voids, mastics and aggregates. Efforts to characterize their permanent deformation characteristics include physical testing, as well as numerical simulation. The later have a number of distinct challenges involving, the characterization of their microstructure as well as the mechanical behavior of their constituents. This study aims to address some of the issues involved in modeling the plastic deformation behavior of ACs. It involves (1) characterization of the viscoelastoplastic behavior of the mastic through laboratory measurements, (2) development of a Volumetrics-based Global Minima (VGM) thresholding algorithm for processing X-ray CT images of the AC microstructure, (3) numerical simulation of the plastic deformation of ACs using the DEM, and (4) verification of the results of the plastic deformation simulation results using creep test data. The methodology to be followed in carrying out these steps is highlighted in Figure 3.1 and described in detail next.

3.2 Experimental Plan

The laboratory experimentation includes:

1. **Rheological Tests on Asphalt Binders and Mastics:** The viscoelastoplastic characterization of binders and mastics will be obtained using a Dynamic Shear Rheometer (DSR). Only one binder type needs to be tested, a PG 76-22, because that is the binder type used in the AC cores subjected to creep testing. Mastics were prepared using this binder unaged and Rolling Thin Film Oven (RTFO) aged. The fines introduced were sizes finer than 75 μm. For each specimen, amplitude sweep tests (AST) will be performed to determine the linear viscoelastic (LVE)

range and limiting strain values using three different angular frequencies, namely 10, 1, and 0.1 rad/sec. Then, frequency sweep tests (FST) will be performed by specifying the maximum LVE range strain as the maximum strain amplitude and testing over a range of angular frequencies from 0.01 to 100 rad/sec. FSTs are primarily used to fit the Burger model parameters in addition to characterize the rutting behavior of the neat and RTFO-aged binders. Fitting the binders and mastic Burger model involves implementing a nonlinear optimization tool in MATLAB® to fit the complex shear modulus ($|G^*|$) and the phase angle (δ) measured values.

2. **Uniaxial Static Creep Tests on AC Mixtures:**

   In this research, the AC mixture data of a Texas DOT funded study (http://ctis.utep.edu/publications/userprogramList_form.php Alvarado et al., (2007) is utilized. The nine AC mixtures were prepared at the University of Texas-El Paso according to the Tex-241-F and Tex-205-F specifications. Three aggregate types, namely hard limestone (HL), granite (G), and soft limestone (SL) were selected from three TxDOT districts. Uniaxial static creep tests in compression at a single chamber temperature of 60°C were performed to assess their rutting resistance potential. The parameters used to characterize the permanent deformation behavior will be the total axial strain and creep compliance with loading time when plotted in linear and log-log scale, respectively. The regression parameters (i.e., the intercept and slope) of the steady-state region in creep compliance curves in addition to the flow time will be used as criteria to investigate the AC mixture rutting behavior.

3. **X-ray CT Scanning of the AC Cores:** The X-ray CT scanning to capture the AC microstructure took place at Texas A&M University. Each of the nine AC cores (150mm height by 100mm diameter) was scanned perpendicular to its axis at 1 mm distance interval to yield 148 slices per core, ignoring the top and bottom slices.

3.3 Development of a Robust Gray Scale Thresholding Algorithm

A new robust thresholding algorithm will be developed that can automate the processing of these AC X-ray CT images. The algorithm will be implemented in the MATLAB® environment. The method will use a global minima percent error approach and utilizes the actual volumetric properties of AC as a thresholding criterion and hence, it is referred to as a Volumetrics-based Global Minima (VGM) thresholding algorithm. It applies to images of sections of AC cores taken perpendicular to the axis at regular distance intervals. Applicable to the AC X-ray CT images, it should have a potential to:

- distinctly delineate the AC mixture constituents gray level boundary thresholds. For this research task, the algorithm seeks to establish two gray level thresholds, a lower threshold corresponding to the air void-mastic boundary, and a higher threshold corresponding to the mastic-aggregate boundary.
- construct the AC images in 3D and sectioning them for 2D representation
- characterize the AC mixture constituents distribution by volume and pixel area
- represent the AC mixture suitable for numerical simulation purposes (example DEM and FEM)
- characterize the aggregate segregation in AC mixtures
- characterize the aggregate image texture in AC mixtures

VGM will be a versatile thresholding algorithm that can also be used to characterize X-ray CT images of other geomaterials.

3.4 Numerical Simulation of AC Mixtures

To numerically predict the AC rutting, a DEM simulation technique will be implemented. A commercially available DEM software called *Particle Flow Code in two-dimensions* (PFC^{2D}) will be utilized to simulate the uniaxial static creep test condition of AC mixtures. PFC^{2D} accepts the processed images from the VGM thresholding algorithm. In PFC^{2D}, the clump logic will be utilized by clustering smaller particles that act as a rigid body material to represent aggregates. On the other hand, mastic particles will be treated as a viscoelastic material mainly responsible for cementing the aggregate particles. The Burger model will be utilized to simulate the viscoelastic behavior of AC mixtures. The parameters of this model will be determined

from the mastic rheological tests. In addition, proper boundary and initial conditions will be used. The microproperties of the linear contact model will include aggregate-mastic particle interaction. Moreover, reasonable assumptions will be made for aggregate-to-aggregate and aggregate-to-mastic contacts. Finally, the permanent deformation of the AC mixtures will be predicted by simulating the uniaxial static creep tests.

3.5 Result Verification and Evaluation of AC Mixtures for Rutting

The predicted and experimentally measured permanent deformation values will be compared and verified statistically. At the end, the rutting resistance of the AC mixture tested and simulated will be evaluated based on their steady-state region regression parameters (i.e., intercept and slope) using creep compliance curves in log-log scale. The flow time, defined as the time at which tertiary flow starts, of the mixtures will also be used to assess their rutting behavior.

Based on the experimental and numerical investigation of the rutting behavior of AC mixtures, summary, conclusions, and recommendations for future research study will be given.

3.6 Summary

This research methodology capitalizes on recent developments, viscoelastoplastic binder characterization and modern numerical simulation techniques. In addition, it will provide a novel automated method for characterizing the AC microstructure using X-ray CT images. Its outcome will be the creation of “virtual” AC samples being subjected to creep loads.

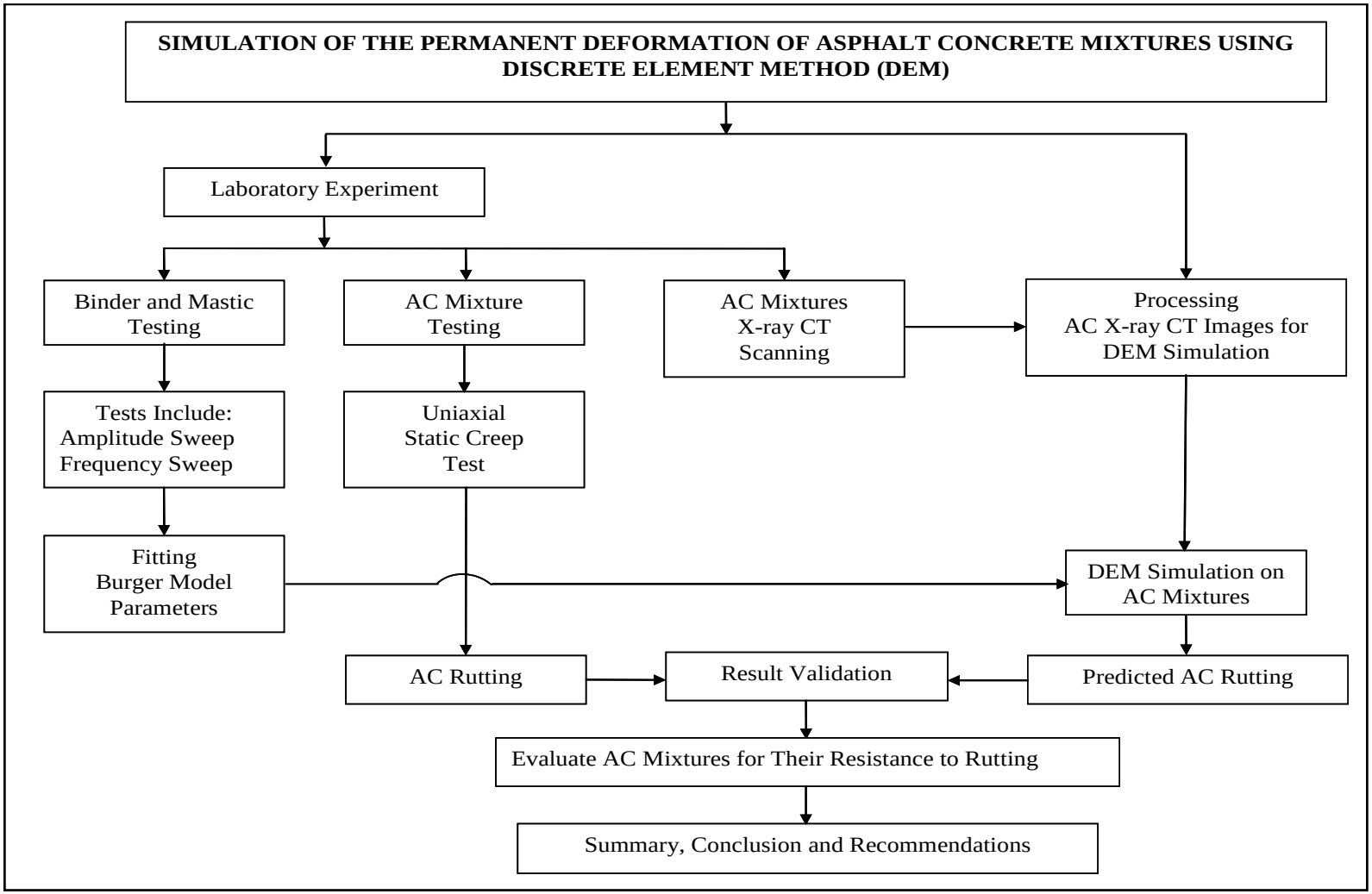

Figure 3.1 Research Methodology Flowchart

Chapter 4

UNIAXIAL STATIC CREEP TESTS ON ASPHALT CONCRTE MIXTURES

4.1 Introduction

This chapter discusses in detail the experimental design procedures used for material selection, specimen preparation and unconfined uniaxial static creep testing on nine AC mixtures. At the end, a summary of data on the resistance of these mixtures to permanent deformation is presented.

4.2 Asphalt Concrete Mixtures and Mix Design

The AC mixture data utilized in this thesis was obtained from a Texas DOT funded study, as described earlier (Alvarado et al.,, 2007). Three aggregate types were selected from three TxDOT districts, namely hard limestone (HL), granite (G), and soft limestone (SL). They are supplied respectively by Vulcan Materials Inc. located in Brownwood, McKelligon Canyon plant operated by CEMEX and located in El Paso, and Martin Marietta Materials at the Beckman plant located in San Antonio, Texas. These aggregates are commonly used in TxDOT paving industries and their performance histories are well documented. For each of these aggregate sources, three AC mixture types were chosen, namely Coarse Matrix High Binder type C (CMHB-C), Porous Friction Course (PFC), and Superpave type C (Superpave-C). The aggregate gradation curves for these mixtures are shown in Figure 4.1. The CMHB-C mix is a coarse-graded mixture composed of 63% coarse aggregates and 37% fine aggregates. In contrast, Superpave-C is a fine-graded mixture consisting of 35% coarse aggregates and 65% fine aggregates. The PFC is a coarse, gap-graded mixture with a high percentage by weight of coarse aggregates. It is composed of 89% aggregates larger than a sieve No. 8.

A total of nine AC cores was produced, each involving a combination of three different mix designs using the selected aggregate types. To minimize the effect of binder

properties on the overall performance results, only one binder grade, a PG 76-22, was used for all mixtures. The binder content varied from 4% to 7.1%, where the lowest and highest value corresponds to the Superpave-C and the PFC mixes, respectively. It should be noted that the CMHB-C mix design did not meet the TxDOT specifications of 15% VMA. Similarly, dust proportion of 0.6 to 1.2 was not met for some of the mixes (Alvarado et al.,, 2007). The mixing and compaction temperature ranges were (192-200^{0}C) and (178-184^{0}C), respectively. As per the Tex-241-F specifications, 1% lime and 0.4% fiber were added for PFC mixtures. The AC mixtures were compacted using Superpave gyratory compactor to achieve a target air void content of 7% for mixtures CMHB-C and Superpave-C and 20% for PFC mixes. The actual test specimens were cored and sawn from a diameter of 150 mm to 100 mm and from a height of 165 mm to 150 mm. The detailed mixture design parameters and the Job Mix Formula (JMF) relevant information for all the nine AC mixtures are summarized in Table 4.1.

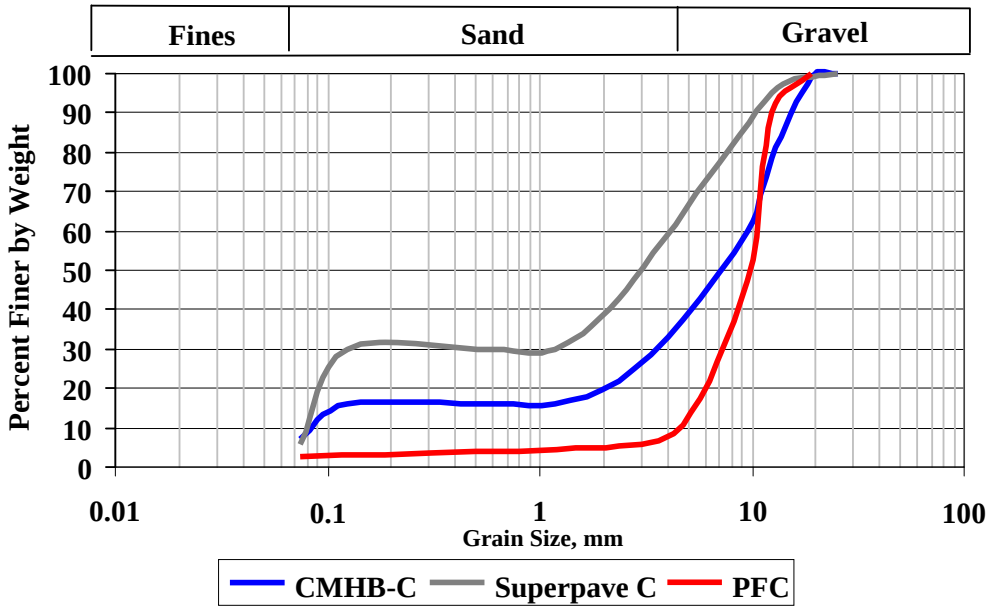

Figure 4.1 Aggregate Gradation Curve for CMHB-C, Superpave-C, and PFC Mixtures

Table 4.1 Asphalt Concrete Mixture Design Parameters (Alvarado et al.,, 2007)

Parameter	Hard Limestone			Granite			Soft Limestone		
	CMHB-C	Superpave-C	PFC	CMHB-C	Superpave-C	PFC	CMHB-C	Superpave-C	PFC
Binder Grade	PG 76-22								
Binder Content,%	4.2	4.0	5.1	5.3	4.8	6.6	5.8	5.2	7.1
Sieve Size Sieve No. (mm)	Percent Passing (%)								
1 (25.0)	100	100	100	100	100	100	100	100	100
3/4 (18.75)	99	99	100	99	99	100	99	99	100
1/2 (12.5)	78.5	95	90	78.5	95	90	78.5	95	90
3/8 (9.38)	60	92.5	47.5	60	92.5	47.5	60	92.5	47.5
No. 4 (4.75)	37.5	77.5	10.5	37.5	77.5	10.5	37.5	77.5	10.5
No. 8 (2.36)	22	43	5.5	22	43	5.5	22	43	5.5
No. 16 (1.18)	16	30	5	16	30	5	16	30	5
No. 30 (0.600)	-	-	4.5	-	-	4.5	-	-	4.5
No. 50 (0.300)	-	-	3.5	-	-	3.5	-	-	3.5
No. 200 (0.075)	7	6	2.5	7	6	2.5	7	6	2.5
Maximum Specific Gravity	2.554	2.572	2.555	2.471	2.520	2.469	2.450	2.515	2.445
Aggregate Bulk Specific Gravity	2.696	2.715	2.673	2.601	2.655	2.526	2.587	2.653	2.527
Binder Specific Gravity	1.02								
Air Voids at N_{design} = 100,%	7.3	7.4	19.5	6.9	6.9	19.6	7.0	6.7	19.3
VMA at N_{design} = 100, %	12.7	12.7	27.2	13.7	13.2	27	14.3	13.7	28
VFA at N_{design} = 100,%	70.2	68.5	26.4	69.7	69.9	25.8	72.5	70.9	28.8
Effective Binder Content, %	3.7	3.6	3.7	4.1	3.9	3.6	4.5	4.1	4.2
Dust Proportion, %	1.7	1.5	0.5	1.3	1.3	0.4	1.2	1.2	0.4

4.2.1 Characterization of Aggregate Physical Properties

Aggregates transmit the wheel loads through internal friction and interlocking. The physical properties of aggregate play a significant role in the performance of the AC pavements Masad, (2002). Aggregates used in the surface of the flexible pavement are subjected to wear under a heavy in-service traffic. Aggregates are subject to crushing and abrasive wear during manufacturing, placing, and compacting AC and therefore must be hard and tough enough to resist degradation and disintegration. Therefore, the aggregate resistance to degradation should be assessed. The Los Angeles (LA) abrasion (Tex-410-A) and Micro-Deval abrasion (Tex-461-A) tests were performed to characterize the physical properties of hard limestone (HL), granite (G), and soft limestone (SL). Table 4.2 illustrates the aggregate properties of these aggregates. It is demonstrated that the test results met the specification.

Table 4.2 Aggregate Properties (Alvarado et al.,, 2007)

Aggregate Tests	Hard Limestone (HL)	Granite (G)	Soft Limestone (SL)	Test Method
Los Angeles % Wt. Loss-Bituminous	23	34	34	Tex-410-A
Mg Soundness-Bituminous[1]	6	13	41	Tex-411-A
Mg Soundness-Stone[2]	5	10	29	Tex-411-A
Polish Value	21	28	25	Tex-438-A
Micro-Deval % Wt. Loss-Bituminous	11.4	9.6	19.7	Tex-461-A
Fine Aggregate Acid Insolubility	5	92	2	Tex-612-J
Micro-Deval %Wt. Loss	15	8.8	20.4	Tex-461-A

[1]Using HMAC Application Sample Size Fractions
[2]Using Other Applications Sample Size Fractions

Masad, (2003) developed an aggregate imaging system (AIMS) to characterize the aggregate physical properties. As illustrated in Figure 4.2, the aggregate particle geometry can be expressed using three distinct physical properties, namely shape (or form), angularity (or roundness), and surface texture.

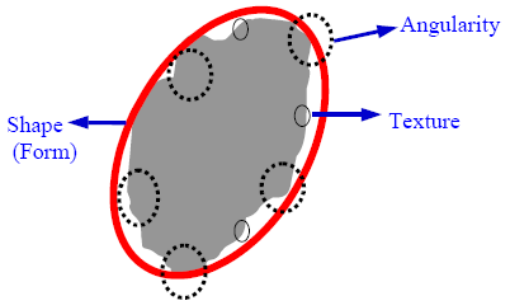

Figure 4.2 Components of Aggregate Shape Properties: Shape, Angularity and Texture (Masad, 2003)

Three different aggregate sizes shown in Table 4.3 from each aggregate were characterized. The properties of aggregate angularity are shown in Figure 4.3. The highest and lowest aggregate angularity was exhibited in granite (G) and soft limestone (SL), respectively. A high angularity index indicates a higher aggregate angularity and yields aggregate interlocking. Characterization of the aggregate surface texture can assist to assess the skidding resistance of the surface course in AC pavements. Chandan et al.,, (2004) implemented a wavelet approach to characterize aggregate texture using AIMS. Figure 4.4 shows the aggregate texture index of the three aggregates used in this study (Alvarado et al.,, 2007). It is clearly shown that granite (G) and soft limestone (SL) yield the highest and lowest texture index values, respectively. Higher texture index yields higher wheel friction and increases safety and vice versa. The sphericity of the aggregates was also characterized using AIMS and a higher sphericity index was obtained for hard limestone (HL) and soft limestone (SL). The granite (G) has the lowest sphericity index and hard limestone (HL) is slightly more spherical than the soft limestone (SL) as illustrated in Figure 4.5. The flatness and elongatedness of the aggregates can be indirectly assessed using the sphericity index (i.e., lower sphericity index indicates a more flat/elongated aggregates).

Table 4.3 Aggregate Sizes Used in AIMS Analysis (Alvarado et al.,, 2007)

Passing	Retained
1/2 in. (12.5 mm)	3/8 in. (9.5 mm)
3/8 in. (9.5 mm)	1/4 in. (6.3 mm)
1/4 in. (6.3 mm)	No. 4 (4.75 mm)

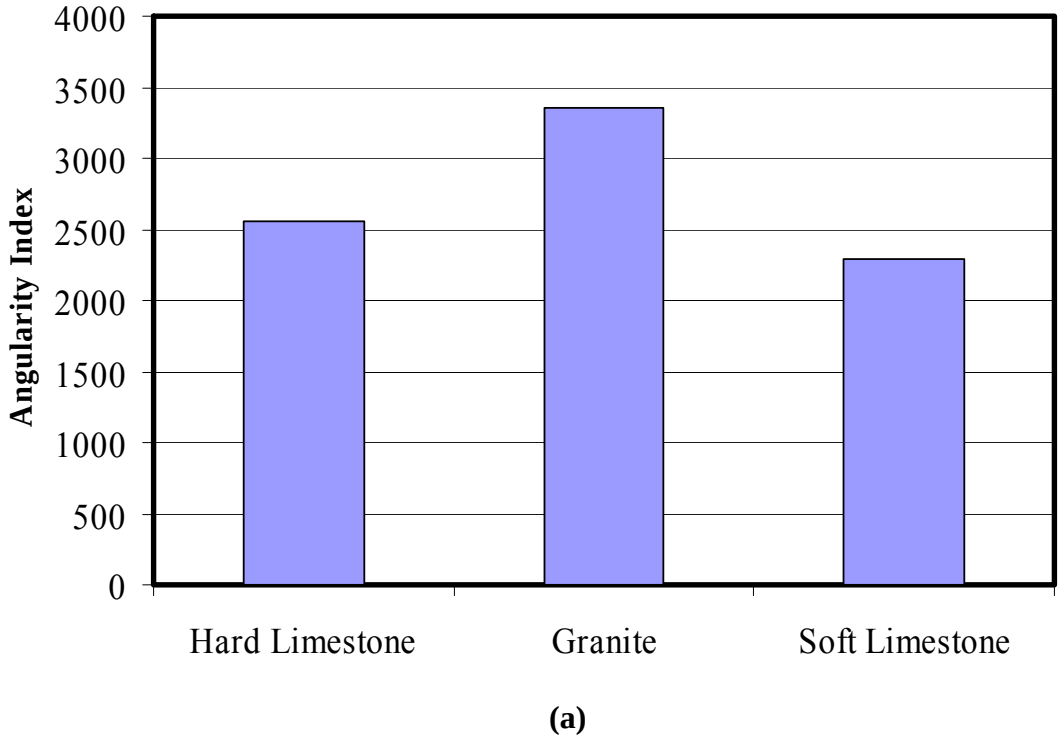

Figure 4.3 Characterization of Aggregate Angularity; (a) 3/8 in. (Alvarado et al.,, 2007)

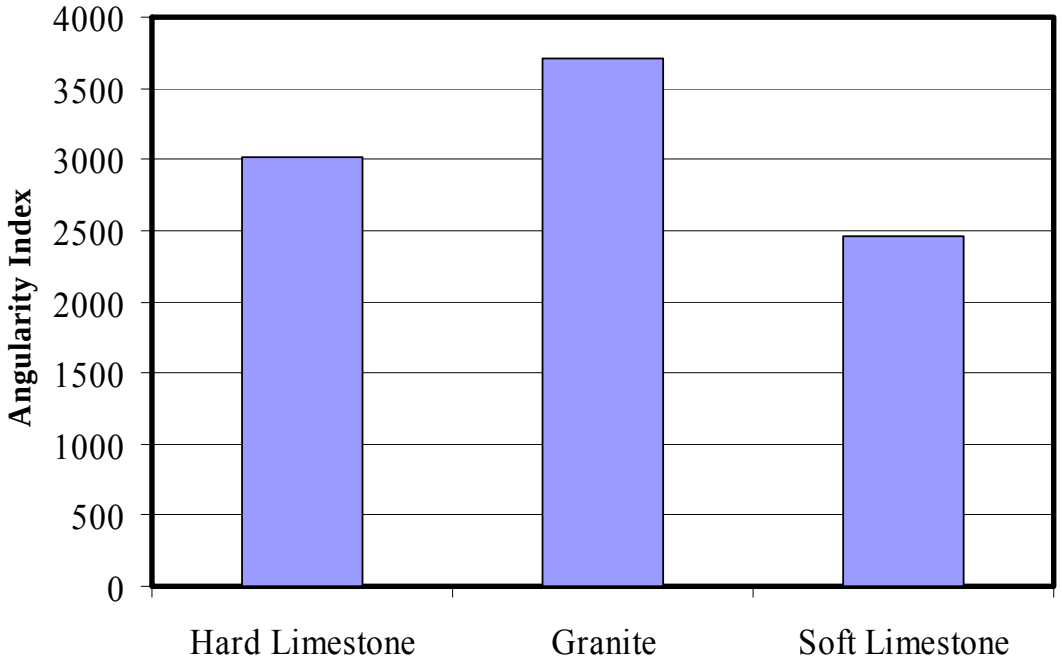

(b)

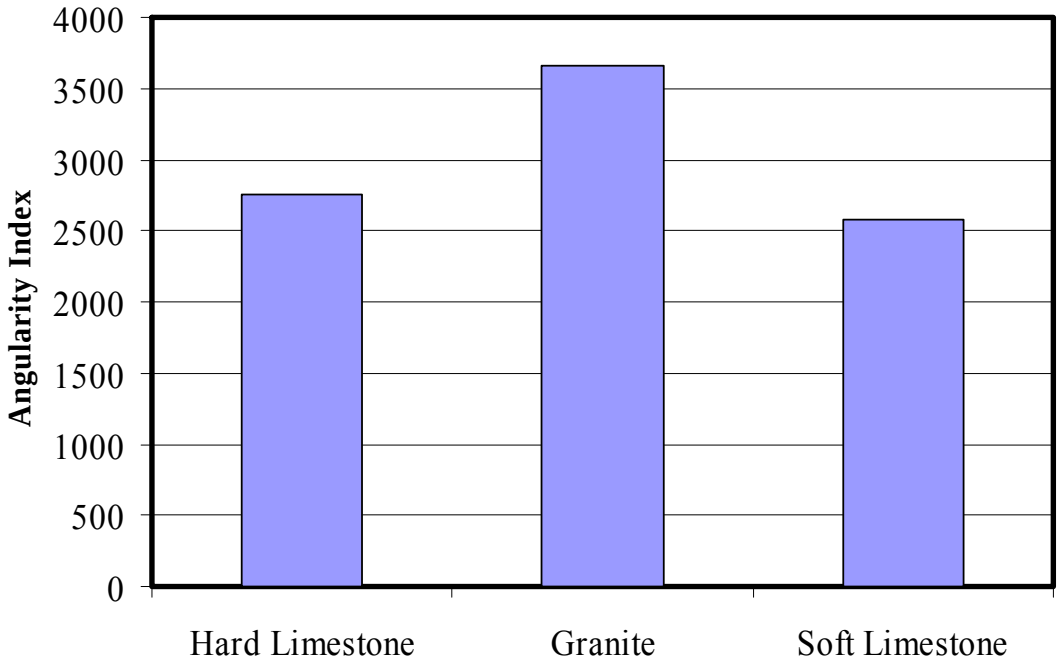

(c)

Figure 4.3 (Continued) Characterization of Aggregate Angularity; (b) 1/4 in. and (c) No. 4 (Alvarado et al., 2007)

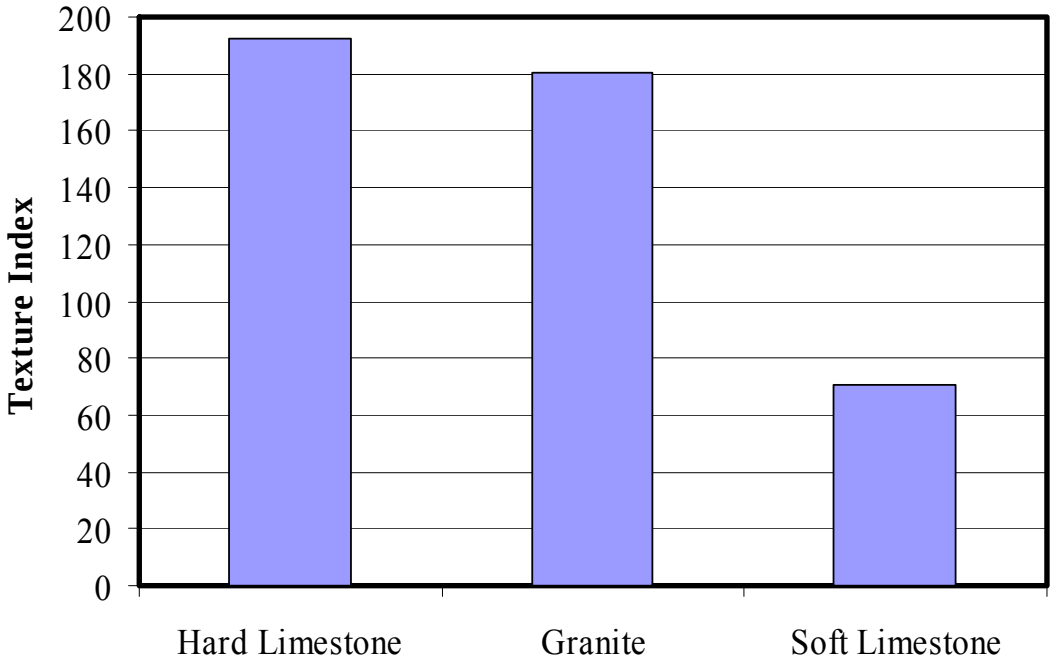

(a)

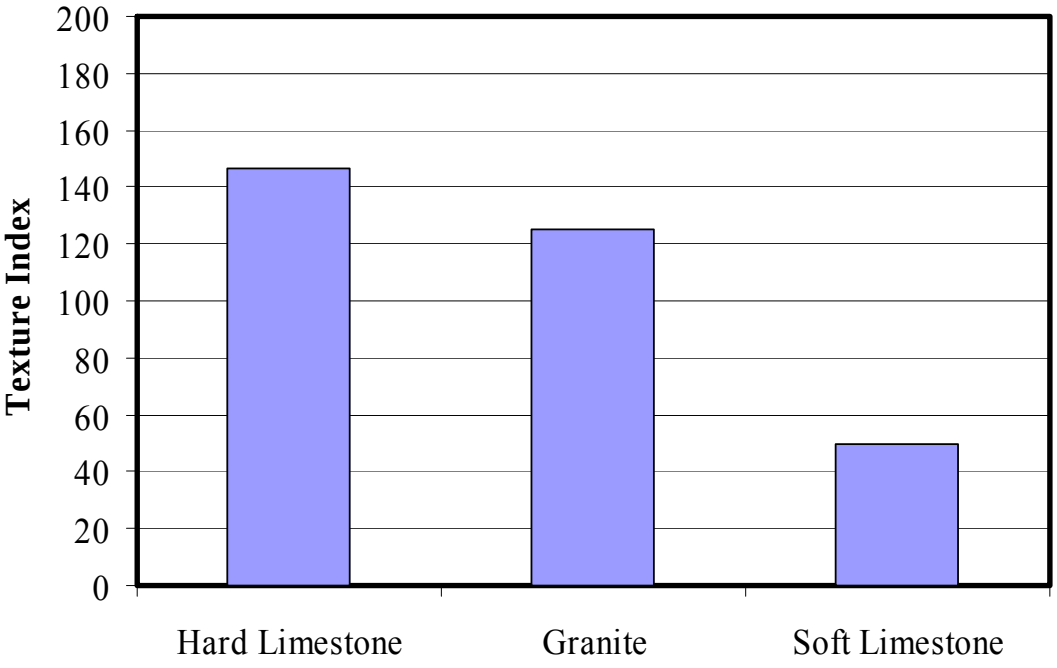

(b)

Figure 4.4 Characterization of Aggregate Surface Texture; (a) 3/8 in. and (b) 1/4 in. (Alvarado et al., 2007)

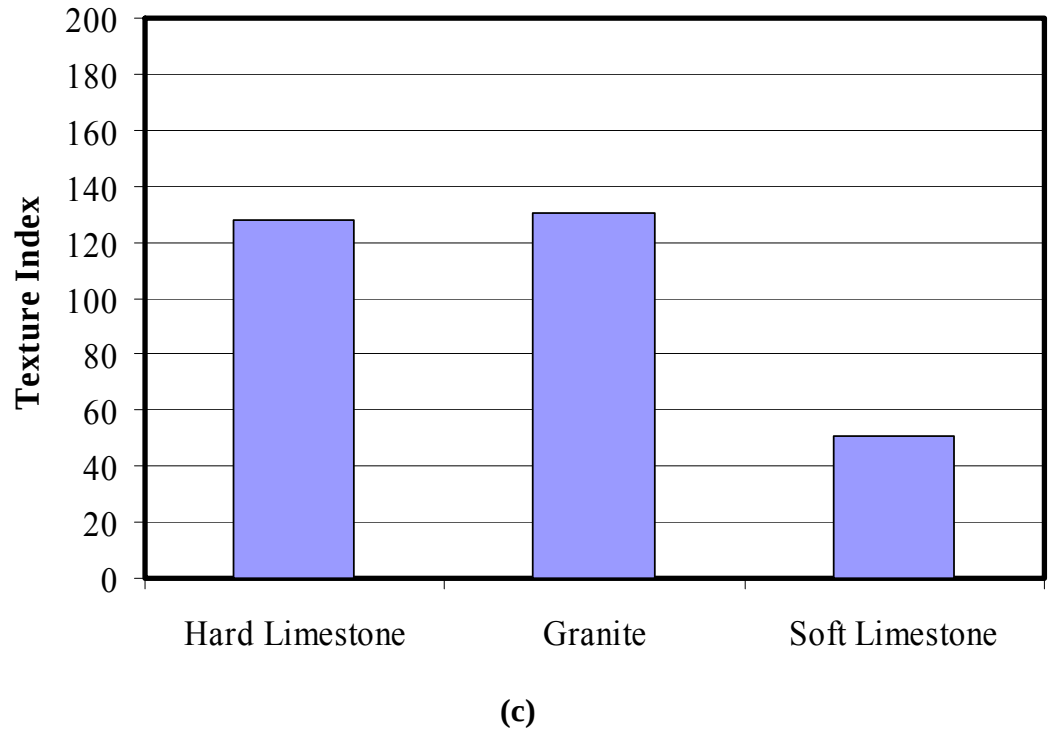

(c)

Figure 4.4 (Continued) Characterization of Aggregate Surface Texture; (c) No. 4 (Alvarado et al., 2007)

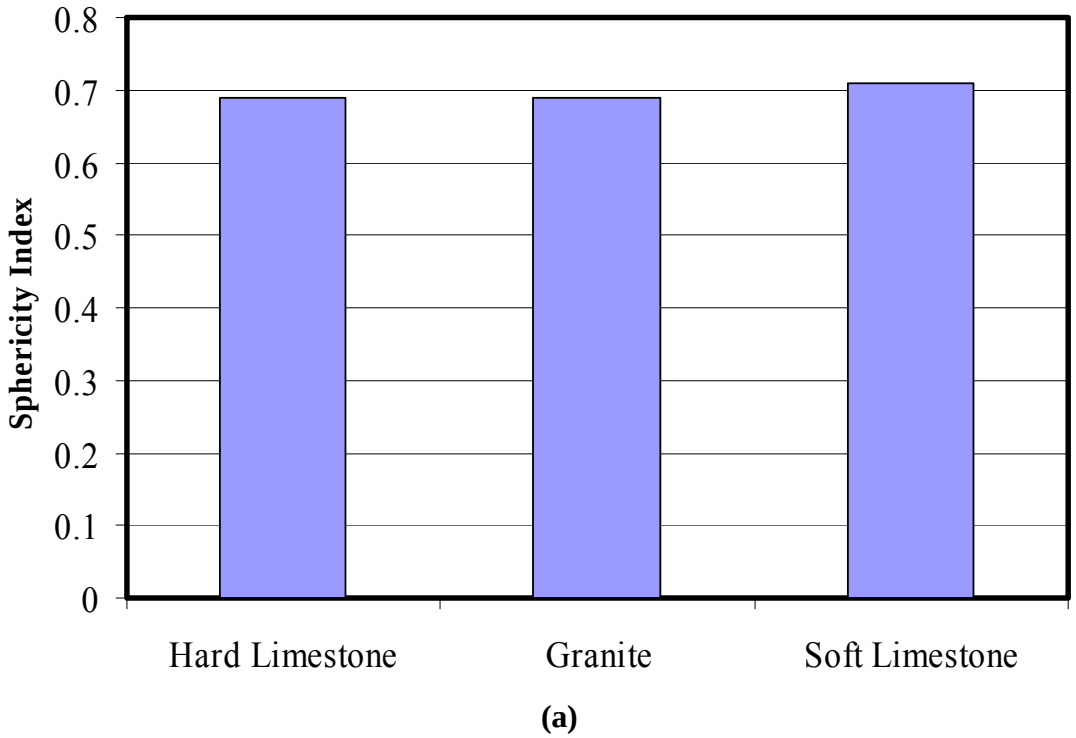

(a)

Figure 4.5 Characterization of Aggregate Sphericity; (a) 3/8 in. (Alvarado et al., 2007)

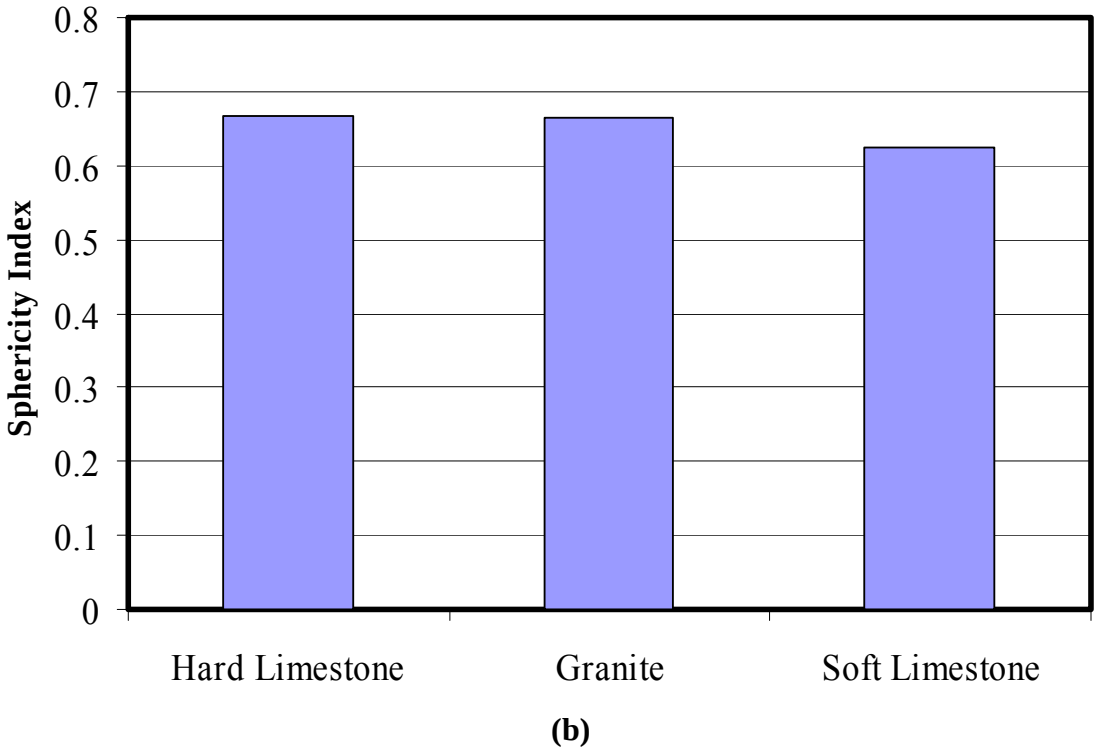

(b)

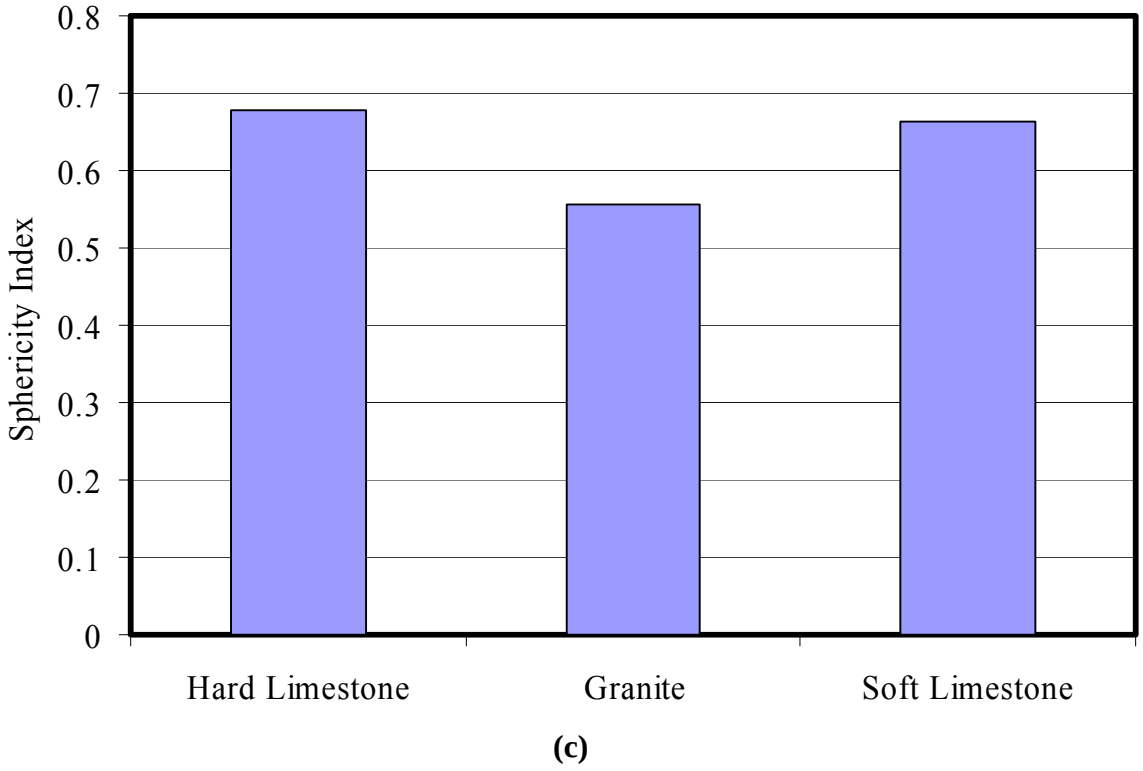

(c)

Figure 4.5 (Continued) Characterization of Aggregate Sphericity; (b) 1/4 in. and (c) No. 4 (Alvarado et al., 2007)

4.2.2 Characterization of Binder Properties

The PG 76-22 binder viscosities at 135^0C and 175^0C temperatures were 2.187 Pa.sec and 0.350 Pa.sec, respectively. The resulting mixing and compaction temperature range were (192-200^0C) and (178-184^0C), respectively. Laboratory characterization of this binder based on the AASHTO T 315 and AASHTO T 240 test protocols produced the results shown Table 4.4. These results represent mean values of three tests. These verification results indicate that the binder met the PG specification consistent with the material properties for PG 76-22.

Table 4.4 PG 76-22 Binder Tests

Test	Method	Test Temperature (^{0}C)	Test Result	Specification
Original Binder				
Dynamic Shear G*/sinδ	T315	60	7.17$^+$ kPa	Min. 1.00 kPa
RTFO Aged Binder				
Mass Loss	T240		<1.0 wt %	Max. 1.0 wt %
Dynamic Shear G*/sinδ	T240	60	18.50$^+$ kPa	Min. 2.20 kPa

$^+$ Average of Three Tests

4.3 Specimen Preparation

This section presents the AC specimen preparation details for conducting the uniaxial static creep tests. It involves aggregate batching, mixing, compaction, sawing and coring. The hard limestone (HL), granite (G) and soft limestone (SL) aggregates were batched consistent with the gradations shown in Tables 4.1. Prior to mixing the binder, these aggregates were pre-heated.

The AC mixture selected mixing and compaction temperature range were (192-200^{0}C) and (178-184^{0}C), respectively. The mixtures were compacted using a *Pine Instrument Corporation* Superpave Gyratory Compactor (SGC) as shown in Figure 4.6. A ram pressures of 600 kPa, a gyration angle and a speed of respectively 1.25 degree and 30 gyrations per minute were used. 150 mm diameter metal plates with same dimensions of paper disks were used. Ordinary grease was used to lubricate the inner surfaces of the mould to prevent sticking of the asphalt concrete mixtures during the compaction process. Using the specified number of gyrations, the compacted specimen had a size of 150 mm diameter and 165 mm height. After compaction, the specimens were placed in horizontally flat surface and were allowed to cool at room temperature for at least 12 hours. Then, the actual test specimens were cored and sawn to a diameter of 100 mm and a height of 150 mm. The resulting specimens were cylindrical with edges free from ridges.

Figure 4.6 Pine Superpave Gyratory Compactor (SGC)

4.4 Uniaxial Static Creep Tests

The behavior of asphalt mixtures under constant load can be captured by performing static creep tests. In the study by Alvarado et al., 2007, a uniaxial unconfined static creep tests (Tex-231-F) on nine AC mixtures were performed using a hydraulic testing machine. The test was carried out on cylindrical specimens, 100 mm in diameter and 150 mm in height. A specimen was placed on the horizontal steel plates and the top surface of the specimen was loaded by a constant load. For each test, the AC specimens were kept in a controlled temperature chamber for 4 hours prior to the start of the actual testing (Tex-231-F). Tests were conducted over a period of three hours at a temperature of 60^0C and a constant stress of 207 kPa. The applied load and axial rate of deformation were continuously recorded using linear variable differential transformers (LVDT). Figure 4.7 shows the loading arrangements of the unconfined static creep tests on AC specimen.

Figure 4.7 Unconfined Static Creep Test Loading Setup

4.5 Experimental Results

In this section, the experimental results containing the axial strain and creep compliance with respect to loading time for the nine AC mixtures are discussed.

4.5.1 Axial Strain

The total axial strain is plotted as a function of the loading time in linear scale after the application of the constant load. Typical results of the unconfined static creep tests for CMHB-C, PFC, and Superpave-C mixtures under constant stress conditions are shown in Figure 4.8 through Figure 4.13. It can be concluded that, mixture HL CMHB-C has the lowest rate of deformation as compared to mixture G CMHB-C, and the SL CMHB-C mixture deforms the most. Similarly, HL PFC and SL PFC mixtures demonstrated less rate of deformation and G PFC deforms severely. On the other hand, G Superpave-C mixture resists rutting while the HL and SL Superpave-C demonstrate similar higher rate of deformation.

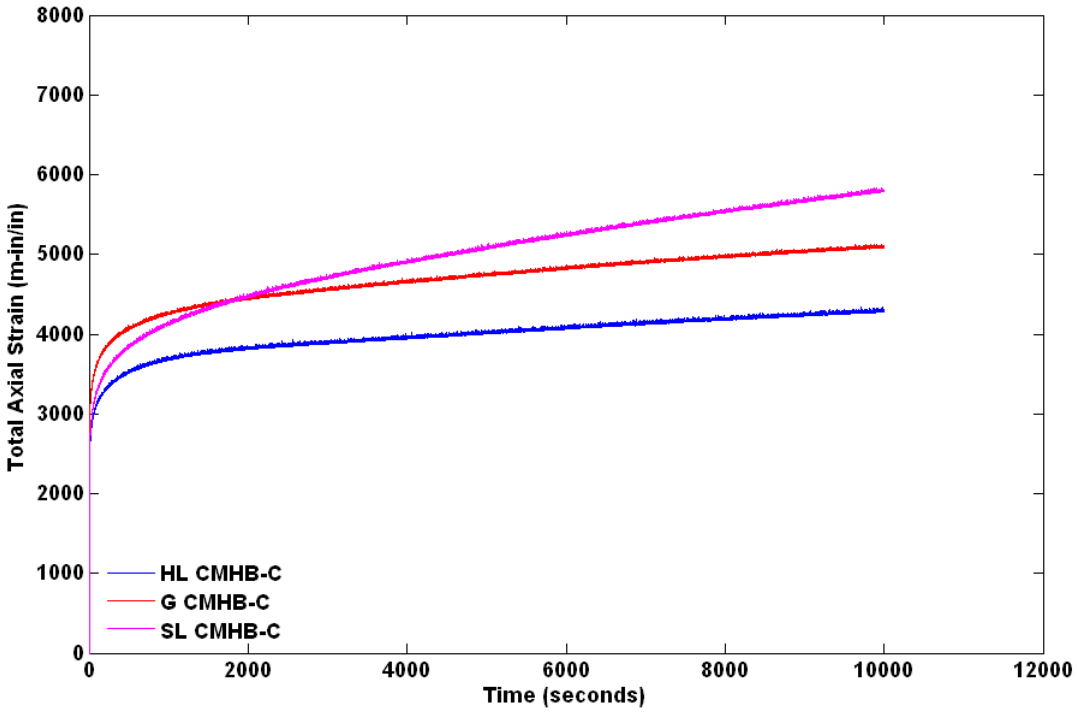

Figure 4.8 Unconfined Static Creep Test Result; Mixture Type CMHB-C

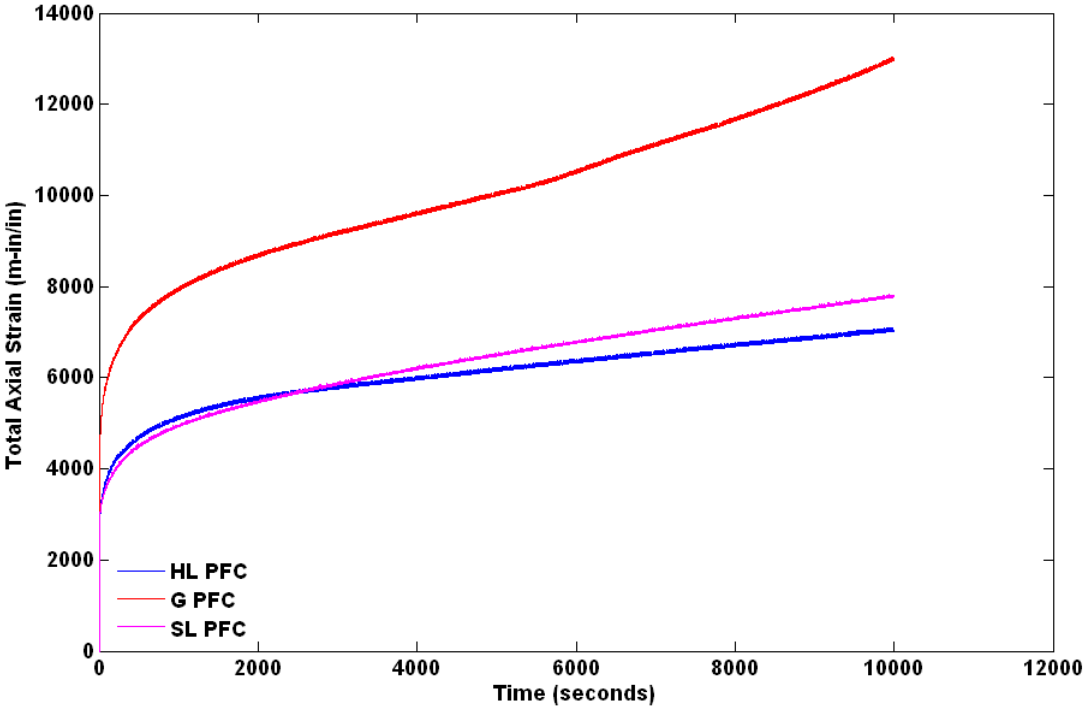

Figure 4.9 Unconfined Static Creep Test Result; Mixture Type PFC

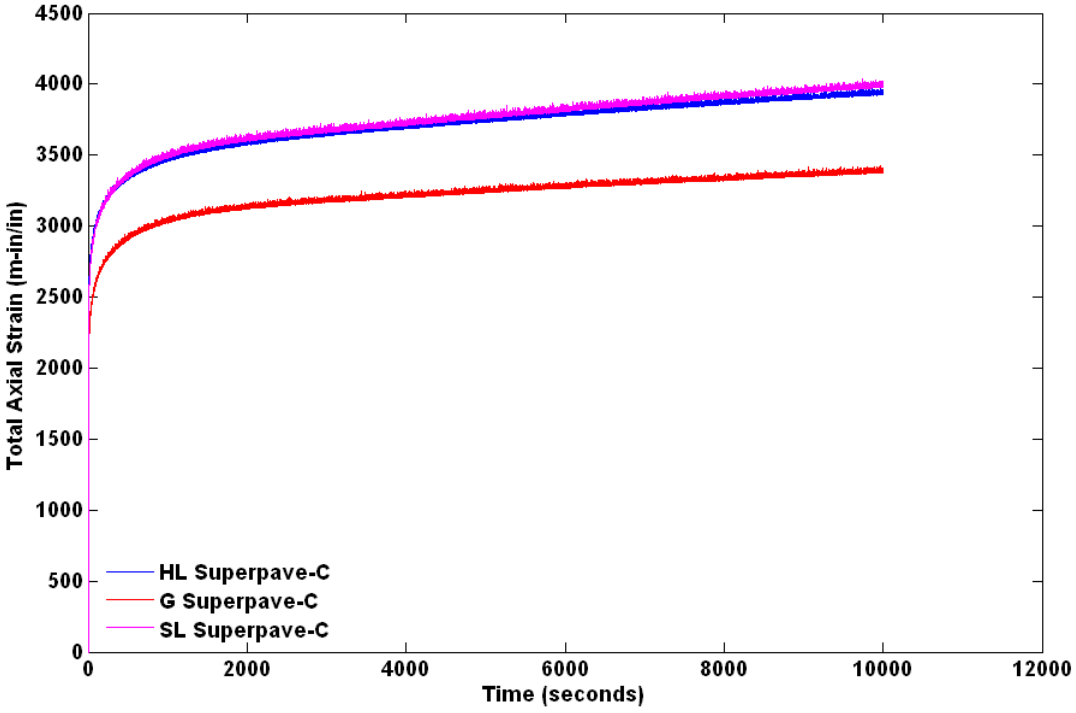

Figure 4.10 Unconfined Static Creep Test Result; Mixture Type Superpave-C

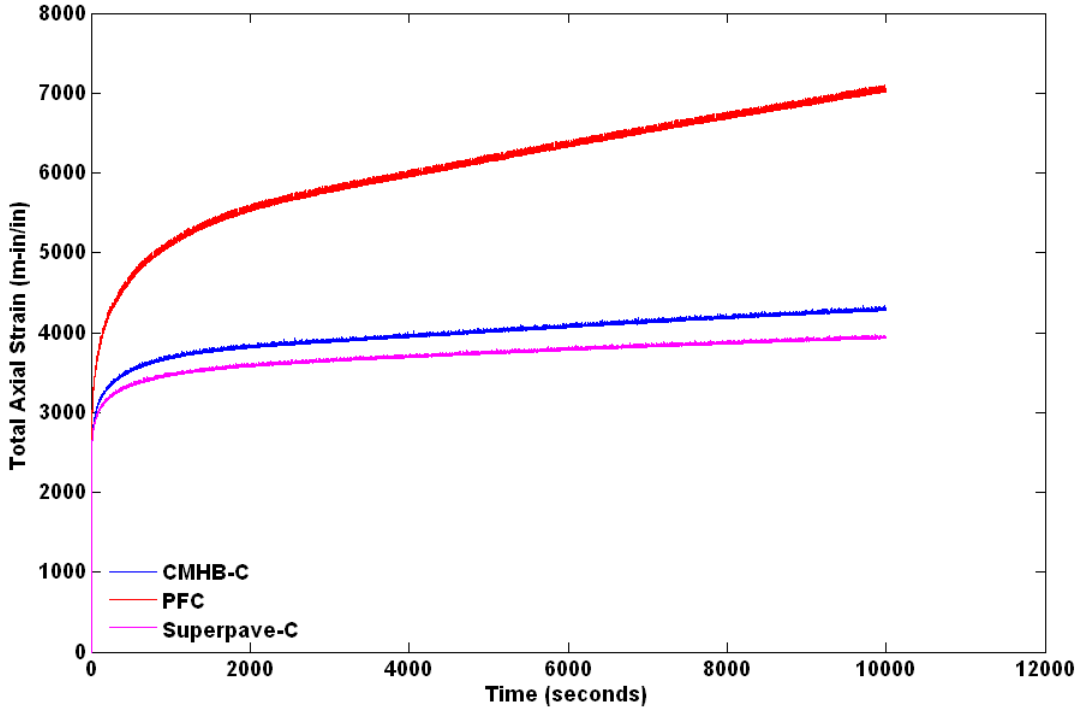

Figure 4.11 Unconfined Static Creep Test Result; Aggregate Type Hard Limestone (HL)

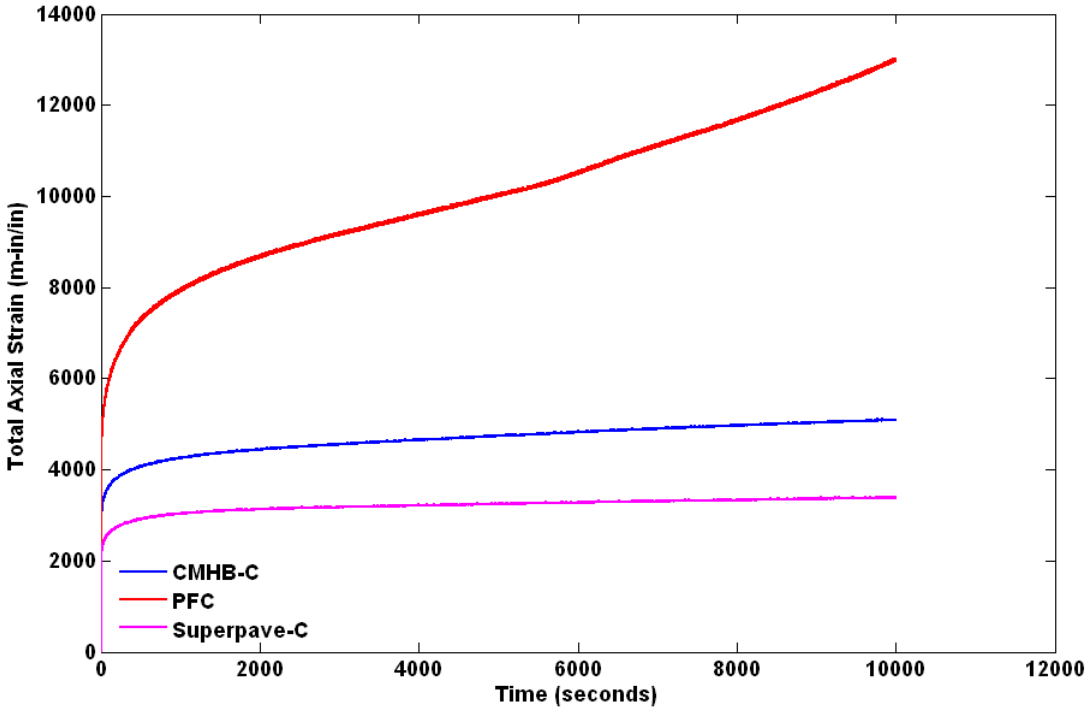

Figure 4.12 Unconfined Static Creep Test Result; Aggregate Type Granite (G)

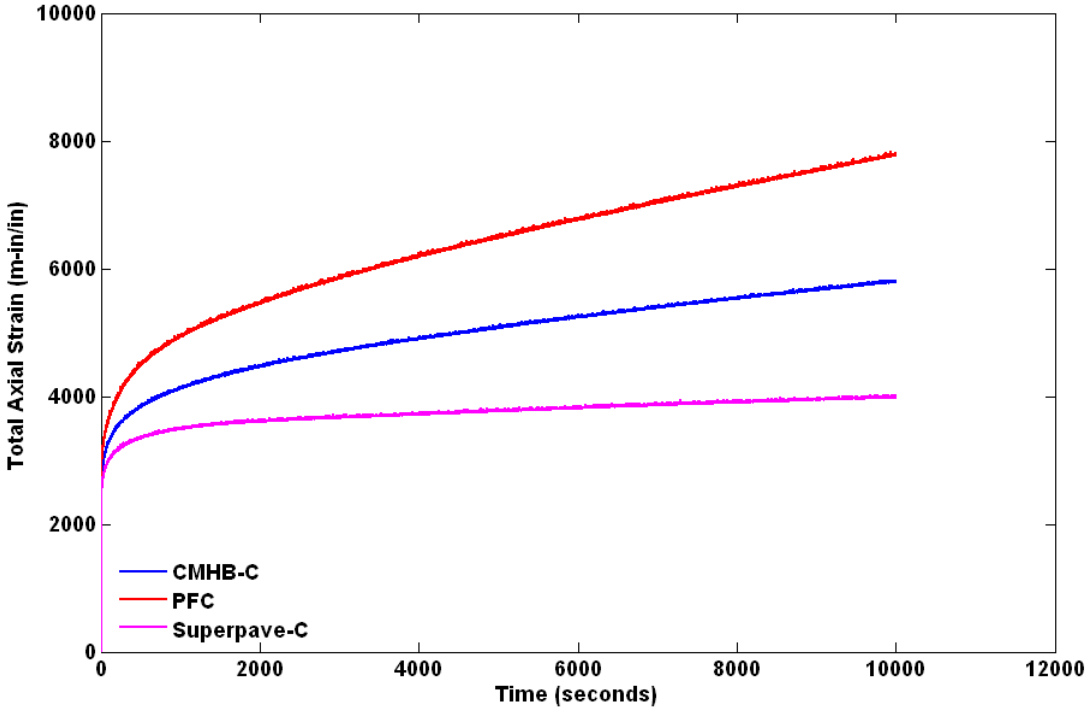

Figure 4.13 Unconfined Static Creep Test Result; Aggregate Type Soft Limestone (SL)

4.5.2 Creep Compliance

To study the deformation behavior of the AC mixtures, the creep compliance is plotted with loading time. Creep compliance is reciprocal of the modulus of elasticity, and can be calculated using:

$$D(t) = \frac{\varepsilon(t)}{\sigma(t)} \tag{4.1}$$

where, $D(t)$ is the creep compliance, $\varepsilon(t)$ is the rate of deformation, and $\sigma(t)$ is the applied stress level, which in this case is constant.

Figure 4.14 shows a typical curve of axial creep compliance as a function of loading time in log-log scale for mixture type HL CMHB-C. The corresponding creep compliance curves for the rest of the mixtures are given in Appendix A. It can be seen from these figures that the creep compliance curve versus loading time can be divided into three distinct regions: primary creep where the strain rate decreases, secondary creep where the strain rate is constant, and the tertiary creep where the strain rate increases.

The secondary creep region is linear. Its slope can be used to characterize the rutting potential of the AC mixtures. Moreover, it defines the steady-state rate of deformation at the specified testing temperature and stress levels. The creep compliance parameter, the intercept and slope of the steady-state region, allows to distinctly separate the time-dependent and time-independent components of the strain response (Witczak et al., 2002). Higher intercept values indicates lower modulus of elasticity (i.e., higher creep compliance) and yield higher permanent deformation. In addition, for a constant intercept value, an increase in the slope parameter yields higher permanent deformation. Table 4.5 shows the creep compliance regression parameters for the nine AC mixtures tested. It can be concluded that, HL CMHB-C and G PFC exhibited the highest and lowest resistance to rutting, respectively. Masad et al., (2003) demonstrated that aggregate type and their geometry influence the AC mixtures rutting resistance behavior. In general, mixtures containing hard limestone (HL) offer satisfactory pavement rutting resistance potentials. On the other hand, mixtures with granite (G) aggregate sources are prone to rutting.

In addition, as illustrated in Figure 4.14 large increase in compliance occurs at a constant volume within the tertiary zone. The starting point of tertiary deformation under constant volume defines the Flow Time (FT). FT is a significant parameter in evaluating AC mixture rutting resistance potential Hafez (1997). Table 4.6 depicts the FTs of the nine AC mixtures. It can be concluded that mixture type G Superpave-C and SL PFC exhibited the highest and lowest FT, respectively. Generally, satisfactory AC pavement performance (i.e., reduced cracking and/or rutting) can be achieved with high FT value and vise versa. In other words, it means that AC mixture with the lowest FT needs early maintenance and rehabilitation program.

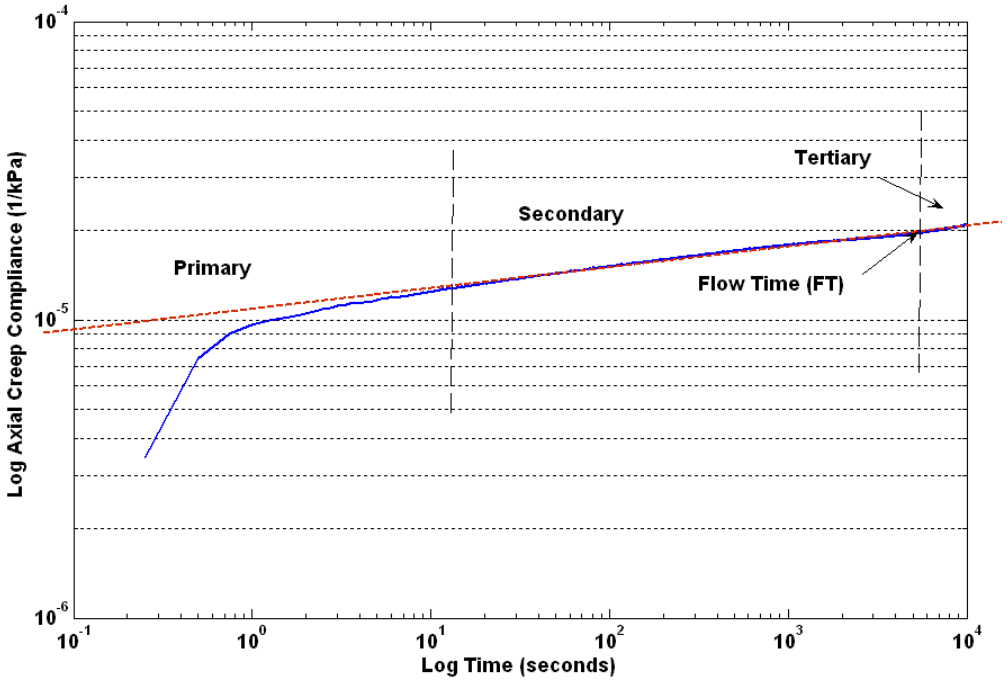

Figure 4.14 Axial Creep Compliance versus Loading Time; Mixture Type HL CMHB-C

Table 4.5 Creep Compliance Regression Parameter

Mixture Type	Intercept ($\times 10^{-5}$) (1/kPa)	Slope ($\times 10^{-7}$) (1/kPa.sec)
HL CMHB-C	0.85	3.01
G CMHB-C	1.00	4.19
SL CMHB-C	0.80	4.51
HL PFC	0.78	1.29
G PFC	1.30	4.51
SL PFC	0.90	5.64
HL Superpave-C	0.88	5.40
G Superpave-C	0.72	4.27
SL Superpave-C	0.83	3.86

Table 4.6 AC Mixture Flow Time (FT)

Mixture Type	Flow Time (FT) (seconds)
HL CMHB-C	6112
G CMHB-C	7110
SL CMHB-C	6467
HL PFC	6232
G PFC	5423
SL PFC	5057
HL Superpave-C	8995
G Superpave-C	8550
SL Superpave-C	9440

4.6 Summary and Conclusions

This chapter presents the unconfined static creep test results on nine AC specimens prepared from three different types of aggregate sources, namely hard limestone (HL), granite (G), and soft limestone (SL). They were prepared with conventional TxDOT mix design methods, namely CMHB-C, PFC, and Superpave-C. Regardless of the aggregate type used, the CMHB-C mixtures demonstrated higher resistance to pavement rutting following mixture type Superpave-C and PFC mixtures are found to be less resistant to rutting.

Chapter 5

PROCESSING ASPALT CONCRETE X-RAY COMPUTED TOMOGRAPHY (CT) IMAGES FOR DEM SIMULATION

5.1 Introduction

Recently, advances imaging techniques have gained popularity in characterizing the microstructure of ACs. Several researchers implemented Digital Image Processing (DIP) techniques to study the microstructure of AC mixtures. These techniques have been used to obtain quantitative information about the air voids, mastic and aggregate distribution, shape of the aggregate particles, aggregate orientation, aggregate gradation, aggregates contacts, aggregate segregation and so on. Moreover, DIP techniques have been effectively utilized to quantify anisotropy and damage in AC mixtures (Tashman, 2003). Despite these developments, identifying the three phases in AC X-ray CT images has been done to a large extent subjectively. This involves establishing the grey level thresholds that separate aggregate from mastic and mastic from air. This chapter presents an innovative approach for processing AC X-ray CT images, in this case, suitable for DEM simulation.

The microstructure of ACs can be captured and characterized using high resolution X-ray CT computed tomography. Recently, X-ray CT has shown great promise in characterizing other composite materials, including Portland cement concretes and soils. Landis and Keane, (1999) and Marinoni et al., (2005) applied imaging techniques to characterize cement-based materials. In soils, X-ray CT images were utilized to assess localized deformations, determine the spatial distribution of soil water content, and characterize the physical properties of particulate materials (Macedo et al., 1999; Alshibli et al., 2000; Kim et al., 2001). A large volume of literature deals with characterizing AC mixtures using CT, including work by (Synolakis et al., 1996; Kuo et al., 1998; Persson, 1998; Masad et al., 1999a, 1999b; Shashidhar, 1999; Masad and Button, 2000; Masad, 2001; Masad et al., 2001; Tashman et al., 2001; Al-Omari et al., 2002; Papagiannakis et

al., 2002; Saadeh et al., 2002; Tashman et al., 2002; Banta et al., 2003; Kim et al., 2003; Al-Omari and Masad, 2004; Wang et al., 2004a, 2004b). Masad and Button, (2004) examined the AC microstructure based on volumetric and imaging techniques and studied their effect on overall performance. Aggregate orientations and their effects on engineering properties of asphalt mixtures are well investigated and characterized using imaging techniques (Masad et al., 1998; Chen et al., 2001, 2002, 2005).

The majority of the studies highlighted above use a combination of DIP and manual/subjective techniques for processing AC images in a format suited to numerical simulation. DIP techniques include image contrast enhancement, image noise removal, thresholding, edge detection and image segmentation. Typically, the gray level threshold that separates aggregates from mastics referred to as thresholding is selected subjectively. Additional pixel modifications are required to adjust the relative proportions of aggregate and mastic to reflect the actual volumetrics of the AC. Isolating the air phase further complicates the problem. To date, there have been few attempts to fully automate this process by solely utilizing DIP techniques (Kose et al., 2000; Yue et al., 2003; Offrell and Magnusson, 2004). Developing an algorithm for processing automatically AC X-ray CT images is inevitable in effectively capturing the microstructure of a large number of AC cores for modeling their mechanical behavior. Consequently, these processes assist to accurately predict the permanent deformation behavior of AC mixtures.

5.2 Image Acquisition using X-ray Computed Tomography (CT)

X-ray computed tomography (CT) is a non-destructive advanced imaging technique that generates two- and three-dimensional high resolution images with the capability of capturing the details of the microstructure. This technique has been used by several researchers to characterize different properties of AC materials. Recently, it is used to effectively quantify air void distribution, aggregate orientation, segregation and surface texture (Masad et al., 1998; Braz et al., 1999; Masad et al., 1999a, 1999b; Sashidhar, 1999; Masad et al., 2001; Tashman et al., 2002; Masad and Button, 2004; Wang et al., 2004a, 2004b; Zelelew and Papagiannakis, 2007).

The data analyzed in the study at hand consist of nine AC cores with their X-ray CT images and are part of a Texas DOT funded study (Alvarado et al., 2007). A

summary of the background information for this data is given in Chapter 4. The high-resolution X-ray CT facility and the components of X-ray CT system are shown in Figure 5.1. Typical steps involved in scanning AC mixtures using X-ray CT are:

- Step 1: The AC specimen is fixed on the stage located between the X-ray source and detector.
- Step 2: The X-ray detector is calibrated.
- Step 3: Digital images are acquired, one for each complete specimen rotation.
- Step 4: Two-dimensional images of specimen sections are captured.
- Step 5: Three-dimensional images are generated by combining the two-dimensional images obtained in Step 4.

Each of the nine AC cores was scanned perpendicularly to its axis at 1 mm distance interval to yield 148 slices per core, ignoring the top and bottom slices. Figure 5.2a shows in raw format of one of these images consisting of 512 x 512 pixels. The resulting resolution is 195 μm per pixel, which does not allow detecting particles larger than roughly particles passing sieve No. 70.

Digital image processing techniques are utilized to characterize the AC X-ray CT images. The resulting processed images are suitable for direct input into numerical simulation methods, namely discrete element method (DEM) and continuum-based finite element method (FEM).

5.3 Digital Image Processing (DIP)

The DIP algorithm involves three stages. The first stage involves image pre-processing for contrast enhancement and noise removal. The second stage is the main thresholding routine accepting as input the enhanced images of the first stage and volumetric information for the AC. It consists of two components, namely volumetrics-driven thresholding and 3-D representation/sectioning. The third stage further enhances particle separation through edge detection and image segmentation techniques. Each of these components is described below.

(a)

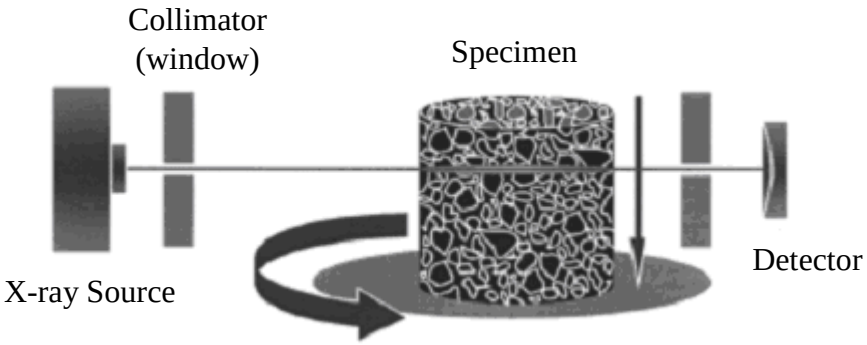

(b)

Figure 5.1 (a) High-resolution X-ray CT Facility and (b) Components of X-ray CT System (Masad et al., 2002)

5.3.1 Image Contrast Enhancement

X-ray CT images of AC core sections consist of pixel representations that vary in gray level between 0 and 255 (i.e., black and white, respectively). An example of such a raw image is shown on Figure 5.2a. Figure 5.2b shows a histogram of the gray level for this image. It shows the gray level intensity in the abscissa and the number of pixels by gray-level in the ordinate. It is evident that the contrast level of such raw images is poor. A number of sophisticated contrast enhancement techniques, such as for example spatial and morphological filtering are available.

In this study, the most commonly used method, called histogram equalization (or linearization), is implemented. It consists of adjusting the gray level intensity of pixels to produce a more even distribution throughout the image. The MATLAB® built-in function *histeq* was used for this purpose (Misiti et al., 2006). Figure 5.2c and 5.2d show the enhanced image using histogram equalization and the corresponding gray level histogram, respectively.

5.3.2 Noise Removal

AC X-rayed CT images include a variety of types of noise. Its main sources are sensor quality, as well as image digitizing and preprocessing. Variations in densities within the individual mastic and aggregate also contribute to image noise. Reducing noise is essential in obtaining enhanced image quality. Two methods are commonly used for de-noising, depending on the noise type, namely mean or/and median filtering (Gonzalez and Woods, 2002; Russ, 2002). In mean filtering, the gray level of each pixel is replaced by the average of the gray level of all pixel values in the pixel's neighborhood. Similarly, in median filtering, the gray level of each pixel is replaced by the median of the gray level of all pixel values in the pixel's neighborhood. The local neighborhood is defined by a window of $N \times N$ pixels in size, referred to as kernel, where N has typically values of 3, 5, 7, 9 and so on. In AC image de-noising, the median filtering technique has been used by several researchers (Yue et al., 1995; Masad et al., 2001; Yue et al., 2003; Chandan et al., 2004).

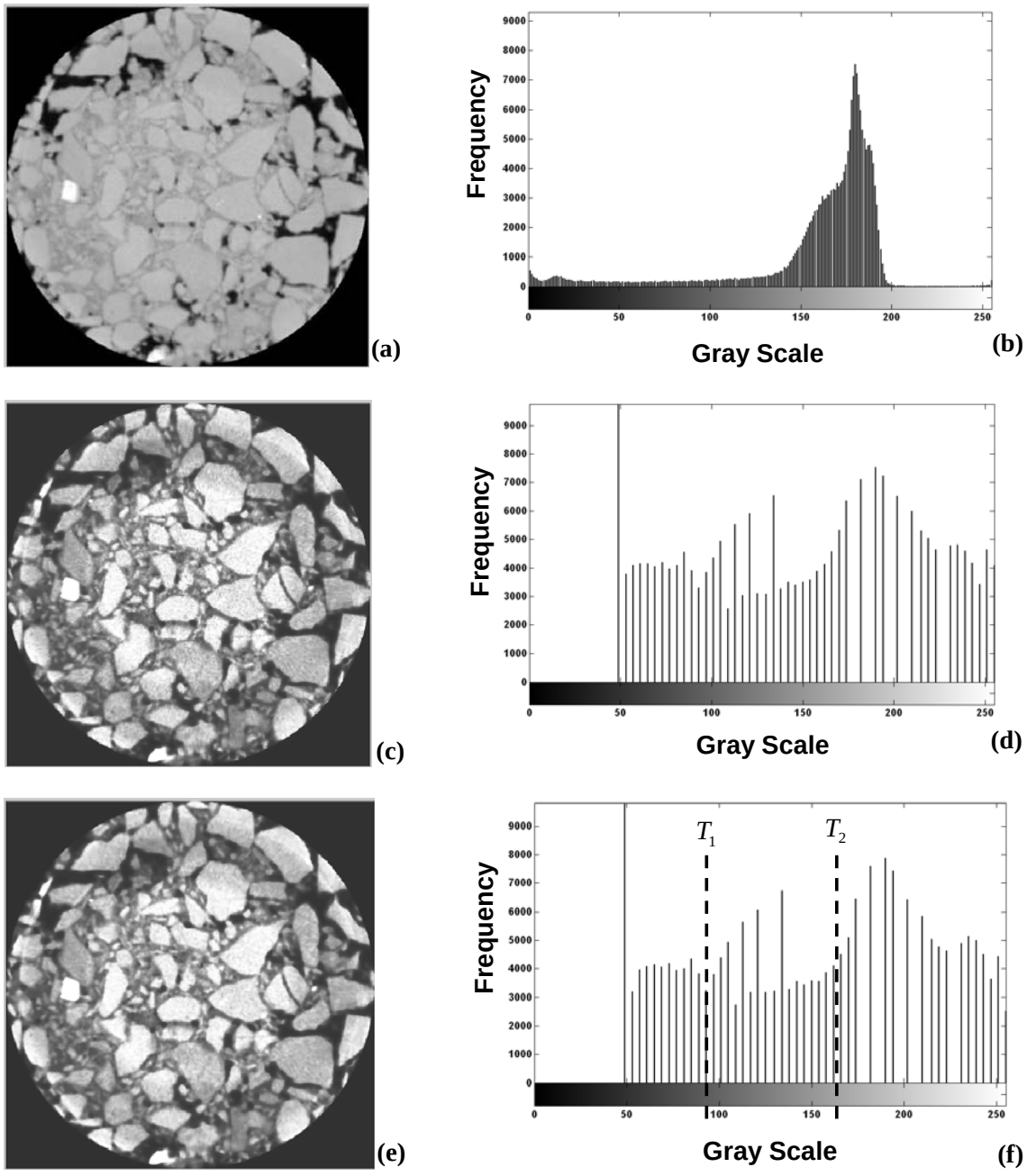

Figure 5.2 Example of AC Image Pre-Processing; (a), (b): Raw Image and its Gray Level Histogram; (c), (d): Contrast Enhanced Image and its Gray Level Histogram; (e), (f): De-noised Image and its Gray Level Histogram

In this research, the median filtering technique is utilized as well. A comparison was made for several kernel sizes ranging from 3×3 to 9×9. Better results were obtained using a 3×3 kernel. Figure 5.2e and 5.2f show the same AC image discussed previously and the corresponding gray level histogram after de-noising is effected using a 3x3 kernel. The improvement in clarity and contrast between Figure 5.2e and 5.2a is significant.

5.3.3 Volumetrics-Based Thresholding Algorithm

Global and local thresholding are the most commonly used methods for identifying different phases in images of composite materials, such as AC. The former depends on overall gray level values, while the latter depends on local gray level information. These techniques are well investigated by several researchers (Rosin, 2001; Portes de Albuquerque et al., 2004; Kim and Park, 2005; Yan et al., 2005). A multi-stage locally adaptive thresholding method using neighborhood processing was also described by Savakis, (1998).

The method described here uses a global minima percent error approach. Its innovation is that it utilizes as thresholding criterion the actual volumetric properties of the AC and hence, it is referred to as a Volumetrics-based Global Minima (VGM) thresholding algorithm (Zelelew and Papagiannakis, 2007b). The algorithm was developed in MATLAB® environment (Misiti et al., 2006). It applies to images of sections of AC cores taken perpendicular to the axis at regular distance intervals. The algorithm seeks to establish two gray level thresholds, a lower threshold T_1 corresponding to the air void-mastic boundary, and a higher threshold T_2 corresponding to the mastic-aggregate boundary. These limits are plotted in Figure 5.2f for illustration purposes. Finding these threshold values involves an iterative process, whereby the gray level of a pixel located at (i, j), denoted by $f(i, j)$, is compared to the seed threshold values to establish whether it is an "object" (pixel value equal to 1) or "background" (pixel value equal to 0), according the following logic:

$$g(i,j)=\begin{cases}1 & if \quad f(i,j)\le T_1 \quad Air\ Voids\\ 0 & if \quad f(i,j)> T_1 \quad Mastics\ and\ Aggregates\end{cases} \tag{5.1a}$$

and

$$h(i,j)=\begin{cases}1 & if \quad f(i,j)\geq T_2 \quad Aggregates \\ 0 & if \quad f(i,j)< T_2 \quad Air\ Voids\ and\ Mastics\end{cases} \tag{5.1b}$$

where, $g(i,j)$ and $h(i,j)$ identify the boundaries between air and mastics/aggregates and aggregates and mastics/air, respectively. Ratios of areas of object over background averaged over all the core sections are compared to the pertinent volumetric properties of an AC core. Threshold values are identified by the minima in these errors. The steps involved in establishing air void-mastic boundary threshold T_1 are given below:

- Step 1: For each section image, assume a seed threshold value T_1 that separates the image into objects (air voids) and background (mastics and aggregates).
- Step 2: Calculate the object and background areas.
- Step 3: Calculate the percent object to background area ratio (i.e., it is proportional to the percent air voids for an AC section).
- Step 4: Calculate the average percent air void content for all the sections of a particular core (i.e., 148 images per AC core).
- Step 5: Compare the Step 4 estimated average air void content to the laboratory established air void content and compute the absolute percent error.
- Step 6: Increase or decrease the threshold value by 1 and repeat Steps 1 to 5.
- Step 7: The optimum T_1 threshold is obtained as the threshold value that minimizes the error in air void estimation.

A similar procedure is followed for establishing the T_2 value as the mastic-aggregate boundary threshold. Obviously, pixels with gray-level intensities between T_1 and T_2 identify the mastic. In performing these calculations, it was assumed that the mastic contains all the fines that cannot be detected by the image resolution i.e., sizes finer than 195 μm. As a result, the mastic volume was assumed to include the aggregates approximately passing sieve No. 50. To reduce computational time, realistic seed threshold ranges need to be used. In this work median seed value of 70 and 110 were selected for T_1 and T_2, respectively. Examples of the error minimization plots for AC mixture type HL CMHB-C are shown in Figure 5.3 and Figure 5.4 respectively for T_1 and T_2 and details for the rest of the mixtures are provided in Appendix B. The actual gray

levels determined are plotted in Figure 5.5 and 5.6, respectively. The highest T_1 value was observed for the Superpave-C mix with the hard limestone (HL) aggregate, while the lowest was for the PFC with hard limestone (HL) aggregate. The highest T_2 value was observed for the CMHB-C mix with the hard limestone (HL) aggregate, while the lowest was for the PFC mix with the granite (G) aggregate. The relationship between air voids and the two thresholds, as shown in Figure 5.7, suggests that T_1 is relatively insensitive to the air void content, while T_2 increases with decreasing air void content. The relationship between aggregate volume and the two thresholds, as shown in Figure 5.8, suggests that T_1 is relatively insensitive to the aggregate volume, while T_2 decreases with decreasing aggregate volume. These two figures provide guidelines for the seed values to be used in thresholding AC images.

Using image analysis techniques, gyratory compaction efforts and distribution of air voids in AC mixtures based on X-ray CT images are characterized (Masad et al., 2002; Tashman et al., 2002, 2003). The air void-mastic and mastic-aggregate threshold is used to characterize AC mixture microstructures. Figure 5.10 shows the distribution of air voids, mastics and aggregates for AC mixture type HL CMHB-C and details for the rest of the mixtures are provided in Appendix B. The resulting average proportions of the three phases, air voids, mastics and aggregates for the nine cores are summarized in Table 5.1, by percent volume of the mix. Table 5.2 summarizes the errors between the VGM estimated volumetric properties and the laboratory ones. The maximum errors observed were 1.43%, 4.33% and 0.92%, respectively. It is important to mention that the top and bottom image 1 mm slices were not utilized in VGM analysis. These results suggest that the VGM thresholding algorithm is quite accurate in preserving AC mixture volumetric properties. This demonstrates the effectiveness of the VGM. It should be noted that this algorithm is versatile and can be adapted in thresholding other composite material X-ray CT images. The results of applying the thresholding algorithm to Figure 5.2e are shown in Figure 5.10 which highlights each of the three AC phases.

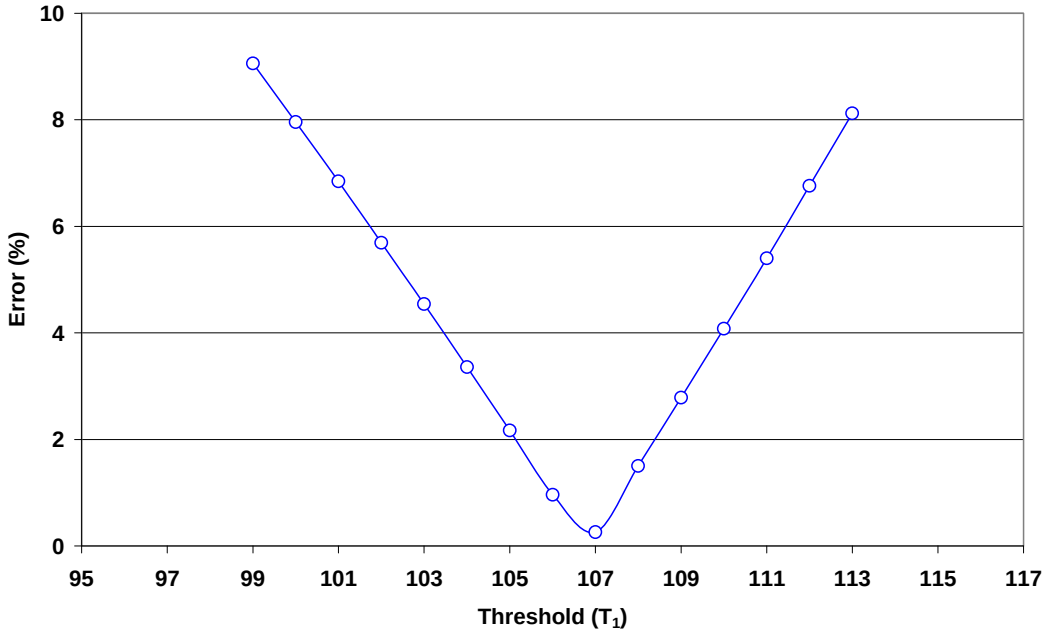

Figure 5.3 Air Void-Mastic Gray Scale Boundary Threshold (T_1 = 107); HL CMHB-C

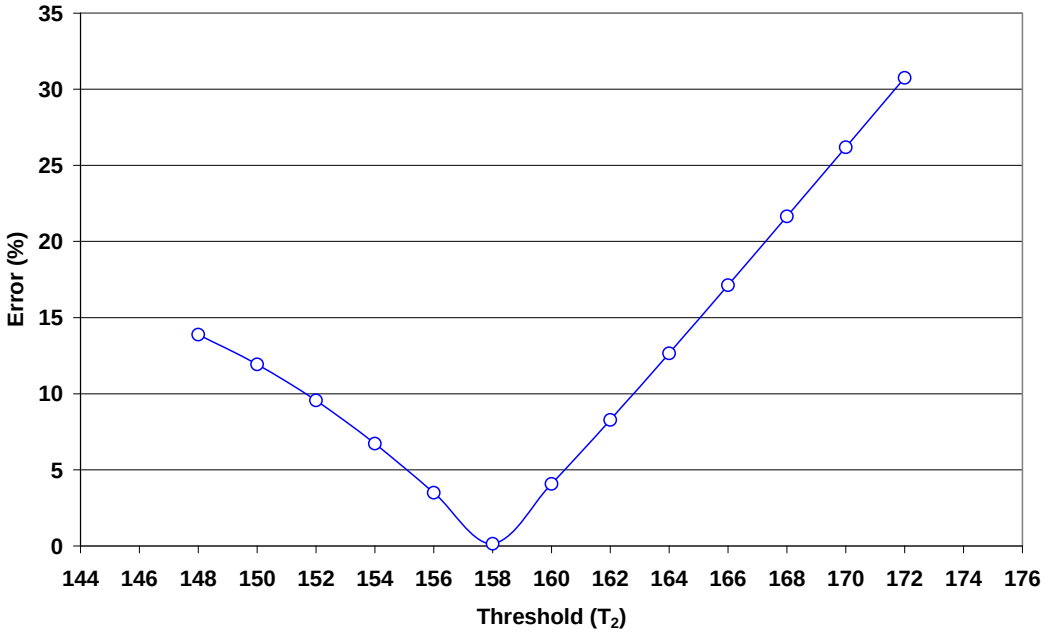

Figure 5.4 Mastic-Aggregate Gray Scale Boundary Threshold (T_2 = 158); HL CMHB-C

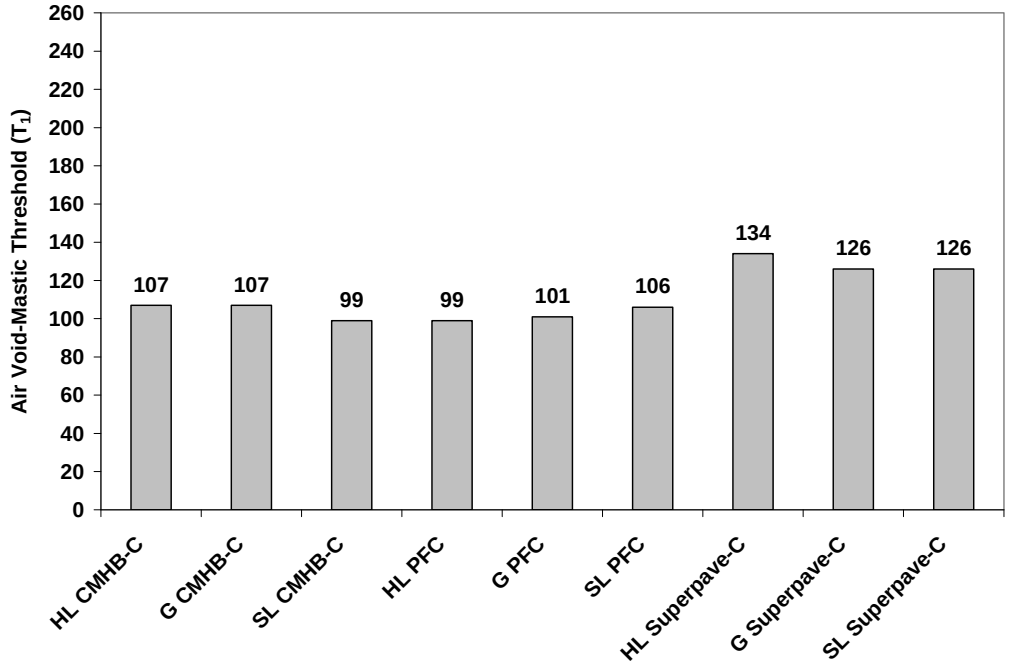

Figure 5.5 Air Void-Mastic Gray Scale Boundary Threshold (T_1)

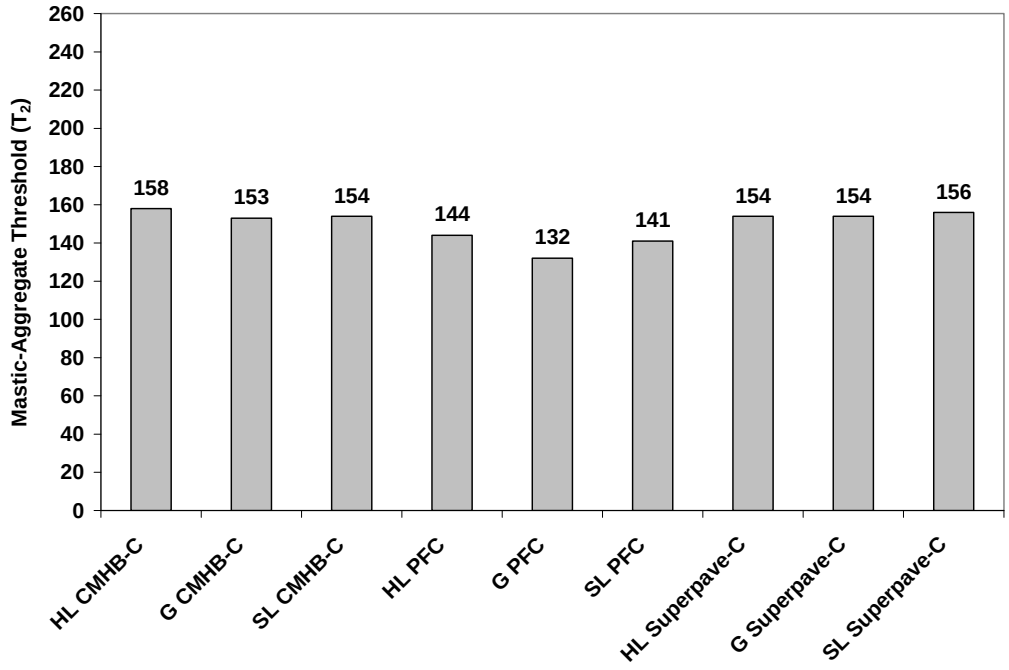

Figure 5.6 Mastic-Aggregate Gray Scale Boundary Threshold (T_2)

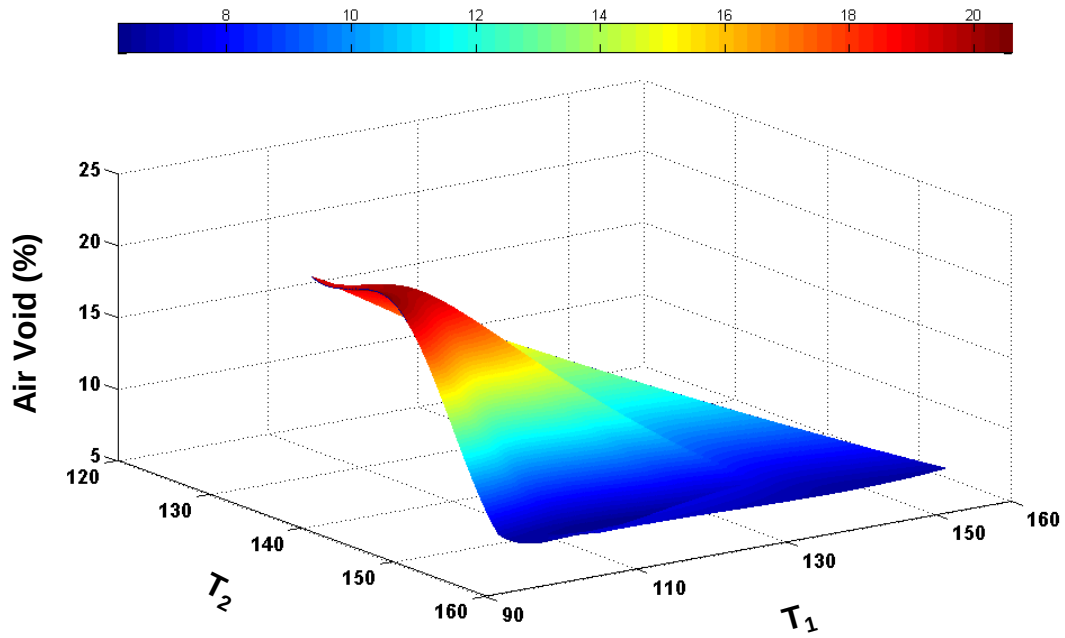

Figure 5.7 Distribution of Measured Percent Air Voids with T_1 and T_2

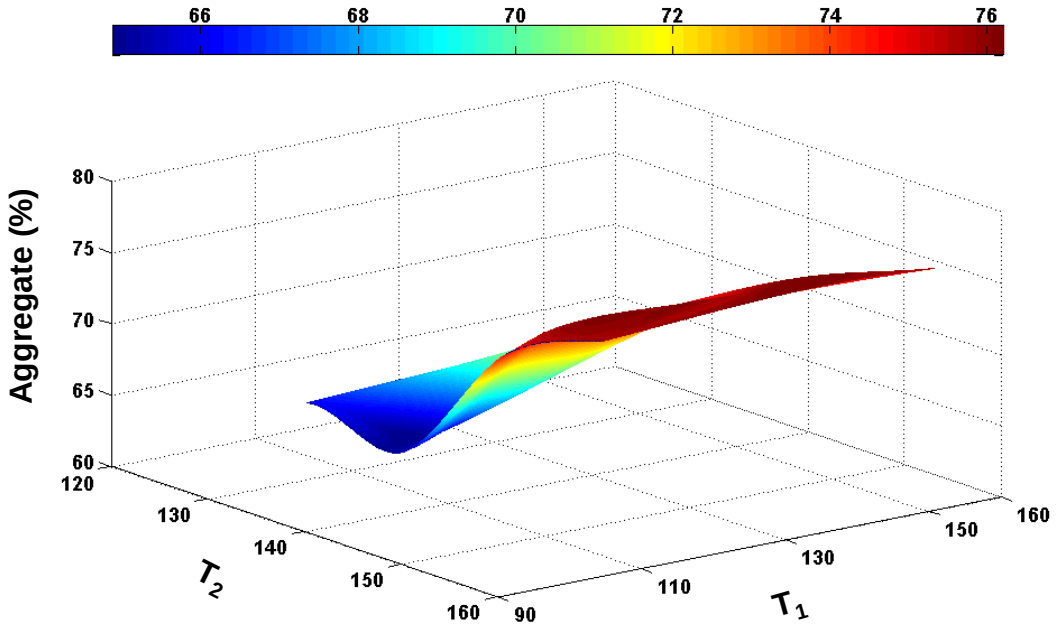

Figure 5.8 Distribution of Measured Percent Aggregates with T_1 and T_2

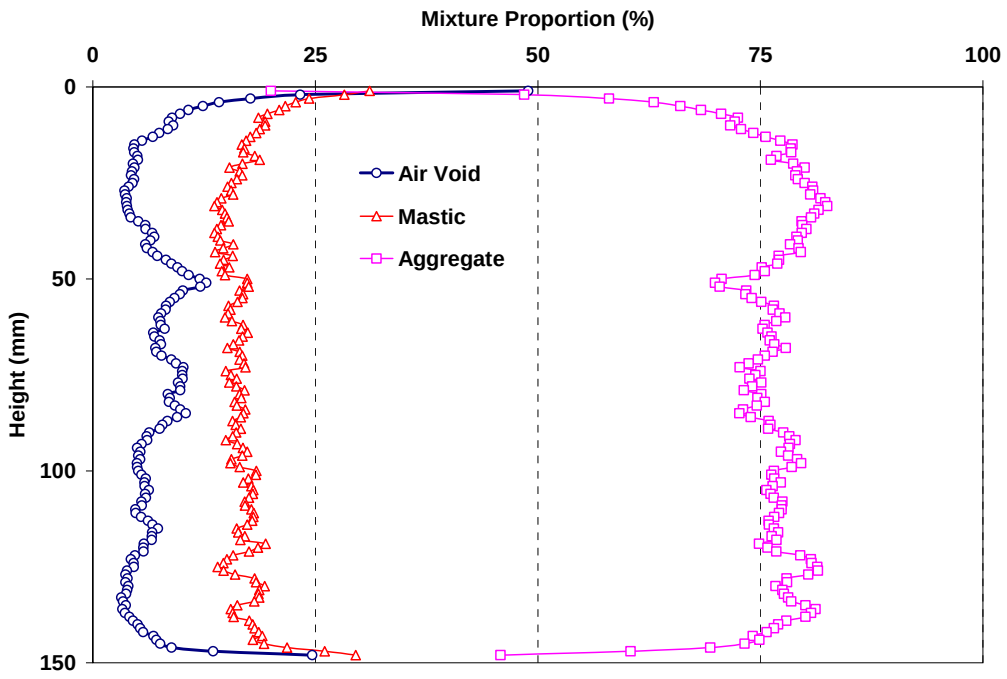

Figure 5.9 Distribution of Air Voids, Mastics, and Aggregates; HL CMHB-C

Table 5.1 Proportions of Air, Mastic and Aggregate Phases (% by volume)

Mixture Type	Air Void (%)	Mastic (%)	Aggregate (%)
HL CMHB-C	7.30	16.98	75.72
G CMHB-C	6.90	17.72	75.38
SL CMHB-C	7.00	18.33	74.67
HL PFC	19.50	14.78	65.72
G PFC	19.60	14.34	66.06
SL PFC	19.30	15.42	65.28
HL Superpave-C	7.40	16.81	75.79
G Superpave-C	6.90	17.39	75.71
SL Superpave-C	6.70	17.84	75.46

HL: Hard Limestone; G: Granite; and SL: Soft Limestone

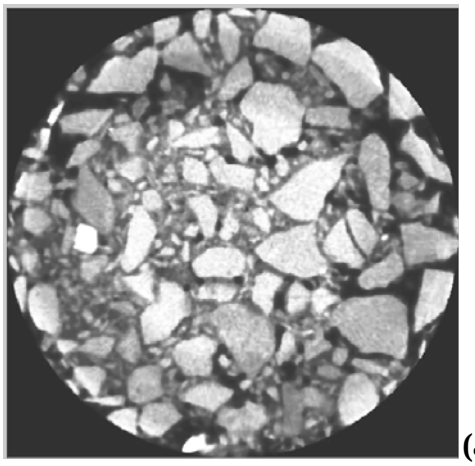
(a)

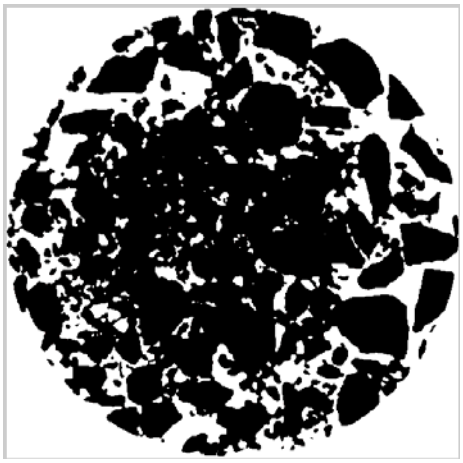
(b)

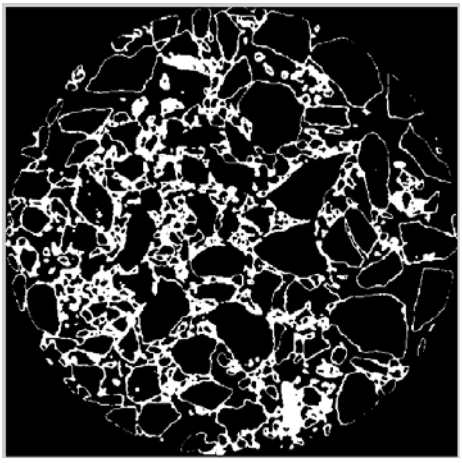
(c)

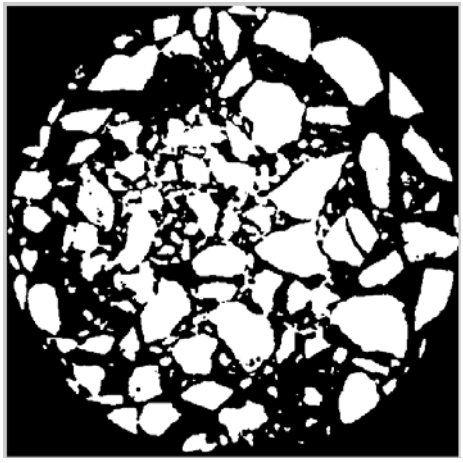
(d)

Figure 5.10 Representation of AC Core Sections (a) Contrast Enhanced and De-Noised Image (b) Air Void Phase in White, (c) Mastic Phase in White, and (d) Aggregate Phase in White

Table 5.2 Comparison of Laboratory Measured and VGM Estimated Mixture Proportions

Mixture Type	Air Void (%)		Absolute Error (%)	Mastic (%)		Absolute Error (%)	Aggregate (%)		Absolute Error (%)
	Measured	Estimated		Measured	Estimated		Measured	Estimated	
HL CMHB-C	7.30	7.32	0.26	16.98	17.07	0.49	75.72	75.61	0.14
G CMHB-C	6.90	6.89	0.19	17.72	18.19	2.66	75.38	74.92	0.61
SL CMHB-C	7.00	6.99	0.17	18.33	18.85	2.86	74.67	74.16	0.69
HL PFC	19.50	19.42	0.39	14.78	14.98	1.33	65.72	65.60	0.18
G PFC	19.60	19.71	0.58	14.34	14.58	1.63	66.06	65.71	0.53
SL PFC	19.30	19.37	0.38	15.42	15.29	0.81	65.28	65.34	0.08
HL Superpave-C	7.40	7.42	0.31	16.81	17.14	1.98	75.79	75.44	0.47
G Superpave-C	6.90	6.96	0.87	17.39	16.64	4.33	75.71	76.41	0.92
SL Superpave-C	6.70	6.60	1.43	17.84	18.40	3.15	75.46	75.00	0.62

HL: Hard Limestone; G: Granite; and SL: Soft Limestone

5.3.4 Three-Dimensional Representation and Sectioning

Assembling the 3-D core images from the 2-D circular sections can be carried out using commercially available software, such as Image-Pro Plus v. 6.2; *3D Constructor* (http://www.mediacy.com/) or *Blob3D* (http://www.ctlab.geo.utexas.edu/). Since the ultimate goal of the image processing work presented here is to simulate the behavior of AC cores in creep using 2-dimesional numerical simulation techniques (i.e., discrete element method, DEM) there was no need to assemble the 3-D images. Instead, a simple routine was added to the VGM thresholding algorithm to assemble rectangular 2-D sections of the AC cores from their circular sections. An example of the resulting 2-D rectangular sections produced by combining from the circular core sections is given in Figure 5.11a for the HL CMHB-C core. Figures 5.11b, 5.11c and 5.11d show the corresponding air, mastic and aggregate phases of this image respectively. Details for the rest of the mixtures are provided in Appendix B. Examining these figures reveals that there is a larger concentration of air voids around the sample periphery than in the middle, despite the fact that Gyratory samples were cored from 150mm to 100 mm in diameter. This agrees with observations from the recent literature (Masad et al., 1999a, 2002; Tashman et al., 2002). In addition, these images can also be used to characterize the directional aggregate segregation in AC mixtures (Zelelew and Papagiannakis, 2007c). These images correspond to section dimensions of 150x100 mm, yielding an area of 15,000 mm^2. A summary of the areas of the three phases for each of the cores tested is shown in Figure 5.12. Interestingly, the three Superpave mixtures had the lowest mastic area and the PFC mixtures have the highest aggregate area.

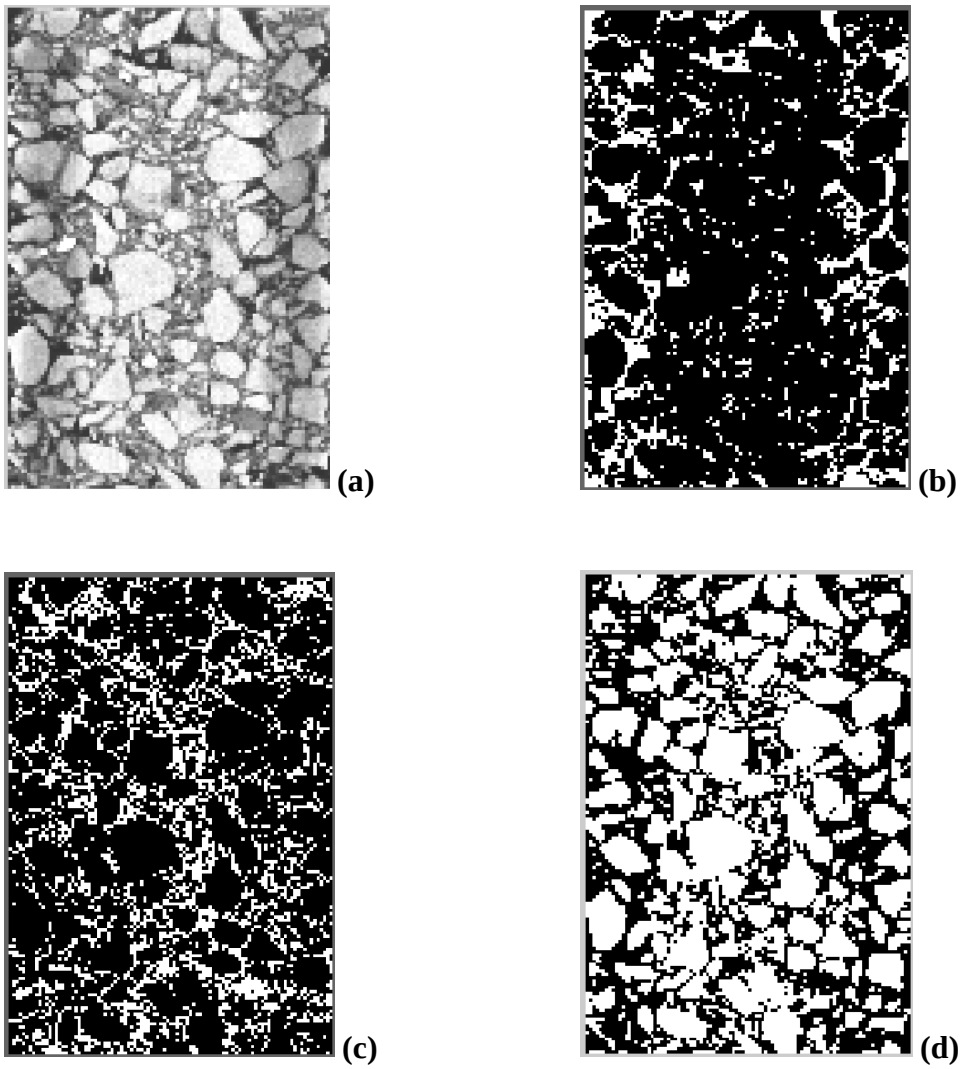

Figure 5.11 Representation of AC Rectangular Sections (a) Processed Image, (b) Air Phase in White, (c) Mastic Phase in White, and (d) Aggregate Phase in White; HL CMHB-C

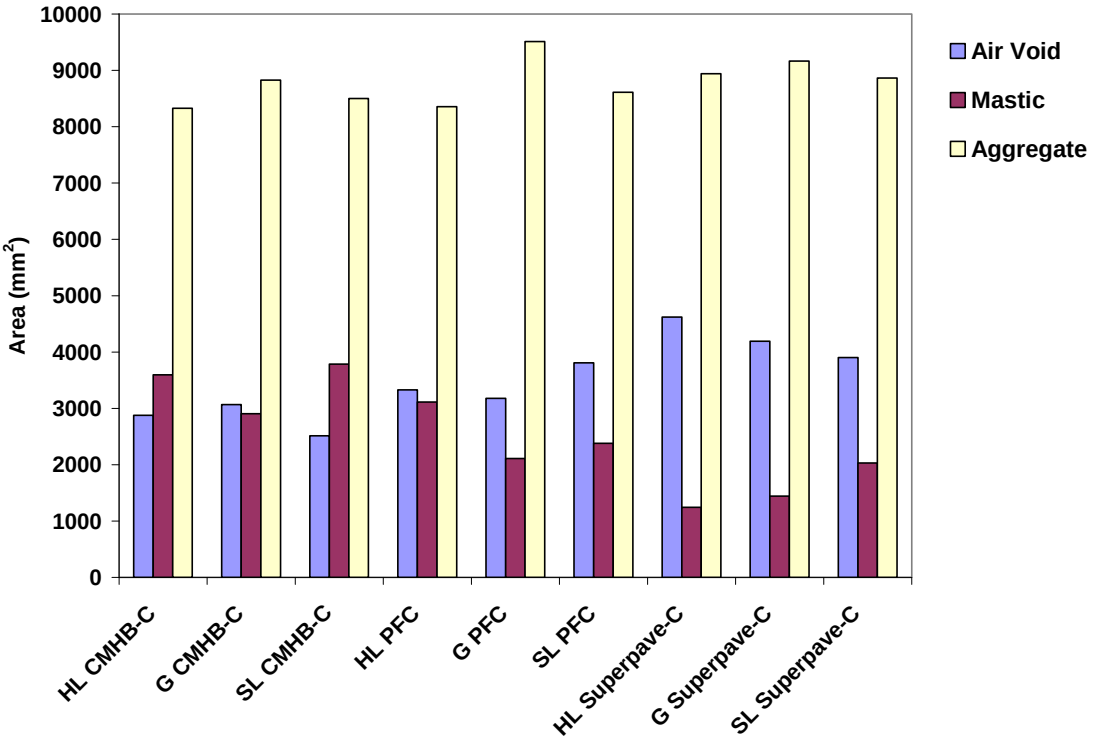

Figure 5.12 Areas of Rectangular Sections Corresponding to the Three Phases

Figure 5.11c and 5.11d show the need for additional image processing to better separate mastics and aggregates that appear to be overlapping or touching. This is carried out through edge detection and image segmentation techniques, as described next.

5.3.5 Edge Detection

Edge detection can enhance the physical boundaries between the three phases in AC. It is typically carried out using a gradient approach. The gradient of an image is the magnitude of the first-derivative of its image function, i.e., gray level $f(i, j)$. The direction of the gradient vector (i.e., the orientation of a unit normal vector perpendicular to the specified edge location), can also be used to quantify the orientation of the sharpest gray level intensity change. A *Sobel* operator is typically used defining gradients as:

$$|\nabla f| = \begin{bmatrix} \frac{\partial f}{\partial i} \\ \frac{\partial f}{\partial j} \end{bmatrix} = \sqrt{\left(\frac{\partial f}{\partial i}\right)^2 + \left(\frac{\partial f}{\partial j}\right)^2} \tag{5.2}$$

The first-order derivatives along the two Cartesian coordinates i and j are given by:

$$\frac{\partial f}{\partial i} = \nabla_i f = \frac{1}{2}[f(i+1, j) - f(i-1, j)] \tag{5.3a}$$

$$\frac{\partial f}{\partial j} = \nabla_j f = \frac{1}{2}[f(i, j+1) - f(i, j-1)] \tag{5.3b}$$

An example of implementing the first-order derivative expression is given in Figure 5.13. The abrupt changes in gray level intensity suggest phase boundaries. Clearly this method is not directly applicable in detecting boundaries between objects of different phases. A variation of this method, known as the *Canny* operator method can be used instead (Canny, 1986). It is also based on the first derivative of gray intensity, but it retains only derivatives that exceed a threshold value. Gradients are calculated as earlier but a Gaussian filter is used to identify which ones are significant. This method was used in the past to detect the aggregate edges from laser road profiling data (Kim et al., 2003). Application of Canny operator in identifying the boundaries of the mastic phase and the aggregate phase for AC mixture type HL CMHB-C images are shown in Figure 5.14a and 5.14b, respectively. Details for the rest of the mixtures are provided in Appendix B. These figures suggest that the Canny operator detects object boundaries, but it does not allow effective separation between them in a number of locales. Image segmentation techniques are used to rectify this problem, as described next.

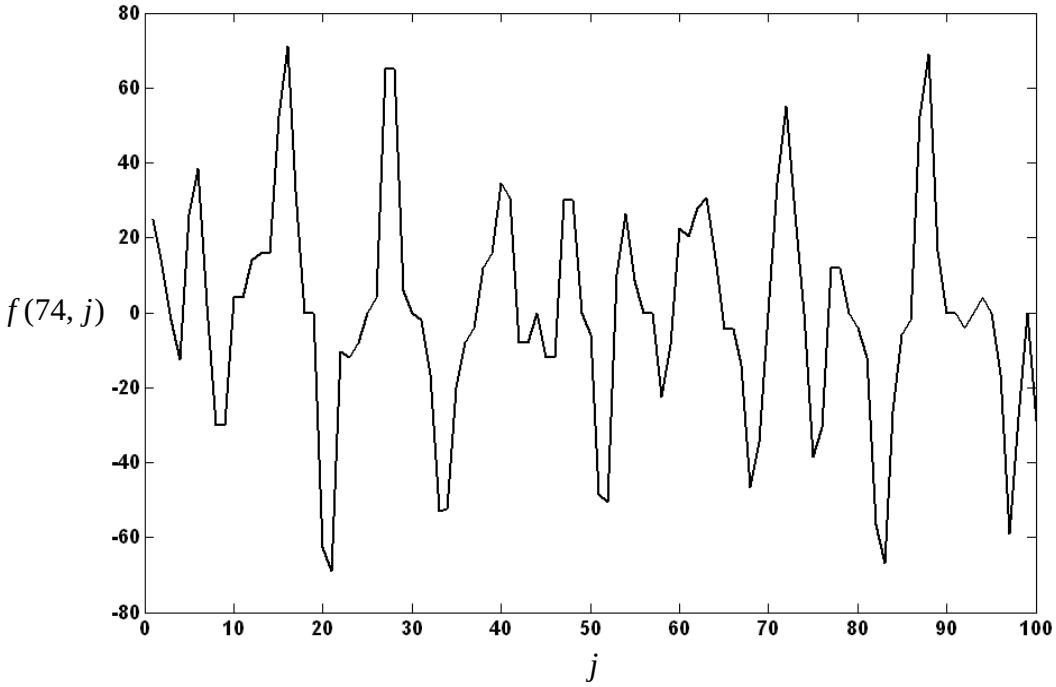

Figure 5.13 First-order Derivative of $f(i, j)$ at $i = 74$ along j Coordinate

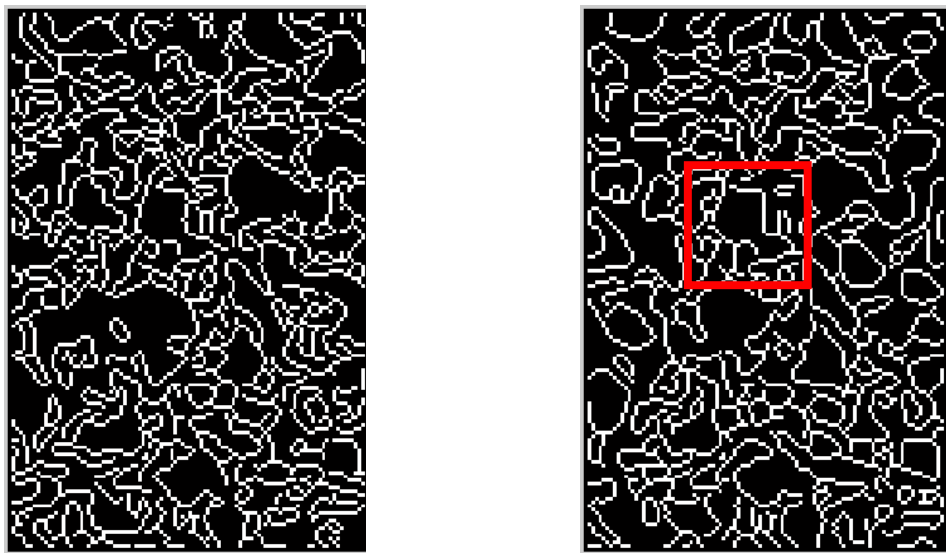

(a) **(b)**

Figure 5.14 Results of Canny Operation (a) Mastic Phase, (b) Aggregate Phase; HL CMHB-C

5.3.6 Image Segmentation

Image segmentation techniques allow differentiating between distinct phases by improving separation between image objects that touch each-other. The most commonly used segmentation technique is the watershed transform (Vincent and Soille, 1991; Hagyard et al., 1996; Bieniek and Moga, 2000; Kim and Kim, 2003). A number of studies have used this technique in civil engineering material applications (Kuo and Freeman, 1998; Ghalib and Hryciw, 1999; Sonka et al., 1999; Kim et al., 2003; Al-Rousan et al., 2007). In this research, the watershed image segmentation technique is utilized to effectively separate the overlapping (or touching) mastic and aggregate objects. The watershed transformation was performed using morphological dilation and erosion operations in MATLAB® (Misiti et al., 2006). Figure 5.15a and 5.15b show the results of watershed image segmentation of the mastic phase and aggregate phase for the AC mixture type HL CMHB-C. Details for the rest of the mixtures are provided in Appendix B. Overlapping aggregates bounded by red color in Figure 5.14b and Figure 5.15b can be used to explain the effects of edge detection and image segmentation techniques. Comparing the aggregate phase before and after segmentation, i.e., Figure 5.11a and 5.15b, respectively, suggests a marked improvement in image quality.

The non-overlapping mastic and aggregate particles should be inputted to numerically simulate the different behavior of ACs. In this research, the numerical simulation technique called Discrete Element Method (DEM) is used to simulate the permanent deformation behavior of ACs in monotonic loading (i.e. creep) conditions.

5.3.7 Preparation of AC Microstructures for DEM Simulation

A simple routine was added to the VGM thresholding algorithm to capture the spatial features of the mastic and aggregate pixels. These values are inputted into a DEM code called *Particle Flow Code in two-dimensions* (PFC^{2D}) to represent the rectangular 2-D sections of the AC cores as shown in Figure 5.16a and 5.16b, respectively. Combining the mastic and aggregate particles, treated respectively as viscoelastic and elastic materials, yield a true representation of AC microstructures. Examples are shown in Figure 5.16 for AC mixture type HL CMHB-C. Details for the rest of the mixtures are provided in Appendix B. It is worthy to mention that the same spatial information can

also be inputted into a continuum-based analysis, called Finite Element Method (FEM). Further discussions on DEM simulation procedures on the generated AC cores are given in Chapter 7 and 8.

The VGM thresholding algorithm software was developed in MATLAB® (Misiti et al., 2006). It includes the digital image processing built-in functions to preprocess, threshold, post-process, and prepares AC core images for DEM simulation purposes. The steps involved are highlighted and summarized in Figure 5.17.

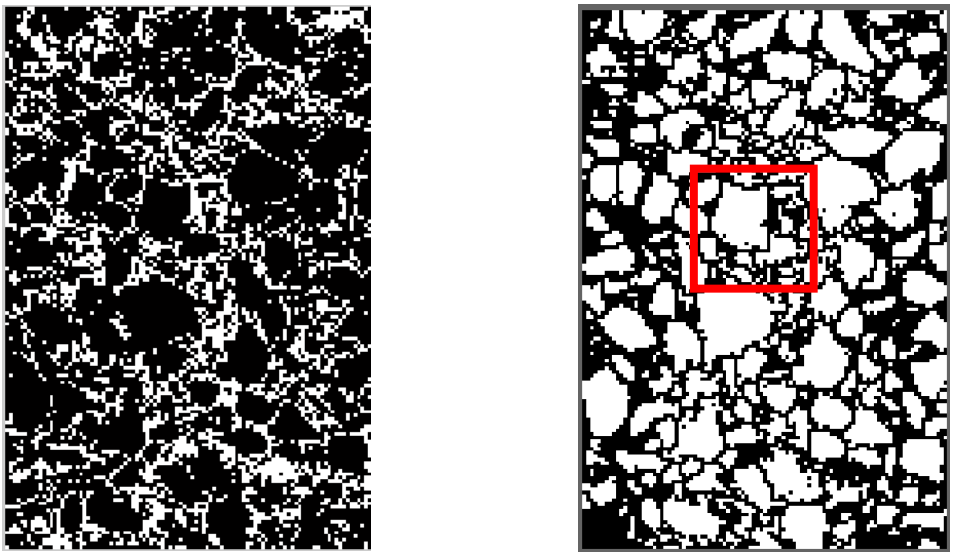

(a) **(b)**

Figure 5.15 Results of Watershed Image Segmentation (a) Mastic Phase, (b) Aggregate Phase; HL CMHB-C

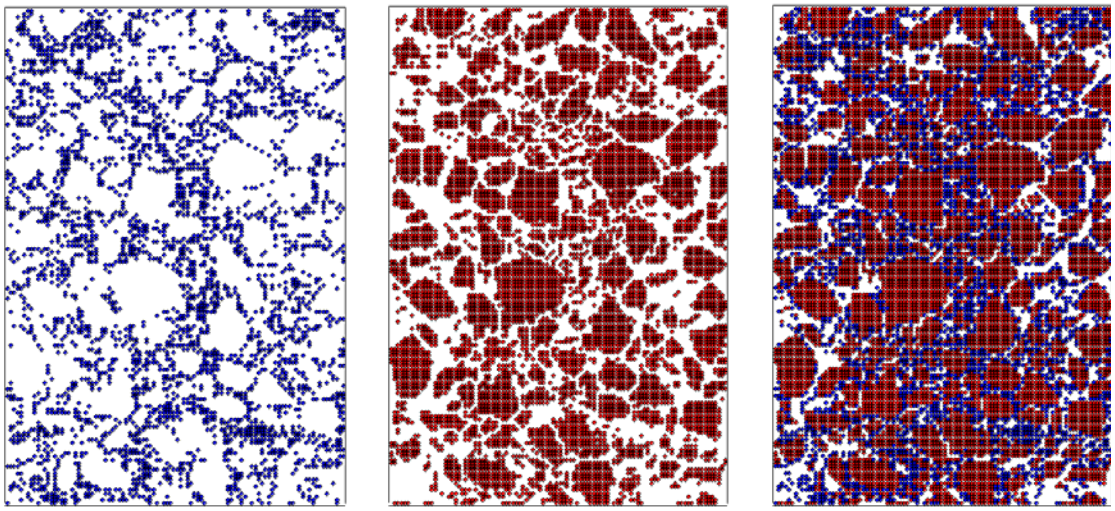

(a) **(b)** **(c)**

Figure 5.16 Representation AC Rectangular Sections for DEM Simulation, (a) Mastic Phase in Blue, (b) Aggregate Phase in Red, and (c) Mixture; HL CMHB-C

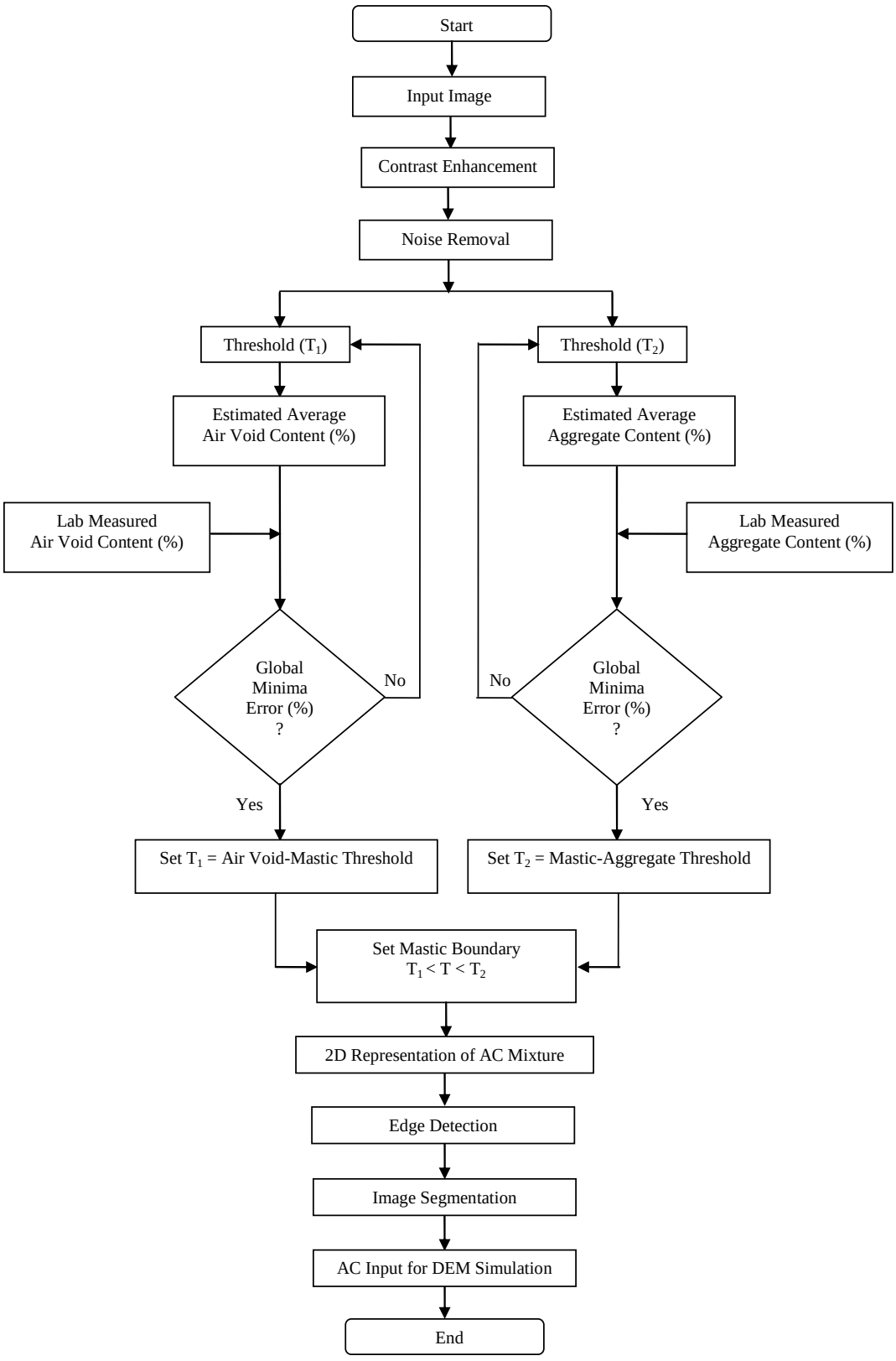

Figure 5.17 Flowchart of the VMG Thresholding and Image Enhancing Algorithm

5.4 Summary and Conclusions

In this Chapter, an automated Digital Image Processing (DIP) technique was described for processing the AC X-ray CT images for DEM simulation. The software implementing this technique, named Volumetric-based Global Minim (VGM), utilizes MATLAB®. The method is based on identifying gray level boundary thresholds between air, mastic and aggregate phases with reference to volumetric information. It involves three stages, namely image preprocessing, thresholding and post-processing. The resulting images are significantly improved compared to the raw X-ray CT images. The post-processed images are represented in 2-D and inputted for DEM simulation. Their quality is sufficient for input into numerical simulations of AC micromechanical behavior. This algorithm was shown to be a major improvement over the largely manual techniques used in the past.

Chapter 6

CHARACTERIZATION OF THE RHEOLOGICAL PROPERTIES OF ASPHALT BINDERS AND MASTICS

6.1 Introduction

The performance of the ACs is greatly influenced by the properties of the asphalt binding materials. Asphalt mastics are blends of asphalt binder and mineral fillers passing sieve No. 200 (sieve size 75 μm). The effects of mineral fillers on AC mixtures have been studied extensively by many researchers (Tunnicliff, 1962; Kallas and Puzinauskas, 1967; Puzinauskas, 1969; Andereson and Goetz, 1973; Harris and Stuart, 1995; Ishai and Craus, 1996; Chen and Peng, 1998; Shashidhar and Romero, 1998; Buttlar et al., 1999; Kim et al., 2003; Kim and Little, 2004; Abbas et al., 2005). The viscoelastic rheological properties of asphalt binders and mastics under an imposed shearing stress are time and temperature dependent and play a significant role in AC mechanical response. There are several studies focused on characterizing the behavior of these materials using viscoelastic rheological models, namely the Maxwell, Kelvin-Voigt, and Burger model (Kim and Little, 2004; Abbas et al., 2005; Yu et al., 2007). Several DEM studies have implemented Burger models in simulating the micromechanical mastic-to-mastic contact behavior (Collop et al., 2004a; You and Buttlar, 2006; Abbas et al., 2005; Hu et al., 2007; Yu et al., 2007). Defining this contact model requires appropriate rheological testing, such as frequency sweep shear or creep tests. Furthermore, fitting this model to the experimental data involves non-linear optimization techniques. Abbas et al., (2004) fitted a Burger contact model using the statistical software called GAUSS v 3.2 (GAUSS, 1996). Data was obtained from frequency sweep DSR testing. Fitting was based on storage and lose modulus values.

In this chapter, the characterization of the viscoelastic rheological properties of the asphalt binders and mastics is presented. The tests were performed on a PG 76-22 unaged and an RTFTO-aged binder and mastics produced with this binder using a

SmartPave® dynamic shear rheometer (DSR) at a single testing temperature of 60^0C. The mathematical formulations of the viscoelastic rheological model parameters, materials tested, and the testing methods involved are briefly discussed. At the end, the non-linear optimization techniques implemented to fit the Burger model parameters to the experimental data are presented. The predicted Burger contact model parameters will be used in a DEM software package called *Particle Flow Code in two-dimensions* (PFC^{2D}) to simulate the creep behavior of AC mixtures, as described in Chapter 8.

6.2 Mathematical Description of Rheological Parameters

The time or frequency dependent behavior of asphalt binders and mastics can be investigated using oscillatory, creep recovery, and relaxation tests. These testes are carried out using two methods of testing, namely the controlled shear rate (CSR) tests that measure the shear stress and phase angle and the controlled shear stress (CSS) tests that measure the shear strain and phase angle. The rheological parameters resulted from these two tests are essentially dependent on the oscillating frequency (ω) and the loading/unloading time (t). Different rheological parameters can be derived assuming a harmonic shear loading of the form given by:

$$\gamma(t) = \gamma_A \, e^{i(\omega t - \delta)} \tag{6.1}$$

where, $\gamma(t)$ is the shear strain or deformation at time t; γ_A is variable shear strain amplitude; δ is phase shift angle in degrees; and i represents $\sqrt{-1}$.

In rheology, it is customary to represent parameters measured from sinusoidal shear load by a complex form, using a star $(*)$. The complex shear modulus (G^*) that describes the viscoelastic behavior of asphalt binders and mastics is the vector sum of storage modulus (G') and loss modulus (G'') given by:

$$G^*(i\omega) = \frac{\tau^*}{\gamma^*} = G'(\omega) + iG''(\omega) \tag{6.2}$$

where, τ represents the shear stress.

As illustrated in Figure 6.1, the real and imaginary parts in Equation (6.2) are given by:

$$G'(\omega) = \frac{\tau_0}{\gamma_0}\cos(\delta) \tag{6.2a}$$

$$G''(\omega) = \frac{\tau_0}{\gamma_0}\sin(\delta) \tag{6.2b}$$

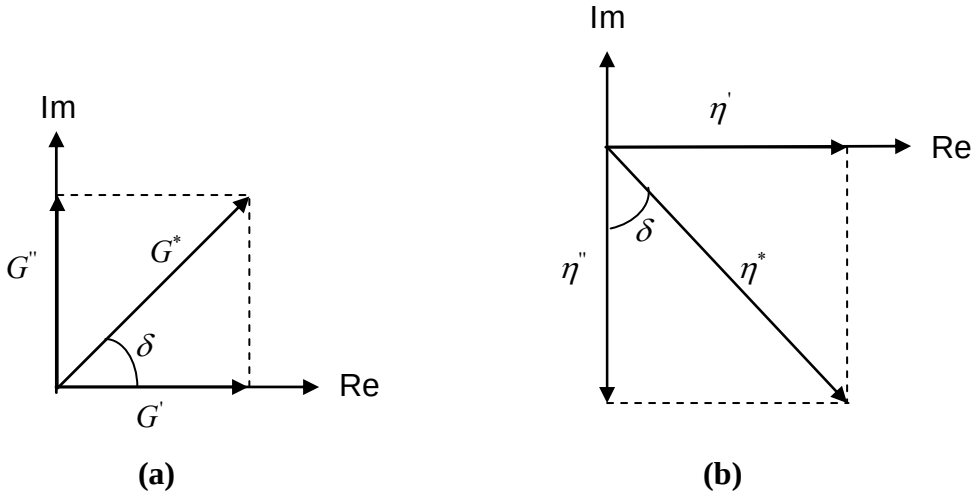

Figure 6.1 Representation of the Viscoelastic Behavior of a Asphalt Binders and Mastics (a) G', G'' and G^*, and (b) η', η'' and η^*

The storage modulus represents the elastic behavior of the material and exhibits reversible deformation behavior (i.e., measures the deformation energy stored during the shear process). On the other hand, the loss modulus represents the viscous behavior of the material and displays irreversible deformation behavior (i.e., measures the deformation energy dissipated during the shear process). Ideal elastic and viscous behavior are reflected by $\delta = 0^0$ and $\delta = 90^0$, respectively. Typically, the asphalt binder and mastic

viscoelastic phase angle ranges between zero and ninety (i.e., $0^0 < \delta < 90^0$). The magnitude of the complex shear modulus is given by:

$$| G^* | = \sqrt{G' + G''} \tag{6.3}$$

Often, the viscoelastic behavior of asphalt binders and mastics can also be described using the loss (or damping) factor function given by:

$$\tan \delta(\omega) = \frac{G''(\omega)}{G'(\omega)} \tag{6.4}$$

Since, the loss factor varies from zero to infinity, this parameter represents the ratio of the energy lost and stored per cycle of the shear process.

Analogous to the shear viscosity of a Newtonian fluid, the complex shear viscosity (η^*) , as illustrated in Figure 6.1, is the vector sum of the real (η') and imaginary (η'') components of viscosity:

$$\eta^*(i\omega) = \frac{\tau}{\dot{\gamma}^*} = \frac{\tau}{(i\omega\gamma^*)} = \eta'(\omega) - i\eta''(\omega) \tag{6.5}$$

The complex shear modulus and the complex shear viscosity can be related by:

$$G^* = i\omega\eta^* \tag{6.6}$$

$$\eta^* = \frac{G^*}{\omega} = \sqrt{(\eta')^2 + (\eta'')^2} \tag{6.7}$$

$$\eta' = \frac{G''}{\omega} \tag{6.7a}$$

$$\eta'' = \frac{G'}{\omega} \tag{6.7b}$$

In summary, the elastic and viscous portion of the viscoelastic component can be expressed using (G' and η'') and (G'' and η'), respectively.

Inverting Equation (6.2) yields the complex shear compliance (J^*) parameter:

$$J^*(i\omega) = \frac{\gamma^*}{\tau^*} = J'(\omega) - iJ''(\omega) \tag{6.8}$$

$$J'(\omega) = \frac{\gamma_0}{\tau_0}\cos(\delta) \tag{6.8a}$$

$$J''(\omega) = \frac{\gamma_0}{\tau_0}\sin(\delta) \tag{6.8b}$$

Equation (6.8a) and (6.8b) represent the storage and loss shear compliance, respectively.

6.3 Viscoelastic Rheological Models

Asphalt binders and mastics exhibit both features of elastic solids and viscous fluids and hence, behave as viscoelastic materials. The main feature of the elastic behavior is to fully store the energy during loading and completely dissipate it during unloading. Consequently, viscoelastic models can store and dissipate energy at varying levels during loading/unloading and can be used to describe the time-dependent shear stress/strain response of asphalt binders and mastics.

The viscoelastic rheological models can accurately describe the behavior of asphalt binders and mastics across a wide range of shear strain rates, shear stress levels and temperatures and therefore largely simulate the real conditions in the field. The phenomenological viscoelastic behavior of asphalt binders and mastics can be characterized well by combining Hook's spring and Newton's dashpot elements in series or in parallel. The most commonly used viscoelastic rheological models for asphalt

binders and mastics are the Maxwell model, the Kelvin-Voigt model, and the Burger model, as illustrated in Figure 6.2. The Maxwell model consists of one linear Hooke's spring and one linear Newton's dashpot connected in series. The Kelvin-Voigt model has these elements connected in parallel. The Burger Model consists of a Maxwell and Kelvin-Voigt element coupled in series.

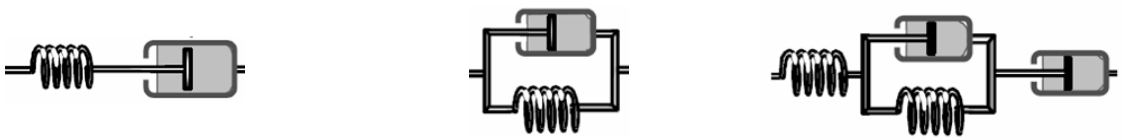

(a) **(b)** **(c)**

Figure 6.2 Viscoelastic Rheological Models; (a) Maxwell Model, (b) Kelvin-Voigt Model, and (c) Burger Model

6.3.1 The Burger Rheological Model

The shear stress-strain behavior of the Burger model can be described using analytical formulations derived in the time or the frequency domain. The viscoelastic behavior of the asphalt binders and mastics rely on the individual Burger model elements. Hence, accurate procedures have to be followed to determine these parameters. In this section, detailed derivation of the stress-strain behavior of the Burger model under oscillatory shear loading/unloading process for both time and frequency domains is presented.

6.3.1.1 Creep Compliance, J(t)

One of the simplest rheological tests that measure the viscoelastic response of the asphalt binders and mastics is the creep test. It involves applying a constant shear stress to the sample for some period of time and monitoring the resulting shear strain. The strain response under constant stress is used to derive the four parameters of the Burger model as illustrated in Figure 6.3.

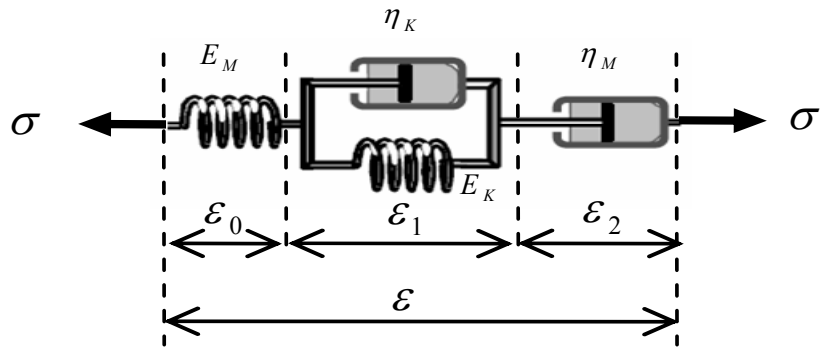

Figure 6.3 Four Element Burger Model

The total strain at time *t* is decomposed into three components:

$$\varepsilon(t) = \varepsilon_0 + \varepsilon_1 + \varepsilon_2 \tag{6.9}$$

The first component is obtained from Hooks' spring as:

$$\varepsilon_0 = \frac{\sigma}{E_M} \tag{6.10}$$

The second component is the stain from the Kelvin element that satisfies the following ordinary differential equation:

$$\dot{\varepsilon}_1 + \frac{E_K}{\eta_K}\varepsilon_1 = \frac{\sigma}{\eta_M} \tag{6.11}$$

The third component represents the Newton's dashpot given by:

$$\dot{\varepsilon}_2 = \frac{\sigma}{E_M} \tag{6.12}$$

where,

E_M and E_K respectively are the Maxwell and Kelvin spring stiffnesses, and

η_M and η_K are the Maxwell and Kelvin dashpot constants, respectively.

The constitutive equation of the Burger model can be obtained by utilizing Laplace transformation to the Equation 6.9, noting that the transferred quantities are functions of the transferred variable *s* instead of the actual time *t*:

$$L\{\varepsilon(t)\} = \hat{\varepsilon}(s) = \hat{\varepsilon}_0(s) + \hat{\varepsilon}_1(s) + \hat{\varepsilon}_2(s) \tag{6.13}$$

$$\hat{\varepsilon}_0 = \frac{\hat{\sigma}(s)}{E_M} \tag{6.14}$$

$$s\hat{\varepsilon}_1 - \varepsilon_1(0) + \frac{E_K}{\eta_K}\hat{\varepsilon}_1 = \frac{\hat{\sigma}(s)}{\eta_M} \tag{6.15}$$

$$s\hat{\varepsilon}_2 - \varepsilon_2(0) = \frac{\hat{\sigma}(s)}{\eta_M} \tag{6.16}$$

Assuming that the initial values of $\varepsilon_1(0) = \varepsilon_2(0) = 0$ and inserting the transformed quantities, Equation (6.14) through (6.16) into Equation (6.13) yields:

$$\hat{\varepsilon}(s) = \hat{\sigma}(s)\left(\frac{1}{E_M} + \frac{1}{\eta_M s} + \frac{1}{E_K + \eta_K s}\right) \tag{6.17}$$

Assuming that the Burger model is subjected to a constant stress (or creep load), the following holds true:

$$\sigma(t) = \sigma_0 H(t) \text{ and } L\{\sigma(t)\} = \hat{\sigma}(s) = \frac{\sigma_0}{s} \tag{6.18}$$

where, $H(t)$ is a unit step function defined by:

$$H(t-a)=\begin{cases}1 & for \quad t \geq a \\ 0 & for \quad t < a\end{cases} \quad \text{or} \quad H(t-a)=\begin{cases}1 & for \quad t > a \\ 1/2 & for \quad t = a \\ 0 & for \quad t < a\end{cases} \tag{6.19}$$

where, t is the time variable and $t = a$ denotes a time at which a step change has been occurred.

Thus, substituting Equation (6.18) into Equation (6.17) yields:

$$\frac{1}{\sigma_0}\hat{\varepsilon}(s)=\frac{1}{E_M s}+\frac{1}{\eta_M s^2}+\frac{1}{E_K s(1+\lambda_2 s)} \tag{6.20}$$

Taking the inverse of Equation (6.20) gives the strain function of the Burger model:

$$\frac{\gamma(t)}{\sigma_0}=\frac{1}{E_M}+\frac{1}{E_K}(1-e^{-\frac{E_K}{\eta_K}t})+\frac{t}{\eta_M} \tag{6.21}$$

The Burger model can also be expressed in terms of the creep compliance when dividing Equation (6.21) by the constant stress:

$$J(t)=\frac{\varepsilon(t)}{\sigma_0}=J_0(1+\frac{t}{\lambda})+J_1(1-e^{-\frac{t}{\Lambda}}) \tag{6.22}$$

where,

$J_0=\frac{1}{E_M}, J_1=\frac{1}{E_K}$, $\lambda=\frac{\eta_M}{E_M}$, $\Lambda=\frac{\eta_K}{E_K}$, λ and Λ represent the relaxation and retardation time of the Burger model, respectively; $\gamma(t)$ is the shear strain as a function of loading time, τ_0 and γ_0 are the initial shear stress and shear strain parameters, respectively. The rest parameters have been previously defined.

6.3.1.2 Retardation Time (Λ)

The retardation time (Λ) can also be used to evaluate the time-dependent behavior of asphalt binders and mastics under constant shear stress (or creep load). It represents the delayed response of the mechanistic model to an applied shear stress level. In the Burger model, the ratio of the dashpot constant to the elastic spring of the Kelvin-Voigt component defines the retardation time and given by:

$$\Lambda = \frac{\eta_K}{E_K} \tag{6.23}$$

6.3.1.3 Relaxation Modulus, G(t)

The stress relaxation test involves application of a constant strain for some period of time and monitor resulting shear stress that decays away with time. The response of the Burger model due to the application of a constant strain can be characterized using the relaxation modulus, $G(t)$ which is equal to the resulting shear stress function divided by the constant strain value.

$$G(t) = \frac{\tau(t)}{\gamma_0} \tag{6.24}$$

Similar to the creep compliance, the constant strain function is defined as:

$$\varepsilon(t) = \varepsilon_0 H(t) \text{ and } L\{\varepsilon(t)\} = \hat{\varepsilon}(s) = \frac{\varepsilon_0}{s} \tag{6.25}$$

Substituting Equation (6.25) into Equation (6.17) yields:

$$\frac{\varepsilon_o}{s} = \hat{\sigma}(s)\left(\frac{1}{E_M} + \frac{1}{s\,\eta_M} + \frac{1}{E_K + s\,\eta_K}\right) \tag{6.26}$$

The relaxation modulus is calculated by taking the inverse Laplace transform of $\hat{\sigma}/\varepsilon_o$ and given by:

$$G(t) = \frac{\left(\eta_M - \frac{\eta_M \eta_K}{R_K} r_1\right) e^{-r_1 t} - \left(\eta_M - \frac{\eta_M \eta_K}{R_K} r_2\right) e^{-r_2 t}}{A} \tag{6.27}$$

where,

$$r_1 \text{ and } r_2 = \frac{(p_1 \pm A)}{2\, p_2} \tag{6.28}$$

$$A = \sqrt{p_1^2 - 4\, p_2} \tag{6.29}$$

$$p_1 = \frac{\eta_M}{R_M} + \frac{\eta_M}{R_K} + \frac{\eta_K}{R_K} \tag{6.30}$$

$$p_2 = \frac{\eta_M \eta_K}{R_M R_K} \tag{6.31}$$

6.3.1.4 Relaxation Time (λ)

Moreover, the relaxation time (λ) can also be used to evaluate the time-dependent behavior of asphalt binders and mastics under constant shear strain. It depicts the calming process after shear deformation taken place under constant shear strain (strain rate). In the Burger model, the ratio of the dashpot constant to the elastic spring of the Maxwell model defines the relaxation time and given by:

$$\lambda = \frac{\eta_M}{E_M} \tag{6.32}$$

Using the Maxwell model ***only***, the viscoelastic behavior of asphalt binders and mastics under shear load can be expressed using the following differential equation:

$$\dot{\gamma} = \frac{\tau}{\eta_M} + \frac{\dot{\tau}}{E_M} \tag{6.33}$$

Solving the differential equation, leads to:

$$\tau(t) = \gamma E_M \exp(-t/\lambda) \tag{6.34}$$

At the time period $t = \lambda$, the following holds true in the relaxation phase of the unloading process:

$$\tau(\lambda) = \gamma E_M \exp(-\lambda/\lambda) = 0.368\,\gamma E_M = 36.8\%\ \tau_{\max} \tag{6.35}$$

This implies that in relaxation phase, the relaxation time λ of the Maxwell model is over when the τ value has decreased to 36.8% of the maximum shear stress $\tau_{\max}$, which reached immediately after the γ step. In other words, in this period of time, the shear stress has already decreased by 63.2% of the initial value of $\tau_{\max}$.

Similarly, the Burger rheological model parameters in frequency domain can be expressed as:

$$D^*(\omega) = D'(\omega) - \mathrm{i}\, D''(\omega) \tag{6.36}$$

$$D'(\omega) = \left(\frac{1}{E_M} + \frac{E_K}{{E_K}^2 + \omega^2 {\eta_K}^2} \right) \tag{6.36a}$$

$$D''(\omega) = \left(\frac{1}{\omega \eta_M} + \frac{\omega \eta_K}{{E_K}^2 + \omega^2 {\eta_K}^2} \right) \tag{6.36b}$$

where,

$D'(\omega)$ and $D''(\omega)$ represent the storage and loss shear modulus, respectively.

In general, the complex shear compliance can also be calculated using:

$$J^* = \frac{1}{G^*} \tag{6.37}$$

Noting that $J' \neq 1/G'$ and $J'' \neq 1/G''$

$$\left|J^*\right| = \sqrt{(J')^2 + (J'')^2} \tag{6.38}$$

$$J'(\omega) = \frac{G'}{(G')^2 + (G'')^2} = \left(\frac{1}{R_M} + \frac{R_K}{{R_K}^2 + \omega^2 {\eta_K}^2}\right) \tag{6.39}$$

$$J''(\omega) = \frac{G''}{(G')^2 + (G'')^2} = \left(\frac{1}{\omega \eta_M} + \frac{\omega \eta_K}{{R_K}^2 + \omega^2 {\eta_K}^2}\right) \tag{6.40}$$

$$\delta = t\text{an}^{-1}\left(\frac{J''}{J'}\right) \tag{6.41}$$

where,

$J'(\omega)$ and $J''(\omega)$ represent the storage and loss shear compliance, respectively.

6.4 Materials and Methods

6.4.1 Sample Preparation

For this research work, only one asphalt binder, a PG 76-22 grade supplied by the Valero Ardmore Refinery in OK, was utilized. This allowed focusing the experimental design of the study on the aggregates and the mix design. The AC mixture volumetric data was briefly explained in Chapter 4. Three AC mixture types commonly used in

TxDOT were selected, namely a Coarse Matrix High Binder type C (CMHB-C), a Porous Friction Course (PFC) and a Superpave type C (Superpave-C) mixtures. Three aggregate sources, namely a hard limestone (HL), a granite (G) and a soft limestone (SL) were used to prepare the AC mixtures. Based on Tex-401-A specifications, sieve analysis was performed on dried aggregates to obtain the percentage of fines passing sieve No. 200 (sieve size 75 μm). Eighteen asphalt mastics were prepared, each with a combination of the three types of fines, the volumetric characteristics of the three mix designs and the two types of binder conditioning. The binder and filler volume fractions for each mastic specimen are given in Table 6.1. In this research, the term unaged and RTFO-aged mastic relate to the condition of the binder used to prepare the mastics

6.4.2 Mixing and Fabrication of Samples

The aggregate fines to binder proportions used in making the mastics for testing were calculated by volume and weight as shown in Table 6.1 and 6.2, respectively. The PG 76-22 binder was preheated at mixing temperature of 163^0C to ensure complete fluidity and then sufficiently stirred to homogenize and remove the air bubbles before pouring to the respective proportions of the fines. RTFO-aged binder tests were performed on original PG 76-22 binder in accordance with AASHTO T240/ASTM D2872 specification procedures (the unaged binder was aged using testing temperature of 163^0C and air flow of 4000 ml/min for 85 minutes). The RTFO-aged binder was used to prepare mastics in order to resemble the short-term aging that takes place during mixing and handling processes and characterize the formation of rutting after a defined period of time, example at early stage of pavement life. The unaged mastics are also included in this study for ascertaining the stiffening effect of the fines. The unaged and RTFO-aged binder mastics were fabricated manually for each filler volume and poured into the standard rubber mold that can hold at least 2 mm thick mastic specimen for Dynamic Shear Rheometer (DSR) rheological testing.

Table 6.1 Mastic Sample Proportions using Unaged and RTFO-aged Binder by Volume

Sample Type	Sample Label	Fine Aggregate Content[+] (%)	Binder Content (%)	Mastic (%)
Unaged Binder	Unaged 76-22	-	100	-
RTFO-aged Binder	RTFO-aged 76-22	-	100	-
Mastic using Unaged Binder	HL CMHB-C	7.235	9.749	16.984
	G CMHB-C	5.763	11.954	17.717
	SL CMHB-C	5.374	12.956	18.330
	HL PFC	4.496	10.284	14.780
	G PFC	1.496	12.845	14.341
	SL PFC	1.682	13.734	15.416
	HL Superpave-C	7.468	9.340	16.808
	G Superpave-C	6.347	11.041	17.388
	SL Superpave-C	5.875	11.963	17.837
Mastic using RTFO-aged Binder	HL CMHB-C	7.235	9.749	16.984
	G CMHB-C	5.763	11.954	17.717
	SL CMHB-C	5.374	12.956	18.330
	HL PFC	4.496	10.284	14.780
	G PFC	1.496	12.845	14.341
	SL PFC	1.682	13.734	15.416
	HL Superpave-C	7.468	9.340	16.808
	G Superpave-C	6.347	11.041	17.388
	SL Superpave-C	5.875	11.963	17.837

[+] Fines Passing Sieve No. 200 (or Sieve Size 75 μm)
HL: Hard Limestone; G: Granite; SL: Soft Limestone

Table 6.2 Mastic Sample Proportions by Weight

Sample Label	Weight Ratio (Mass of Fines[+]/Mass of Binders)
HL CMHB-C	1.96 : 1
G CMHB-C	1.23 : 1
SL CMHB-C	1.05 : 1
HL PFC	1.15 : 1
G PFC	0.29 : 1
SL PFC	0.30 : 1
HL Superpave-C	2.13 : 1
G Superpave-C	1.50 : 1
SL Superpave-C	1.28 : 1

[+] Fines Passing Sieve No. 200 (or Sieve Size 75 μm)
HL: Hard Limestone; G: Granite; SL: Soft Limestone

6.5 Dynamic Shear Rheometer (DSR)

The deformation and flow behavior of asphalt binders and mastics under creep and recovery, relaxation and oscillatory tests can be measured using parallel-plate measuring system as given in Figure 6.4. The geometer of the parallel-plate is determined by the plate radius (R) and the distance between the two parallel plates (H). AASHTO TP 05 recommends (R = 12.5 mm and H = 1 mm) and (R = 4 mm and H = 2 mm) respectively for unaged and RTFO-aged binder specimens. However, the mastic testing procedures are not yet standardized by AASHTO. In this research project, the later parallel-plate geometry was adopted for mastic testing due to the presence of additional stiffness from the mineral filler volume.

DSR is a conventional testing method world wide in industries and research centers used to characterize the rheological properties fluid-like materials such as asphalt binders and mastics. A typical SmartPave® DSR device from *Anton Paar* Germany GmbH is shown in Figure 6.5. The special features of this device may include: torque range 0.5 to 125000 μNm; speed range 0.0001 to 3000 rpm; frequency range 0.0001 to

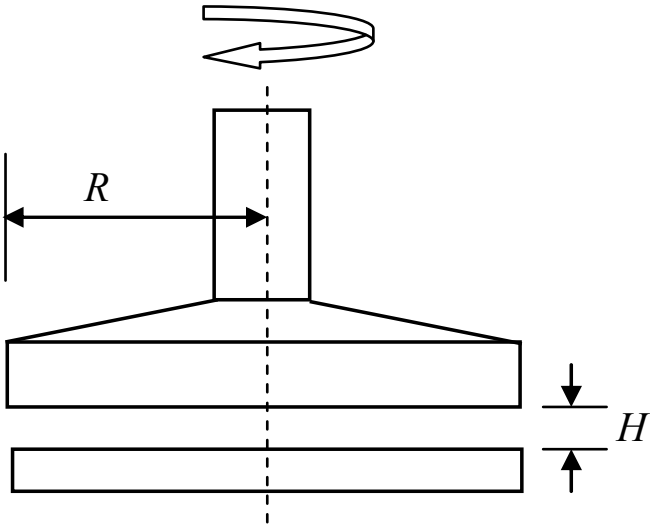

Figure 6.4 Parallel-Plate Measuring System

Figure 6.5 SmartPave® DSR (*Anton Paar* Germany GmbH)

100 Hz. In this research, the maximum torque required to shear the stiffest mastic sample was about 60000 μNm. Moreover, it has heating and cooling temperature control, automatic temperature calibration and gap setting system. The data acquisition system provides a record of several shear stress-strain responses parameters such as complex shear modulus, storage and loss shear modulus, and phase angle. In addition, it has user friendly software called Rheoplus® that generates different rheological parameters supported by graphical representation as well.

6.5.1 Preparation of the Apparatus

The following DSR testing procedures, some of them are illustrated in Figure 6.5, were followed when testing the asphalt binder and mastic specimens at the University of Texas at San Antonio (UTSA) Geomaterial Laboratory:

- Connect the air supply and air drier that work at a pressure less than 72 Psi.
- Switch on the DSR instrument.
- Switch on the computer and start the rheometer software.
- Switch on the fluid circulator component.
- Initialize the instrument. During this process, the measuring head will move automatically to the top position to check the gap sensor (Figure 6.6a).
- Select the required testing temperature (in this research project, the testing temperature was 60^0C) (Figure 6.6b).
- Chose measuring system (25 mm plate diameter for unaged binder and 8 mm plate diameter for RTFO-aged binder and mastic samples) (Figure 6.6c).
- Mount the measuring system. Push up the sleeve of the coupling and insert the upper end of the measuring system into the coupling. Make sure to align the markers on the measuring system and the coupling. Pull down the sleeve to fix the measuring system. To remove the measuring system, push up the sleeve and take out the system (Figure 6.6d).
- Check the thermal equilibrium status again (Figure 6.6b).
- Establish zero-gap between the upper and lower plates.
- Establish 1 mm plate gap for unaged binder samples and 2 mm plate gap for RTFO-aged binder and mastic samples (Figure 6.6e).

- Move the measuring system up to the lift position.
- Load the specimen and then lower the measuring system to the required plate gap (Figure 6.6f).
- Trim the excess sample using heated spatulas (a torch or lighter can be used to preheat the spatulas) (Figure 6.6g).
- Move the upper hood down to cover the sample. The hood maintains uniform temperature during testing (Figure 6.6h).
- Again check the thermal equilibrium status (Figure 6.6b).
- Start the rheological testing and record the measurements (Figure 6.6i).
- After completion of each test, move up the measuring system and clean the plates (Figure 6.6j, k, and l).
- Start the next testing by again re-mounting the selected measuring system.

6.5.2 Rheological Tests on Asphalt Binders and Mastics

The most commonly used rheological tests to characterize different properties of asphalt binders and mastics include: amplitude sweep, frequency sweep, temperature sweep, creep recovery, multiple stress creep recovery, and relaxation tests. These tests can be performed using SmartPave® DSR device. The loading conditions for each of these tests are different. For example, the testing mechanism in oscillatory tests that include amplitude and frequency sweep tests, involves applying harmonic shear stress or strain on the specimen by the upper plate keeping the lower plate fixed. In this process, the specimen is sandwiched between the two parallel plates and should adhere the plates without slipping in order to deform uniformly.

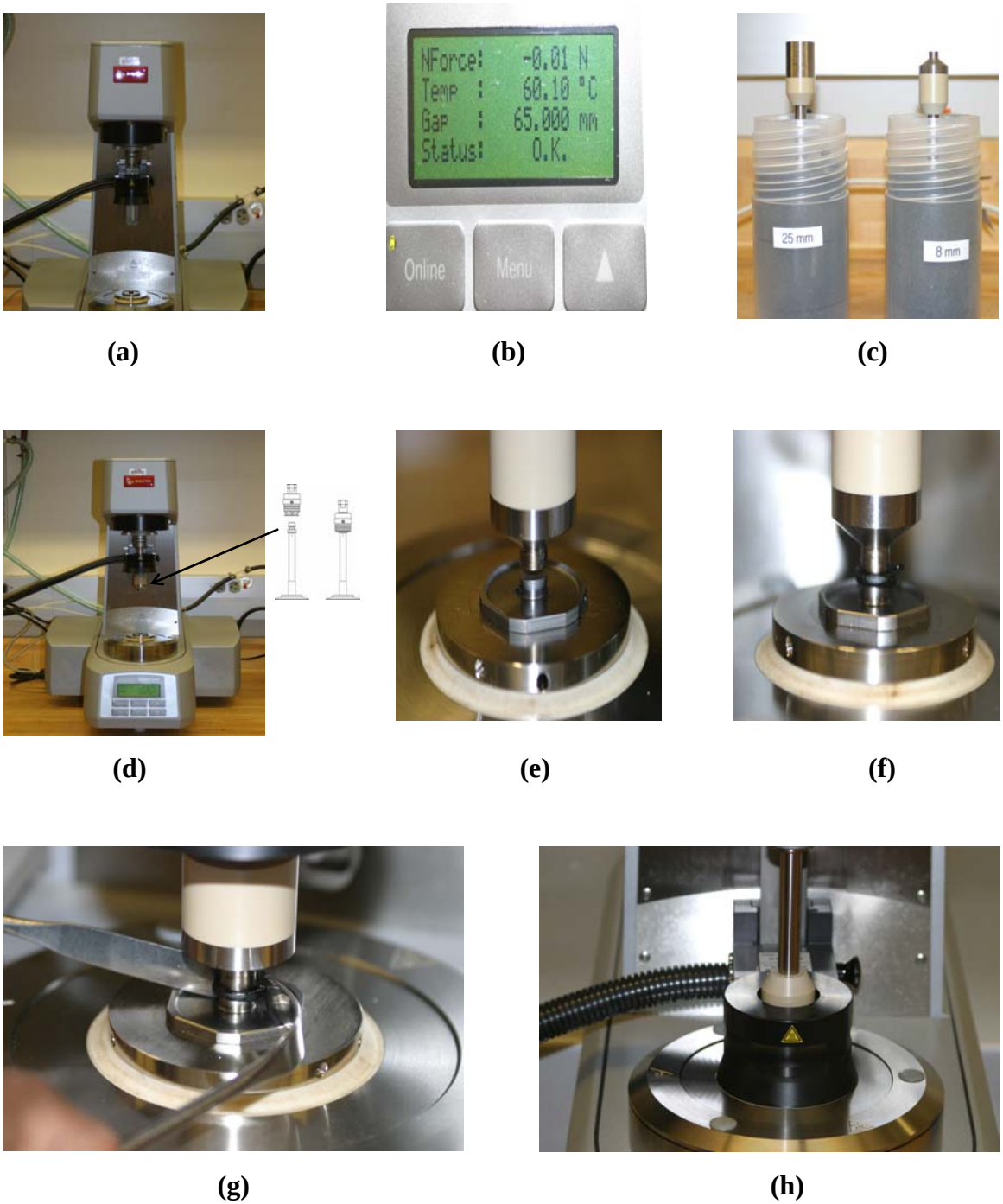

Figure 6.6 Schematic Illustration of SmartPave® DSR Testing

(i)

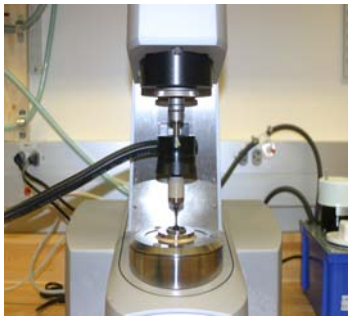

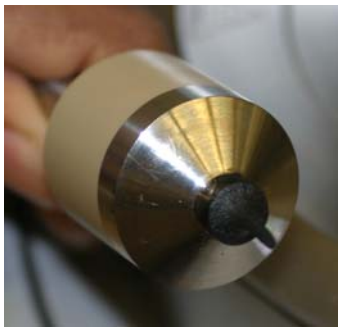

(j) (k) (l)

Figure 6.6 (Continued) Schematic Illustration of SmartPave® DSR Testing

Selection of the test method depends on the intended application. For this study, DSR testing was used to:

- define the limits of linear viscoelasticity (LVE) for the asphalt binders and mastics, given the oscillating loading frequency and,
- determine the Burger model constants of the asphalt binders and mastics that correspond to the LVE range.

As described next, these two goals were achieved through CSR amplitude sweep tests and frequency sweep tests, respectively.

6.5.2.1 Amplitude Sweep Test

In the Strategic Highway Research Program (SHRP) A-369 project, strain amplitude sweep tests were referred to as strain sweep tests. These tests are mostly carried out for the purpose of determining the limits of the linear viscoelastic (LVE) range of asphalt binders and mastics. In this range, the structure of the specimen is stable and the rheological properties are independent of the applied shear stress or strain. In this research the LVE is used to identify the strain level below which viscoelastic behavior can be described with a Burger model. For strain levels higher than the LVE, the behavior of the specimen no longer obeys the Newtonian law and hence requires advanced partial differential equations to characterize the non-linear behavior.

Amplitude sweep tests involve inputting variable strain amplitudes (usually from 0.01 to 100 %) at constant angular frequency (example, 10rad/sec). These tests were performed using CSR testing mode to determine the LVE range of the asphalt binder and mastic specimens at a single testing temperature, 60^0C. Three distinct constant angular frequencies $\omega = 0.1,\ \omega = 1,$ and $\omega = 10$ rad/sec were used. As illustrated in Figure 6.7 and 6.8, the change of complex shear modulus (G^*) was monitored over the applied shear strain level for HL CMHB-C unaged and RTFO-aged mastic samples. Similar details for the rest of the mixtures are given in Appendix C. These figures show that in the LVE range, the $|G^*|$ value decreases linearly with increasing strain level. Considering Figure 6.8, the limiting shear strain value corresponds to the upper limit of LVE range equals 50%, 15%, and 10% for angular frequencies of 0.1, 1, and 10 rad/sec, respectively. Similar values for all the asphalt binder and mastic samples are presented in Table 6.3. It can be concluded that at higher angular frequencies, the asphalt binder and mastic samples behave stiffer and more brittle and therefore have lower limiting LVE values.

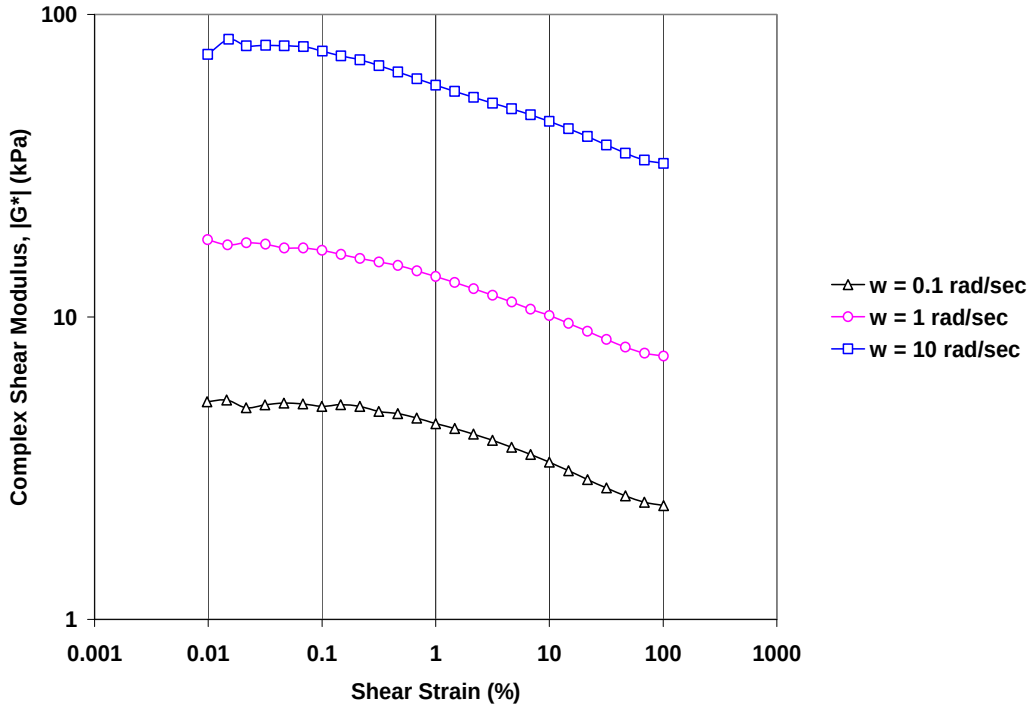

Figure 6.7 Amplitude Sweep Test Result; HL CMHB-C Unaged Mastic

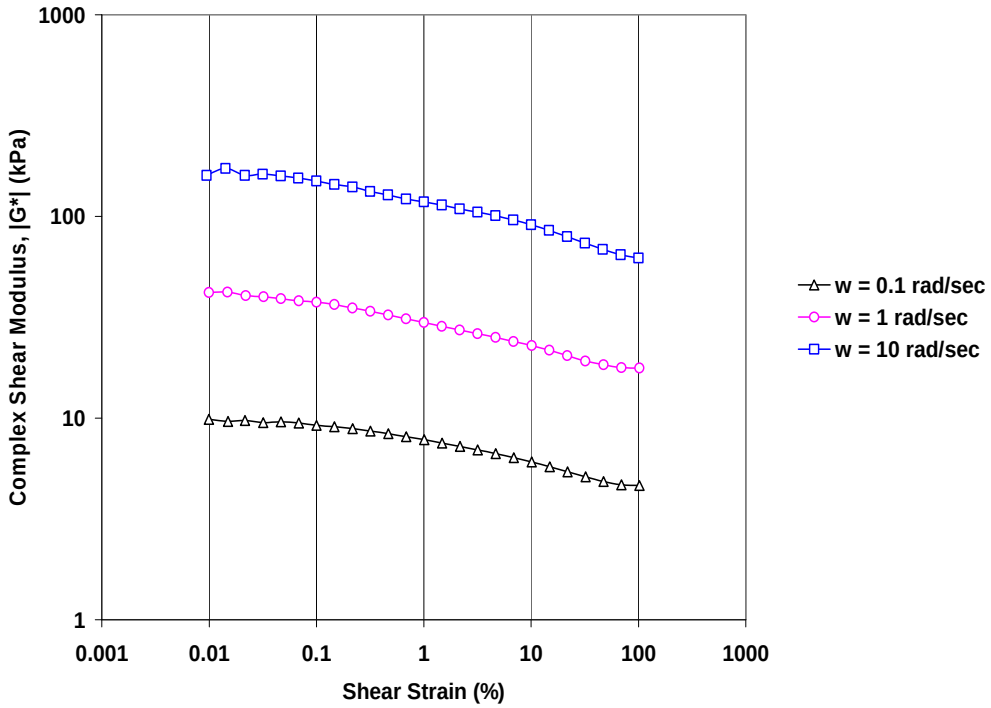

Figure 6.8 Amplitude Sweep Test Result; HL CMHB-C RTFO-aged Mastic

Table 6.3 Limiting Shear Strain Identifying the LVE Range

Sample Type	Sample Label	Limiting Shear Strain (%)		
		ω = 0.1 rad/sec	ω = 1 rad/sec	ω = 10 rad/sec
Unaged Binder	Unaged 76-22	50	30	20
RTFO-aged Binder	RTFO-aged 76-22	70	40	30
Mastic using Unaged Binder	HL CMHB-C	50	30	15
	G CMHB-C	30	20	10
	SL CMHB-C	15	10	7
	HL PFC	50	30	10
	G PFC	30	20	10
	SL PFC	30	20	10
	HL Superpave-C	45	30	10
	G Superpave-C	40	30	10
	SL Superpave-C	30	20	10
Mastic using RTFO-aged Binder	HL CMHB-C	50	15	10
	G CMHB-C	40	20	10
	SL CMHB-C	15	10	7
	HL PFC	15	10	7
	G PFC	30	20	10
	SL PFC	15	10	7
	HL Superpave-C	50	15	10
	G Superpave-C	30	15	10
	SL Superpave-C	15	10	7

HL: Hard Limestone; G: Granite; SL: Soft Limestone

Low angular frequency ranges simulate best the creep behavior of asphalt binders and mastics. Thus, the maximum limiting shear strains were obtained by extrapolating the limiting shear strain values using the selected angular frequencies. As illustrated in Figure 6.9 for the HL CMHB-C samples, the RTFO-aged binder samples exhibited higher maximum LVE shear strain levels compared to the mastics prepared with unaged binders. On the other hand, lower LVE values were apparent for RTFO-aged mastics samples. The same observation was made for all the asphalt binder and mastic samples presented in Appendix C. Moreover, the maximum limiting shear strain value is depicted in Table 6.4 for all asphalt binder and mastic samples considered. It can be concluded that all mastic samples with soft limestone (SL) demonstrated lower maximum shear strain values as compared to the other mastic samples. As it will be mentioned in Chapter 8, the maximum limiting shear strains play a significant role in assigning values to the Burger contact model parameters in linear and non-linear viscoelastic ranges.

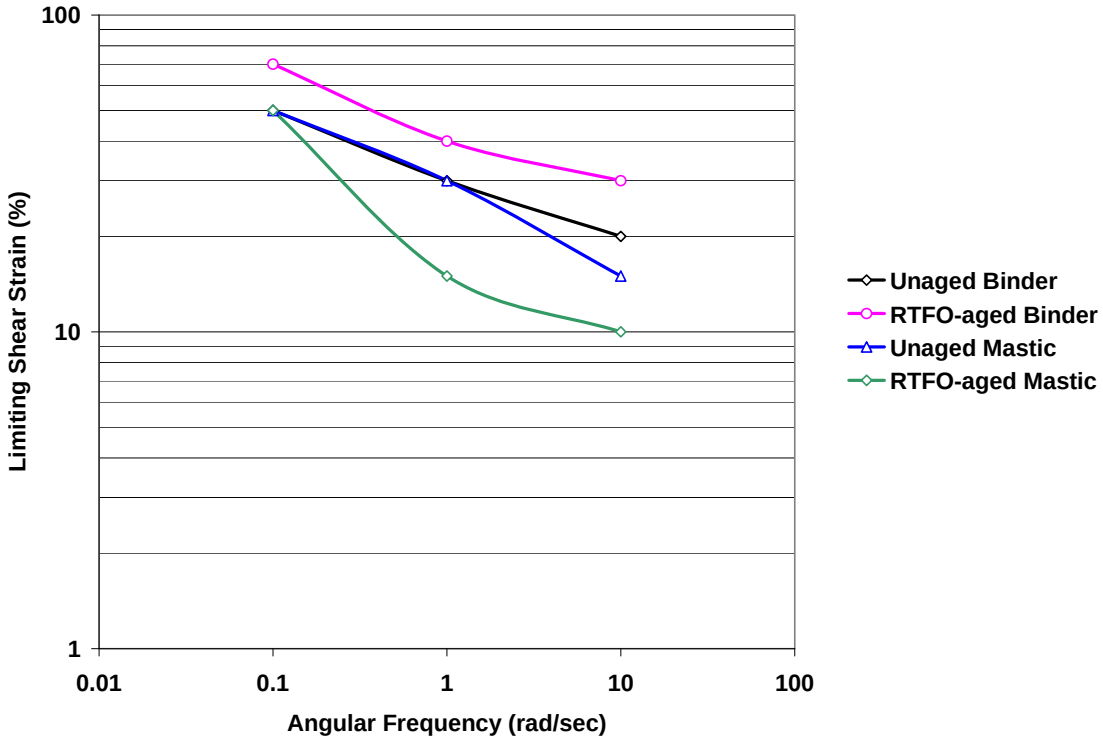

Figure 6.9 LVE Range at Different Angular Frequencies; HL CMHB-C

Table 6.4 Maximum Limiting Shear Strain Values

Sample Type	Sample Label	Limiting LVE Strain (%)
Unaged Binder	Unaged 76-22	52.0
RTFO-aged Binder	RTFO-aged 76-22	73.0
Mastic using Unaged Binder	HL CMHB-C	52.0
	G CMHB-C	31.0
	SL CMHB-C	15.5
	HL PFC	52.0
	G PFC	31.0
	SL PFC	31.0
	HL Superpave-C	46.5
	G Superpave-C	41.0
	SL Superpave-C	31.0
Mastic using RTFO-aged Binder	HL CMHB-C	53.5
	G CMHB-C	42.0
	SL CMHB-C	15.5
	HL PFC	15.5
	G PFC	31.0
	SL PFC	15.5
	HL Superpave-C	53.5
	G Superpave-C	31.5
	SL Superpave-C	15.5

HL: Hard Limestone; G: Granite; SL: Soft Limestone

Once the limiting LVE value is established, other rheological tests can be performed to identify the linear viscoelastic properties within the LVE range. Frequency sweep tests were performed within the LVE range to characterize the viscoelastic behavior of asphalt binders and mastics.

6.5.2.2 Frequency Sweep Test

Frequency sweep tests are commonly performed to investigate the original (unaged) and RTFO-aged binder plastic deformation resistance behavior. These tests involve inputting variable angular frequency (usually 0.01 to 100 rad/sec) at constant shear strain amplitude within the LVE range (example, γ_A = 10 %). Frequency sweep tests show the changes in the viscoelastic behavior of the material under the application of shear strain or stress and hence can be used to examine the time-dependent behavior of asphalt binders and mastics. In other words, the short- and long-term behavior of these materials that simulate the low- and high-traffic conditions respectively can be characterized.

In this research project, the main objective of performing frequency sweep tests is to characterize the viscoelastic behavior of the asphalt binders and mastics. These tests were performed under CSR mode using the strain amplitude (γ_A) equals the maximum limiting shear stain value and with angular frequencies ranging from 0.01 to 100 rad/sec. Figure 6.10 shows a typical frequency sweep test performed on HL CMHB-C RTFO-aged mastic sample that retains 53.5% of maximum limiting shear strain value as given in Table 6.4. The complex shear modulus increases linearly with the inputted frequency range. The phase angle of this mastic sample at higher angular frequency is about 65 degrees that demonstrates the viscous behavior dominancy. Similar observations were made for the rest of the mixtures as presented in Appendix C.

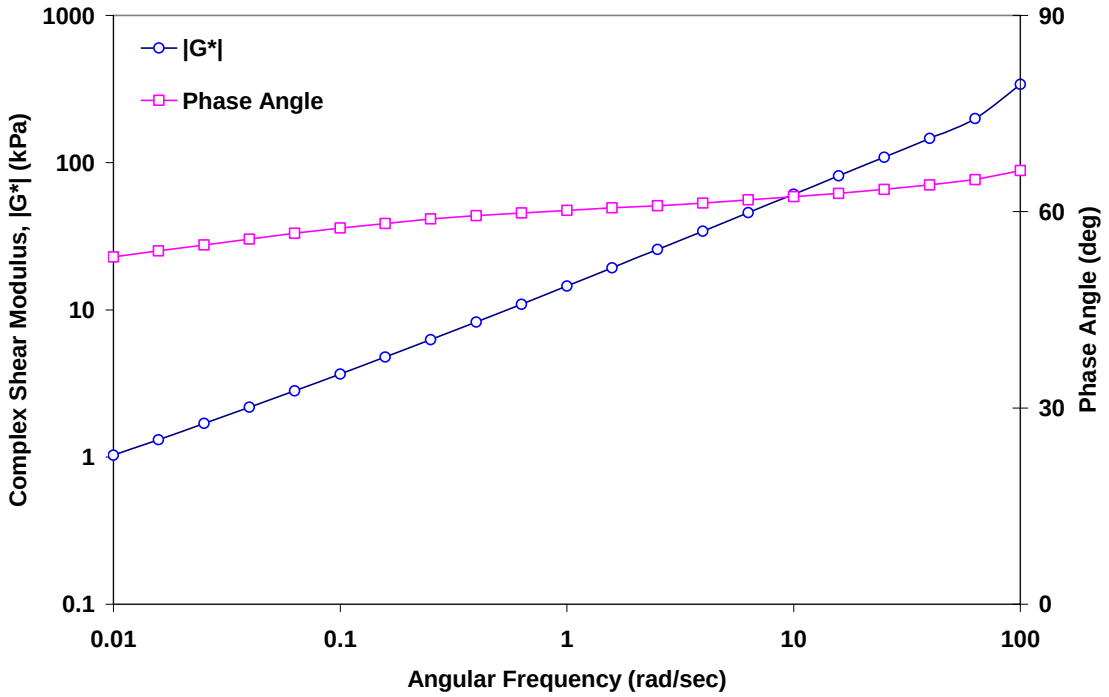

Figure 6.10 Frequency Sweep Test Result, γ_A = 53.5%; HL CMHB RTFO-aged Mastic

6.6 Fitting Burger Models to Experimental Data

The stress-strain behavior of the Burger model under different rheological testing methods is described in time and frequency domains using mathematical formulations presented in Section 6.2 and 6.3. The frequency sweep test data results obtained from different asphalt binder and mastic samples were used to fit the Burger model parameters using non-linear statistical optimization techniques. The complex shear modulus and phase angle of each frequency sweep tests are used to predict the Burger model parameters. For this purpose, Equation 6.37 through 6.42 were utilized.

The Burger model parameters are crucial components for modeling the micromechanical behavior of AC mixtures. Fitting these parameters to the experimental data is not trivial and hence it was necessary to evaluate alternative statistical software packages that could be used for this purpose. Three statistical software packages that utilize the non-linear optimization techniques were evaluated for this purpose: (1) the "Solver" option in Microsoft Excel. This method was utilized to predict the Burger model parameters; however the results were highly dependent on the initial values inputted for the model parameters; (2) the GAUSS statistical software version 8.0 (GAUSS, 2007).

This method is computationally intensive for the purpose of minimizing the objective function given in Equation 6.42. Abbas, (2004) implemented GAUSS version 3.2 (GUASS, 1996) to predict the Burger model parameters using Newton-Raphson and Nelder-Meade algorithms. It was found that the complex shear modulus values were best predicted and however, they fall short to satisfactorily fit the phase angle experimental data; and (3) the non-linear optimization statistical tool in MATLAB® (Misiti et al., 2006). This method utilizes the large-scale algorithm options that handles the bound constraints, and solve the non-linear system of equations. Hence, it is suitable to minimize the objective function given in Equation 6.42 and predict the Burger model parameters utilizing the lower and upper bounds of the model parameters.

6.6.1 Statistical Fitting Technique

Fitting the non-linear experimental data involves utilizing non-linear optimization technique that minimizes the error resulted from the predicted and experimentally measured data. Papagiannakis et al., (2002) evaluated several objective functions to fit the Burger model parameters and found that the objective function, proposed by (Baumgaertel and Winter, 1989), provided best fit. As given in Equation 6.42, the objective function to be minimized computes the sum of squares of the error using storage and loss shear modulus parameters. Recently, this method was also implemented to fit the Burger model parameters (Abbas, 2004).

$$objective\ \text{function} = \sum_{j=1}^{m}\left(\left[\frac{G'(\omega_j)}{G'^{o}_{j}} - 1\right]^2 + \left[\frac{G''(\omega_j)}{G''^{o}_{j}} - 1\right]^2\right) \tag{6.42}$$

where, G'^{o}_{j} and G''^{o}_{j} are experimenally measured storage and loss shear modulus at the j^{th} frequency ω_j ; G'_j and G''_j are statistically predicted storage and loss shear modulus at the j^{th} frequency ω_j; and m is the number of data points, in this case equals 21.

A simple program was written in MATLAB® (Misiti et al., 2006) that implements the built-in non-linear optimization function to fit the measured data as presented in Appendix C. Thus, the complex shear modulus and phase angle of the asphalt binders and mastic samples were predicted using Equation 6.37 and 6.41, respectively. As show in Figure 6.11, the Burger model yields a fairly correlated fit when the complex shear modulus experiment data was used. On the other hand, marginal fitting quality was obtained for the phase angle (Figure 6.12). A similar trend was observed for the rest of the asphalt binders and mastics. The reason is that the Burger model is overly simple and cannot capture the complex viscoelastic behavior of binders and mastics. Additional elastic and viscous elements would have to be included to improve the quality of fit. The fitted Burger model parameters for all asphalt binder and mastic samples considered are presented in Table 6.5.

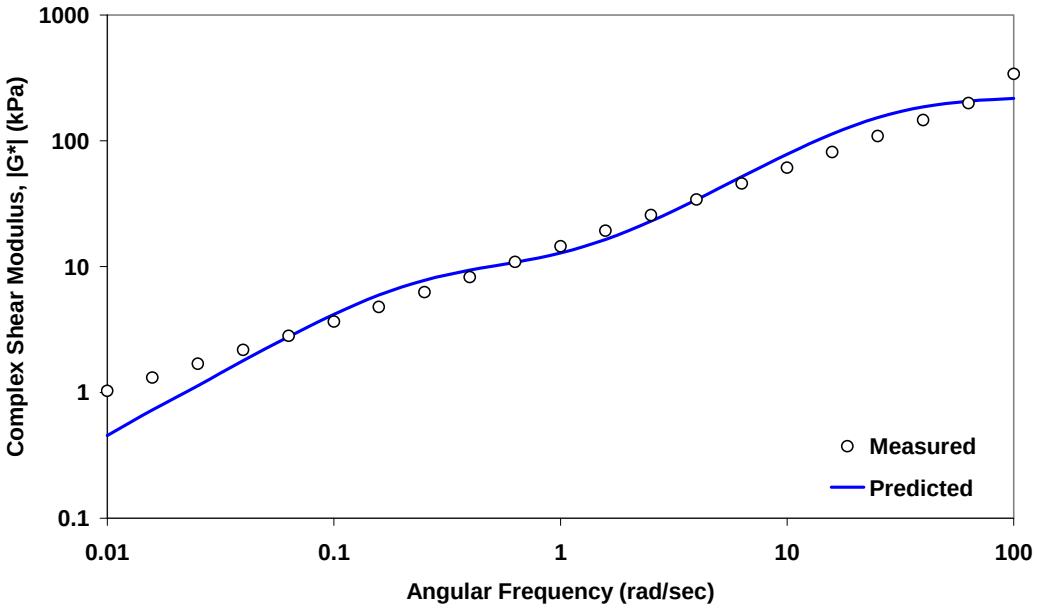

Figure 6.11 Measured and Predicted $|G^*|$ using Burger Model;
HL CMHB-C RTFO-aged Mastic

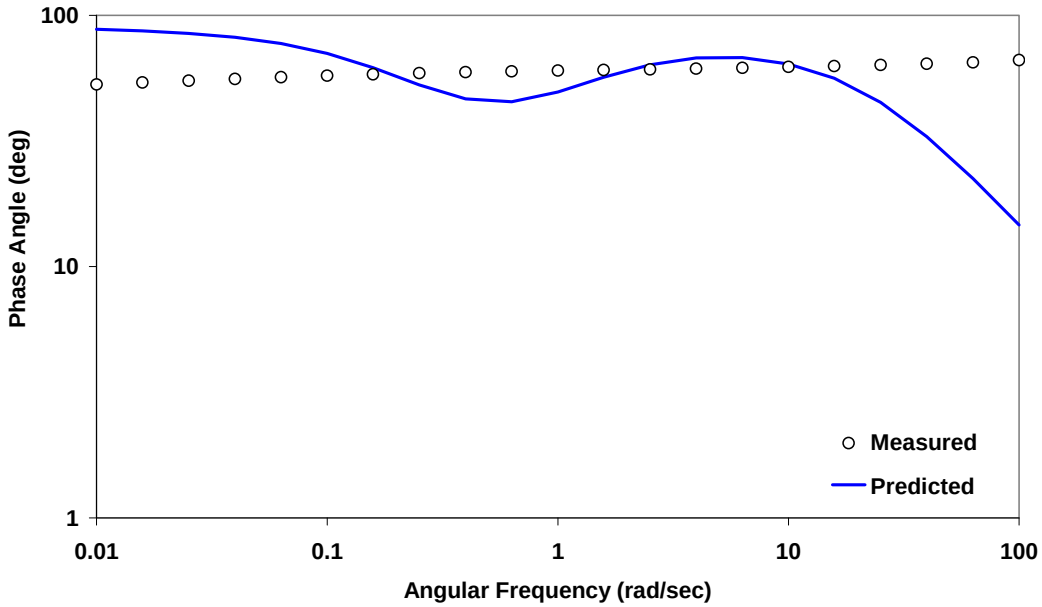

Figure 6.12 Measured and Predicted Phase Angle using Burger Model;
HL CMHB-C RTFO-aged Mastic

In addition, the relaxation and retardation times were also used to characterize the time-dependent behavior of the asphalt binders and mastics. As depicted in Table 6.6, the relaxation time of the original binder was 0.0641 and for the mastics it ranges from 0.0350 sec of SL PFC unaged mastic to 0.2022 sec of HL CMHB-C RTFO-aged mastic. Similarly, the retardation time of the original binder was 0.4164 and for the mastics it ranges from 0.2285 sec of G PFC unaged mastic to 0.8073 sec of HL CMHB-C RTFO-aged mastic. This demonstrates that the additional stiffness from the mineral fillers did not significantly affect the time-dependent behavior of asphalt binders and mastics as shown graphically in Figure 6.13 and 6.14. In general, the retardation times are higher than the relaxation times. This implies that the delayed response of the Burger model was predominant which is mainly attributed from the Kelvin-Voigt element. Similar findings were also obtained by (Abbas, 2004).

Table 6.5 Fitting the Burger Model Parameters

Sample Type	Sample Label	Burger Model Parameters			
		E_M (kPa)	η_M (kPa.sec)	E_K (kPa)	η_K (kPa.sec)
Unaged Binder	Unaged 76-22	40.0006	2.5645	1.6909	0.7041
RTFO-aged Binder	RTFO-aged 76-22	60.0004	6.0183	2.1753	1.0928
Mastic using Unaged Binder	HL CMHB-C	199.9935	24.8558	7.9213	4.3809
	G CMHB-C	175.0029	8.5438	9.0283	2.9139
	SL CMHB-C	149.9992	8.9306	9.2346	2.6212
	HL PFC	120.0118	15.3280	6.6236	3.9696
	G PFC	100.0011	3.7769	7.2145	1.6488
	SL PFC	100.0000	3.4994	4.9016	1.1544
	HL Superpave-C	200.0141	25.3693	9.1507	5.9714
	G Superpave-C	120.0063	15.1816	9.8864	3.7798
	SL Superpave-C	150.0048	10.4383	10.3191	3.2786
Mastic using RTFO-aged Binder	HL CMHB-C	225.0446	45.4928	13.1130	10.5862
	G CMHB-C	200.0200	30.4480	9.6397	6.3361
	SL CMHB-C	149.9998	19.9957	10.9111	4.3360
	HL PFC	220.0117	20.4781	12.9337	6.7759
	G PFC	90.0131	10.5062	8.9394	3.2866
	SL PFC	80.0115	7.4460	7.6228	3.1818
	HL Superpave-C	260.0253	40.3797	13.7607	10.3791
	G Superpave-C	280.0136	40.2700	8.9535	7.0699
	SL Superpave-C	200.0013	25.0422	12.3273	4.8074

HL: Hard Limestone; G: Granite; SL: Soft Limestone

Table 6.6 Relaxation and Retardation Times of the Burger Model

Sample Type	Sample Label	Relaxation Time	Retardation Time
		η_M / E_M (seconds)	η_K / E_K (seconds)
Unaged Binder	Unaged 76-22	0.0641	0.4164
RTFO-aged Binder	RTFO-aged 76-22	0.1003	0.5024
Mastic using Unaged Binder	HL CMHB-C	0.1243	0.5531
	G CMHB-C	0.0488	0.3228
	SL CMHB-C	0.0595	0.2838
	HL PFC	0.1277	0.5993
	G PFC	0.0378	0.2285
	SL PFC	0.0350	0.2355
	HL Superpave-C	0.1268	0.6526
	G Superpave-C	0.1265	0.3823
	SL Superpave-C	0.0696	0.3177
Mastic using RTFO-aged Binder	HL CMHB-C	0.2022	0.8073
	G CMHB-C	0.1522	0.6573
	SL CMHB-C	0.1333	0.3974
	HL PFC	0.0931	0.5239
	G PFC	0.1167	0.3677
	SL PFC	0.0931	0.4174
	HL Superpave-C	0.1553	0.7543
	G Superpave-C	0.1438	0.7896
	SL Superpave-C	0.1252	0.3900

HL: Hard Limestone; G: Granite; SL: Soft Limestone

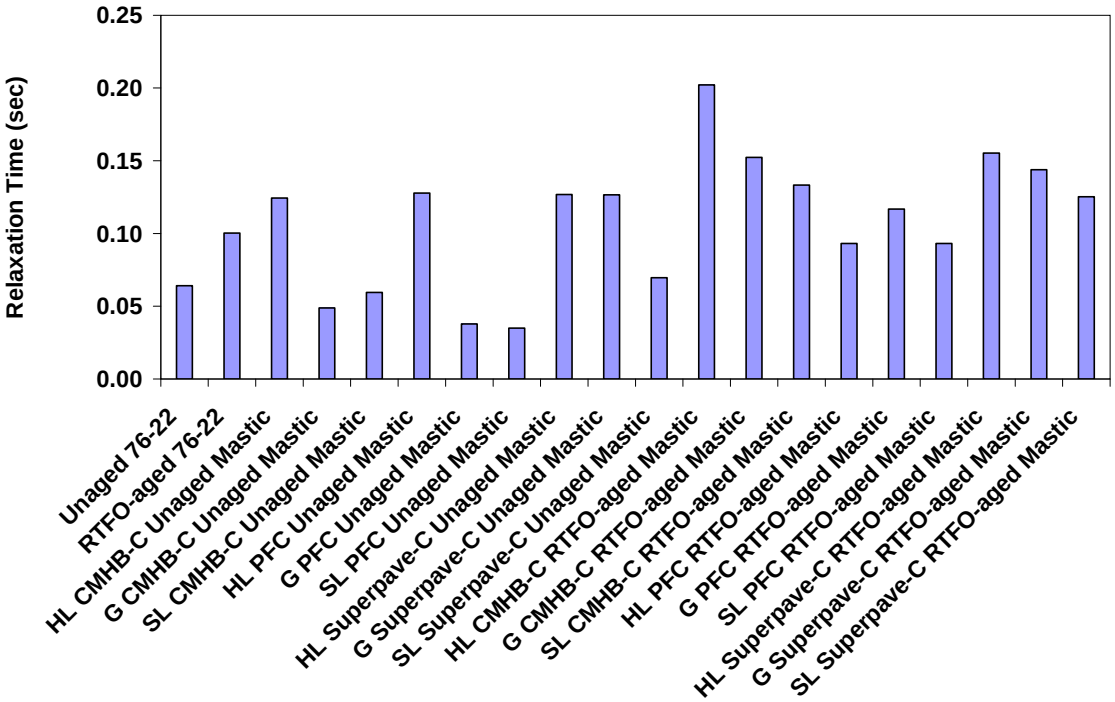

Figure 6.13 Relaxation Times of Asphalt Binders and Mastics

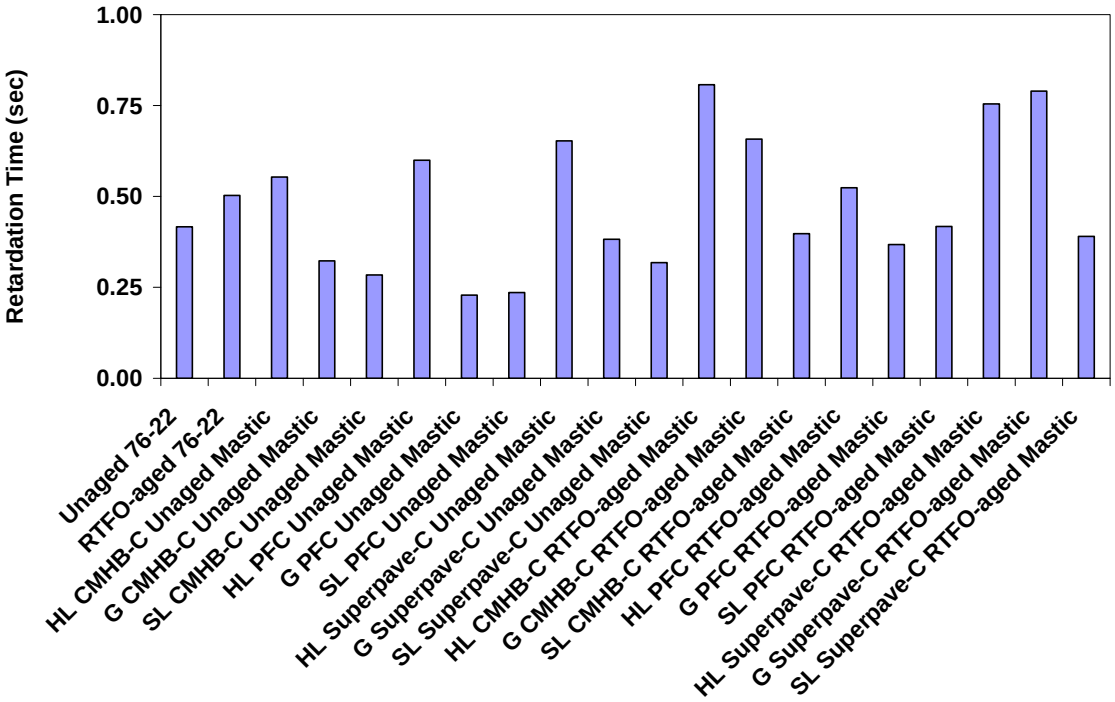

Figure 6.14 Retardation Times of Asphalt Binders and Mastics

As illustrated in Figure 6.15, the ratio of the mastic dynamic shear modulus to the binder dynamic shear modulus at an angular frequency of 10 rad/sec ranges from 1.7 of SL PFC unaged mastic to 7.8 of HL CMHB-C RTFO-aged mastic. In general, the mastic mixtures with hard limestone (HL) yielded high stiffness values followed by mastic mixtures with granite (G) and the least was observed in soft limestone (SL) mastic mixtures.

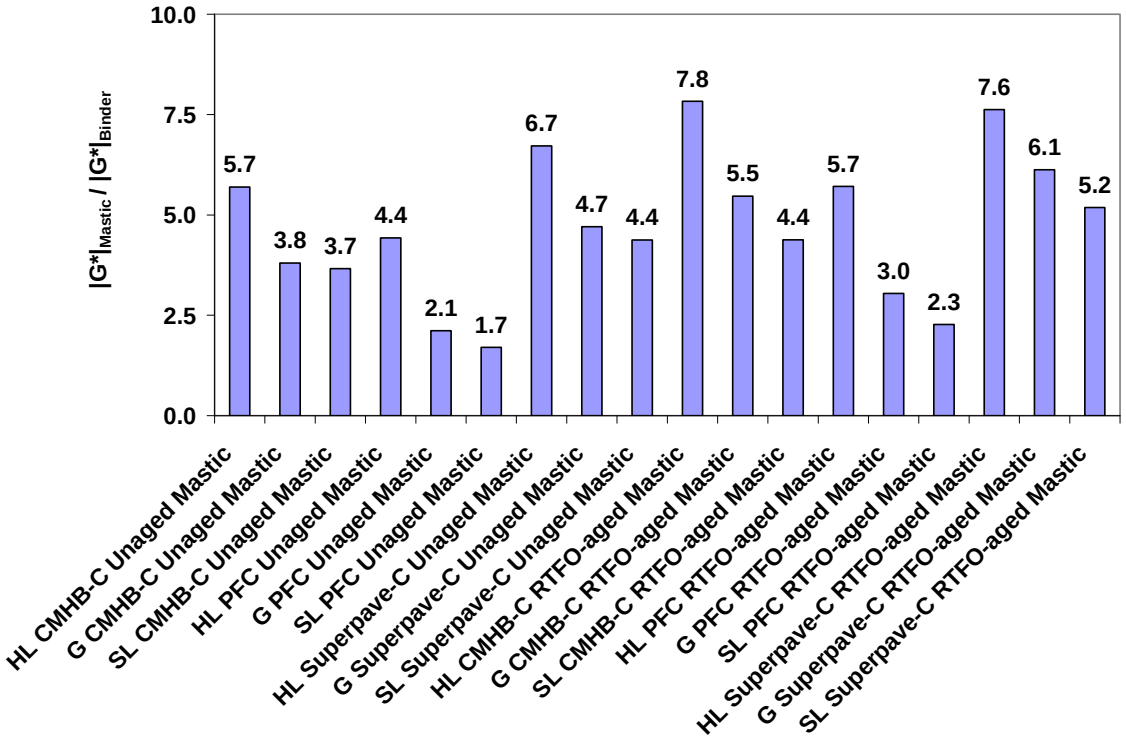

Figure 6.15 Effects of Fines on the Dynamic Shear Modulus of Unaged and RTFO-aged Mastics

6.7 Summary and Conclusions

This chapter presented the characterization of viscoelastic rheological properties of asphalt binders and mastics using oscillatory tests, namely amplitude and frequency sweep tests. The former was utilized to determine the linear viscoelastic (LVE) range and the maximum limiting shear strain values at different angular frequencies. The later was used to characterize the viscoelastic properties of asphalt binders and mastics. A simple program was written in MATLAB® that implements the built-in non-linear optimization

function to fit the complex shear modulus and phase angle measured data in frequency domain and characterize the Burger model parameters. The Burger model yields a fairly correlated fit when the complex shear modulus experiment data was used and marginal fitting was obtained when the phase angle was considered.

Moreover, the time-dependent behavior of the asphalt binders and mastics was characterized using relaxation and retardation times. The relaxation time of the original binder was 0.0641 and for the mastics it ranges from 0.0350 sec of SL PFC unaged mastic to 0.2022 sec of HL CMHB-C RTFO-aged mastic. Similarly, the retardation time of the original binder was 0.4164 and for the mastics it ranges from 0.2285 sec of G PFC unaged mastic to 0.8073 sec of HL CMHB-C RTFO-aged mastic. In general, the retardation times were found to be higher than the relaxation times and thus the delayed response of the Burger model was dominant. It was demonstrated that the additional stiffness from the mineral fillers did not significantly affect the time-dependent behavior of asphalt binders and mastics. In general, the mastic mixtures with hard limestone (HL) yielded high stiffness values followed by mastic mixtures with granite (G) and the least was observed in soft limestone (SL) mastic mixtures.

Chapter 7

DISCRETE ELEMENT METHOD (DEM) OVERVIEW

7.1 Background

Discrete Element Method (DEM) is a numerical simulation model capable of simulating the micromechanical behavior of granular assemblies. The development of DEM in the early 1970's is attributed to Cundall, (1971) for the analysis of rock-mechanics problems and then applied to soils by Cundall and Strack, (1979). In its two-dimensional version, this model involves circular particles (disks) interacting through normal and shear springs and a Coulomb frictional element that simulate material failure in shear. The rigid circular particles can be bonded to represent the mechanical behavior of solid materials such as rock.

The interaction of the particles in DEM is a dynamic process since the particle motion is dependent on the physical properties of the granular assembly. In DEM, vanishingly small time-stepping and an explicit numerical scheme are utilized, such that interaction among particles is monitored contact by contact and the motion of the particles is traced particle by particle (Cundall and Strack, 1979). The use of an explicit numerical scheme makes it possible to simulate the non-linear interaction of large assemblies of particles that exhibit physical instability without excessive memory requirements.

The contact forces and displacements of a granular assembly of particles are found by tracing the movements of the individual particles. The forces acting on any particle are determined by its interaction with its neighboring particles. The simulation processes in DEM involves two dependent schemes: first application of Newton's second law (equation of motion) to the particles and second application of a force-displacement law at the particle contacts. The first scheme is responsible for determining the motion of each particle arising from the contact and body forces acting upon it. The second scheme is used to update the contact forces arising from the relative motion at each particle contact. Furthermore, Newton's second law is integrated twice for each particle to

provide updated new positions and rates of displacement. The particle acceleration is computed and then integrated for velocities and displacements at each time increment. In DEM, measures of stresses can be defined as the average quantities over a representative volume. This procedure allows estimating the micro-stresses for the assembly considered. On the other hand, strain rates are computed using a velocity-gradient tensor based on a best-fit procedure that minimizes the error between the predicted and measured velocities within the representative volume. In DEM, more complex physical properties of the material, example aggregate shape and size can be similarly represented and modeled using clusters of particles forming particle clumps. In the following section, brief descriptions of a DEM software package called *Particle Flow Code in two-dimensions* (PFC^{2D}) are given with reference to PFC^{2D} manual.

7.2 Introduction to PFC^{2D}

Particle Flow Code in two-dimensions, abbreviated as PFC^{2D}, is a commercial software developed by Itasca Consulting Group, Inc. PFC^{2D} is classified as a discrete element code based on the definition given by Cundall and Hart, (1992). PFC^{2D} can be viewed as a simplified implementation of the DEM algorithms because it involves only rigid circular particles. It allows finite displacements and rotations of discrete bodies, including complete detachment, and recognizes new contacts automatically as the calculation progresses. The movement and interaction of stressed assemblies of rigid circular particles can be modeled using PFC^{2D}. Few assumption used in PFC^{2D} include: (1) circular particles are treated as a rigid body elements; and (2) ball-to-ball contact occur over a vanishingly small area (i.e., at a point). Walls in PFC^{2D} can be used to specify initial boundary conditions and impose user-defined velocities for the purpose of compaction and confinement. The interaction of the ball-to-wall is governed by the contact forces that arise at contacts. Since the wall motion (platen velocity) is specified by the user, the Newton's second law is valid only for ball particles contacting either ball or wall. In addition, the ball-to-wall contacts are accounted for using the force-displacement law scheme. Hence, in PFC^{2D} the term contacts are used to refer either ball-to-ball contact or ball-to-wall contact. Moreover, wall-to-wall contacts may be considered, if present.

7.2.1 Contact Detection Technique

Detection of particle contacts is an important step in DEM calculations before each calculation cycle begins. In PFC^{2D}, verification of the particle contact is a simple and quick procedure. Assuming particle A is centered at (x_1, y_1) and particle B is centered at (x_2, y_2) in a Cartesian coordinate system, they are in contact if the distance d between their centers satisfies:

$$d \le \sqrt{(x_1 - x_2)^2 + (y_1 - y_2)^2} \tag{7.1}$$

In other words, particles are considered to be in contact only if the distance between their centers is less than the sum of their radii. A brief description of the contact detection technique and its implementation in DEM code is presented in Cundall, (1988).

7.2.2 Calculation Cycle

The calculation cycle in PFC^{2D} is a time-stepping explicit algorithm scheme that requires repeated applications of Newton's second law to each particle and a force-displacement law to each contact. The time-step interval chosen should be very small so that the rate of displacement and acceleration of the particles are constant over this interval. The calculation cycle ends when the unbalanced forces within particles reach a negligible value, (i.e., this value is zero for static problems). Moreover, the wall positions are updated based on the specified user-defined wall velocities. The schematic illustrations of these processes are given in Figure 7.1.

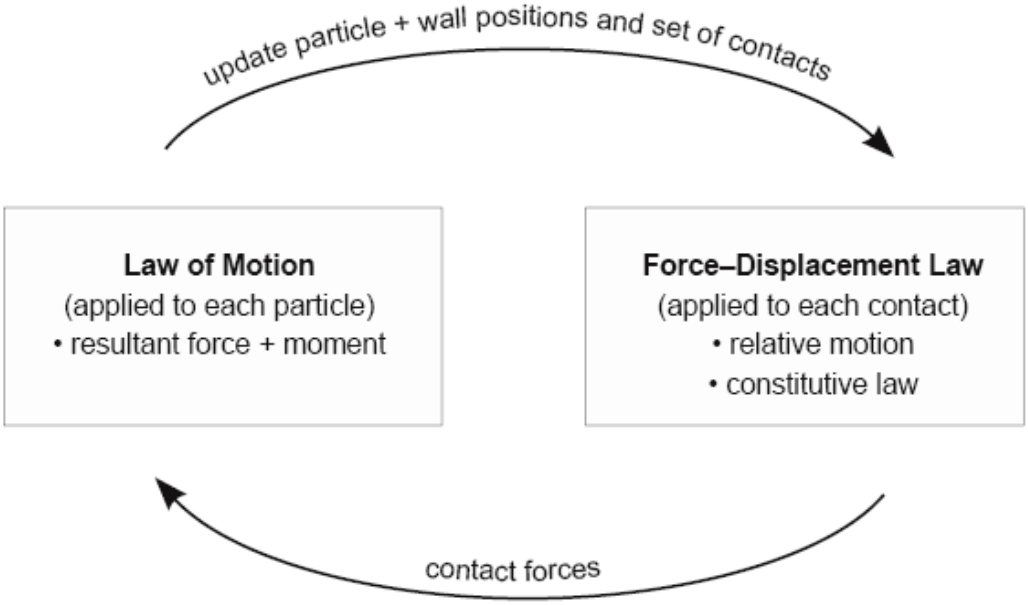

Figure 7.1 Illustration of Calculation Cycle in PFC^{2D} (After PFC^{2D} Manual, 2002)

7.2.2.1 Contact Force-displacement Law

The force-displacement law relates the relative displacement between two bodies at a contact to the contact force acting on these bodies. The contact force vector F_i can be resolved into normal (F^n) and shear (F^s) component vectors with respect to the contact plane as:

$$F_i = F^n n_i + F^s t_i \tag{7.2}$$

where n_i and t_i are the unit vectors that define the contact plane. The magnitude of the normal contact force is calculated by:

$$F^n = K^n U^n \tag{7.3}$$

where U^n is the overlap and K^n is the contact normal stiffness at the contact.

The shear force is computed in an incremental fashion and relates the incremental displacement to the contact force. When the contact is formed, the elastic shear force is assigned a zero value. The shear displacement increment, ΔU^s, produces an increment of elastic shear force, ΔF^s that is given by:

$$\Delta F^s = -k^s \Delta U^s \tag{7.4}$$

$$F^s \leftarrow F^s + \Delta F^s \leq \mu F^n \tag{7.5}$$

where k^s is the contact shear stiffness and μ is the particle friction coefficient.

The contact normal and shear stiffness values are determined by the contact-stiffness models presented in section 7.2.4.1. It is worth to note that the contact normal stiffness is in essence the secant modulus that relates the total displacement and force, while the contact shear stiffness is the tangent modulus that relates incremental displacement and force.

7.2.2.2 Equation of Motion

Newton's laws of motion provide the fundamental relationship between particle motion and the forces causing the motion. The motion of a single rigid particle is determined by the resultant force and moment vectors acting upon it and can be described in terms of the translational and rotational of the particle and their corresponding equations are given by Equation 7.6 and 7.7, respectively.

$$F = m(\ddot{x} - g) \tag{7.6}$$

$$M = \mathrm{I}\dot{\omega} \tag{7.7}$$

where, F is the resultant force (i.e., the sum of all externally applied forces acting on the particle); m is the total mass of the particle; $\ddot{x}$ is the acceleration of the particle; g is the

gravitational body force; M is the resultant moment acting on the particle; I is the moment of inertia of the particle; and $\dot{\omega}$ is the corresponding angular acceleration.

By integrating the particle's acceleration provides its new position and velocity. The particle accelerations and velocities calculated from the equation of motion are assumed to be constant over each time step. The contact force-displacement law is then used to calculate the new contact forces.

7.2.3 Damping

Since DEM is a dynamic process, some form of mechanism should be used to dissipate the kinetic energy. The instability of the granular system is attributed to the complex inter-particle interaction and particle surface waves. In PFC^{2D}, energy is dissipated through two mechanisms, namely friction and damping. Friction occurs during sliding when the absolute value of the shear force at each contact exceeds the limit of maximum shear force. Damping is necessary for the ultimate equilibrium of a granular assembly. In PFC^{2D}, three forms of kinetic energy damping are implemented, namely local damping, combined damping and viscous damping. Local and combined damping act on each particle, while viscous damping acts at each particle contact. Local damping applies a damping force with a magnitude proportional to the unbalanced forces exerted on each ball. Combined damping is a variation of local damping, where a steady-state solution involves a significant uniform motion. Viscous damping adds a normal and a shear dashpot at each contact. In PFC^{2D}, local damping is always active by default, however, the combined and viscous damping have to be activated by the user. Damping does not affect the equilibrium of the forces in the system. It does, however, reduces the number of calculation cycles needed to reach equilibrium (Cundall and Strack, 1979).

7.2.4 Contact Models

In PFC^{2D}, every particle contact involves two elements (i.e., either ball-to-ball or ball-to-wall) and occurs at a single point (i.e., at vanishingly small area) through which the contact force acts. A contact model describes the complex physical behavior occurring at a contact. The three contact models implemented in PFC^{2D} are:

- the contact-stiffness models (linear contact model and simplified Hertz-Mindlin model) that provide an elastic relation between the contact force and relative displacement.
- the slip model (frictional slip), that enforces a relation between shear and normal contact forces, and
- the bonding model, that serves to limit the total normal and shear forces.

These models are briefly summarized below.

7.2.4.1 Contact-Stiffness Model

The contact-stiffness model relates the contact forces and relative displacements in the normal and shear directions. PFC^{2D} provides two contact-stiffness models: a linear model and a simplified Hertz-Mindlin model. The linear contact model is defined by the normal and shear stiffnesses of the two contacting entities, as shown in Figure 7.2. In this model the forces and relative displacements are linearly related by the constant contact stiffness. In the linear contact model, the normal secant stiffness is equal to the normal tangent stiffness. On the other hand, in the Hertz-Mindlin model the forces and relative displacements are nonlinearly related by a variable contact stiffness, and thus it allows more flexibility in defining contact behavior. The linear contact law is more widely used and it is in general adequate in describing contact stiffness.

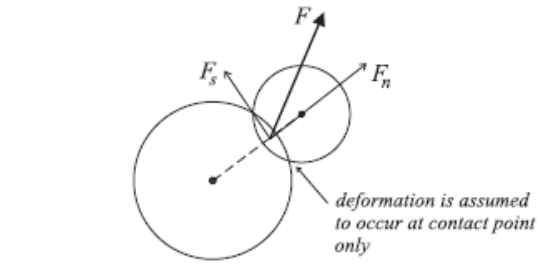

Linear contact law

$$F_n = k_n U_n$$

$$\Delta F_s = k_s \Delta U_s$$

Figure 7.2 Linear Contact Model in PFC^{2D} (After PFC^{2D} Manual, 2002)

The contact normal secant stiffness and shear tangent stiffness of two contacting bodies (example particle A and B) are given respectively by:

$$K^n = \frac{k_n^{[A]} k_n^{[B]}}{k_n^{[A]} + k_n^{[B]}} \tag{7.8}$$

$$K^s = \frac{k_s^{[A]} k_s^{[B]}}{k_s^{[A]} + k_s^{[B]}} \tag{7.9}$$

where $k_n^{[A]}$ and $k_n^{[B]}$ are the particle normal stiffnesses and $k_s^{[A]}$ and $k_s^{[B]}$ are the particle shear stiffnesses.

7.2.4.2 Slip Models

The slip model is an intrinsic property of the contacting bodies. The slip model in PFC^{2D} allows two bodies in contact to slide relative to one another. It provides no normal strength in tension and allows slipping to occur by limiting the shear force that can be transmitted. The slip condition is checked by calculating the maximum allowable shear contact force $(F_{\max}^s)$ and comparing it with the product of the normal component of the contact force (F^n) and multiplied by the particle coefficient of friction (μ), as given in Equation 7.10:

$$F_{\max}^s = \begin{cases} \geq \mu \mid F^n \mid & \textit{Slip occur} \\ < \mu \mid F^n \mid & \textit{No slip} \end{cases} \tag{7.10}$$

7.2.4.3 Bonding Models

The complex behavior of the material can be modeled by allowing the particles to be bonded together at their contact points. In PFC^{2D}, particle-to-particle contact may have a contact bond and a parallel bond. A contact bond reproduces the effect of adhesion acting over the vanishingly small area of the contact point and this bond breaks when the inter-particle forces acting at any contact exceed the bond strength. A contact bond has

no resistance to rolling and allows tensile forces to develop at a contact. On the other hand, parallel bonds reproduce the effect of cementation in the contact and can transmit both forces and moments between particles. Moreover, parallel bonds are appropriate to prevent rolling without slipping at contact points. Bonded contacts are considered non-sliding, regardless of the value of their shear force. Schematic illustration of the bonding models is given in Figure 7.3.

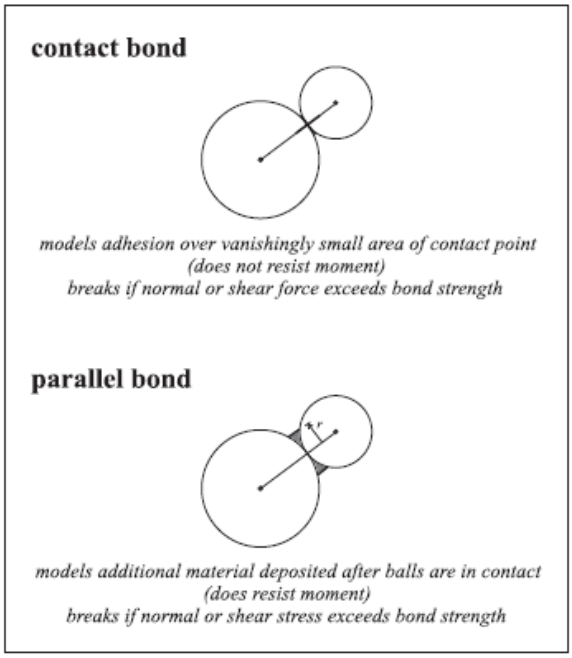

Figure 7.3 Bonding Models in PFC^{2D} (After PFC^{2D} Manual, 2002)

7.2.4.4 The Burger's Model

PFC^{2D} utilizes Burger's model to represent viscoelastic behavior at particle contact points. The Burger model consists of two viscoelastic elements, namely a Maxwell element and a Kelvin element. These models are connected in series in normal and shear directions. The required parameters for the Burger's model are stiffness (represented by a Hook's spring) and viscosity (represented by a Newtonian dashpot) in the Maxwell and Kelvin sections. As shown in Figure 7.4, eight parameters are required to fully define the Burger's model besides the frictional element in shear direction.

The following section describes the derivation of the incremental contact forces and the associated displacements of a stressed assembly of particles utilizing Burger's model at their contact point. Note that in the notation $\pm$, the positive and negative sign denote for normal and shear direction, respectively. Referring to the PFC^{2D} 2002 manual, the Burger's model implemented in PFC^{2D} has the following properties:

- normal stiffness for Kelvin section (K_{k_n})
- normal viscosity for Kelvin section (C_{k_n})
- normal stiffness for Maxwell section (K_{m_n})
- normal viscosity for Maxwell section (C_{m_n})
- shear stiffness for Kelvin section (K_{k_s})
- shear viscosity for Kelvin section (C_{k_s})
- shear stiffness for Maxwell section (K_{m_s})
- shear viscosity for Maxwell section (C_{m_s})
- friction coefficient (f_s)

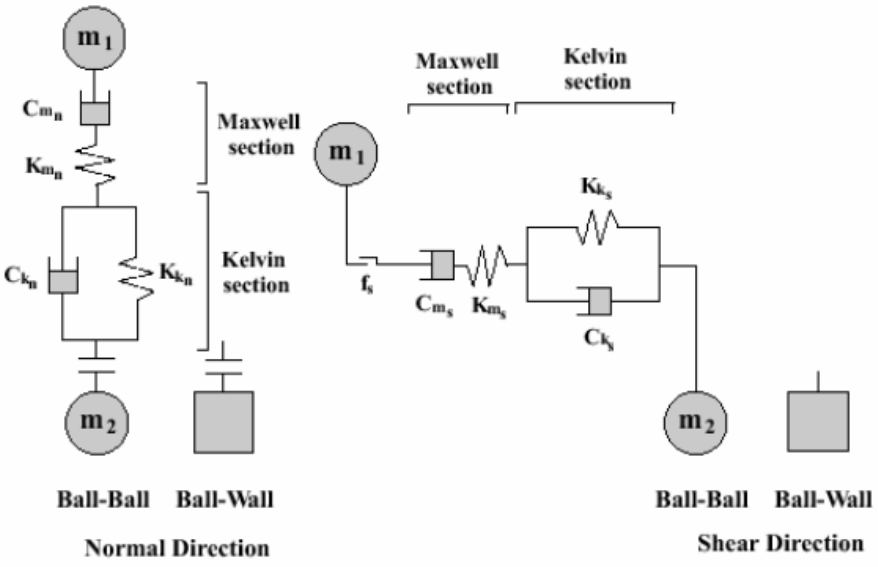

Figure 7.4 The Burger's Model in PFC^{2D} (After PFC^{2D} Manual, 2002)

The total displacement of the Burger's model $u,$ is the sum of the displacement of the Kelvin section (u_k) and that of the Maxwell section (u_{m_K}, u_{m_C}) of the model and given by:

$$u = u_k + u_{m_K} + u_{m_C} \tag{7.11}$$

The total rate of displacement and acceleration of the Burger's model are given by equation (7.12) and (7.13), respectively:

$$\dot{u} = \dot{u}_k + \dot{u}_{m_K} + \dot{u}_{m_C} \tag{7.12}$$

$$\ddot{u} = \ddot{u}_k + \ddot{u}_{m_K} + \ddot{u}_{m_C} \tag{7.13}$$

The contact force, $f,$ using the Kelvin section and the first derivative, are given by:

$$f = \pm K_k u_k \pm C_k \dot{u}_k \tag{7.14}$$

$$\dot{f} = \pm K_k \dot{u}_k \pm C_k \ddot{u}_k \tag{7.15}$$

Using the stiffness K_m and viscosity C_m of the Maxwell section:

$$f = \pm K_m u_{m_K} \tag{7.16}$$

$$\dot{f} = \pm K_m \dot{u}_{m_K} \tag{7.17}$$

$$\ddot{f} = \pm K_m \ddot{u}_{m_K} \tag{7.18}$$

$$f = \pm C_m \dot{u}_{m_C} \tag{7.19}$$

$$\dot{f} = \pm C_m \ddot{u}_{m_C} \tag{7.20}$$

The second-order differential equation for contact force f is given by:

$$f + \left[\frac{C_k}{K_k} + C_m\left(\frac{1}{K_k} + \frac{1}{K_m}\right)\right]\dot{f} + \frac{C_k C_m}{K_k K_m}\ddot{f} = \pm C_m \dot{u} \pm \frac{C_k C_m}{K_k}\ddot{u} \tag{7.21}$$

The rate of displacement of the Kelvin section is given by:

$$\dot{u}_k = \frac{-K_k u_k \pm f}{C_k} \tag{7.22}$$

Using the central difference approximation and finite difference scheme for the time derivative, and taking average values for u_k and f :

$$\frac{u_k^{t+1} - u_k^t}{\Delta t} = \frac{1}{C_k}\left[-\frac{K_k(u_k^{t+1} + u_k^t)}{2} \pm \frac{f^{t+1} + f^t}{2}\right] \tag{7.23}$$

Therefore,

$$u_k^{t+1} = \frac{1}{A}\left[Bu_k^t \pm \frac{\Delta t}{2C_k}(f^{t+1} + f^t)\right] \tag{7.24}$$

where,

$$A = 1 + \frac{K_k \Delta t}{2C_k} \tag{7.25}$$

$$B = 1 - \frac{K_k \Delta t}{2C_k} \tag{7.26}$$

The displacement and the first derivative of the Maxwell section are given by:

$$u_m = u_{m_K} + u_{m_C} \tag{7.27}$$

$$\dot{u}_m = \dot{u}_{m_K} + \dot{u}_{m_C} \tag{7.28}$$

Substituting of Equation (7.17) and Equation (7.19) into Equation (7.28) yields:

$$\dot{u}_m = \pm\frac{\dot{f}}{K_m} \pm \frac{f}{C_m} \tag{7.29}$$

By using a central difference approximation of the finite difference scheme and taking the average value for f gives:

$$\frac{u_m^{t+1} - u_m^t}{\Delta t} = \pm\frac{f^{t+1} - f^t}{K_m \Delta t} \pm \frac{f^{t+1} + f^t}{2C_m} \tag{7.30}$$

Therefore,

$$u_m^{t+1} = \pm\frac{f^{t+1} - f^t}{K_m} \pm \frac{\Delta t(f^{t+1} + f^t)}{2C_m} + u_m^t \tag{7.31}$$

The total displacement and the first derivative of the Burger's model are given by:

$$u = u_k + u_m \tag{7.32}$$

$$\dot{u} = \dot{u}_k + \dot{u}_m \tag{7.33}$$

By using the finite difference scheme for the time derivative,

$$u^{t+1} - u^{t} = u_k^{t+1} - u_k^{t} + u_m^{t+1} - u_m^{t} \tag{7.34}$$

Substituting Equation (7.24) and (7.31) into Equation (7.34), the contact force, f^{t+1}, is given by:

$$f^{t+1} = \pm\frac{1}{C}\left[u^{t+1} - u^{t} + \left(1 - \frac{B}{A}\right)u_k^{t} \mp Df^{t} \right] \tag{7.35}$$

where:

$$C = \frac{\Delta t}{2C_k A} + \frac{1}{K_m} + \frac{\Delta t}{2C_m} \tag{7.36}$$

$$D = \frac{\Delta t}{2C_k A} - \frac{1}{K_m} + \frac{\Delta t}{2C_m} \tag{7.37}$$

The contact force f^{t+1} can be calculated from the known values of u^{t+1}, u^{t}, u_k^{t}, and f^{t}. Consequently, the average stress and strain rate tensors within the measurement volume can be computed using the contact forces acting at the contact.

7.2.5 Clump

Large aggregates in the AC mixtures can be effectively represented using clumped particles that are generated by assembling several circular particles into clusters that act as a single rigid body with deformable boundaries. The advantage of clumping is that there is no need to analyze the contact relationships between clumped particles, which results in computational effort savings. The particles in the clump translate and rotate as a rigid body motion. The motion of a clump is determined by the resultant force and moment vectors acting upon it. Contacts within the clump are skipped during the calculation cycle, resulting in saving computational time and memory. Particles within a

clump may overlap to any extent and contact forces are not generated between these particles. However, any contact forces that exist when the clump is created or when a particle is added to the clump will be preserved unchanged during cycling. Obviously, the contacts with particles surrounding the clump need to be analyzed.

7.2.6 Stress and Strain-Rate Measurement

In PFC^{2D}, contact forces and particle displacements are computed using the force-displacement contact law. These quantities are useful when studying the material behavior on a micro-scale. Measures of stress can be defined as the average quantities over a representative volume in the particulate system. The average stress $\overline{\sigma}_{ij}$ in a volume V of the material is defined by:

$$\overline{\sigma}_{ij} = \frac{1}{V}\int_{V} \sigma_{ij} dV \tag{7.38}$$

where σ_{ij} is the stress tensor acting throughout the volume. For a particulate material, stresses exist only in the particles, thus the integral can be replaced by a sum over the N_p particles contained within V as:

$$\overline{\sigma}_{ij} = \frac{1}{V}\sum_{N_p} \overline{\sigma}_{ij}^{(p)} V^{(p)} \tag{7.39}$$

where $\overline{\sigma}_{ij}^{(p)}$ is the average stress in particle (p). Similarly, the average stress in a particle (p) can be written as:

$$\overline{\sigma}_{ij}^{(p)} = \frac{1}{V^{(p)}}\int_{V^{(p)}} \sigma_{ij}^{(p)} dV^{(p)} \tag{7.40}$$

Thus, the average stresses can also be expressed directly in terms of the discrete contact forces:

$$\overline{\sigma}_{ij}^{(p)} = -\frac{1}{V^{(p)}} \sum_{N_c} x_i^{(c)} F_j^{(c)} \tag{7.41}$$

where, $x_i^{(c)}$ is the location and $F_j^{(c)}$ is the force acting at contact (c). The negative sign is used to ensure that the compressive and tensile forces produce negative and positive stresses respectively.

On the other hand, the procedure employed to measure local strain rates within a granular assembly differs from that used to measure local stresses. Strain rates are computed using a velocity-gradient tensor based on a best-fit procedure that minimizes the error between the predicted and measured velocities within the representative volume. The strain-rate tensor is the symmetric portion of the velocity-gradient tensor. The complete derivations of the strain-rate tensor equations can be found in PFC^{2D} manual.

7.3 Summary and Conclusions

In this chapter, an overview of the development and working framework of the Discrete Element Method (DEM) is presented. The operational principles and special features of the DEM software package called *Particle Flow Code in two-dimensions* (PFC^{2D}) were briefly discussed. In the material characterization context, DEM is a suitable tool for studying the macroscopic behavior of ACs, while taking into account their microstructure. The reasons are:

- AC mixture is a discontinues media and can be considered as a granular material.
- The AC aggregate particles can be effectively represented by clusters or clumps of circular particles (disks) and their physical properties can be easily characterized (example gradation, shape, size, and orientation).
- The asphalt binder or mastics can be treated as a viscoelastic material cementing the aggregate particles which can be treated as elastic material. Moreover, the viscoelastic DEM contact model parameters can be

characterized using Dynamic Shear Rheometer (DSR) tests, namely frequency sweep and creep tests.

- The target percent air void can be used as a limiting value for compaction process of the granular assembly.
- The aggregate-to-aggregate friction and interlocking behavior can be reasonably assumed if experimental tests on aggregates are expensive.
- The macroproperties of the AC mixture can be predicted using the microproperties generated from DEM simulation results.
- AC mixture permanent deformation tests can be realistically simulated using DEM and hence used to evaluate their rutting resistance potential.

Chapter 8

DEM SIMULATION OF UNIAXIAL STATIC CREEP TESTS ON ASPHALT CONCRETE MIXTURES USING PFC^{2D}

8.1 Introduction

This chapter presents the methodology and the results of the *Particle Flow Code in two-dimensions* (PFC^{2D}) simulation of the uniaxial static creep behavior of AC mixtures. It utilizes the AC microstructure information described in Chapter 5, the mastic viscoelastic models described in Chapter 6 and the DEM approach described in Chapter 7. Furthermore, it compares the resulting creep behavior predictions with the creep laboratory data described in Chapter 4.

8.2 Overview of AC Mixture and Mastic Characterization

8.2.1 Overview of AC Creep Data

The AC mixture data utilized in this thesis was obtained from a Texas DOT funded study (Alvarado et al., 2007). Three aggregate types were selected from three TxDOT districts, namely hard limestone (HL), granite (G), and soft limestone (SL). These aggregates are commonly used in TxDOT paving industries and their performance histories are well documented. For each of these aggregate sources, three AC mixture types were chosen, namely Coarse Matrix High Binder type C (CMHB-C), Porous Friction Course (PFC), and Superpave type C (Superpave-C). To minimize the effect of binder properties on the overall performance results, only one binder grade, a PG 76-22, was used for all mixtures. A total of nine AC cores was produced, each involving a combination of three different mix designs using the selected aggregate types. The unconfined uniaxial creep tests were performed using a hydraulic testing machine on these mixtures to characterize their rutting resistance behavior. The test was carried out on cylindrical specimens, 100 mm in diameter and 150 mm in height. Tests were

conducted over a period of three hours at a chamber temperature of 60^0C and a constant stress of 207kPa. The applied load and axial rate of deformation were continuously recorded using linear variable differential transducers (LVDT). An example showing the measured total axial strains with loading time is shown in Figure 8.1 for aggregate type hard limestone (HL). Brief mixture design processes, characterization of the aggregate and binder properties, and experimental results in terms of axial strain and creep compliance are well documented in Chapter 4. It was found that regardless of the aggregate type used, the CMHB-C mixtures demonstrated higher resistance to pavement rutting following mixture type Superpave-C and PFC mixtures are found to be susceptible to permanent deformation.

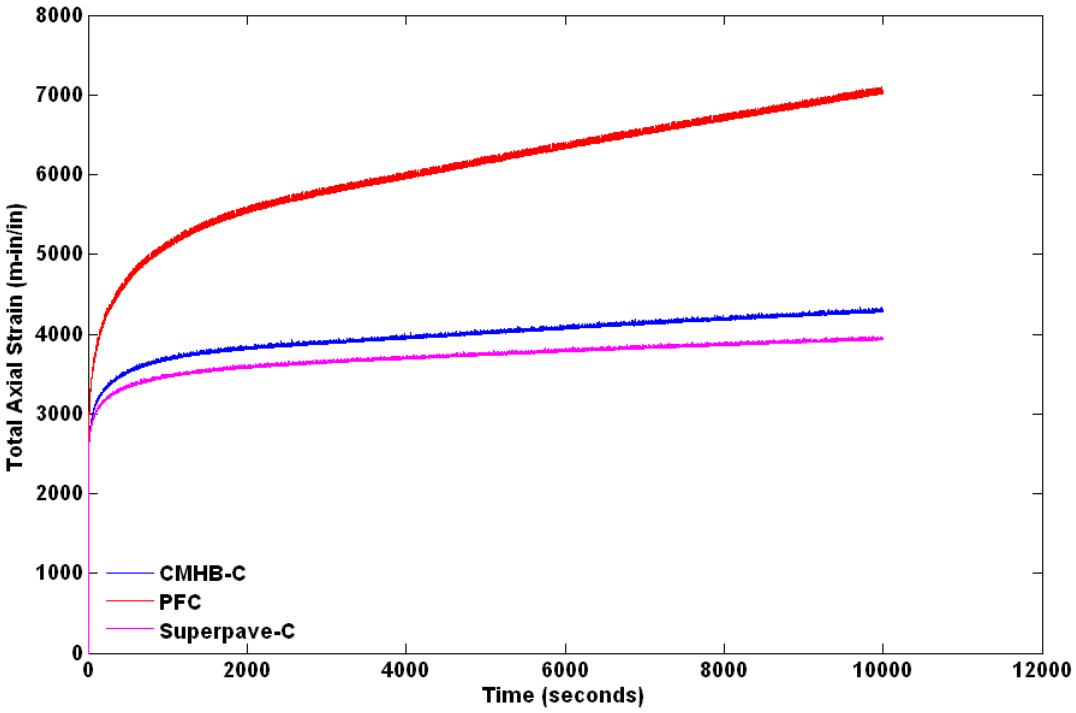

Figure 8.1 Experimentally Measured Axial Strains with Loading time;
Hard Limestone (HL)

8.2.2 Overview of AC Microstructural Data

A cylindrical specimen measuring 100 mm in diameter by 150 mm in height was scanned using high resolution X-ray facility to capture their microstructure. An automated Digital Image Processing (DIP) method, called Volumetric-based Global Minima (VGM) thresholding algorithm, was implemented in MATLAB® environment as presented in Chapter 5. It was used to process the AC X-ray CT images of the nine AC cores mentioned previously. An example of the image processing steps is shown in Figure 8.2 for the HL CMHB-C mix. Appendix B contains similar information for the remaining mixtures.

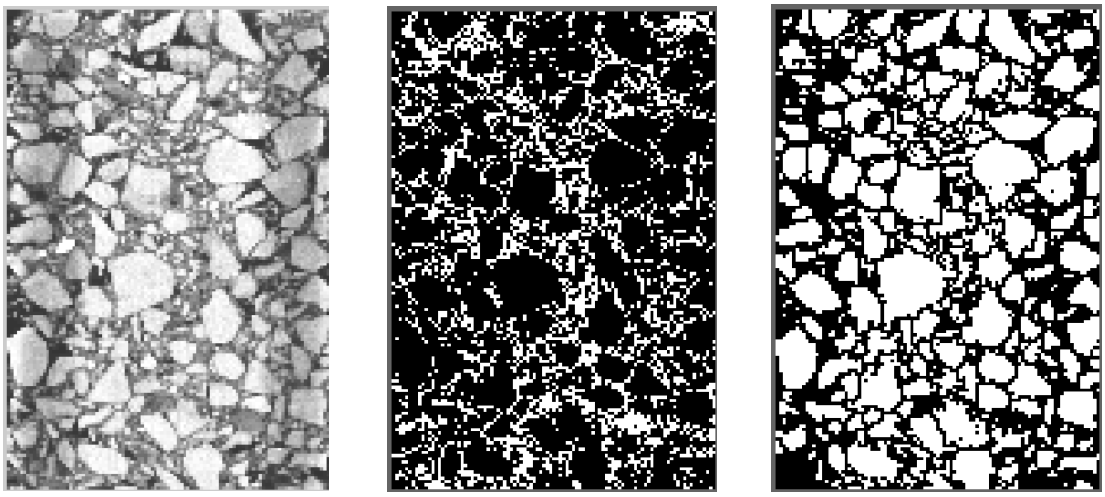

(a) **(b)** **(c)**

Figure 8.2 Representation of AC Two-dimensional Rectangular Sections (a) Processed Image, (b) Mastic Phase in White, and (c) Aggregate Phase in White; HL CMHB-C

8.2.3 Overview of Mastic Viscoelastic Model

Amplitude and frequency sweep tests were carried out on mastic samples using SmartPave® Dynamic Shear Rheometer (DSR), Controlled Shear Rate (CSR) testing mode, at a single testing temperature, 60^0C. Amplitude sweep tests were utilized to determine the linear viscoelastic (LVE) by inputting variable strain amplitudes, e.g., from 0.01 to 100 % at constant angular frequency, e.g., 10 rad/sec. Three distinct constant angular frequencies $\omega = 0.1,\ \omega = 1,$ and $\omega = 10$ rad/sec were used. The maximum limiting shear strains were obtained by extrapolating the limiting shear strain values using the

selected angular frequencies. This shear strain value plays a significant role in assigning values to the Burger contact model parameters in linear and non-linear viscoelastic ranges.

On the other hand, the frequency sweep tests were performed on mastic samples to determine the Burger model constants that correspond to the LVE range. These tests were performed using the strain amplitude (γ_A) equals the maximum limiting shear stain value and with angular frequencies ranging from 0.01 to 100 rad/sec. A simple program was written in MATLAB® environment that implements the built-in non-linear optimization function. The Burger model parameters were characterized using the storage and loss shear modulus measured data in frequency domain. The Burger model yields a fairly correlated fit when the complex shear modulus experimental data was utilized and marginal fitting was obtained when the phase angle was considered. The readers are referred to Chapter 6 for brief descriptions of the mathematical formulations of the mastic viscoelastic rheological model parameters, the testing methods involved, and characterization procedures.

8.3 Numerical Implementation

In Chapter 7, an overview of the DEM approach was presented. In summary, the simulation processes in DEM involves two inter-dependent schemes. First application of Newton's second law (equation of motion) to the particles and second application of a force-displacement law at the particle contacts. In this scheme, specifying the initial and boundary condition is important, as discussed later. DEM can predict the average stresses over a representative volume. This procedure allows estimating the micro-stresses for the granular assembly considered. On the other hand, the strain rates are computed using a velocity-gradient tensor based on a best-fit procedure that minimizes the error between the measured and predicted velocities within the measurement volume. In the following section, the DEM simulation processes on the AC mixture model are presented.

8.3.1 AC Mixture Model in PFC^{2D}

As pointed out earlier, the AC mixtures consisting of air voids, mastics and aggregates are uniquely heterogenous geomaterials and modeling their micromechanical

behavior is a challenging task. In addition, the current material testing practices are not sufficient to characterize all of the mixture components, e.g., mastic-to-aggregate and aggregate-to-aggregate contacts. By utilizing DEM, the more complex properties of AC mixture responses can be efficiently modeled using circular particles or disks with appropriate contact models and material properties that can simulate the viscoelastic and elastic properties of the mastics and aggregates, respectively. In DEM, the physical properties of the aggregate particles can be similarly represented and modeled using clusters of particles forming particle clumps. The advantage of this is that there is no need to solve the inter-particle force-displacement equations for clumped objects, thus economizing computing effort and memory. Therefore, this modeling technique is particularly suitable to investigate the micromechanical behavior of AC mixtures. In general, the approach towards modeling the micromechanical behavior of the AC mixtures using PFC^{2D} involves five major steps as illustrated in Figure 8.3 and described in the following subsequent sections.

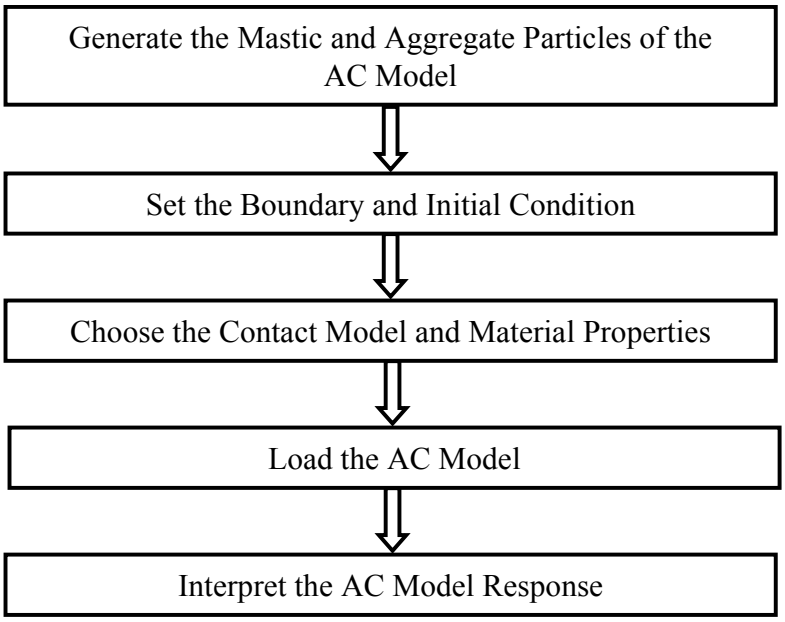

Figure 8.3 Steps Involved in Modeling AC Mixtures using PFC^{2D}

8.3.2 Mastic and Aggregate Particle Generation

The first step in the preparation of the AC model is to identify the mixture components as mastic and aggregate particles. This procedure was successfully accomplished by using the VGM thresholding algorithm. Particle generation in PFC^{2D} can be implemented in two ways, depending on the model application: (1) using the *BALL* command that generates particles, independently of the existing objects, whose sizes and specified locations are exactly determined and (2) using the *GENERATE* command that generates particles randomly located and whose sizes follow Gaussian distribution. The former method was utilized to generate the mastic and aggregate particles, since VGM characterizes the spatial features of the image pixels such as their Cartesian coordinate locations and geometry. An example illustrating the AC model particle generation for mixture type HL CMHB-C is given in Figure 8.4.

In PFC^{2D}, the aggregate irregular shape can be represented by clumping two or more circular particles together. As mentioned in Chapter 7, the unique advantage of utilizing PFC^{2D} for AC mixture micromechanical simulation is its ability to clump particles using the *FISH* clump function. The pixels of the boundaries of the aggregate objects are generated using VGM and then inputted into PFC^{2D} to form a rigid block of aggregate particle by utilizing the clump function as shown in Figure 8.4b. The combinations of mastic and aggregate particles yield a realistic representation of the AC mixture model that can be used to simulate the rutting resistance behavior of the AC mixtures. It is worthy to mention that the percent air voids computed from VGM can also be inputted as the porosity of the AC PFC^{2D} mixture model.

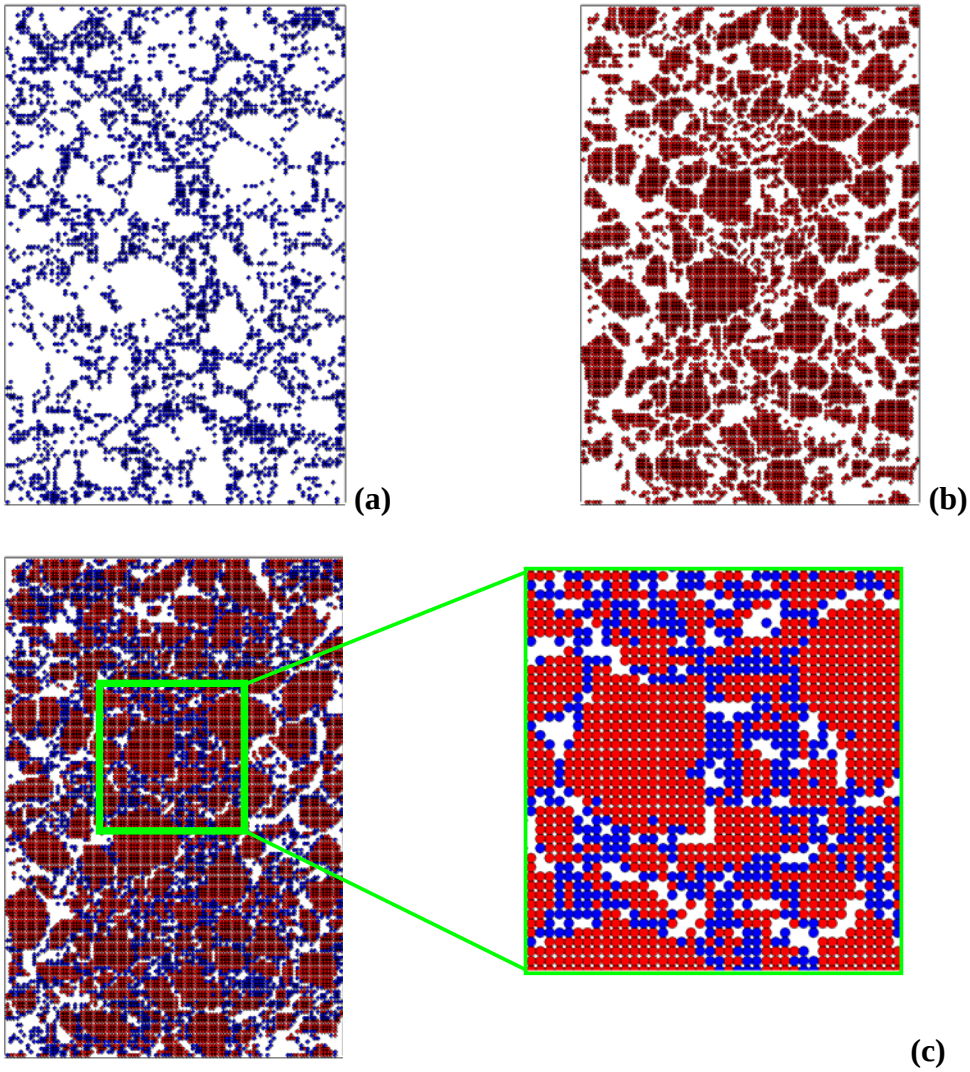

Figure 8.4 Example to Illustrate the AC Model Particle Generation (a) Mastic Particles in Blue, (b) Aggregate Particles in Red, and (c) AC PFC^{2D} Mixture Model; HL CMHB-C

8.3.3 Boundary and Initial Conditions

Four rigid walls (platens) are used as the boundary constraining the AC microstructural models. The boundary walls can be moved by specifying a wall velocity. In the case of uniaxial compression loading conditions, the upper wall can be used to load the AC model by specifying a wall velocity, while fixing the lower platen. A negligible confining wall velocity can be assumed for the lateral walls to simulate the actual atmospheric pressure effects on the AC core specimen inside the testing chamber. The AC model is loaded in a strain-controlled fashion by specifying the upper wall velocity.

In PFC^{2D}, a numerical "servo-mechanism" implemented via *FISH* function is devised automatically to maintain the prescribed wall velocity. The stresses and strains of the AC model are determined in a macro-fashion and quantified using the *HISTORY* logic. Moreover, particles can also serve as a boundary of the AC model and their movement can be controlled either based on velocity or forces acting on the particles. In this research, walls were used as boundaries of the AC model.

In order to establish the isotropic stress state of the AC model, the initial stress conditions within the mastic and aggregate particles need to be established. The AC model can be loaded by specifying wall velocities and the stress and strain state of the model can be determined using *FISH* functions. The stresses are computed by dividing the total force acting on the wall by the wall area. The following section describes the procedures used to achieve an isotropic stress state in the granular assembly.

The confining stresses are kept constant by adjusting the lateral wall velocities using a numerical servo-mechanism that is implemented by *FISH* functions. The servo-control adjusts the wall velocities by reducing the difference between the measured and required stresses respectively denoted by σ^m and σ^r. The equation for wall velocity implemented in a servo-mechanism utilizing the "gain" parameter, *G* is given by:

$$\dot{u}^{(w)} = G(\sigma^m - \sigma^r) = G(\Delta\sigma) \tag{8.1}$$

The maximum increment in wall force arising from the wall movement in one time-step can be computed by:

$$\Delta F^{(w)} = k_n^{(w)} N_c \dot{u}^{(w)} \Delta t \tag{8.2}$$

where, $\Delta F^{(w)}$ is the change in force; N_c and $k_n^{(w)}$ represent the number of contacts and the average stiffness of the contacts on the wall, respectively.

Dividing Equation (8.2) by the area of the wall yields the change in mean wall stress, $\Delta\sigma^{(w)}$ given by:

$$\Delta\sigma^{(w)} = \frac{k_n^{(w)} N_c \dot{u}^{(w)} \Delta t}{A^{(w)}} \tag{8.3}$$

For stability, the absolute value of the change in wall stress should be lower than the absolute value of the difference between the measured and computed stresses, $\Delta\sigma$ and hence the stability requirement, has the form:

$$|\Delta\sigma^{(w)}| < \alpha |\Delta\sigma| \tag{8.4}$$

where, $\alpha < 1$ is a relaxation factor.

Substituting Equation (8.1) and (8.3) into Equation (8.4) gives:

$$\frac{k_n^{(w)} N_c G |\Delta\sigma| \Delta t}{A^{(w)}} < \alpha |\Delta\sigma| \tag{8.5}$$

Thus, the "gain" parameter used in Equation (8.1) can be determined using:

$$G = \frac{\alpha A^{(w)}}{k_n^{(w)} N_c \Delta t} \tag{8.6}$$

As presented in section 8.3.5, the uniaxial static creep test simulations were performed using the differential density scaling option, where the time-step Δt equals unity and the resulting relaxation factor is 0.5.

The specified isotropic stress should be set at a low value relative to the material strength, such as for example 1% of the uniaxial compressive strength (Itasca, 2002). In this study, an initial isotropic stress magnitude of 0.20 MPa was assumed. This stress can adequately reduce the magnitude of locked-in stresses, resulting in the particle

configuration shown in Figure 8.5 for mixture HL CMHB-C. Similarly, the same procedure was followed to generate the AC PFC^{2D} models for the rest of the mixtures.

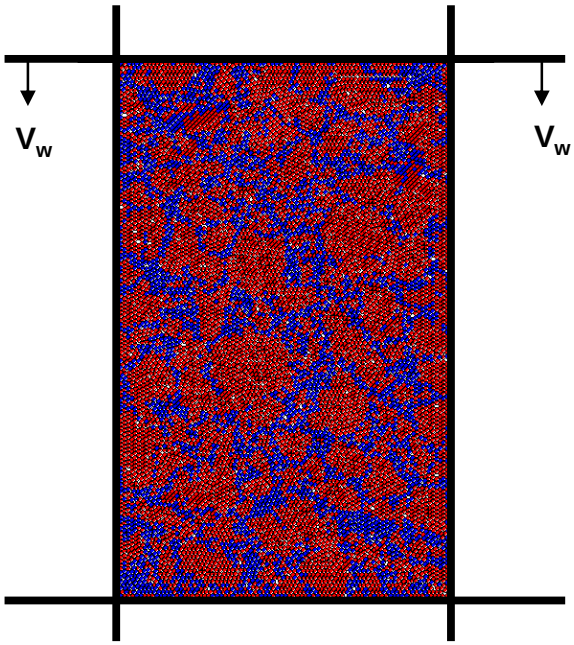

Figure 8.5 Initial Isotropic Stress State in the AC model; HL CMHB-C

8.3.4 Contact Model and Material Properties

The AC mixture model responses are greatly influenced by the particle contact behavior and their associated material properties. Therefore, before imposing the uniaxial static creep load on the AC model, the contact models and the material properties governing the interaction between mastic and aggregate particles and the boundary wall need to be defined. Brief descriptions of the contact models, namely the linear and simplified Hertz-Mindlin models were presented in Chapter 7. A contact model describes the physical behavior occurring at the contact between particles. A schematic representation of the interaction between the AC model particles (i.e., mastic-mastic, mastic-aggregate, and aggregate-aggregate) and boundary walls (i.e., wall-mastic and wall-aggregate) is shown in Figure 8.6. In this study, these interactions were defined using two contact models, namely the linear contact model and the viscoelastic contact model. The former is described using two parameters, namely normal and shear

stiffnesses, while the later is described using the Burger viscoelastic contact model, presented in Chapter 7, utilizing the four mechanical constants along the normal and shear direction.

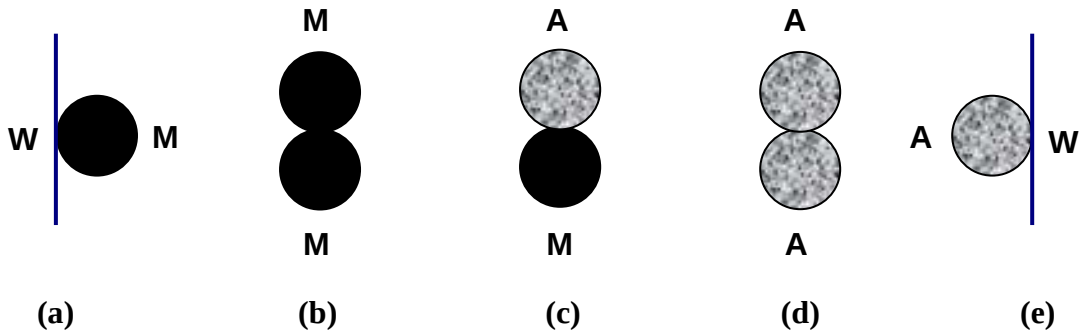

Figure 8.6 Schematic Representation of Particle-to-Particle and Particle-to-Wall Interaction in the AC PFC^{2D} Model; (a) Wall-Mastic (W-M), (b) Mastic-Mastic (M-M), (c) Aggregate-Mastic (A-M), (d) Aggregate-Aggregate (A-A), and (e) Wall-Aggregate (W-A)

The contact model was used to define the aggregate-to-aggregate, wall-mastic, and wall-aggregate interactions. Previous studies show that the aggregate elastic modulus value of 30 GPa would predict satisfactory Simple Performance Test (SPT) parameters (Abbas et al., 2005). For the present work, this assumption was used in addition to assigning the rigid wall stiffnesses to be 10 times stiffer than the particles stiffness so as to simulate the real experimental testing conditions. Moreover, an aggregate-to-aggregate contact friction coefficient $\mu = 0.5$, which corresponds to an angle of internal friction of 27^0, was assumed.

On the other hand, the mastic-to-mastic contacts were defined using the Burger viscoelastic models described in Chapter 6. The Burger model constants in shear were derived by direct fitting on mastic frequency sweep DSR data obtained in the LVE range of the mastics as shown in Table 6.5. The Burger model elastic constants in normal were derived from the shear elastic constants through:

$$\frac{E}{G} = 2(1+\nu) \tag{8.7}$$

Assuming a Poisson's ratio of $\nu = 0.40$ gives a normal to shear stiffness ratio of $K_n/K_s = 2.8$. The viscous elements of the mastic Burger models in normal were assumed to be identical to those in shear. This is consistent with the literature (e.g., Abbas et al.,,, 2002).

The creep deformation of ACs under dry conditions, involves plastic deformation in the mastic-to-mastic contacts, i.e., cohesive failure in this bond (Proceeding of the 2nd International Workshop on Moisture Sensitivity, College Station TX, 2007). Presentations in this workshop suggest that adhesive failure, i.e., breaking of the aggregate-to-mastic bond, is of concern only under the action of moisture, (a phenomenon referred to as stripping). For the purposes of this study, it was assumed that this type of mastic-to-mastic bond failure occurs when the strain limits of the LVE range are reached. For strain levels higher than those limits, the normal and shear stiffnesses of the Burger models were assigned negligible (i.e., practically zero) values, as illustrated in Table 8.1.

Table 8.1 Assigning the Burger Contact Model Parameters: Mastic-Mastic (M-M) and Aggregate-to-Mastic (A-M) Interaction; HL CMHB-C RTFO-aged Mastic Sample

Shear Strain (%)	Mastic-to-Mastic (M-M) Interaction[+]		Aggregate-to-Mastic (A-M) Interaction[+]	
	Normal Direction	Shear Direction	Normal Direction	Shear Direction
$\gamma < 53.5$	$E_M = 630.1249$ $\eta_M = 45.4928$ $E_K = 36.7164$ $\eta_K = 10.5862$	$E_M = 225.0446$ $\eta_M = 45.4928$ $E_K = 13.1130$ $\eta_K = 10.5862$	$E_M = 630.1249$ $\eta_M = 45.4928$ $E_K = 36.7164$ $\eta_K = 10.5862$	$E_M = 225.0446$ $\eta_M = 45.4928$ $E_K = 13.1130$ $\eta_K = 10.5862$
$\gamma \geq 53.5$	$E_M = \rightarrow 0$ $\eta_M = 45.4928$ $E_K = \rightarrow 0$ $\eta_K = 10.5862$	$E_M = \rightarrow 0$ $\eta_M = 45.4928$ $E_K = \rightarrow 0$ $\eta_K = 10.5862$	$E_M = 630.1249$ $\eta_M = 45.4928$ $E_K = 36.7164$ $\eta_K = 10.5862$	$E_M = 225.0446$ $\eta_M = 45.4928$ $E_K = 13.1130$ $\eta_K = 10.5862$

[+] $K_n/K_s = 2.8$; E_M and E_K are in kPa; and η_M and η_K are in kPa.sec

In the LVE range, the aggregate-to-mastic contact laws used were the same as the Burger models used for the mastic-to-mastic contact laws. Since adhesive failure was not an issue in simulating the creep tests available, no provisions of failure were made for the aggregate-to-mastic bond.

8.3.5 Uniaxial Static Creep Loading on the AC Model

In this study, nine AC mixtures were prepared from three different aggregate sources, namely hard limestone (HL), granite (G) and soft limestone (SL) involving a single PG 76-22 binder. The mix design procedure and the characterization of the aggregate and binder properties were presented in Chapter 4. Creep data for these cores were available under a constant load of 207kPa in compression and a chamber testing temperature of 60^{o}C.

Considerable effort was expended in establishing the wall velocity that best simulates the laboratory creep tests over the length of testing period. Several simulation trials were carried out using different wall velocities, ranging from 0.3 to 0.9 m/sec. The AC model and the corresponding axial stresses were monitored and compared with the experimental creep stress values, as illustrated in Figure 8.7. The axial stresses were computed by dividing the total reaction forces on the upper wall by the wall area. It was found that the magnitude of the axial DEM predicted stresses were not converging to the experimental creep stress, especially in the initial stage of the creep simulations. It was believed that the disturbances arising from the unbalanced contact forces generated from the complex wall-mastic-aggregate interactions produced highly variable axial stresses, as shown in Figure 8.7. Based on the observation made from this analysis, a wall velocity of 0.70 m/sec was selected to simulate the creep load of 207kPa. Note that the 0.7 m/sec curve reaches asymptotically the 207kPa stress level, until about 8000 sec, where apparently the strain levels at the mastic-to-mastic contacts exceeds the LVE range. To simulate the AC model responses due to the creep simulated load, a total of 10800 calculation cycles was required yielding a clock running time of 3 hrs per simulation using the differential density scaling option, where the time-step Δt equals unity.

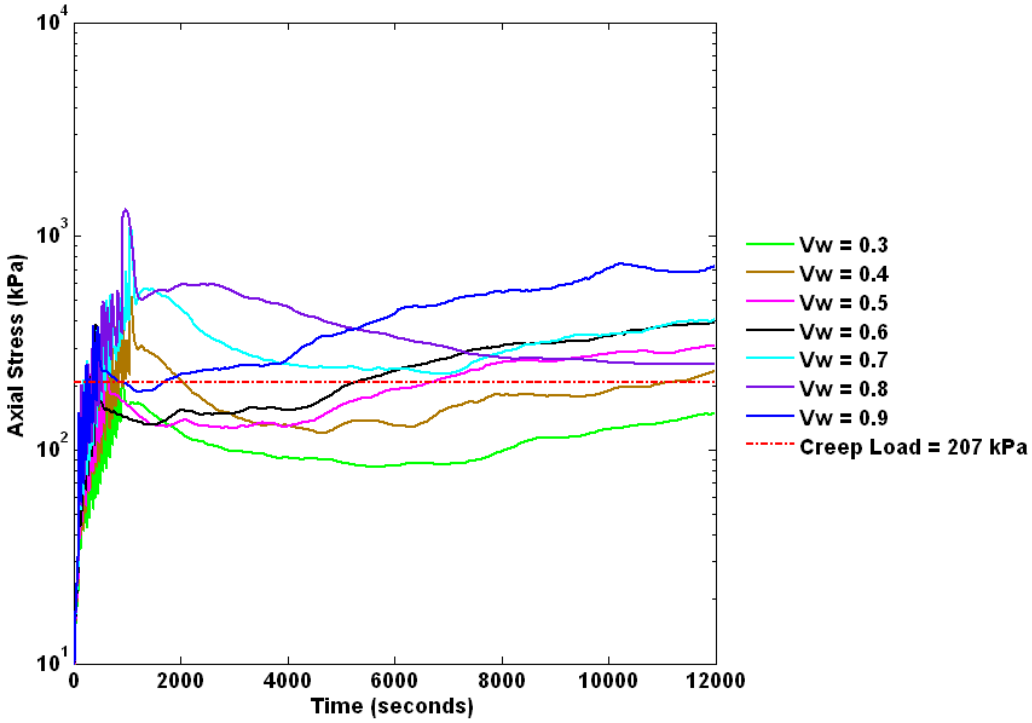

Figure 8.7 Example to Illustrate a Method of Establishing Upper Platen Velocity to Simulate the Experimental Creep Load

8.4 Simulation Results

The primary objective of DEM simulation of unconfined uniaxial static creep tests on AC models is to predict the permanent deformation behavior of the AC mixtures. As previously presented, the boundary wall conditions, contact models and the material properties of the bonded assembly of each of the AC models were utilized. An upper platen velocity of 0.7 m/sec was used to simulate the static creep load of 207kPa. The experimental measured average axial deformation for each AC specimen was computed by averaging the readings from the two axial LVDTs mounted at 1/3 of the sample height. The average deformation values were divided by the gauge length of 100 mm to yield the total axial strain. So as to compare and validate the DEM predicted results, similar procedures were implemented to compute the total axial strains of the AC model using the *FISH* functions embedded in the servo-mechanism option implemented in PFC^{2D}.

Based on the observation made from the trial DEM simulation results, the permanent deformation behavior of the AC model is highly dependent on the micromechanical properties of the bonded assembly composed of mastic and aggregate particles. Thus, it is important to investigate the effects of some of the micromechanical entities of the AC model assembly on the permanent deformation behavior of the AC mixtures. In this study, the contact stiffness ratio (K_n/K_s), Poisson's ratio (ν), and aggregate-to-aggregate contact friction coefficient (μ) were identified as the crucial parameters that affect the deformation behavior of the AC mixture model. The following section briefly presents the effects of K_n/K_s and μ on the evolution of axial strains of the AC model.

8.4.1 Effects of Contact Stiffness Ratio (K_n/K_s) on the Permanent Deformation Behavior of AC Mixtures

The contact stiffness ratio *(K_n/K_s)* has a great influence on the micromechanical behavior of the AC models consisting of mastic and aggregate particles. Collop et al., (2004a) demonstrated that the bulk modulus of idealized AC DEM model showed a linear dependency on the normal contact stiffness and the Poisson's ratio was found to be dependent on only the ratio of the shear contact stiffness to the normal contact stiffness. Moreover, Landry et al., (2006) studied the influence of stiffness ratio on the DEM simulated results of the direct shear tests.

Therefore, the effect of *(K_n/K_s)* on the evolution of the rate of deformation behavior of the AC mixture model was studied. For this purpose, Poisson's ratio values of ν = 0.10, 0.20, 0.30, and 0.40 were selected yielding contact stiffness ratio of K_n/K_s = 2.2, 2.4, 2.6, and 2.8, respectively. The contact stiffness ratio was calculated using Equation (8.7). Moreover, only one aggregate-to-aggregate contact friction coefficient $\mu = 0.5$ was selected to simulate the unconfined uniaxial static creep tests. The results presented in Figure 8.8 for mixture type HL CMHB-C indicate that the contact stiffness ratio does not appreciably affect the apparent permanent deformation resistance behavior of the AC model. It can be seen from these figures that the regression parameters of the steady-state region of the axial strain curves and flow time of the AC model do not change significantly with K_n/K_s. In addition, the experimentally measured axial strains

are also shown in Figure 8.17 and are favorable with the DEM predicted values when a contact stiffness ratio of 2.8 was considered. Similar findings were obtained for the rest of the mixture types as presented in Appendix D.

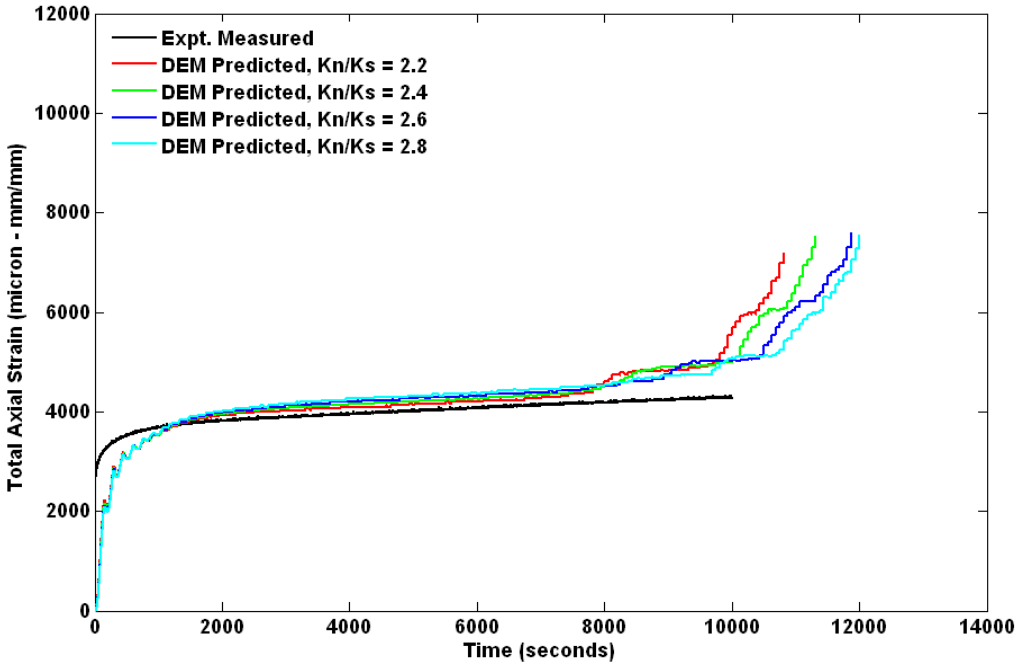

Figure 8.8 Effects of Contact Stiffness Ratio (K_n/K_s) on Axial Strain, $\mu = 0.5$; HL CMHB-C

8.4.2 Effects of Aggregate-to-Aggregate Contact Friction (μ) on the Permanent Deformation Behavior of AC Mixtures

It is well recognized that the aggregate physical properties play a significant role in defining AC performance. Recent advanced studies have demonstrated that the rutting resistance potential of AC mixtures rely on the method of microstructural characterization and are mainly contributed from aggregate-to-aggregate contact friction and interlocking (Masad, 2002; Tashman, 2003). In addition, You and Buttlar, (2001) showed that insufficient aggregate-to-aggregate contact friction and interlocking significantly affects the dynamic modulus DEM simulation results. Recently, Kruyt and Rothenburg, (2006) studied the micromechanical origin of macroscopic frictional behavior of cohesionless granular materials. In their study, two-dimensional DEM biaxial

simulations were performed on loose and dense granular assemblies with various inter-particle friction coefficient (μ) including, $\mu \to 0$ and $\mu \to \infty$. The effects of μ on the macroscopic characteristics, such as shear strength, dilatancy rate, energy distribution, and energy dissipation were investigated. Moreover, Landry et al., (2006) studied the influence of friction coefficient on the DEM simulated results of the direct shear tests.

Thus, the second parameter that was studied for its influence on the permanent deformation behavior of the AC mixture models was the aggregate-to-aggregate friction coefficient, μ. Therefore, the effect of this parameter on the evolution of axial strain was studied. For this purpose, several aggregate-to-aggregate contact friction coefficients were selected, namely μ (Mu) = 0 (i.e., AC mixture idealized as loose sand), 0.1, 0.2, 0.3, 0.4, 0.5, and ∞ (i.e., AC mixture idealized as rigid/intact rock). For this purpose, only one contact stiffness ratio of K_n/K_s = 2.8 was selected to simulate the unconfined uniaxial static creep tests. The simulation results obtained are presented in Figure 8.9 for mixture type HL CMHB-C. These results suggest that the aggregate-to-aggregate contact friction coefficient significantly affect the permanent deformation behavior of the AC mixtures. It was found that μ is inversely proportional to the slope of the steady-state region of the axial stain curves and increases with the intercept. Moreover, the flow time (FT) of the AC model increases with μ. In addition, the experimentally measured axial strain results are also shown in Figure 8.9 and are in good agreement with the DEM predicted values when the aggregate-to-aggregate contact friction coefficient of 0.5 was considered. It is worthy to mention that the axial strain values in primary stage of the creep curve do not appreciably change with increase or decrease of the aggregate-to-aggregate contact friction coefficient. Similar findings were obtained for the rest of the mixture types as presented in Appendix D.

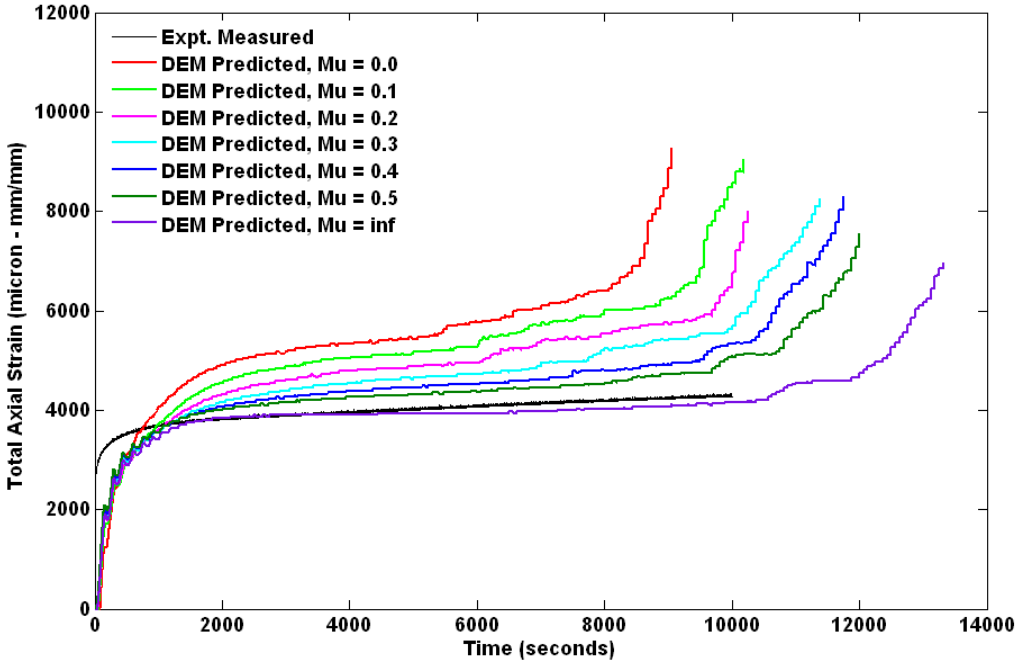

Figure 8.9 Effects of Aggregate-to-Aggregate Contact Friction (μ) on Axial Strain, K_n/K_s = 2.8; HL CMHB-C

The above DEM simulation results demonstrated that K_n/K_s = 2.8 and μ = 0.5 yielded satisfactory AC model responses as compared to the experimentally measured results. Thus, in the following section, the experimentally measured and DEM predicted axial strains and creep compliance values are compared and validated statistically.

8.4.3 Axial Strain

The experimentally measured and DEM predicted total axial strains are shown in Figure 8.10 through 8.18 using contact stiffness ratio of 2.8 and aggregate-to-aggregate contact friction coefficient of 0.5. It can be seen from these figures that the axial strain response is a function of loading time containing three distinct regions: a primary region where the strain rate decreases; a secondary (or steady-state) region where the strain rate is constant; and a tertiary region where the strain rate increases. In general, the shape of experimentally measured and DEM predicted axial strain curves are similar. Nonetheless, the tertiary response is not appreciably presented in the experimentally measured responses.

In the primary stage of the creep curve, the predicted axial strains were underestimated for all AC mixture models. It was believed that the lack of a unique way of imposing the prescribed wall velocity on the bonded AC model induced this problem, as clearly shown in Figure 8.7. Moreover, specifying lateral wall boundary conditions may contribute particle disturbances upon loading. In general, the predicted axial strains for Superpave-C mixtures deviate significantly from the experimentally measured values. These mixtures retain higher directional aggregate segregation indices yielding higher concentrations of aggregate particles at the middle and mastic phases along the edges of the mixture (Zelelew and Papagiannakis, 2007c). A closer look at the processed X-ray CT images shown in Figure B.41 through B.43 and their corresponding rectangular DEM models presented in Figure B.49 through B.51 suggest significant segregation in some of the AC cores. Thus, in these mixtures, the energy is mostly dissipated through aggregate-to-aggregate contact friction rather than mastic-to-mastic and mastic-to-aggregate interaction. This phenomenon results in a stiffer and less viscoelastic responding AC microstructure as reported in Figure 8.16 through Figure 8.18.

In the secondary or steady-state region of the creep curve, the axial strains for all AC models were satisfactorily predicted. This justifies that the permanent deformation behavior of the AC mixture models were sufficiently captured and simulated. Therefore, the regression parameters of this region were used to characterize the permanent deformation behavior of AC mixtures models. The absolute error of the intercept of steady-state region is lower than 2.5%, 8.5%, and 13.5% for mixture type CMHB-C, PFC, and Superpave-C, respectively. In addition, the absolute error of slope of this region is not higher than 1 % for mixtures CMHB-C and PFC and 25% for Superpave-C mixtures. In general, the steady-state region regression parameters were satisfactorily predicted for CMHB-C and PFC mixtures, especially for mixture type HL CMHB-C as depicted in Table 8.2.

The deformation behavior of the AC mixture models in tertiary region was fully simulated. However, the experimental observations (i.e., axial strain versus loading time curves) fall short to distinctly characterize the AC model behavior in this region.

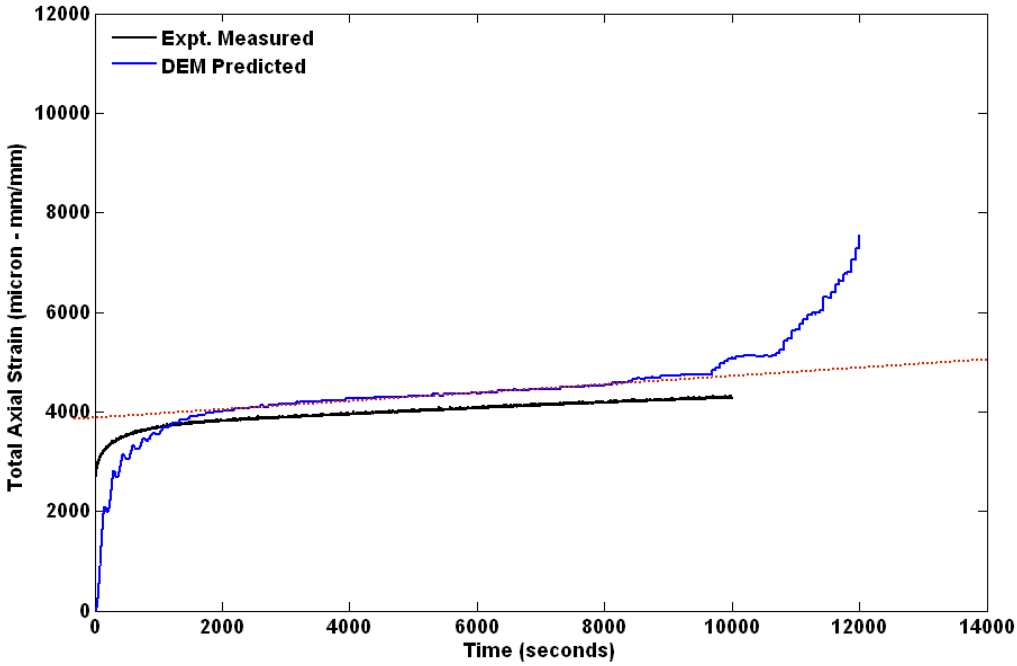

Figure 8.10 Measured and Predicted Axial Strain, $K_n/K_s = 2.8$ and $\mu = 0.5$; HL CMHB-C

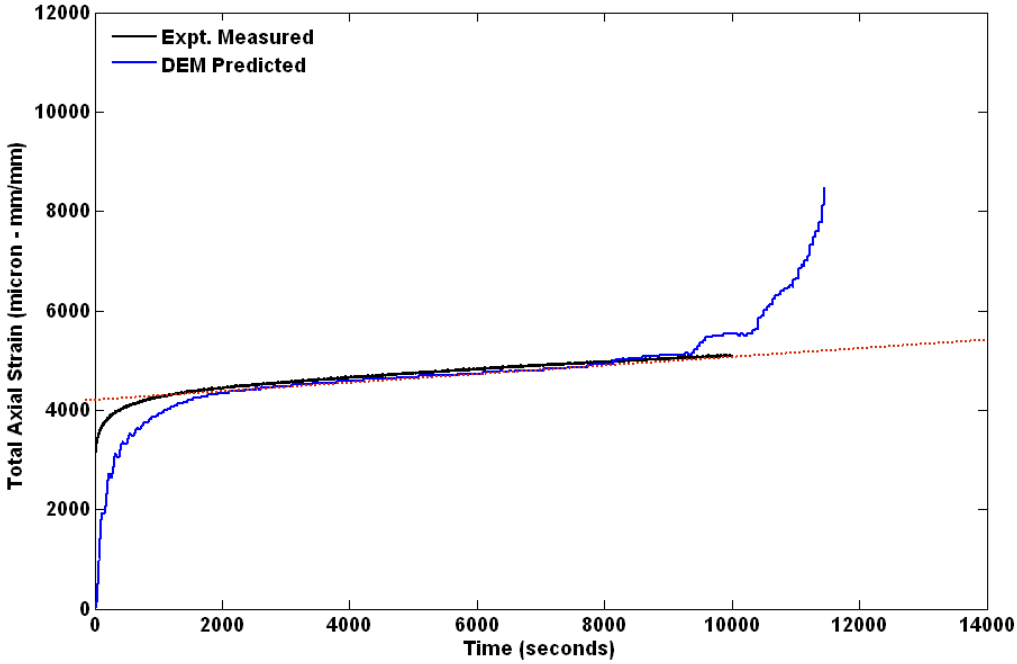

Figure 8.11 Measured and Predicted Axial Strain, $K_n/K_s = 2.8$ and $\mu = 0.5$; G CMHB-C

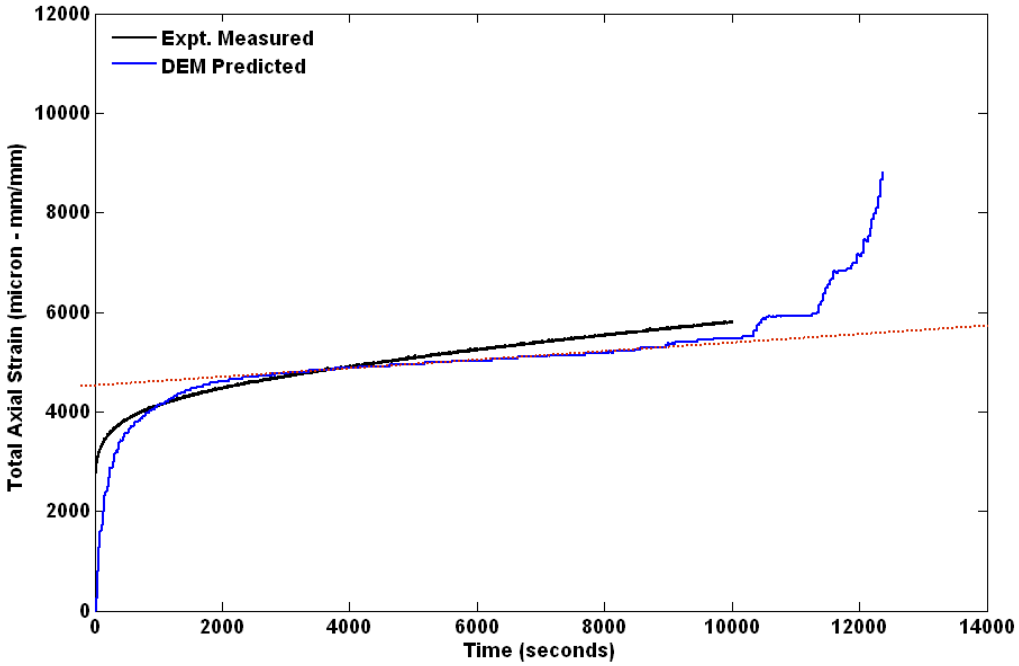

Figure 8.12 Measured and Predicted Axial Strain, $K_n/K_s = 2.8$ and $\mu = 0.5$; SL CMHB-C

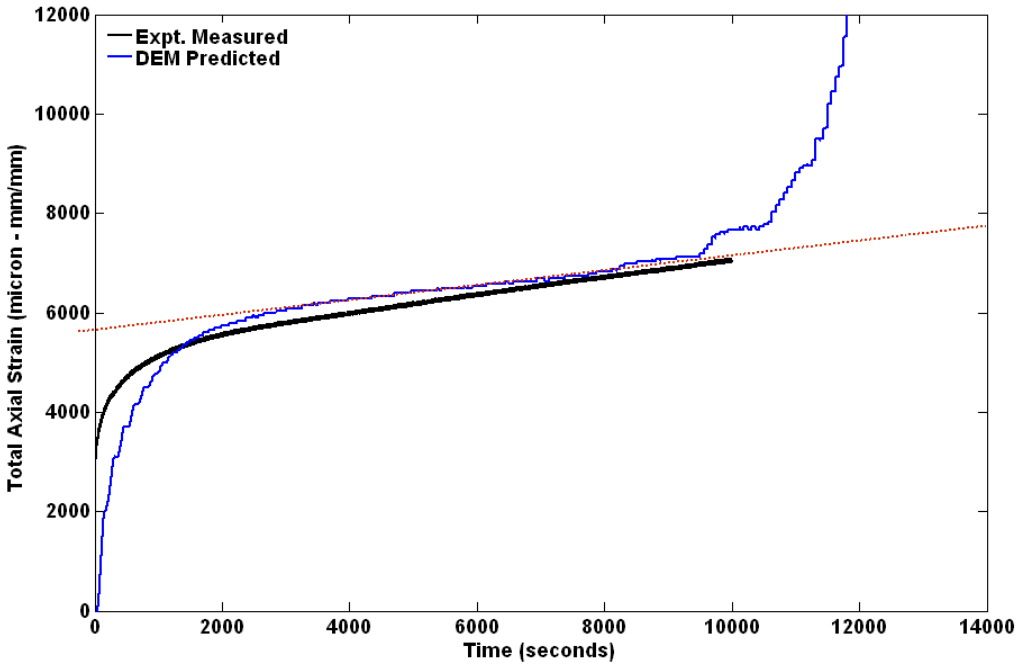

Figure 8.13 Measured and Predicted Axial Strain, $K_n/K_s = 2.8$ and $\mu = 0.5$; HL PFC

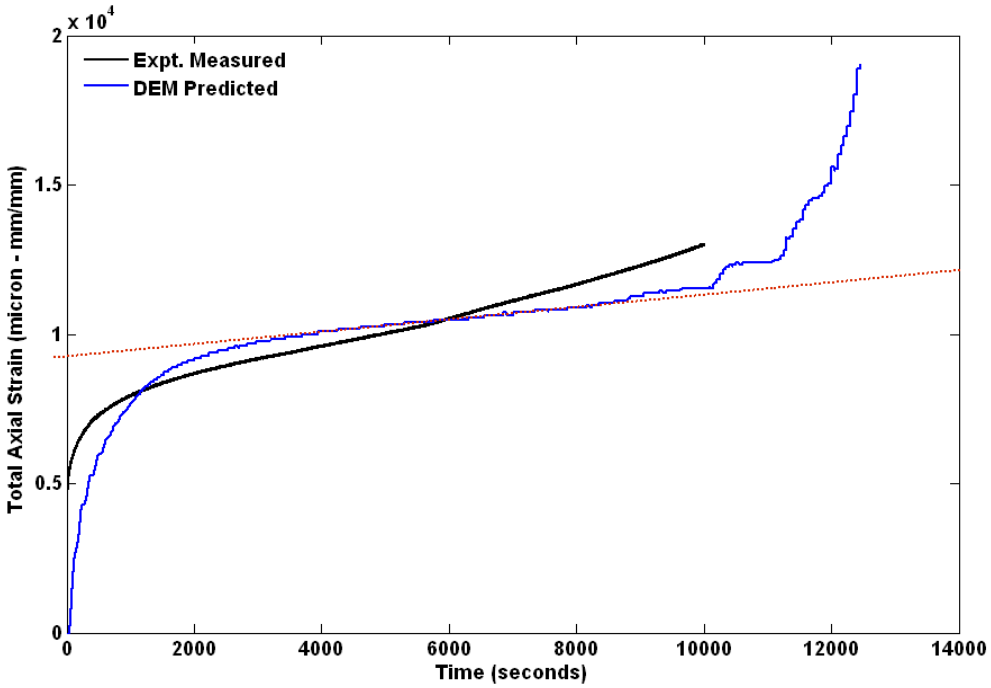

Figure 8.14 Measured and Predicted Axial Strain, $K_n/K_s = 2.8$ and $\mu = 0.5$; G PFC

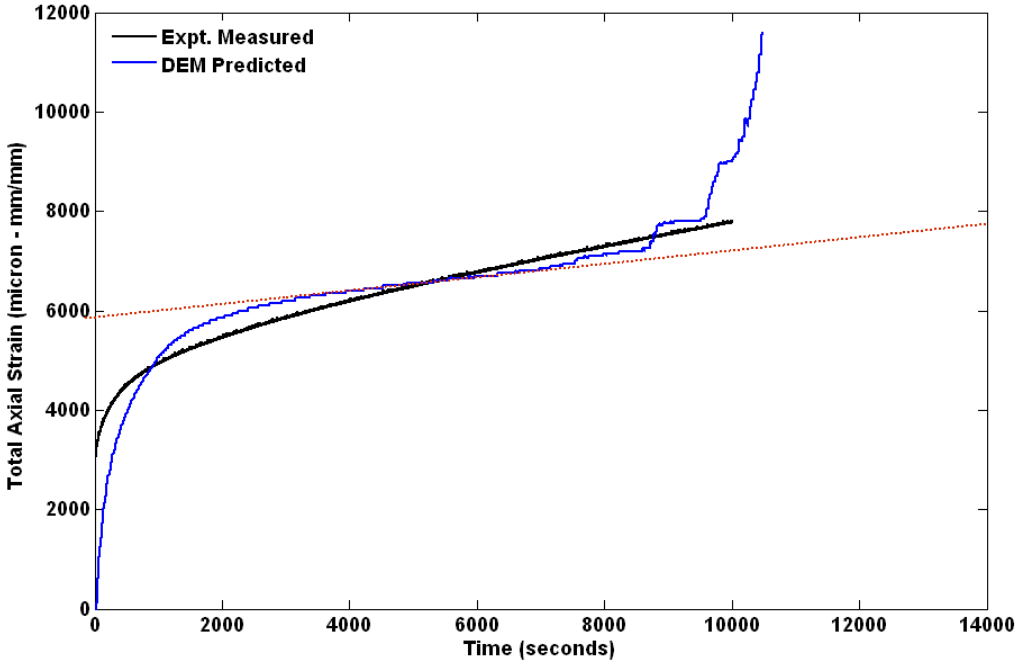

Figure 8.15 Measured and Predicted Axial Strain, $K_n/K_s = 2.8$ and $\mu = 0.5$; SL PFC

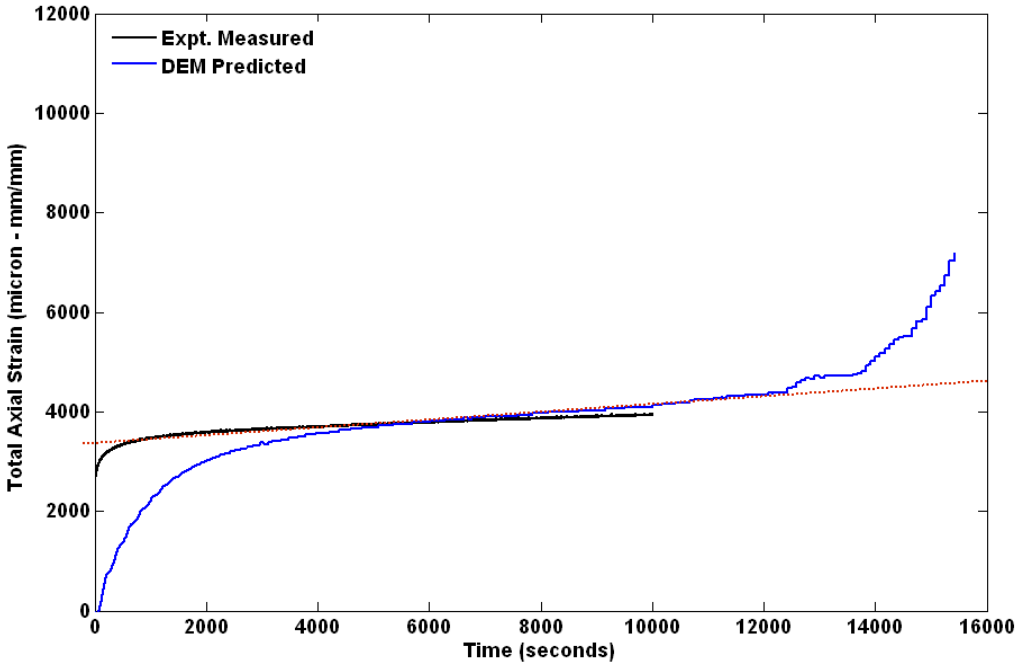

Figure 8.16 Measured and Predicted Axial Strain, $K_n/K_s = 2.8$ and $\mu = 0.5$; HL Superpave-C

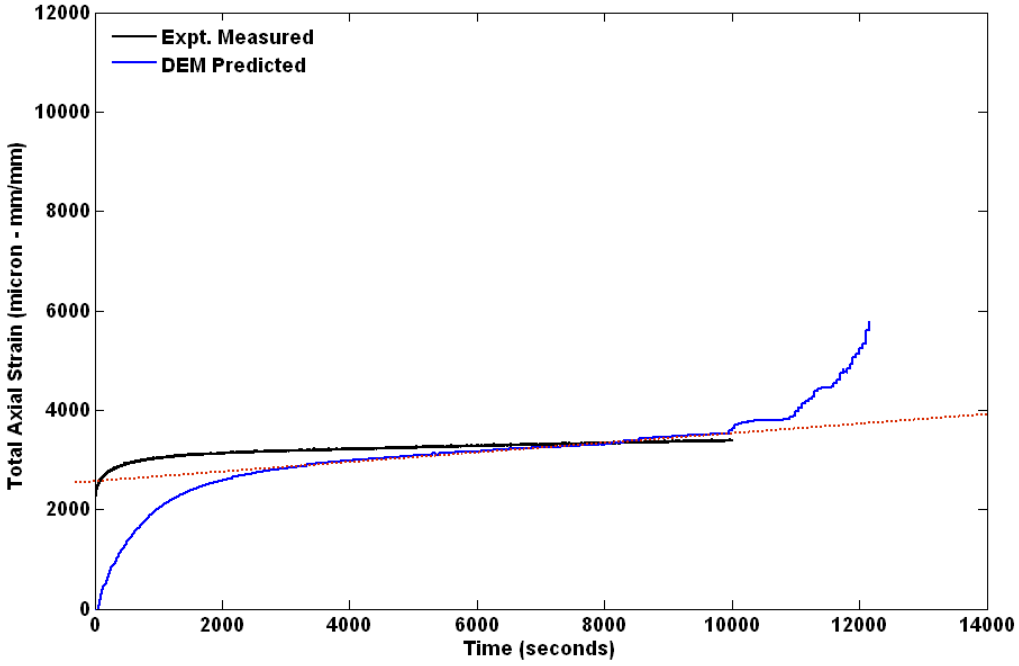

Figure 8.17 Measured and Predicted Axial Strain, $K_n/K_s = 2.8$ and $\mu = 0.5$; G Superpave-C

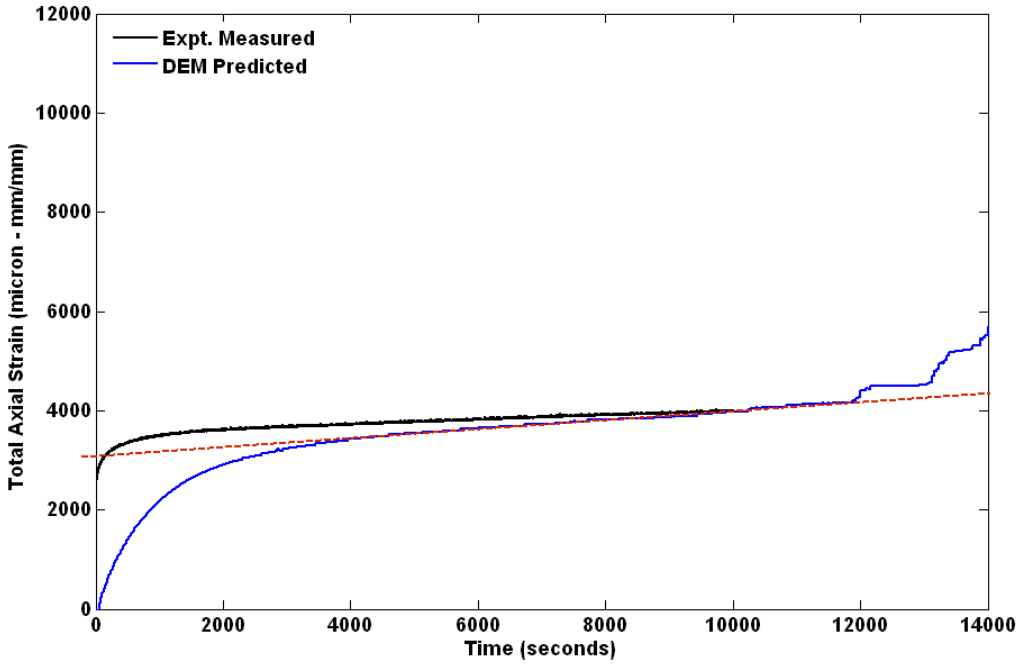

Figure 8.18 Measured and Predicted Axial Strain, $K_n/K_s = 2.8$ and $\mu = 0.5$; SL Superpave-C

Table 8.2 Axial Strain Steady-state Region Regression Parameters

Mixture Type	Intercept ($\times 10^{-6}$ mm/mm)		Absolute Error (%)	Slope ($\times 10^{-7}$ mm/mm) /sec		Absolute Error (%)
	Measured	Predicted		Measured	Predicted	
HL CMHB-C	3820	3900	2.09	2.62	2.64	0.76
G CMHB-C	4160	4150	0.24	3.83	3.85	0.52
SL CMHB-C	4240	4350	2.59	5.80	5.70	1.72
HL PFC	5720	5800	1.39	3.97	3.92	1.26
G PFC	8500	9000	5.88	8.37	8.10	3.23
SL PFC	5450	5900	8.26	8.89	8.75	1.57
HL Superp-C	3700	3200	13.51	1.47	1.86	26.53
G Superp-C	2850	2500	12.28	2.01	2.50	24.38
SL Superp-C	3300	3000	9.09	2.98	3.63	21.81

8.4.4 Creep Compliance

As described in Chapter 4, the main advantage of using creep compliance as a parameter to characterize the permanent deformation behavior of the AC mixtures is that it allows to distinctly separating the time-independent and time-dependent components of the strain response. The DEM predicted creep compliance was computed by dividing the axial strain component by the non-constant creep load that corresponds to a wall velocity of 0.7 m/sec. As presented in Figure 8.19 for mixture HL CMHB-C, the DEM predicted creep compliance is plotted with loading time and can be divided into three distinct regions: a primary region where the strain rate decreases; a secondary region where the strain rate is constant; and a tertiary region where the strain rate increases. The corresponding creep compliance curves for the rest of the AC mixtures are given in Appendix D.

The DEM predicted creep compliance curves in primary stage do not match with the experimentally measured values, predominantly due to the non-constant imposed creep load by the upper platen. The steady-state region of the creep compliance curve can be used to characterize the permanent deformation behavior of the AC mixtures. Therefore, the regression parameters of this region were used to characterize the permanent deformation behavior of AC mixtures models as depicted in Table 8.3. The absolute error for the intercept of steady-state region for mixture type CMHB, PFC, and Superpave-C is lower than 2.5%, 19.5%, and 72.5%, respectively. In addition, when considering the slope of this region, the absolute error is less than 1.5 %, 5.0% and 18.0 % respectively. In general, satisfactory steady-state region regression parameters were predicted for mixture type CMHB and PFC. In general, for the experimentally measured and DEM predicted change in volume of the AC mixtures increases during the primary and secondary creep stages.

However, as shown in Figure 8.19, the experimental static creep test tertiary response using the creep compliance curves is hardly recorded. Similar observations were made for the rest of the AC mixtures presented in Appendix A. The tertiary region is predominantly associated with pure plastic shear deformation where no volume change occurs. Thus, the beginning of the shear deformation under constant volume corresponds to the Flow Time (FT).

The experimentally measured and DEM predicted FT of the AC mixtures are depicted in Table 8.4. The minimum and maximum FT absolute errors correspond to 7.0% of G Superpave-C and 42.0% of G PFC, respectively.

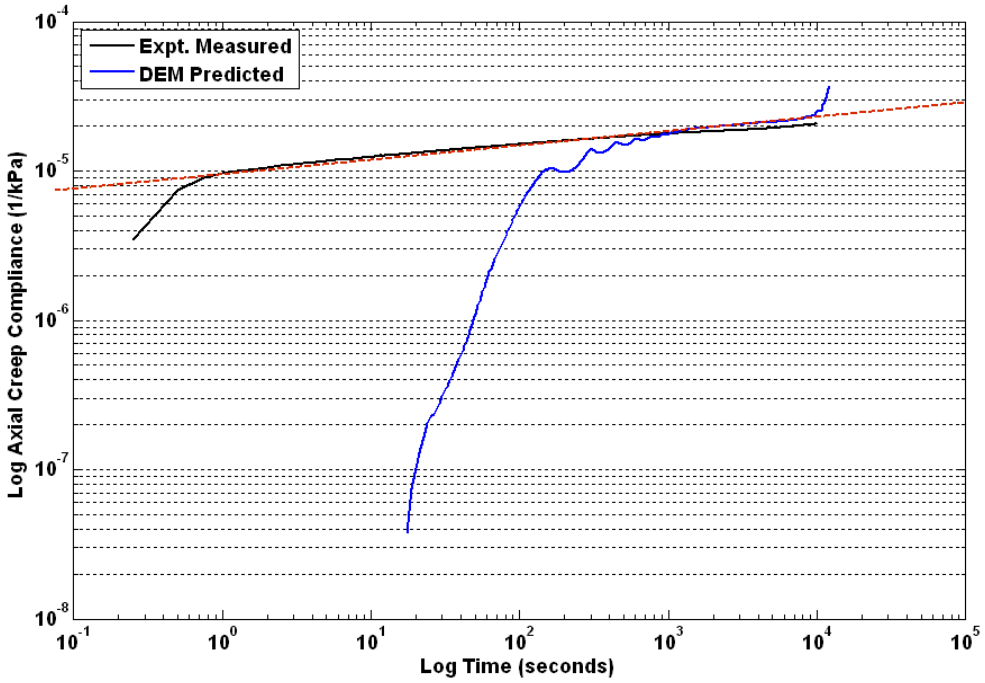

Figure 8.19 Measured and Predicted Axial Creep Compliance, $K_n/K_s = 2.8$ and $\mu = 0.5$; HL CMHB-C

Table 8.3 Creep Compliance Steady-state Region Regression Parameters

Mixture Type	Intercept ($\times 10^{-5}$) (1/kPa)		Absolute Error (%)	Slope ($\times 10^{-7}$) (1/kPa.sec)		Absolute Error (%)
	Measured	Predicted		Measured	Predicted	
HL CMHB-C	0.85	0.84	1.17	3.01	3.05	1.33
G CMHB-C	1.00	0.98	2.00	4.19	4.17	0.48
SL CMHB-C	0.80	0.78	2.50	4.51	4.53	0.44
HL PFC	0.78	0.75	3.85	1.29	1.35	4.65
G PFC	1.30	1.05	19.23	4.51	4.72	4.66
SL PFC	0.90	0.75	16.67	5.64	5.81	3.01
HL Superp-C	0.88	0.30	65.90	5.40	6.02	11.48
G Superp-C	0.72	0.20	72.22	4.27	4.92	15.22
SL Superp-C	0.83	0.40	51.81	3.86	3.17	17.87

Table 8.4 Flow Times (FT) Parameter of the AC Mixture

Mixture Type	Flow Time (FT) (seconds)		Absolute Error (%)
	Measured	Predicted	
HL CMHB-C	6112	8500	39.07
G CMHB-C	7110	9250	30.09
SL CMHB-C	6467	9000	39.17
HL PFC	6232	7438	19.35
G PFC	5423	7700	41.99
SL PFC	5057	5914	16.95
HL Superpave-C	8995	10250	13.95
G Superpave-C	8550	9150	7.02
SL Superpave-C	9440	11480	21.61

8.5 Summary and Conclusions

This chapter presents the DEM simulation results of unconfined uniaxial static creep compression tests on nine AC mixtures using *Particle Flow Code in two-dimensions* (PFC^{2D}) software. The AC core X-ray CT images were processed using an automated Digital Image Processing (DIP) software, called Volumetric-based Global Minima (VGM) thresholding algorithm software developed in MATLAB® environment. The air, mastic and aggregate phases of the AC mixture were identified separately based on their gray scale intensity boundary thresholds. The pixel spatial features of these objects were inputted into PFC^{2D} to represent their corresponding two-dimensional rectangular AC DEM model.

The boundary wall constraints of the AC model were specified and the initial isotropic stress state was established before installing the contact models and the material properties of wall-mastic-aggregate interactions. The aggregate-to-aggregate interaction was characterized using Coulomb's frictional law. Moreover, the mastic-to-mastic and the mastic-to-aggregate interactions were characterized using the Burger viscoelastic contact model. The maximum limiting shear strain value of the LVE range was considered as a bond breaking point when the former interaction was considered. On the other hand, the later interaction was characterized using Burger viscoelastic contact model regardless of the magnitude of the breaking shear strain limits. An upper wall velocity of 0.7 m/sec was established and found to simulate the imposed creep load of magnitude 207kPa.

Moreover, the effect of contact stiffness ratio (K_n/K_s) and aggregate-to-aggregate contact friction coefficient (μ) on the deformation behavior of the AC model were investigated. It was found that the ratio K_n/K_s does not appreciably affect the apparent permanent deformation resistance behavior of the AC model. The experimentally measured axial strain results are in good agreement with the DEM predicted axial strain values when the contact stiffness ratio of 2.8 was considered. In addition, μ is directly and inversely proportional to the intercept and slope of the steady-state region of the axial strain curves, respectively. Moreover, the Flow Time (FT) of the AC model increases with μ. The experimentally measured axial strain results are in good agreement with the DEM predicted axial strain values when $\mu = 0.5$ was considered. Therefore, a contact

stiffness ratio of 2.8 and aggregate-to-aggregate contact friction coefficient of 0.5 were considered for all AC models to compare and validate the DEM predicted material responses (i.e., axial strain and creep compliance) with the experimentally observations.

The total axial strains of the AC model were predicted and compared with the experimentally measured results. It was found that the experimentally measured and DEM predicted axial strain curves were found to be similar in shape. In the primary stage of the creep curve, the predicted axial strains were underestimated for all AC models. In the secondary or steady-state region of the creep curve, the axial strains for all AC models were satisfactorily predicted. This suggests that the steady-state permanent deformation behavior of the AC mixtures was satisfactorily simulated. The absolute error of the intercept of steady-state region is lower than 2.5%, 8.5%, and 13.5% for mixture type CMHB-C, PFC, and Superpave-C, respectively. In addition, the absolute error of slope of this region is not higher than 1% for mixtures CMHB-C and PFC and 25% for Superpave-C mixture. In general, the steady-state region regression parameters, namely the intercept and slope, were satisfactorily predicted for CMHB-C and PFC mixtures, especially for mixture type HL CMHB-C.

In addition, the DEM predicted creep compliance results were compared with the experimentally measured values. It was found that the primary stage of the DEM predicted creep compliance curves did not agree with the experimentally measured values due to the highly variable load imposed by the upper platen. Furthermore, the steady-state region of the creep compliance curve was used to characterize the permanent deformation behavior of the AC models. The absolute error for the intercept of steady-state region for mixture type CMHB, PFC, and Superpave-C is lower than 2.5%, 19.5%, and 72.5%, respectively. In addition, when considering the slope of this region, it is less than 1.5 %, 5.0% and 17.5%, respectively. In general, satisfactory steady-state region parameters were predicted for mixture type CMHB and PFC. In addition, the minimum and maximum FT absolute errors correspond to 7.0% of G Superpave-C and 42.0% of G PFC, respectively.

In general, the experimentally measured and DEM predicted axial strain curves are similar in shape, nevertheless the tertiary response is not appreciably presented in the experimental static creep tests when axial strain curves are considered. On the other hand,

excluding the primary stage of the creep compliance curves, the measured and predicted secondary and tertiary regions exhibit satisfactory results. Based on the measured and DEM predicted axial strains and creep compliance values, the deformation behavior of the AC mixtures were characterized and can be concluded that regardless of the aggregate type used CMHB-C mixtures demonstrated higher resistance to pavement rutting following Superpave-C mixtures and PFC mixtures are found to be less resistant to rutting.

Chapter 9

CONCLUSIONS AND RECOMMENDATIONS

9.1 Conclusions

This research was devoted to simulate the permanent deformation behavior of AC mixtures using a numerical simulation technique called Discrete Element Method (DEM). For this purpose, a DEM software package called *Particle Flow Code in two-dimensions* (PFC^{2D}) was utilized to simulate the unconfined uniaxial static creep tests in compression and predict the plastic deformation behavior of the AC mixtures.

Nine AC mixtures were prepared using three different aggregate sources, namely hard limestone (HL), granite (G), and soft limestone (SL) and a single PG 76-22 binder. Three mix designs typical of TxDOT practice were used, namely a Coarse Matrix High Binder type C (CMHB-C), a Porous Friction Course (PFC), and a Superpave type C (Superpave-C). Laboratory experiment of unconfined uniaxial static creep tests were performed on these mixtures to investigate their rutting resistance potential under a creep load of 207kPa and a testing chamber temperature of 60^0C. Based on the experimental observations, it was found that regardless of the aggregate type used CMHB-C mixtures demonstrated higher resistance to pavement rutting following the Superpave-C mixtures and PFC mixtures are found to be less resistant to rutting.

A high-resolution X-ray CT facility was utilized to capture the AC microstructure of cores of these mixtures. The cores were compacted with a Superpave Gyratory Compactor (SGC) and were drilled to dimensions of 100 mm diameter by 150 mm height. X-ray CT yielded 148 horizontal slices per core. Each of the horizontally sliced image consisted of 512 x 512 pixels. The resulting image resolution was 195 μm per pixel that does not allow detecting the AC mixture particles larger than roughly particles passing sieve No. 70.

State-of-the-art Digital Image Processing (DIP) techniques were utilized to process these AC X-ray CT images in a format suitable for input into the DEM simulation. An automated DIP algorithm was developed for this purpose, called

Volumetric-based Global Minim (VGM) thresholding algorithm using MATLAB®. VGM identifies the gray scale intensity boundary thresholds between the air-mastic and the mastic-aggregate phases with reference to volumetric information. It involves three interdependent stages, namely image preprocessing, gray scale thresholding and post-processing. The first stage involves image pre-processing for contrast enhancement and noise removal. The second stage is the main thresholding routine accepting as input the enhanced images of the first stage and volumetric information for the AC. It consists of two components, namely volumetrics-driven thresholding and three-dimensional representation and sectioning. The third stage further enhances particle separation through edge detection and image segmentation techniques. A simple routine was added to the VGM thresholding algorithm to assemble rectangular two-dimensional sections of AC cores from their circular sections. In addition, VGM generates the pixels of the boundaries of the aggregate particles in order to suitably input into the numerical simulation processes. It was demonstrated that the VGM processed images are suitable for numerical simulation input. This algorithm was shown to be a major improvement over the largely manual techniques used in the past. Therefore, the resulted processed two-dimensional image was inputted into PFC^{2D} software to represent the AC mixture model for simulation purposes.

Rheological tests on asphalt binders and mastics were performed using the Dynamic Shear Rheometer (DSR) device to characterize their viscoelastic properties. Two oscillatory tests were carried out, namely amplitude sweep test and frequency sweep tests. The former was used to determine the linear viscoelastic (LVE) range and the maximum limiting shear strain parameter. The Burger model parameters were characterized by utilizing the later test results. Moreover, the time-dependent behavior of the asphalt binders and mastics was characterized using relaxation and retardation times. The retardation times were found out to be higher than the relaxation times and thus the delayed response of the Burger model was dominant. It was demonstrated that the additional stiffness from the mineral fillers did not significantly affect the time-dependent behavior of asphalt binders and mastics. In general, the mastic mixtures with hard limestone (HL) yielded high stiffness values followed by mastic mixtures with granite (G) and the least was observed in soft limestone (SL) mastic mixtures. Further, the

Burger viscoelastic model parameters were utilized to augment the micromechanical DEM simulation of the AC mixtures.

The VGM processed AC images were input into the PFC^{2D} software and the contact models between particles were defined. The aggregate-aggregate interaction was characterized using Coulomb's frictional law. Moreover, the mastic-mastic and mastic-aggregate interactions were characterized using the Burger viscoelastic contact model. The maximum limiting shear strain value of the LVE range was considered as a bond breaking point when the former interaction was considered. On the other hand, the later interaction was characterized using Burger viscoelastic contact model regardless of the magnitude of the breaking shear strain limits. The boundary wall constraints of the AC model were specified and the initial isotropic stress state was established before installing the contact models and the material properties of wall-mastic-aggregate interactions. An upper wall velocity of 0.7 m/sec was established and barely found to simulate the imposed creep load of magnitude 207kPa.

Moreover, the effect of contact stiffness ratio (K_n/K_s) and aggregate-to-aggregate contact friction coefficient (μ) on the deformation behavior of the AC model were investigated. It was found that the ratio K_n/K_s does not appreciably affect the apparent permanent deformation resistance behavior of the AC model. In addition, the aggregate-to-aggregate contact friction (μ) is directly and inversely proportional to the intercept and slope of the steady-state region of the axial strain curves, respectively. Moreover, the Flow Time (FT) of the AC model increased with increasing μ value. In general, the experimentally measured axial strain results were in good agreement with the DEM predicted axial strain values, given a contact stiffness ratio and an aggregate-to-aggregate contact friction coefficient equal to 2.8 and 0.5, respectively. Thus, these values were considered for all AC models to compare and validate the DEM predicted material responses (i.e., axial strain and creep compliance) with the experimentally observations.

It was found that the experimentally measured and DEM predicted axial strain curves were found to be similar in shape. In the primary stage of the creep curve, the predicted axial strains were underestimated for all AC models. In the secondary or steady-state region of the creep curve, the axial strains for all AC models were satisfactorily predicted. This suggests that the steady-state permanent deformation

behavior of the AC mixtures was satisfactorily simulated. The absolute error of the intercept of steady-state region is lower than 2.5%, 8.5%, and 13.5% for mixture type CMHB-C, PFC, and Superpave-C, respectively. In addition, the absolute error of slope of this region is not higher than 1% for mixtures CMHB-C and PFC and 25% for Superpave-C mixture. In general, the steady-state region regression parameters of the axial strain curves, namely the intercept and slope, were satisfactorily predicted for CMHB-C and PFC mixtures, especially for mixture type HL CMHB-C. The deformation behavior of the AC mixture models in tertiary region was fully simulated. However, the experimental observations (i.e., axial strain versus loading time curves) fall short to distinctly characterize the AC model behavior in this region.

In addition, the DEM predicted creep compliance results were compared with the experimentally measured values. In general, the DEM predicted creep curves were similar in shape to the experimentally obtained ones, despite the fact that the latter did not always include the tertiary part of the deformation. It was found that the primary stage of the DEM predicted creep compliance curves did not agree with the experimentally measured values. This was probably due to the way the loading at the upper platen boundary was handled. On the other hand, the predictions of the slope of the secondary part of the creep curve were quite accurate, resulting in errors of less than 1.5 %, 5.0% and 17.5% for the CMHB-C, PFC, and Superpave-C mixtures, respectively. The error in the estimated intercept of the creep curve was 2.5%, 19.5%, and 72.5%, respectively. Finally, the maximum errors in Flow Time (FT) estimation respectively were 39.17%, 41.99%, and 21.61%.

Overall, it can be concluded that the DEM approach can be effectively used to predict the creep compliance curve of AC mixtures. Accordingly, the three mixtures tested rank in terms of their resistance to plastic deformation in the following order; first the Superpave-C followed by the CMHB-C and then the PFC mixtures. The reason for the poor performance of the later is the high percent air voids and the severe segregation evident in the X-ray CT images for these mixtures.

9.2 Limitations

The modeling approach utilized had a number of limitations highlighted below:

- DEM approach was two-dimensional, hence any three-dimensional effects of the AC microstructure were lost.
- The maximum image resolution was 195 μm, hence any aggregate fines smaller than about Sieve No. 70 could not be identified.
- The binder viscoelastic behavior was characterized in shear only due to lack of a suitable high-temperature test that allows binder characterization under normal stresses. As a result, assuming that the shear and normal viscoelastic properties were related via the Poisson's ratio was unavoidable. Furthermore, this value of the Poisson's ratio had to be assumed.
- The handling of the upper boundary platen by PFC^{2D} generated solution instability in the initial stages of creep load imposition.
- The cohesive failure assumed for the mastic was shear strain-level based. In reality, cohesive failure takes place in response to limiting shear and normal stress and strain.

9.3 Recommendations for Future Study

Considering the above mentioned research challenges, the future scope of the study may include the following:

- VGM can be easily modified to process the AC X-ray CT images for three-dimensional analysis. Thus, realistic representation of the AC mixture model can be obtained by utilizing PFC^{3D} software. Thus, the in-situ or laboratory tested material responses can be truly simulated to predict intrinsic micromechanical behavior of the AC mixtures.
- The Burger viscoelastic model needs to be generalized, (i.e., include a larger number of viscous and damping elements) to better describe the complex mastic behavior.
- The mastic failure criteria need to be generalized to account for the detailed normal and shear stress/strain state at the contacts.

- Failure criteria need to be expanded to describe adhesive failure, (i.e., breaking of the bond between aggregate and mastic), which is typical under high moisture conditions.
- The need to implement the last two failure criteria will require the development of user-defined visco-elasto-plastic contact models into DEM software.

REFERENCES

1. AASHTO T315 (2002) “Standard Method of Test for Determining the Rheological Properties of Asphalt Binder Using a Dynamic Shear Rheometer (DSR)” American Association of State Highway and Transportation officials, Washington, D. C.
2. AASHTO T 240 (1997) “Effects of Heat and Air on a Moving Film of Asphalt (Rolling Thin-Film Oven Test)” American Association of State Highway and Transportation officials, Washington, D. C.
3. AASHTO TP 62-03 (2001) “Standard Method of Test for Determining Dynamic Modulus of Hot-mix Asphalt Concrete Mixture” American Association of State Highway and Transportation officials, Washington, D.C.
4. Abbas, A. (2004) “Simulation of the Micromechanical Behavior of Asphalt Mixtures using the Discrete Element Method” Ph.D. Dissertation, Civil Engineering Department, Washington State University, Pullman, WA.
5. Abbas, A., Papagiannakis, A.T., and Masad, E. (2004) “Linear and Non-linear Viscoelastic Analysis of the Microstructure of Asphalt Concretes.” Journal of Materials in Civil Engineering, 16, pp. 133-139.
6. Abbas, A., Papagiannakis, A.T., Masad, E., and Shenoy A. (2005) “Modelling Asphalt Mastic Stiffness using Discrete Element Analysis and Micromechanics-based Models” The International Journal of Pavement Engineering, 6(2), pp. 137-146.
7. Abbas, A., Papagiannakis, A.T., Masad, E., and Harman T. (2007) “Micromechanical Modeling of the Viscoelastic Behavior of Asphalt Mixtures using the Discrete Element Method.” International Journal of Geomechanics, 7(2), pp. 131-139
8. Aboudi, J. (1991) “Mechanics of Composite Materials - A Unified Micromechanical Approach”, Elsevier, Amsterdam.

9. Al-Omari, A. and Masad, E. (2004) “Three Dimensional Simulation of Fluid Flow in X-Ray CT Images of Porous Media.” International Journal for Numerical and Analytical Methods in Geomechanics, 28, pp. 1327-1360.
10. Al-Omari, A., Tashman, L., Masad, E., Cooley, A., and Harman, T. (2002) “Proposed Methodology for Predicting HMA Permeability.” Journal of the Association of Asphalt Paving Technologists, 71, pp. 30-58.
11. Al-Rousan, T., Masad, E., Tutumluer, E., and Pan, T. (2007) “Evaluation of Image Analysis Techniques for Quantifying Aggregate Shape Characteristics.” Journal of Construction and Building Materials, 21(5), pp. 978-990.
12. Alshibli, K.A., Sture, S., Costes, N.C., Frank, M.L., Lankton, M.R., Batiste, S.N., and Swanson, R.A. (2000) “Assessment of Localized Deformations in Sands using X-Ray Computed Tomography.” Geotechnical Testing Journal, 23(3), pp. 274-299.
13. Alvarado, C., Mahmoud, E., Abdallah, I., Masad, E., Nazarian, S., Langford, R., Tandon, V., and Button, J. (2007) “Feasibility of Quantifying the Role of Coarse Aggregate Strength on Resistance to Load in HMA.” TxDOT Project No. 0-5268 and Research Report No. 0-5268.
14. Anderson, D.A. and Goetz, W.H. (1973) “Mechanical Behavior and Reinforcement of Mineral Filler-Asphalt Mixtures” Proceeding of Association of Asphalt Paving Technologists, 42, pp. 37-66.
15. Anderson, D.A., Christensen, D.W., Bahia, H.U., Dongre, R., Sharma, M.G., Antle, C.E., Button, J. (1994) “Binder Characterization and Evaluation Volume 3: Physical Characterization” Strategic Highway Research Program, National Research Council, Washington, D.C.
16. Andrew, D., Kim, J. R., and Newcomb, D. E. (1993) “Permanent Deformation in Asphalt Concrete” Journal of Materials in Civil Engineering, 5(1), pp. 112-128.
17. Anton Paar Germany GmbH, (2007) “SmartPave Asphalt Dynamic Shear Rheometer (DSR)”
18. Bahia, H., Zhai, H., Bonnetti, K., Kose, S. (1999) “Nonlinear Viscoelastic and Fatigue Properties of Asphalt Binders.” Journal of Association of Asphalt Paving Technologists, 68, pp. 1-34.

19. Bahuguna, S., Panoskaltsis, V. P., and Papoulia, K. D. (2006) “Identification and Modeling of Permanent Deformations of Asphalt Concrete” Journal of Engineering Mechanics, 132 (3), pp. 231- 239.
20. Bangash, T. and Munjiza, A. (2002a) “A Computationally Efficient Beam Element for FEM/DEM Simulations of Structural Failure and Collapse.” Geotechnical Special Proceedings of the Third International Conference on Discrete Element Methods; Numerical Modeling of Discontinua, Santa Fe, NM, United States, 117, pp. 133-137.
21. Bangash, T. and Munjiza, A. (2002b) “FEM/DEM Modelling of R.C. Beams under Impact” Structures and Materials Conference 7th International Conference on Structures under Shock and Impact, Montreal, Quebec, Canada, 11(7), pp. 519-528.
22. Banta, L., Cheng, K., and Zaniewski, J. (2003) “Estimation of Limestone Particle Mass from 2D Images.” Powder Technology, 132, pp. 184 -189.
23. Baumgaertel, M. and Winter, H.H. (1989) “Determination of Discrete Relaxation and Retardation Time Spectra from Dynamic Mechanical Data.” Rheological Acta, 28, pp. 511-519.
24. Bierawski, L.G. and Maeno, S. (2006) “DEM-FEM Model of Highly Saturated Soil Motion Due to Seepage Force.” Journal of Waterway, Port, Coastal and Ocean Engineering, 132(5), pp 401-409.
25. Bieniek, A. and Moga, A. (2000) “An Efficient Watershed Algorithm based on Connected Components.” Pattern Recognition, 33 (6), pp.907-916.
26. Braz, D., Motta, L. M. G., and Lopes, R. T. (1999) “Computed Tomography in the Fatigue Test Analysis of an Asphalt Mixture.” Applied Radiation and Isotopes, 50(4), pp. 661-671.
27. Brown, S.F. and Cooper, K. E. (1980) “A Fundamental Study of the Stress-Strain Characteristics of a Bituminous Material.” The Association of Asphalt Paving Technologist, 49-80, pp. 476-499.
28. Buttlar, W.G. and You, Z. (2001) “Discrete Element Modeling of Asphalt Concrete: A Micro-fabric Approach.” Transportation Research Record 1757,

Transportation Research Board, National Research Council, Washington, D.C., pp. 111-118.

29. Buttlar, W.G. and Roque, R. (1996) “Evaluation of Empirical and Theoretical Models to Determine Asphalt Concrete Stiffnesses at Low Temperatures.” International Journal of the Association of Asphalt Paving Technologist, 65-96, pp. 99-141.
30. Canny, J. (1986) “A Computational Approach to Edge Detection.” IEEE Transactions on Pattern Analysis and Machine Intelligence, 8 (6), pp. 679-698.
31. Chandan, C., Sivakumar, K., Masad, E., and Fletcher, T. (2004) “Application of Imaging Techniques to Geometery Analysis of Aggregate Particles.” Journal of Computing in Civil Engineering, 18 (1), pp. 75-82.
32. Chang, C.S. and Gao, J. (1997) “Rheological Modeling of Randomly Packed Granules with Viscoelastic Binders of Maxwell Type.” Computers and Geotechnics, 21, pp. 41-63.
33. Chang, K.G. and Meegoda, J.N. (1997) “Micromechanical Simulation of Hot Mix Asphalt.” Journal of Engineering Mechanics, 123 (5), pp. 495-503.
34. Chen, J.S. and Liao, M.C. (2002) “Evaluation of Internal Resistance in Hot-mix Asphalt Concrete.” Construction and Building Materials, 16, pp. 313-319.
35. Chen, J.S., Shiah, M.S., and Chen, H.J. (2001) “Quantification of Coarse Aggregate Shape and its Effect on Engineering Properties of Hot-Mix Asphalt Mixtures.” Journal of Testing and Evaluation, 29, pp. 513–519.
36. Chen, J.S., Wong, S.Y., and Lin, K.Y. (2005). “Quantification of Movements of Flat and Elongated Particles in Hot-mix Asphalt Subject to Wheel Load Test.” Journal of Materials and Structures, 38(3), pp. 395-402.
37. Cheung, C.Y., Cocks, A.C.F, and Cebon, D. (1999) “Isolated Contact Model of an Idealized Asphalt Mix.” International Journal of Mechanical Sciences, 41, pp. 767-792.
38. Collop, A.C., Cebon, D., and Hardy, M.S.A. (1995) “Viscoelastic Approach to Rutting in Flexible Pavements”, Journal of Transportation Engineering, 121, pp. 82-93.

39. Collop, A.C., McDowell, G.R., and Lee, Y.W. (2006) “Modelling Dilation in an Idealized Asphalt Mixture using Discrete Element Modelling.” Granular Matter, 8, pp. 175-184.
40. Cundall P.A. (1971) “A Computer Model for Simulating Progressive Large Scale Movements in Blocky Rock Systems.” In: Proceedings of the Symposium of International Society of Rock Mechanics, Nancy, France; 1 (II-8).
41. Cundall P.A. (2001) “A Discontinuous Future for Numerical Modeling in Geomechanics.” Proceedings of the Institution of Civil Engineering, Geotechnical Engineering, 149 (1), pp. 41-47.
42. Cundall, P.A. and Strack, O.D. (1979) “Discrete Numerical Model for Granular Assemblies.” Geotechnique, 29(1), pp. 47-65.
43. Dai, Q., Sadd, M.H., and You, Z. (2006) “A Micromechanical Finite Element Model for Linear and Damage-coupled Viscoelastic Behavior of Asphalt Concrete.” International Journal for Numerical and Analytical Methods in Geomechanics, 30, pp. 1135-1158.
44. Desai, C.S. and Zhang, D. (1987) “Viscoplastic Model for Geologic Materials with Generalized Flow Rule.” International Journal for Numerical and Analytical Methods in Geomechanics, 11, pp. 603-620.
45. Dessouky, S. (2005) “Multiscale Approach for Modeling Hot Mix Asphalt.” Ph.D. Dissertation, Civil Engineering Department, Texas A&M University, College Station, TX.
46. Ghalib, A.M., and Hryeiw, R.D. (1999) “Soil Particle Size Distribution by Mosaic Imaging and Watershed Analysis.” Journal of Computing in Civil Engineering, 13 (2), pp. 80-87.
47. Gonzalez, R.C. and Woods, R.E. (2002) “Digital Image Processing.” Upper Saddle River, NJ. Prentice-Hall.
48. Gupta, G., Zbib, A., El-Ghannam, A. Khraisheh, M., and Zbib, H. (2005) “Characterization of a Novel Bioactive Composite using Advanced X-Ray Computed Tomography.” Composite Structures, Fifth International Conference on Composite Science a Technology ICCST/5, 71(3-4), pp. 423-428.

49. Hagyard, D., Razaz, M., and Atkin, P. (1996) “Analysis of Watershed Algorithms for Gray Scale Images.” In: Proceedings of the IEEE International Conference on Image Processing, 3, pp. 41-44.
50. Hafez, I. (1997) “Development of a Simplified Asphalt Mix Stability Procedure for use in Superpave Volumetric Mix Design.” Ph.D. Dissertation, Civil Engineering Department, University of Maryland, College Park, MD.
51. Harvey, J.T. and Popescu, L. (2000) “Rutting of Caltrans Asphalt Concrete and Asphalt-Rubber Hot Mix Under Different Wheels, Tires and Temperatures – Accelerated Pavement Testing Evaluation.” Pavement Research Center, Institute of Transportation Studies, University of California, Berkeley.
52. Hopman, P.C., Valkering, C.P., and Vander Heide, J.P.J. (1992) “Mixes and Five Design Procedures: Search for a Performance Related Mix Design Procedure.” The Association of Asphalt Paving Technologist, 61, pp. 188-216.
53. Huang, B., Mohamad, L., and Wathugala, W. (2002) “Development of a Thermo-Viscoplastic Constitutive Model for HMA Mixtures.” In: Presented at the Association of Asphalt Paving Technologists 77th Annual Meeting (CD ROM), Colorado Springs, CO.
54. Hu, X., Feng, S., Liu, Y., and Tian, L. (2007) “3-D Distinct Element Modeling for Viscoelastic Asphalt Mastics.” Transportation Research Record 3015, Transportation Research Board, National Research Council, Washington, D.C., In Press.
55. Judycki, J., (1992) “Nonlinear Viscoelastic Behavior of Conventional and Modified Asphaltic Concrete under Creep.” Materials and Structures, 25, pp. 95-101.
56. Kallas, B.F. and Puzinauskas, V.P. (1967) “A study of Mineral Fillers in Asphalt Paving Mixtures.” Proceeding of Association of Asphalt Paving Technologist, 36, pp. 493-528.
57. Khanzada, S. (2000) “Permanent Deformation in Bituminous Mixtures.” Ph.D. Dissertation, University of Nottingham.

58. Kim, D.Y. and Park, J.W. (2005) “Connectivity-based Local Adaptive Thresholding for Carotid Artery Segmentation using MRA Images.” Image and Vision Computing, 23, pp. 1277-1287.
59. Kim, H., Hass, C.T., and Rauch, A.F. (2003) “3D Image Segmentation of Aggregates from Laser Profiling.” Computer-Aided Civil and Infrastructure Engineering, 18, pp. 254-263.
60. Kim, H., Rauch, A.F., Hass, C.T., and Browne, C. (2001) “A Prototype Laser Scanner for Characterizing Size and Shape Parameters in Aggregates.” Proceedings of the 9the Annual Symposium, ICAR, Austin, TX.
61. Kim, J.B. and Kim, H.J. (2003) “Multiresolution-based Watersheds for Efficient Image Segmentation.” Pattern Recognition Letters, 24 (1-3), pp. 473-488.
62. Kim, J.R., Dresher, A., and Newcomb, D.E. (1997) “Rate Sensitivity of Asphalt Concrete in Triaxial Compression.” Journal of Materials in Civil Engineering, 9(2), pp. 76-84.
63. Kim, Y. and Little D. (2004) “Linear Viscoelastic Analysis of Asphalt Mastics.” Journal of Materials in Civil Engineering, 16 (2), pp. 122-132.
64. Kose, S., Guler, M., Bahia, H.U., and Masad, E. (2000) “Distribution of Strains within Hot-mix Asphalt Binders: Applying Imaging and Finite Element Techniques.” Transportation Research Record 1728, Transportation Research Board, National Research Council, Washington, D.C., pp. 21-27.
65. Kruyt, N.P. and Rothenburg, L. (2006) “Shear Strength, Dilatancy, Energy and Dissipation in Quasi-static Deformation of Granular Materials” Journal of Statistical Mechanics: Theory and Experiment, P07021, pp. 1-13.
66. Kuo, C-Y. and Freeman, R.B. (1998) “Image Analysis Evaluation of Aggregates for Asphalt Concrete Mixtures.” Transportation Research Record 1615, Transportation Research Board, National Research Council, Washington, D.C., pp. 65-71.
67. Kuo, C-Y., Rollings, R.S., and Lynch, L.N. (1998). “Morphological Study of Coarse Aggregates using Image Analysis.” Journal of Materials in Civil Engineering, 10(3), pp. 135-142.

68. Landis, E.N. and Keane, D.T. (1999) “X-ray Microtomography for Fracture Studies in Cement-based Materials.” Proceedings of SPIE-The International Society for Optical Engineering, 3772, pp. 105-113.
69. Landry, H., Lague, C., and Roberge, M. (2006) “Discrete Element Representation of Manure Products” Computers and Electronics in Agriculture, 51, pp. 17-34.
70. Lee, H.J. and Kim, R.Y., (1998) “Viscoelastic Constitutive Model for Asphalt Concrete Under Cyclic Loading”, Journal of Engineering Mechanics, 124 (1), 32-40.
71. Long, F.M. (2001) “Permanent Deformation of Asphalt Concrete Pavements: A Nonlinear Viscoelastic Approach to Mix Analysis and Design.” Ph.D. Dissertation, University of California Berkeley.
72. Macedo, A., Vaz, C.M.P., Naime, J.M., Cruvinel P.E., and Crestana, S. (1999) “X-Ray Microtomography to Characterize the Physical Properties of Soil and Particulate Systems.” Powder Technology, 101, pp. 178-182.
73. Marinoni, N., Pavese, A., Foi, M., and Trombino, L. (2005) “Characterization of Mortar Morphology in Thin Sections by Digital Image Processing.” Cement and Concrete Research, 35, 1613-1619.
74. Masad, E. (2001) “Review of Imaging Techniques for Characterizing the Shape of Aggregates used in Asphalt Mixes.” Proceeding 9th Annual International Center for Aggregate Research (ICAR) Symposium (CD-ROM), Austin, Texas.
75. Masad, E. (2003) “The Development of a Computer Controlled Image Analysis System for Measuring Aggregate Shape Properties.” National Cooperative Highway Research Program NCHRP-IDEA Project 77 Final Report, Transportation Research Board, National Research Council, Washington, D.C.
76. Masad, E. and Button, J.W. (2000) “Unified Imaging Approach for Measuring Aggregate Angularity and Texture.” In: The International Journal of Computer-Aided Civil and Infrastructure Engineering-Advanced Computer Technologies in Transportation Engineering, 15(4), pp. 273-280.
77. Masad, E. and Button, J. (2004) “Implications of Experimental Measurements and Analysis of the Internal Structure of Hot-Mix Asphalt.” Transportation Research Record 1891, Transportation Research Board, Washington D.C., pp. 212-220.

78. Masad, E., Jandhyala, V.K., Dasgupta, N., Somadevan, N., and Sashidhar, N. (2002) “Characterization of Air Voids Distribution in Asphalt Mixes using X-Ray Computed Tomography.” Journal of Materials in Civil Engineering, 14(2), pp. 122-129.
79. Masad, E., Little, D.N., Tashman, L., Saadeh, S., Al-Rous, T., and Sukhwani, R. (2003) “Evaluation of Aggregate Characteristics Affecting HMA Concrete Performance,” Research Report ICAR 203-1, The Aggregate Foundation of Technology, Research, and Education, Arlington, VA.
80. Masad, E., Muhunthan, B., Shashidhar, N., and Harman, T. (1998) “Aggregate Orientation and Segregation in Asphalt Concrete.” Geotechnical Special Publication, 85, pp. 69-80.
81. Masad, E., Muhunthan, B., Shashidhar, N., and Harman, T. (1999a). “Internal Structure Characterization of Asphalt Concrete using Image Analysis.” Journal of Computing in Civil Engineering, 13(2), pp. 88-95.
82. Masad E., Muhunthan B., Shashidhar N., and Harman, T. (1999b). “Quantifying Laboratory Compaction Effects on the Internal Structure of Asphalt concrete.” Transportation Research Record 1681, Transportation Research Board, National Research Council, Washington, D.C., pp. 179-185.
83. Masad, E. and Niranjanan, S. (2002) “Microstructural Finite Element Analysis of the Influence of Localized Strain Distribution on Asphalt Mix Properties.” Journal of Engineering Mechanics, 129 (10), pp. 1105-1114.
84. Masad, E., Somadevan, N., Bahia, H.U., and Kose, S. (2001) “Modeling and Experimental Measurements of Strain Distribution in Asphalt Mixes.” Journal of Transportation Engineering, 127(6), pp. 477-485.
85. Masad, E., Tashman, L., Somedavan, N., and Little, D. (2002b) “Micromechanics-based Analysis of Stiffness Anisotropy in Asphalt Mixtures” Journal of Materials in Civil Engineering, 14(5), pp. 374-383.
86. McLean, D.B. and Monismith C.L. (1974) “Estimation of Permanent Deformation in Asphalt Concrete Layers due to Repeated Traffic Loading.” Highway Research Board, 510, pp 14-30.

87. Misiti, M., Misiti, Y., Oppenheim, G., and Poggi, J.M. (2006) “MATLAB R2006b Program.” The Math Works, Inc., Natick, Massachusetts.
88. Morris, J.P., Rubin, M.B., Block, G.I., and Bonner, M.P. (2006) “Simulations of Fracture and Fragmentation of Geologic Materials using Combined FEM/DEM Analysis.” International Journal of Impact Engineering, 33(1-12), pp. 463-473.
89. Offrell, P. and Magnusson, R. (2004). “In Situ Photographic Survey of Crack Propagation in Flexible Pavements.” The International Journal of Pavement Engineering, 5 (2), pp. 91-102.
90. Onate, E. and Rojek, J. (2004) “Combination of Discrete Element and Finite Element Methods for Dynamic Analysis of Geomechanics Problems.” Computer Methods in Applied Mechanics and Engineering, 193 (27-29), pp 3087-3128.
91. Panneerselvam, D. (2005) “Mechanics of Asphalt Concrete: Analytical and Computational Studies.” Ph.D. Dissertation, Case Western Reserve University, Cleveland OH.
92. Papagiannakis, A.T., Abbas, A., Masad, E. (2002) “Micromechanical Analysis of Viscoelastic Properties of Asphalt Concrete.” Transportation Research Record 1789, Transportation Research Board, National Research Council, Washington, D.C., pp. 113-120.
93. Papagiannakis, A.T., Abbas, A., and Masad, E. (2002) “Numerical Modeling of the Viscoelastic Properties of Asphalt Concretes.” 5th European Conference on Numerical Methods in Geotechnical Engineering.
94. Park, S.W., Kim, R., and Schapery, R.A., (1996) “A Viscoelastic Continuum Damage Model and its Application to Uniaxial Behavior of Asphalt Concrete.” Mechanics of Materials, 24, pp. 241-255.
95. Particle Flow Code in Two-dimensions (PFC^{2D}) Manual (2003), Version 3.1, Itasca Consulting Group, MN.
96. Persson, A. (1998) “Image Analysis of Shape and Size of Fine Aggregates.” Engineering Geology, 50, pp. 177-186.
97. Perzyna, P. (1984) “Constitutive Modeling of Dissipative Solids for Postcritical Behavior and Fracture.” Journal of Engineering Materials and Technology, 106, pp. 410-419.

98. Portes de Albuquerque, M., Esquef, I.A., Gesualdi, Mello A.R., and Portes de Albuquerqueb (2004) “Image Thresholding using Tsallis Entropy.” Pattern Recognition Letters, 25(9), pp.1059-1065.
99. Rojek, J. (2006) “Combined Discrete/Finite Element Modelling of Geotechnical Problems” In 35th Solid Mechanics Conference (SolMech-06), Cracow, Poland.
100. Rosin, P.L. (2001) “Unimodal Thresholding.” Pattern Recognition, 34(11), pp. 2083-2096.
101. Rothenburg, L., Bogobowicz, A., Haas, R., Jung, F.W., and Kennepohl, G. (1992) “Micromechanical Modelling of Asphalt Concrete in Connection with Pavement Rutting Problems.” Proceedings of the 7th International Conference on Asphalt Pavements, pp. 230-245.
102. Rowe, G.M., Brown, S.F., Sharrock, M.J., and Bouldin, M.G. (1995) “Visco-Elastic Analysis of Hot Mix Asphalt Pavement Structures.” Transportation Research Record 1482, Transportation Research Board, National Research Council, Washington, D.C., pp. 44-51.
103. Russ, J.C. (2002) “The Image Processing Handbook.” Boca Raton, FL. CRC.
104. Saadeh, S., Tashman, L., Masad, E., and Mogawer, W. (2002) “Spatial and Directional Distribution of Aggregates in Asphalt Mixes.” Journal of Testing and Evaluation, 30(6), pp. 483-491.
105. Sadd, M.H. and Gao, J.Y. (1998) “Contact Micromechanics Modeling of the Acoustic Behavior of Cemented Particulate Marine Sediments.” Proceedings of 12th ASCE Engineering Mechanics Conference, La Jolla, CA.
106. Savakis, A.E. (1998) “Adaptive Document Image Thresholding using Foreground and Background Clustering.” In: International Conference on Image Processing, 3, pp. 785-789.
107. Scarpas, A., Al-Khoury, R., Van Gurp, C., and Erkens, S.M. (1997a) “Finite Element Simulation of Damage Development in Asphalt Concrete Pavements.” Proceedings of 8th International Conference on Asphalt Pavements, University of Washington, Seattle, WA, 673-692.
108. Scarpas, A., Blaauwendraad, J., Al-Khoury, R., and Van Gurp, C. (1997b) “Experimental Calibration of a Viscoplastic-fracturing Computational Model.”

Proceedings of the International Conference on Computational Methods and Experimental Measurements, CMEM, pp. 643-652.

109. Schapery, R.A. (1984) “Correspondence Principles and a Generalized J-integral for Large Deformation and Fracture Analysis of Viscoelastic Media.” International Journal of Fracture, 25, pp.195-223.
110. Seibi, A.C., Sharma, M.G., Ali, G.A., and Kenis, W.J. (2001) “Constitutive Relations for Asphalt Concrete under High Rates of Loading.” Transportation Research Record 1767, Transportation Research Board, National Research Council, Washington, D.C., pp. 111-119.
111. Sepehr, K., Harvey, O.J., Yue, Z.Q., and El Husswin H.M. (1994) “Finite Element Modeling of Asphalt Concrete Microstructure.” Proceedings of 3rd International Conference of Computer-Aided Assessment and Control Localized Damage, Udine, Italy.
112. Shashidhar, N. (1999) “X-ray Tomography of Asphalt Concrete.” Transportation Research Record 1681, Transportation Research Board, National Research Council, Washington, D.C., pp. 186-192.
113. Shashidhar, N., Zhong, X., Shenoy, A.V., and Bastian, E.J. (2000) “Investigating the Role of Aggregate Structure in Asphalt Pavements.” 8th Annual Symposium Proceedings on Aggregates, Asphalt Concrete, Base, and Fines, Denver Co.
114. Si, Z. (2001) “Charaterization of Microdamage and Healing of Asphalt Concrete Mixtues.” Ph.D. Dissertation, Texas A&M University, College Station, TX.
115. Sonka, M., Hlavac, V., and Boyle, R. (1999) “Image Processing, Analysis, and Machine Vision.” PWS Publishing, Pacific Grove.
116. Soares, J.B., Colares de Freitas, F.A., Allen, D.H. (2003) “Considering Material Heterogeneity in Crack Modeling of Asphalt Mixtures.” Transportation Research Record 1832, Transportation Research Board, National Research Council, Washington, D.C., pp. 113-120.
117. Sousa, J.B., Craus, J., C.L., Monismith (1991) “Summary Report on Permanent Deformation in Asphalt Concrete.” Strategic Highway Research Program, National Research Council, Washington, D.C., Report No. SHRTP-A/IR-91-104.

118. Sousa, J.B., Deacon, J.A., Monismith, C.L. (1991) ”Effect of Laboratory Compaction Method on Permanent Deformation Characteristics of Asphalt-Aggregate Mixtures.” Asphalt Paving Technologist 60-91, pp. 533-585.
119. Sousa, J.B., Deacon, J.A., Weissman, S.L., Leahy, R.B., Harvey, J.T., Paulsen, G., Coplantz, J.S., and Monismith, C.L. (1994) “Permanent Deformation Response of Asphalt Aggregate Mixes.” Strategic Highway Research Program, National Research Council, Washington, D.C., Report No. SHR-A-415.
120. Sousa, J.B., Tayebali, A., Harvey, J., Hendricks, P., and Monismith, C.L. (1993) “Sensitivity of Strategic Highway Research Program A-003A Testing Equipment to Mix Design Parameters for Permanent Deformation and Fatigue.” Transportation Research Record 1384, Transportation Research Board, National Research Council, Washington, D.C., pp. 69-79.
121. Sousa, J.B., Weissman, S.L., Sackman, J.L., and Monismith, C.L. (1993) “A Nonlinear Elastic Viscous with Damage Model to Predict Permanent Deformation of Asphalt Concrete Mixes.” Transportation Research Record 1384, Transportation Research Board, National Research Council, Washington, D.C., pp. 80-93.
122. Sousa, J.B. and Weissman, S.L. (1994) “Modeling Permanent Deformation of Asphalt-Aggregate Mixes.” Journal of the Association of Asphalt Paving Technologists, 63-94, pp. 224-257.
123. Strack, O.D. and Cundall, P.A., (1978) “The Distinct Element Method as a Tool for Research in Granular Media.” Report Eng 76-20711, National Science Foundation, Department of Civil and Mining Engineering, University of Minnesota, MN.
124. Superpave Asphalt Binder Specification (1994), Asphalt Institute, in Lexington Kentucky.
125. Synolakis, C.E., Zhou, Z., and Leahy, R.M. (1996) “Determination of Internal Deformation Field in Asphalt Cores using X-Ray Computer Tomography.” Transportation Research Record 1526, Transportation Research Board, National Research Council, Washington, D.C., pp. 135-141.

126. Takemura, T. and Oda, M. (2004) “Stereology-based Fabric Analysis of Microcracks in Damaged Granite.” Tectonophysics, 387 (1-4), pp. 131-150.
127. Tarumi, Y. and Hakuno, M. (1987) “A Granular Assembly Simulation for the Liquefaction of Sand and Quick Sand” Bulletin of the Earthquake Research Institute, University of Tokyo, 62 (4), pp. 535-577.
128. Tashman, L. (2003) “Microstructural Viscoplastic Continuum Model for Asphalt Concrete.” Ph.D. Dissertation, Civil Engineering Department, Texas A&M University.
129. Tashman, L., Masad, E., Angelo, J. D., Bukowski, J., and Harman, T. (2002) “X-Ray Tomography to Characterize Air Void Distribution in Superpave Gyratory Compacted Specimens.” International Journal of Pavement Engineering, 3(1), pp. 19-28.
130. Tashman, L., Masad E., Little D., and Zbib H.(2005) “A Microstructure-based Viscoplastic Model for Asphalt Concrete.” International Journal of Plasticity, 21, pp. 1659-1685.
131. Tashman, L., Masad, E., Peterson, B., and Saleh, H. (2001) “Internal Structure Analysis of Asphalt Mixes to Improve the Simulation of Superpave Gyratory Compaction to Field Conditions.” Journal of the Association of Asphalt Paving Technologists, 70, pp. 605-645.
132. Tashman, L., Masad, E., Zbibi, H.M., Little, D., Kaloush, K. (2005) “Microstructure Viscoplastic Continuum Model for Permanent Deformation in Asphalt Pavements.” Journal of Engineering Mechanics 131 (1), pp. 48-57
133. Tex-241-F (2005) “Superpave Gyratory Compacting of Test Specimens of Bituminous Mixtures.” Texas Department of Transportation (TxDOT).
134. Tex-410-A (1999) “Abrasion of Coarse Aggregate Using the Los Angeles Machine.” Texas Department of Transportation (TxDOT).
135. Tex-411-A (1999) “Soundness of Aggregate Using Sodium Sulfate or Magnesium Sulfate.” Texas Department of Transportation (TxDOT).
136. Tex-438-A (1999) “Accelerated Polish Test for Coarse Aggregate.” Texas Department of Transportation (TxDOT).

137. Tex-612-J (2000) “Acid Insoluble Residue for Fine Aggregate.” Texas Department of Transportation (TxDOT).
138. Tex-461-A (2005) “Degradaton of Coarse Aggregate by Micro-deval Abrasion.” Texas Department of Transportation (TxDOT)
139. Tex-231-F (2005) “Static Creep Test.” Texas Department of Transportation (TxDOT)
140. Tunicliff, D.G. (1962) “A Review of Mineral Filler.” Proceeding of Association of Asphalt Paving Technologists, 21, pp. 118-150.
141. Uddin, W. (1999) “A Micromechanical Model for Prediction of Creep Compliance and Viscoelastic Analysis of Asphalt Pavements.” A Paper Presented at the 78th Annual Meeting of TRB, Washington, D.C.
142. Ullidtz, P. (2001) “Distinct Element Method for Study of Failure in Cohesive Particulate Media.” Transportation Research Record 1757, Transportation Research Board, National Research Council, Washington, D.C., pp.127-133.
143. Van de loo P.J. (1978) “The creep test: A key Tool in Asphalt Mix Design and in the Prediction of Pavement Rutting.” Journal of Association of Asphalt Paving Technologists, 47, pp. 522-557.
144. Van de loo P.J. (1976) “Practical Approach to the Prediction of Rutting in Asphalt Pavements: The Shell Method” Transportation Research Record 616, Transportation Research Board, National Research Council, Washington, D.C., pp.15-21.
145. Van de loo P.J. (1974) “Creep Testing, A Simple Tool to Judge Asphalt Mix Stability.” Journal of Association of Asphalt Paving Technologists, 43, pp.253-285.
146. Vincent, L. and Soille, P. (1991) “Watersheds in Digital Spaces: An Efficient Algorithm based on Immersion Simulations.” IEEE Transactions on Pattern Analysis and Machine Intelligence, 13(6), pp. 583-593.
147. Wang, L.B., Paul, H.S., Harman, T., and Angelo, J.D. (2004a) “Characterization of Aggregates and Asphalt Concrete using X-Ray Computerized Tomography: A State-of-the-art Report.” Journal of the Association of Asphalt Paving Technologists, 73, pp. 467-500.

148. Wang, L.B., Frost, J.D., and Lai, J.S. (2004b) “Three-dimensional Digital Representation of Granular Material Microstructure from X-Ray Tomography Imaging.” Journal of Computing in Civil Engineering, 18(1), pp. 28-35.
149. Weissman, S.L. (1997) “The Mechanics of Permanent Deformation in Asphalt-Aggregate Mixtures: a Guide to Laboratory Test Selection.” Symplectic Engineering Corporation.
150. Witczak, M., Kaloush, K., Pellinen, T., El-Basyouny, M., Von Quintus, H. (2002) “Simple Performance Test for Superpave Mix Design.” National Cooperative Highway Research Program, NCHRP Report 465, Transportation Research Board, Washington, D.C.
151. Yan, F., Zhang, H., Ronald Kube, C.R. (2005) “A Multistage Adaptive Thresholding Method.” Pattern Recognition Letters, 26(8) pp.1183-1191.
152. You, Z. and Buttlar, W.G. (2006) “Micromechanical Modeling Approach to Predict Compressive Dynamic Moduli of Asphalt Mixture using the Distinct Element Method” Transportation Research Record 1970, Transportation Research Board, National Research Council, Washington, D.C., pp. 73-83.
153. You, Z. and Buttlar, W. G. (2002) “Stiffness Prediction of Hot Mixture Asphalt (HMA) based upon Microfabric Discrete Element Modeling (MDEM)” cedinging of 4th International Conference on Road and Airfield Pavement Technology, China, (1), pp. 409-417.
154. You, Z. and Buttlar, W. G. (2004) “Discrete Element Modeling to Predict the Modulus of Asphalt Concrete Mixtures’’ Journal of Materials in Civil Engineering, 16 (2), pp. 140-146.
155. Yu, L., Shi-Feng, R., and Guang-Hu, X. (2007) “Discrete Element Simulation of Asphalt Mastics Based on Burgers Model.” Journal of Southwest Jiaotong University Journal of Southwest Butler University, 1 (15), pp. 20-26.
156. Yue, Z.Q., Bekking, W., and Morin, I. (1995) “Application of Digital Image Processing to Quantitative Study of Asphalt Concrete Microstructure.” Transportation Research Record 1492, Transportation Research Board, National Research Council, Washington, D.C., pp. 53-60.

157. Yue, Z.Q., Chen, S., and Tham, L.G. (2003) “Finite Element Modeling of Geomaterials using Digital Image Processing.” Computers and Geotechnics, 30, pp. 375-397.
158. Zelelew, H.M. and Papagiannakis, A.T. (2007c). “Wavelet-based Characterization of Aggregate Segregation in Asphalt Concretes” Journal of Materials in Civil Engineering (In-review)
159. Zelelew, H.M, Papagiannakis, A.T., and Muhunthan, B., (2007a) “Simulation of Permanent Deformation of Asphalt Concrete using Discrete Element Method (DEM): A Viscoplastic Contact Model” 18th Engineering Mechanics Division Conference (EDM), Blacksburg, VA.
160. Zelelew, H.M. and Papagiannakis, A.T. (2007b) “A Volumetrics Thresholding Algorithm for Processing Asphalt Concrete X-Ray CT Images” International Journal of Pavement Engineering (In-review)
161. Zhang, S., Wagner, G., Medyanik, S.N., Liu, W.K., Yu, Y.H., and Chung, Y.W. (2004) “Experimental and Molecular Dynamics Simulation Studies of Friction Behavior of Hydrogenated Carbon Films.” Surface and Coatings Technology, 177-178, pp. 818-823.
162. Zhong, X. and Chang, C.S. (1999) “Micromechanical Modeling for Behavior of Cementitious Granular Materials.” Journal of Engineering Mechanics, 125 (11), pp.1280-1285.
163. Zhu, H. and Nodes, J.E. (2000) “Contact Based Analysis of Asphalt Pavement with the Effect of Aggregate Angularity.” Mechanics of Materials, 32, pp. 193-202.
164. Zhang, D., Xing, J., Zhu, F. (2004) “3-D Beam-particle Model for Simulating Fracture in Rock Material.” Yantu Lixue/Rock and Soil Mechanic, (25), pp. 33-36.

Appendix A

AXIAL CREEP COMPLIANCE CURVES

A.1 Characterization of the Axial Creep Compliance Regression Parameters

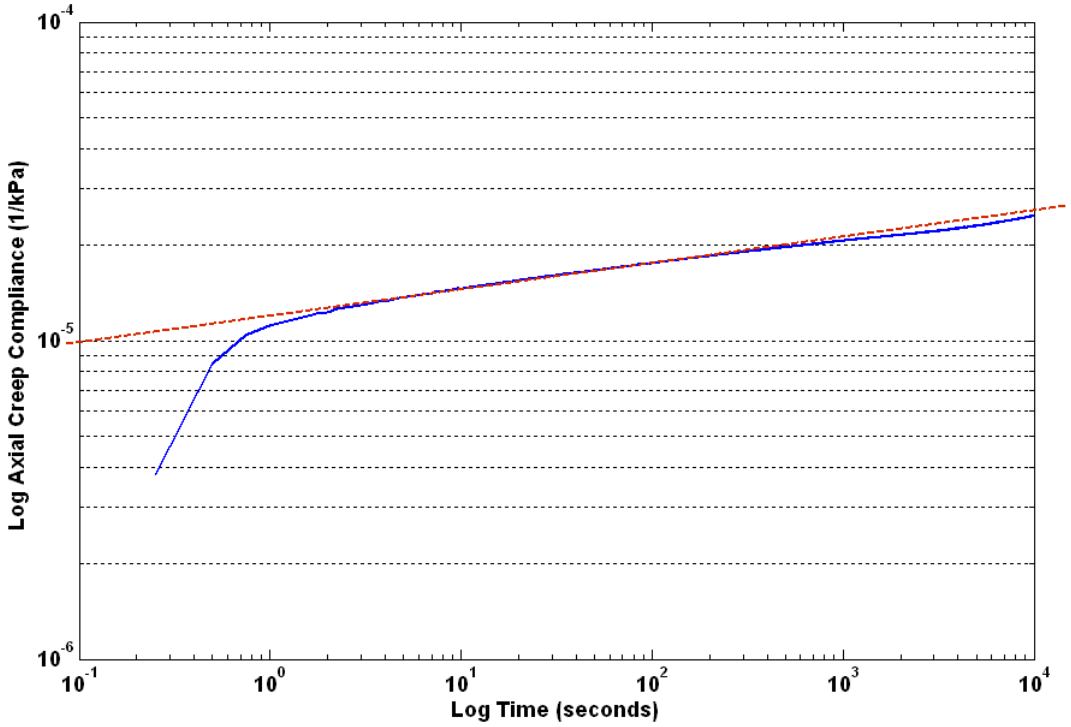

Figure A.1 Axial Creep Compliance versus Loading Time; Mixture Type G CMHB-C

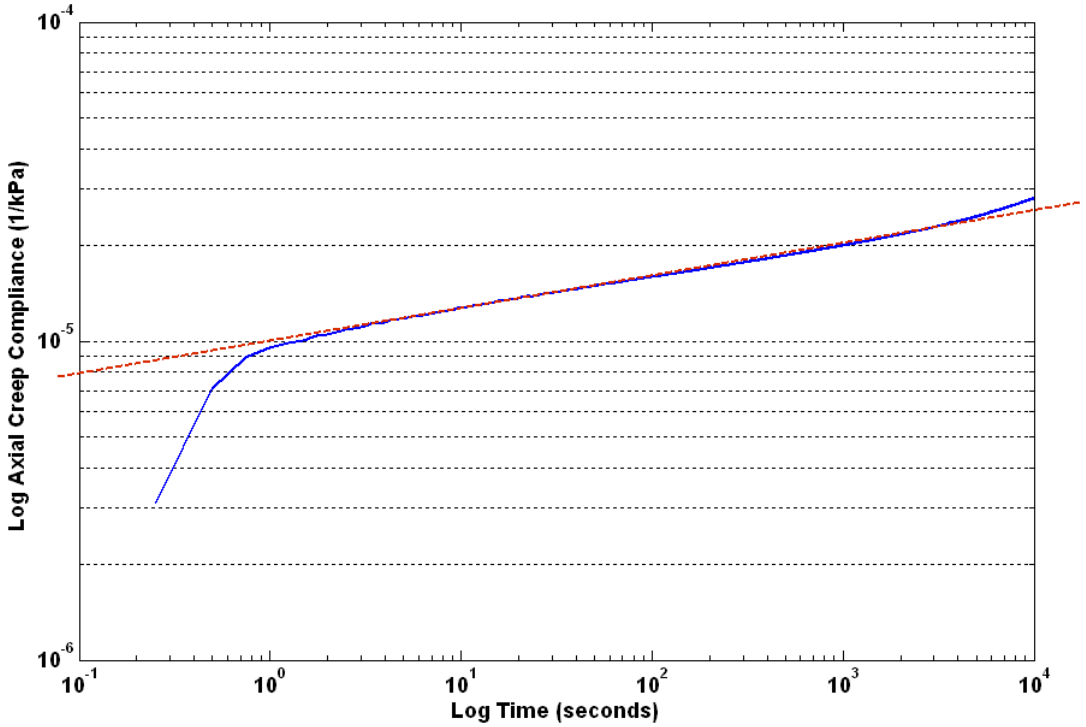

Figure A.2 Axial Creep Compliance versus Loading Time; Mixture Type SL CMHB-C

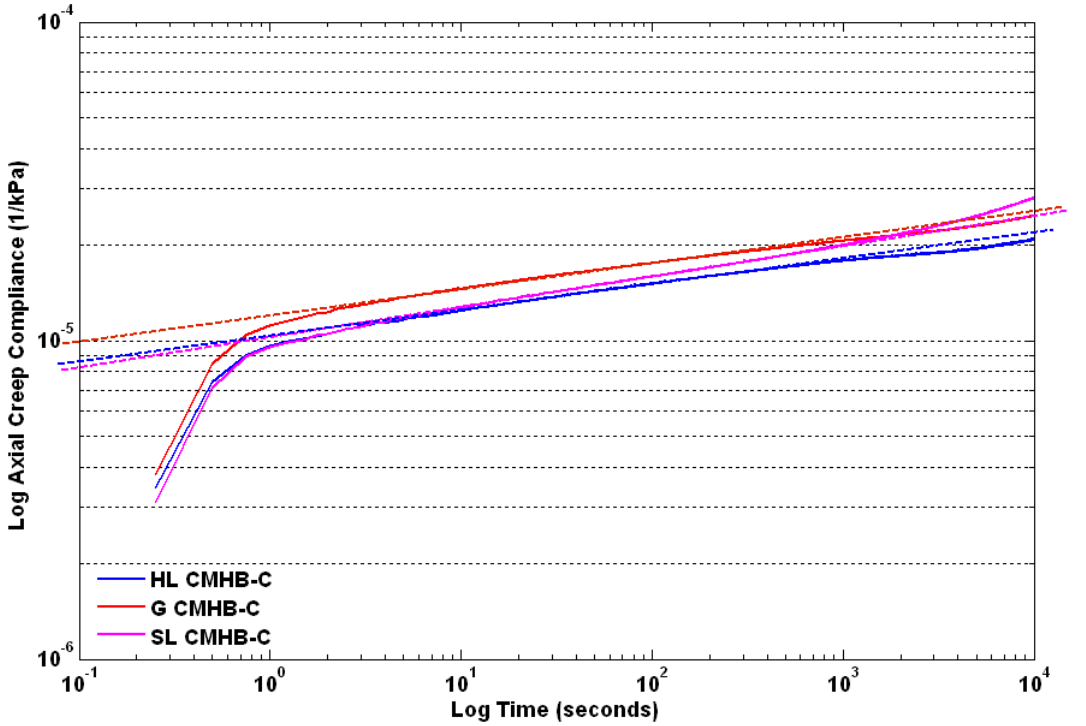

Figure A.3 Axial Creep Compliance versus Loading Time; Mixture Type CMHB-C

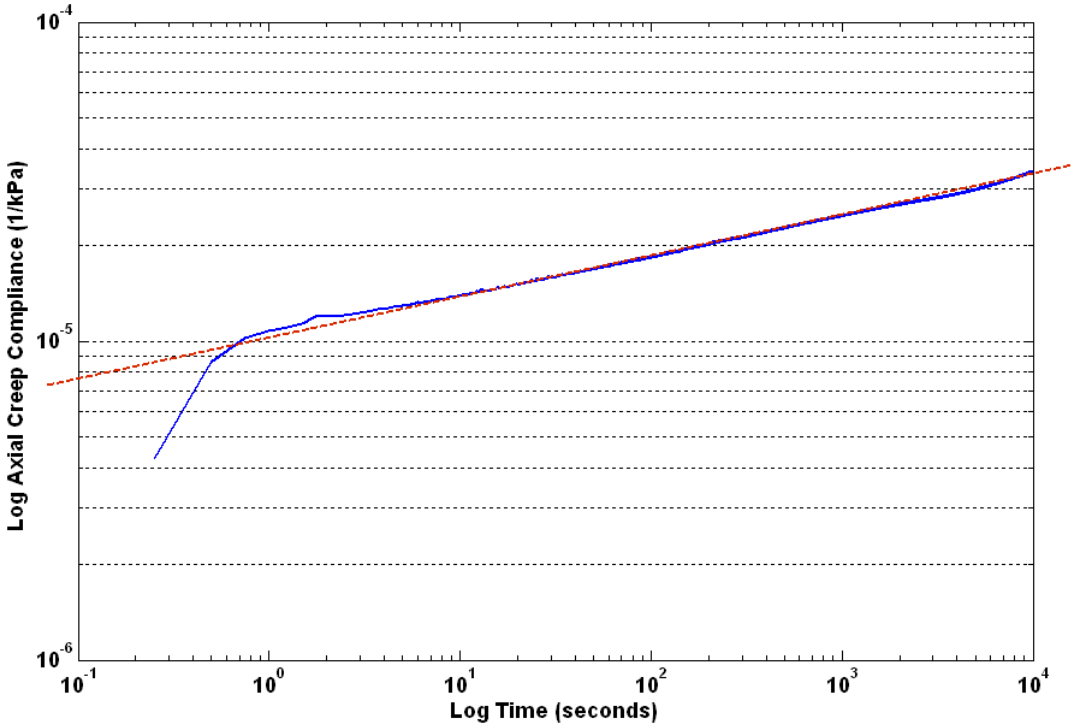

Figure A.4 Axial Creep Compliance versus Loading Time; Mixture Type HL PFC

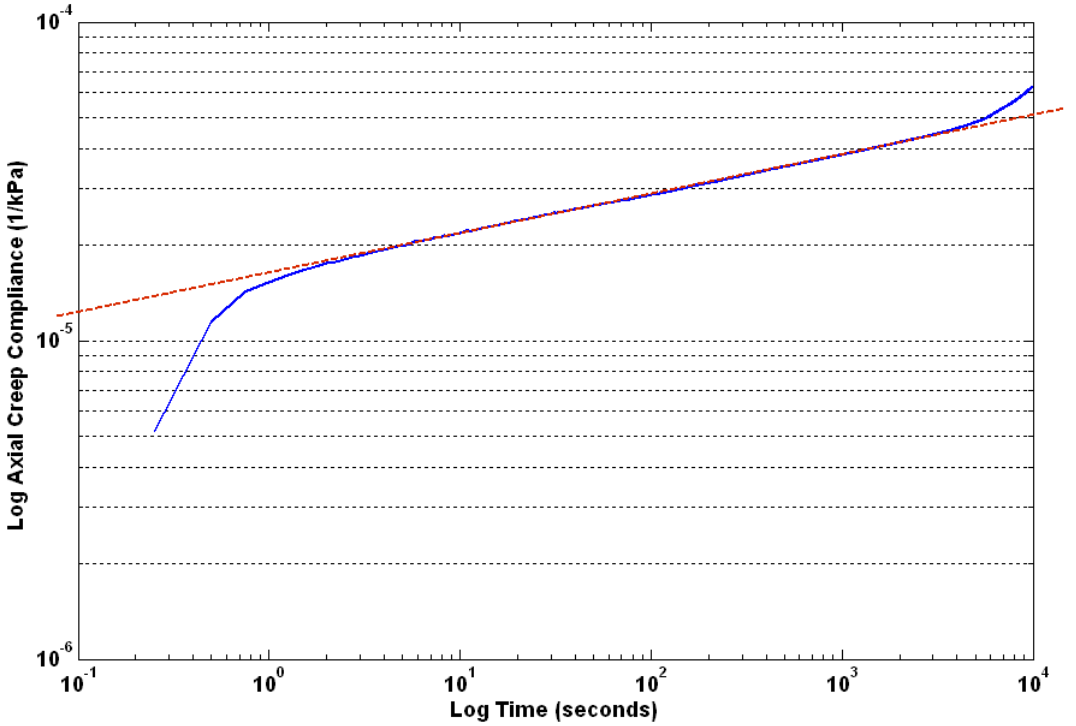

Figure A.5 Axial Creep Compliance versus Loading Time; Mixture Type G PFC

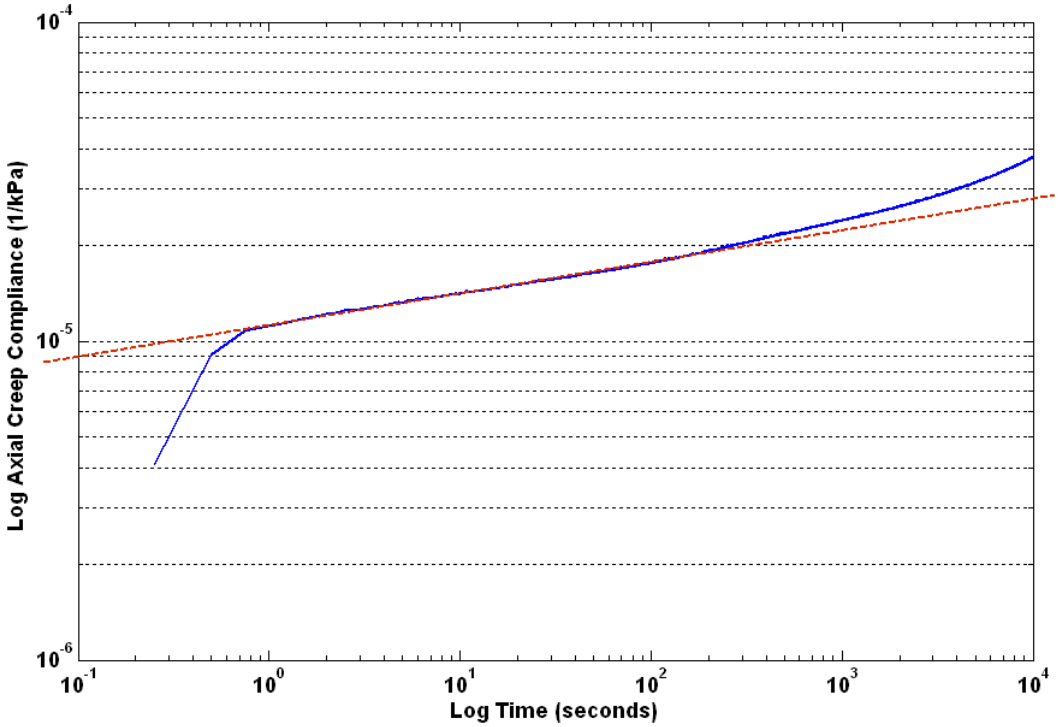

Figure A.6 Axial Creep Compliance versus Loading Time; Mixture Type SL PFC

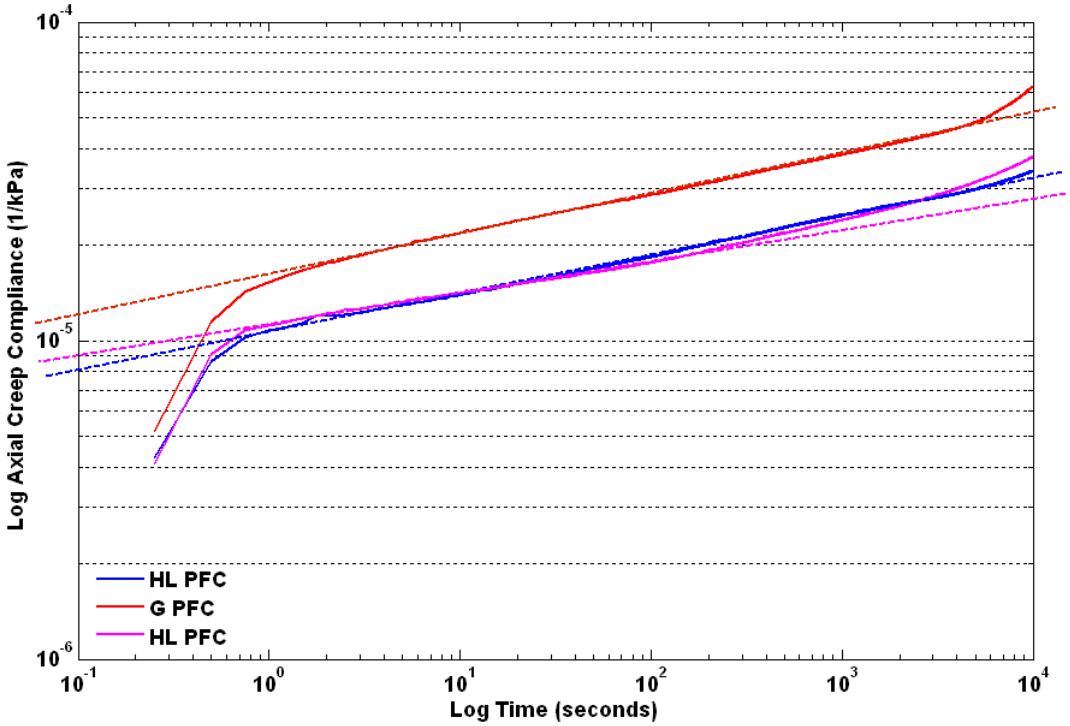

Figure A.7 Axial Creep Compliance versus Loading Time; Mixture Type PFC

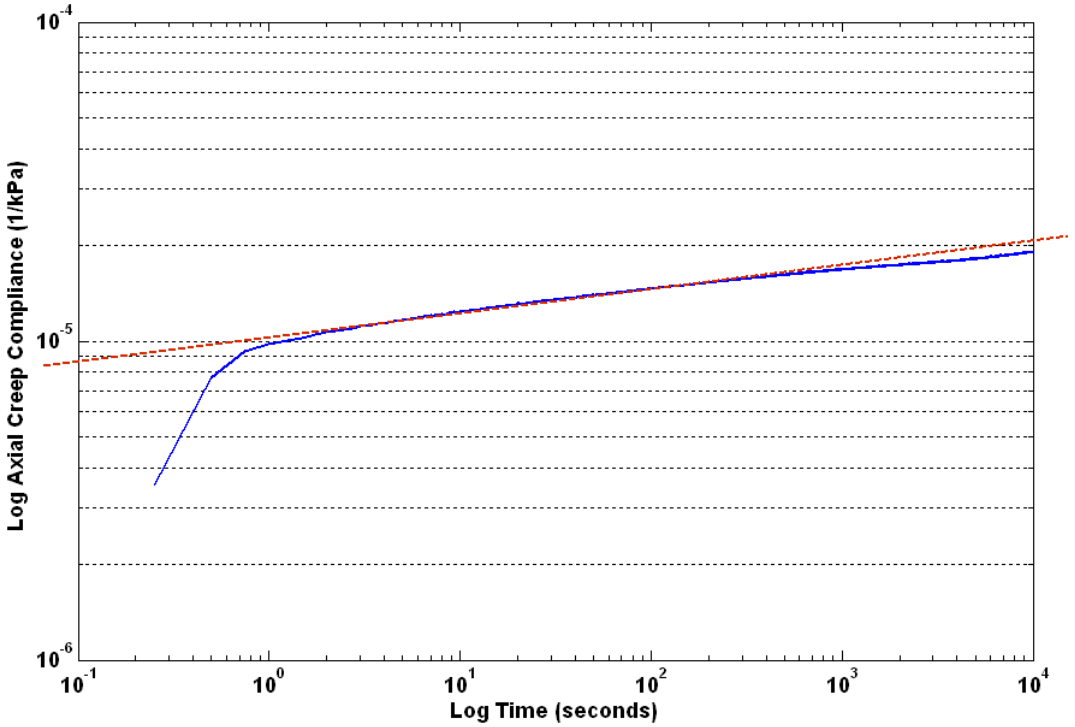

Figure A.8 Axial Creep Compliance versus Loading Time; Mixture Type HL Superpave-C

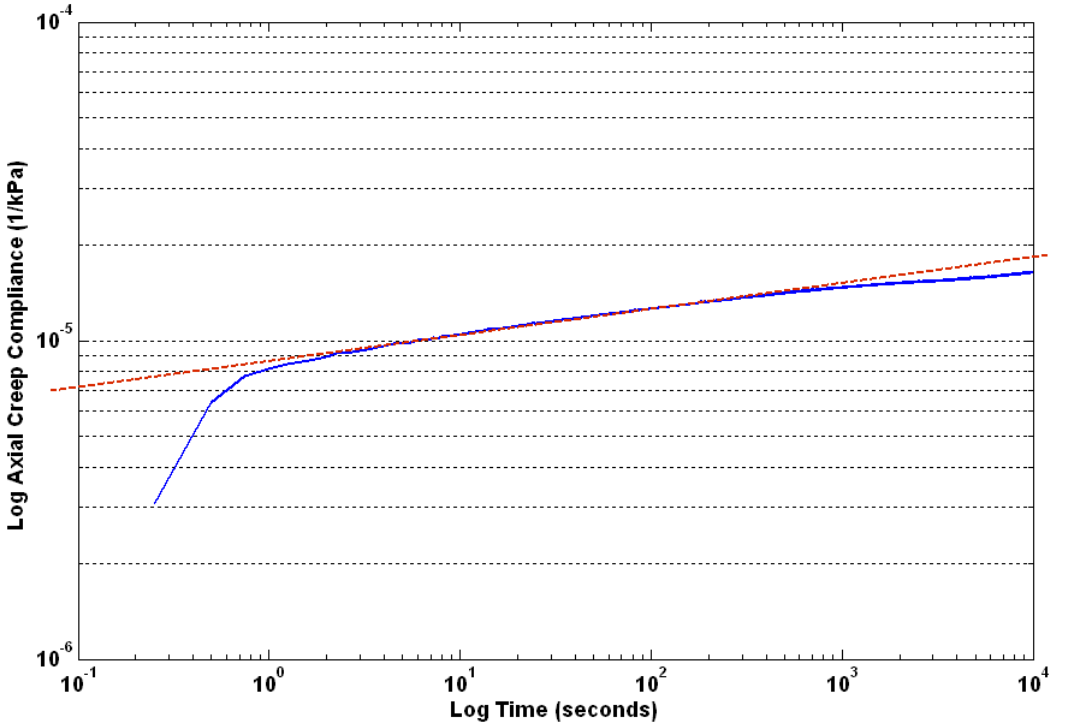

Figure A.9 Axial Creep Compliance versus Loading Time; Mixture Type G Superpave-C

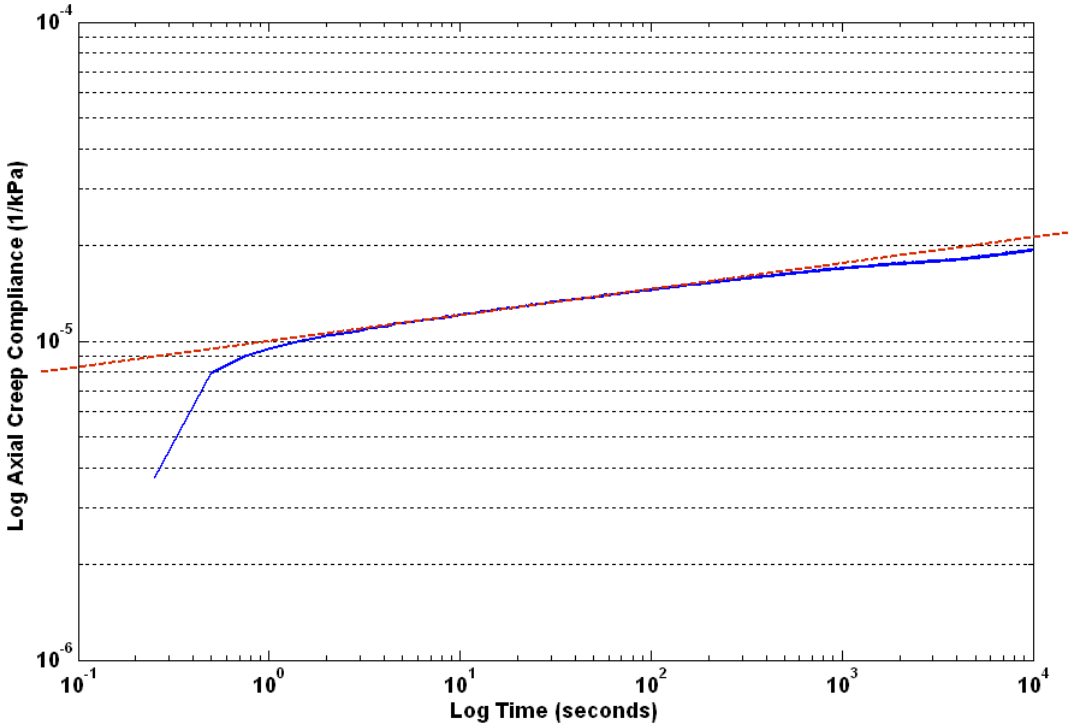

Figure A.10 Axial Creep Compliance versus Loading Time; Mixture Type SL Superpave-C

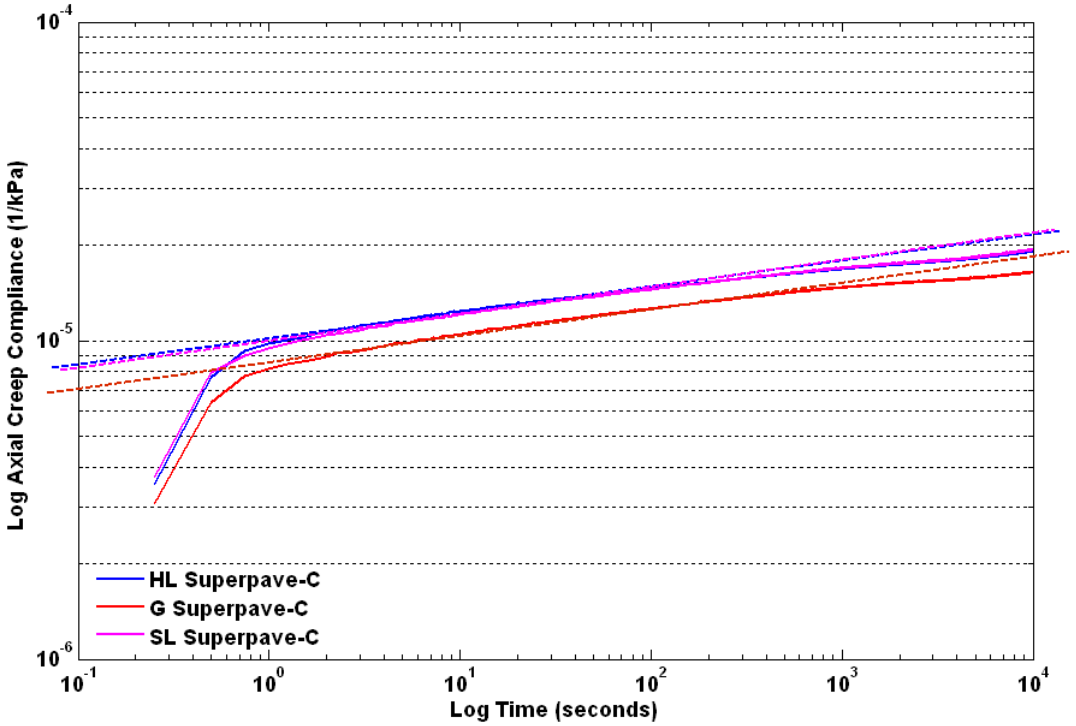

Figure A.11 Axial Creep Compliance versus Loading Time; Mixture Type Superpave-C

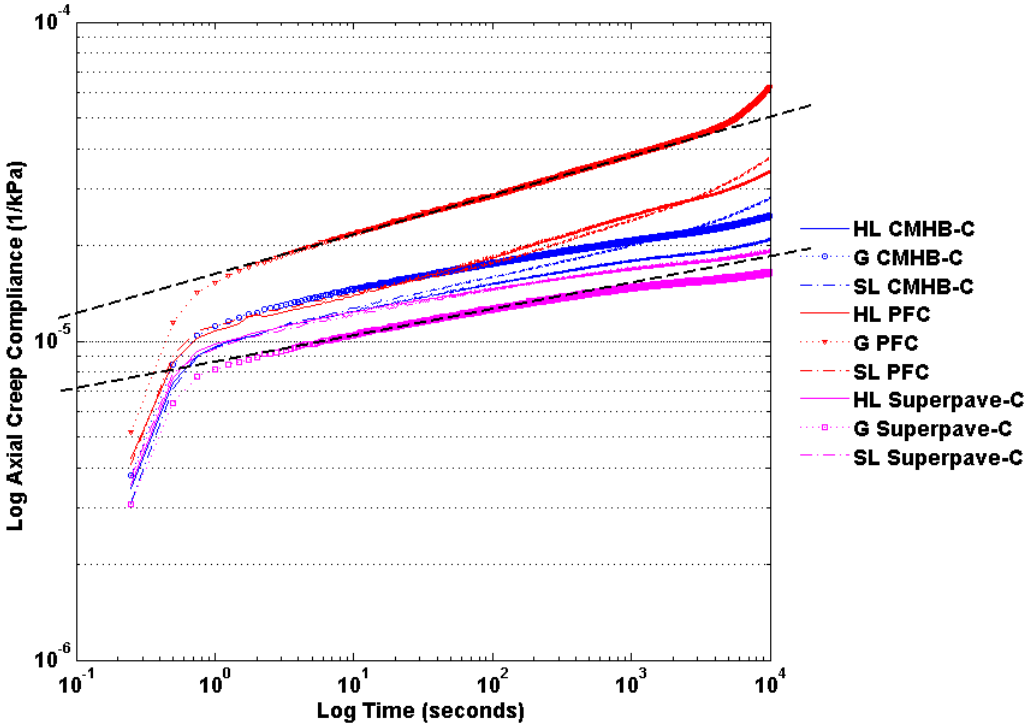

Figure A.12 Axial Creep Compliance versus Loading Time

Appendix B

VOLUMETRICS-BASED GLOBAL MINIMA (VGM) THRESHOLDING ALGORITHM OUTPUTS

B.1 Characterization of Gray Scale Boundary Threshold of AC Microstructure

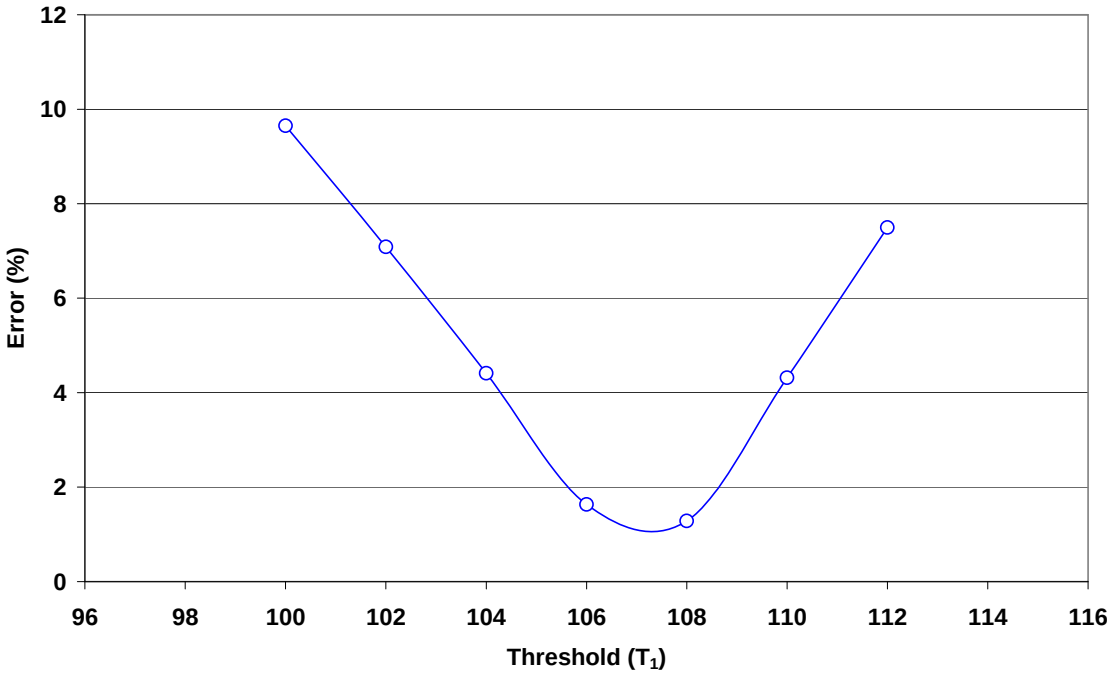

Figure B.1 Air Void-Mastic Boundary Threshold (T_1 = 107); G CMHB-C

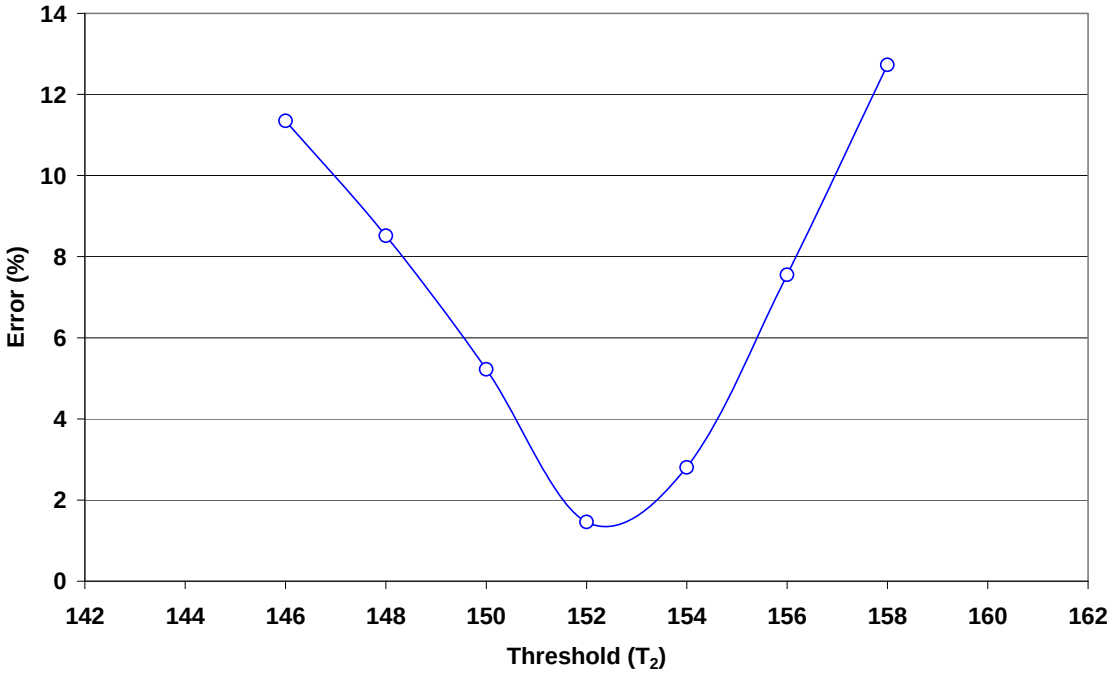

Figure B.2 Mastic-Aggregate Boundary Threshold (T_2 = 153); G CMHB-C

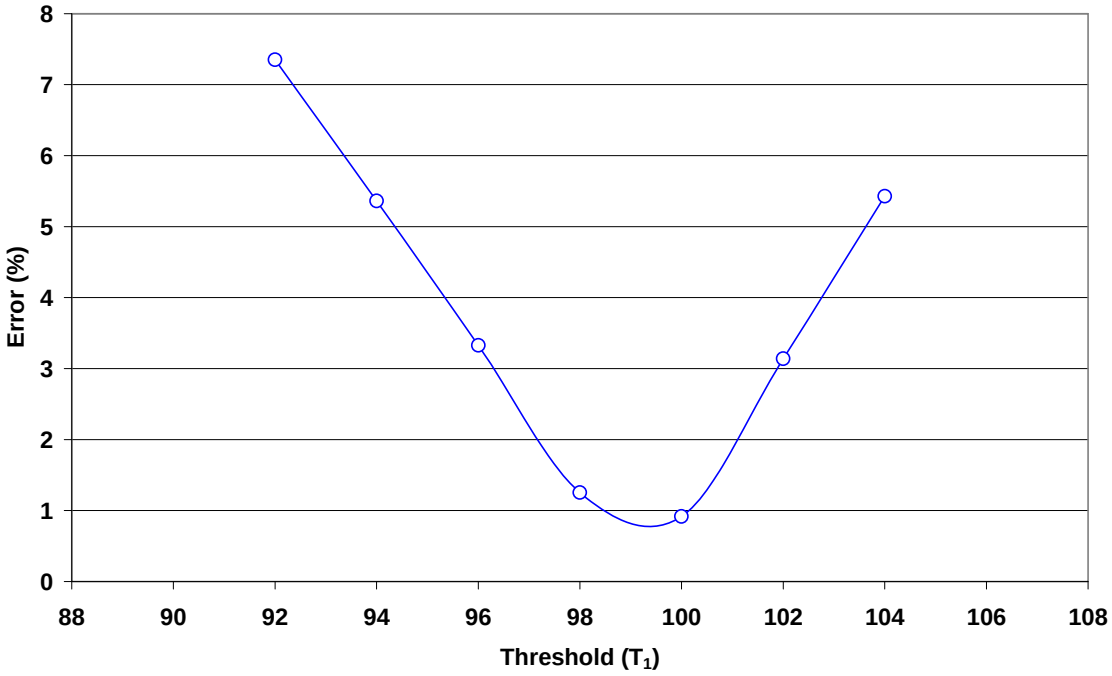

Figure B.3 Air Void-Mastic Boundary Threshold (T_1 = 99); SL CMHB-C

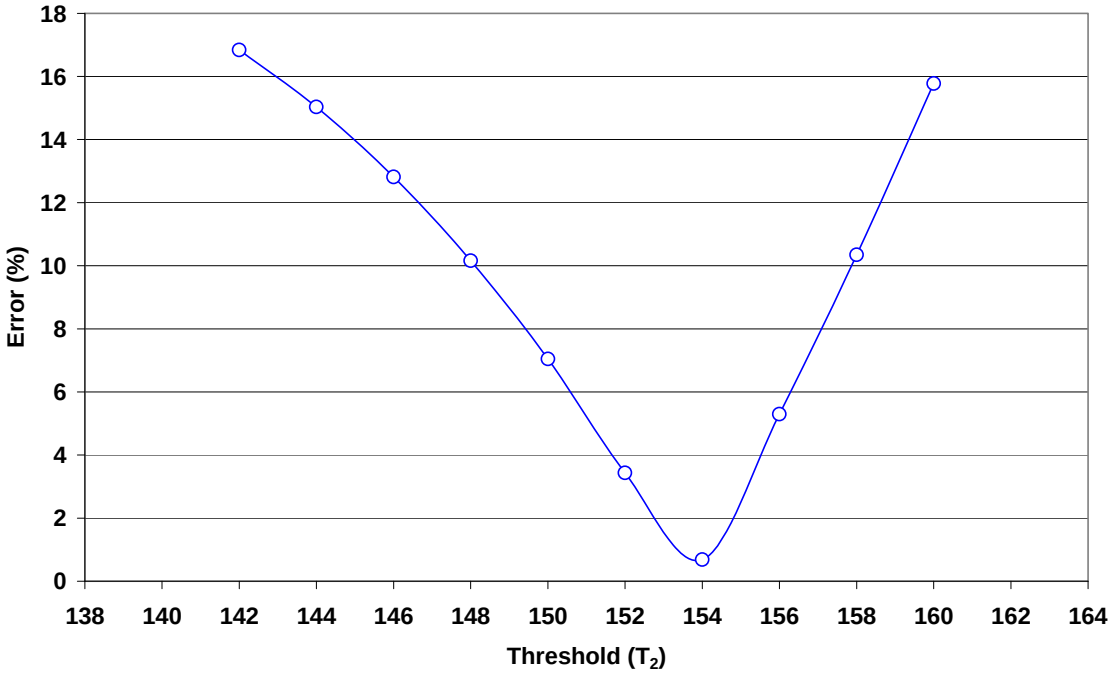

Figure B.4 Mastic-Aggregate Boundary Threshold (T_2 = 154); SL CMHB-C

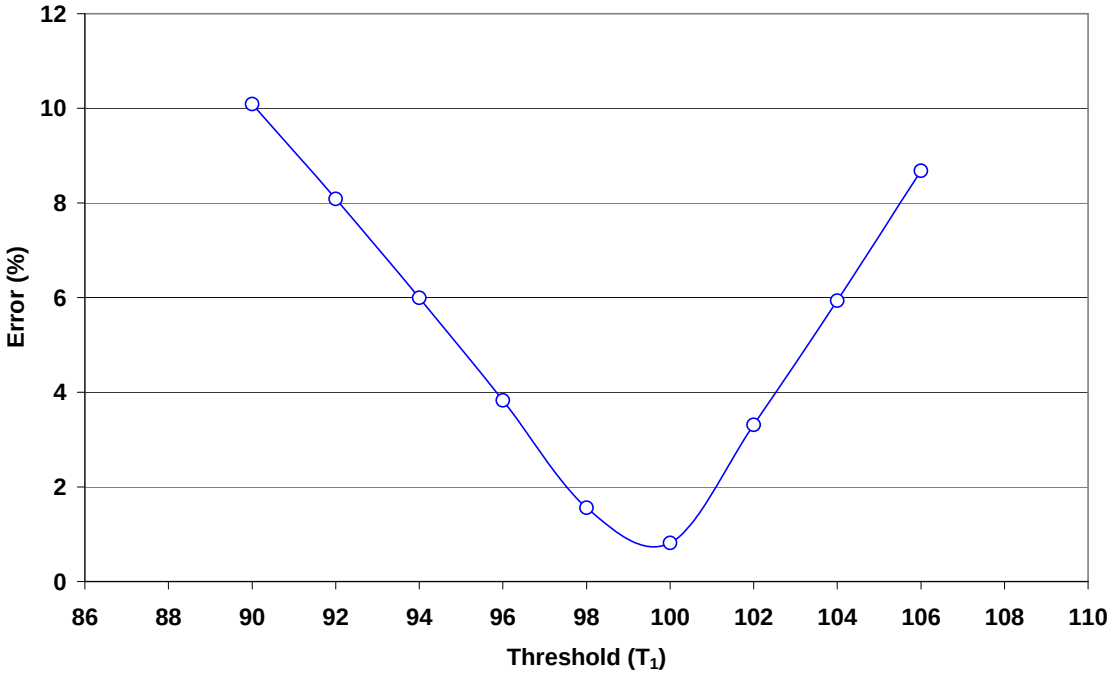

Figure B.5 Air Void-Mastic Boundary Threshold (T_1 = 99); HL PFC

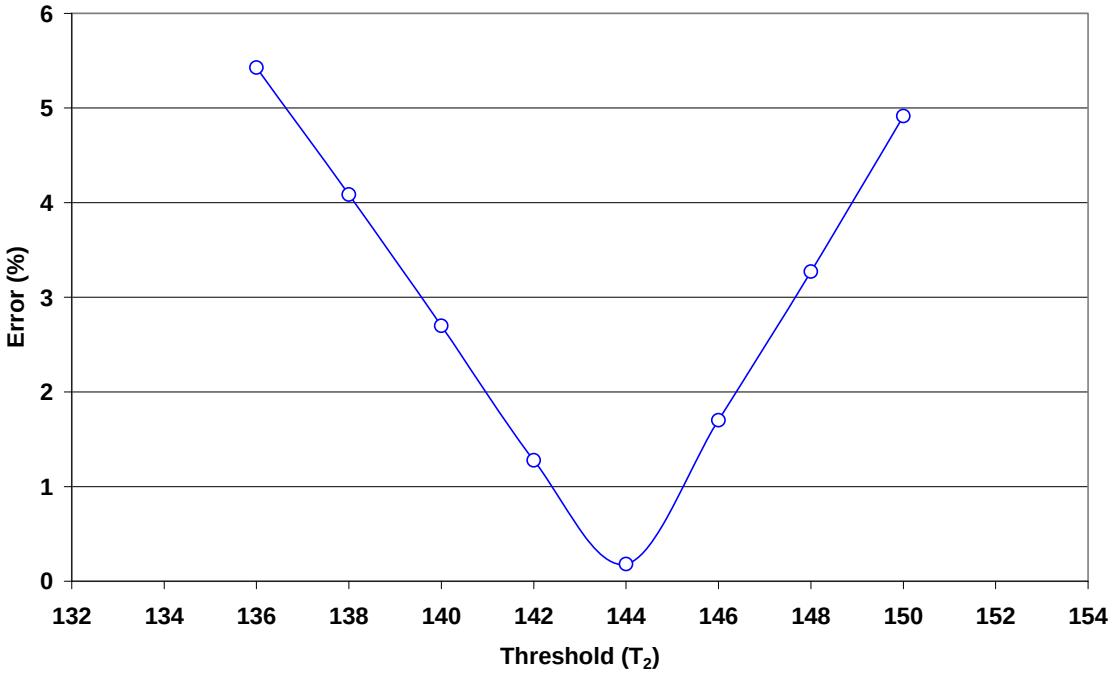

Figure B.6 Mastic-Aggregate Boundary Threshold (T_2 = 144); HL PFC

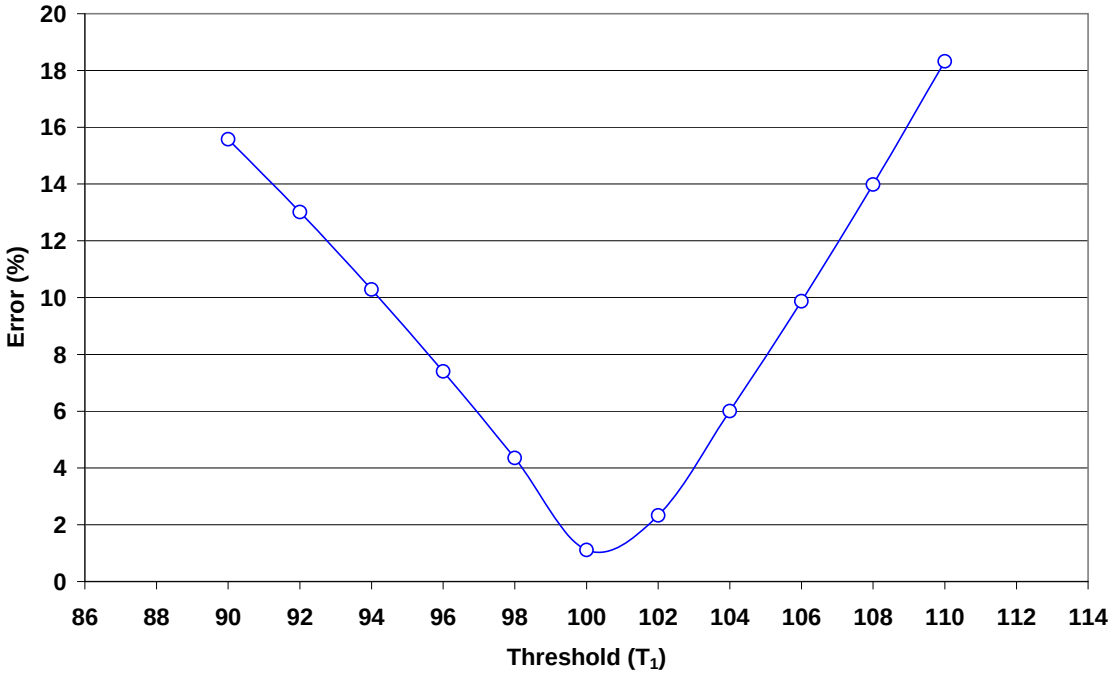

Figure B.7 Air Void-Mastic Boundary Threshold (T_1 = 101); G PFC

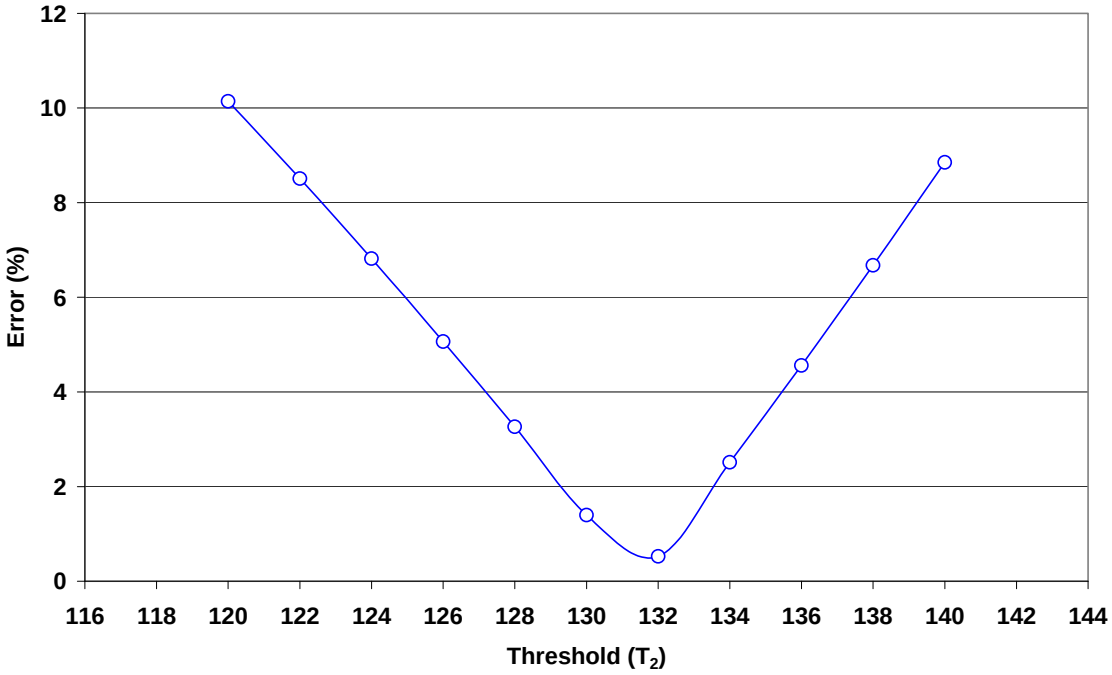

Figure B.8 Mastic-Aggregate Boundary Threshold (T_2 = 132); G PFC

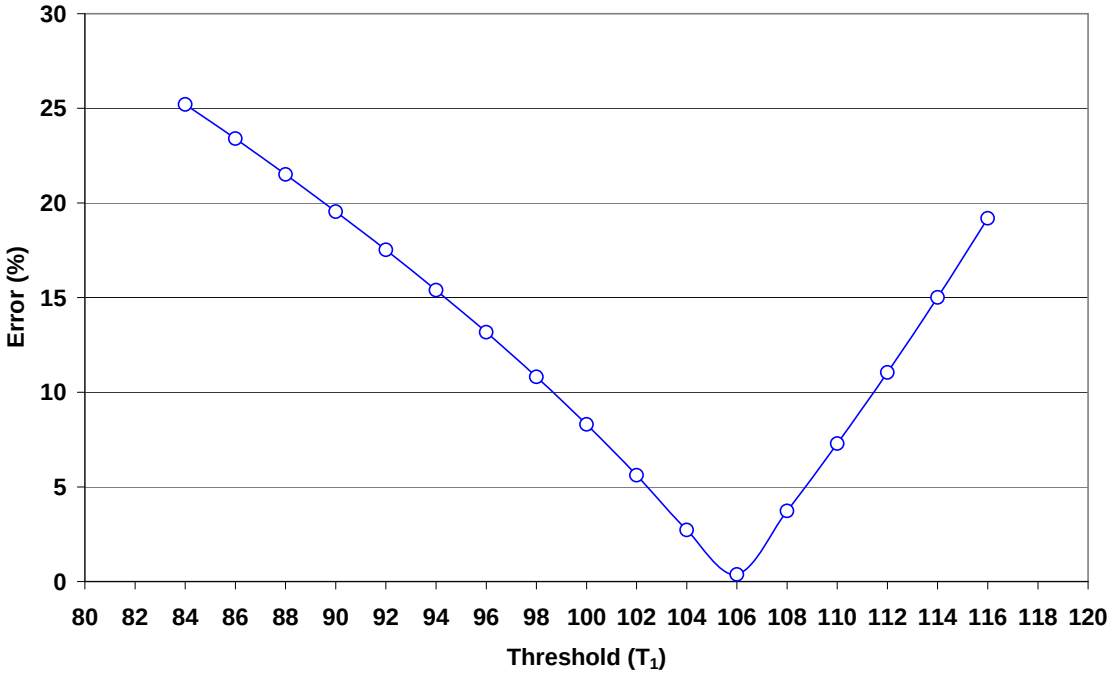

Figure B.9 Air Void-Mastic Boundary Threshold (T_1 = 106); SL PFC

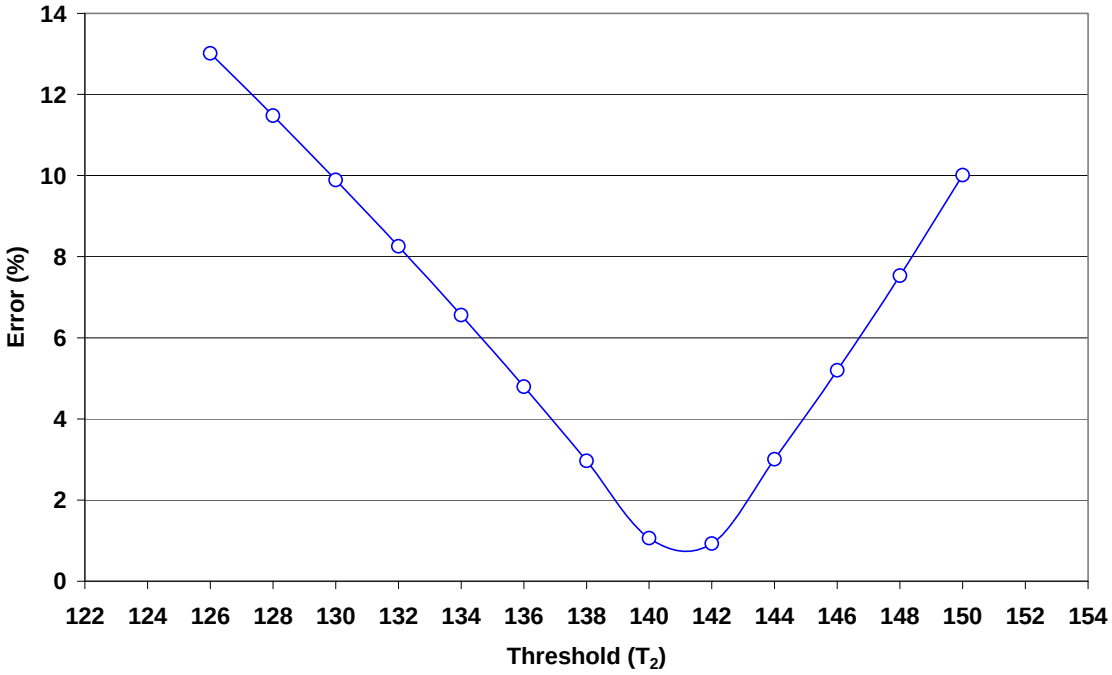

Figure B.10 Mastic-Aggregate Boundary Threshold (T_2 = 141); SL PFC

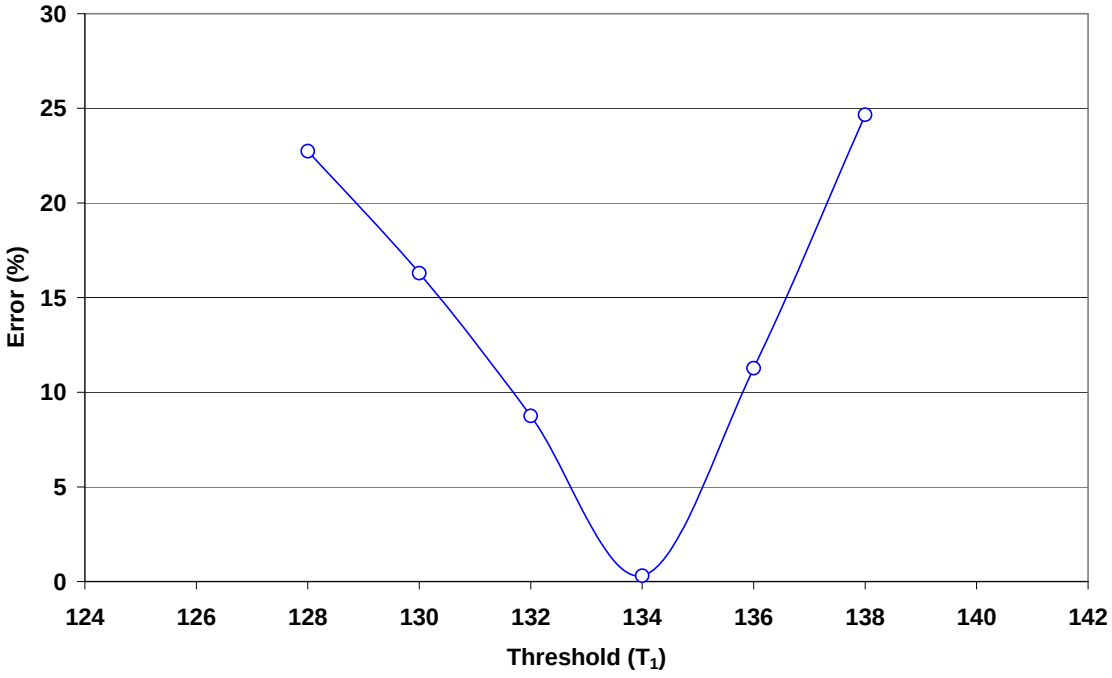

Figure B.11 Air Void-Mastic Boundary Threshold (T_1 = 134); HL Superpave-C

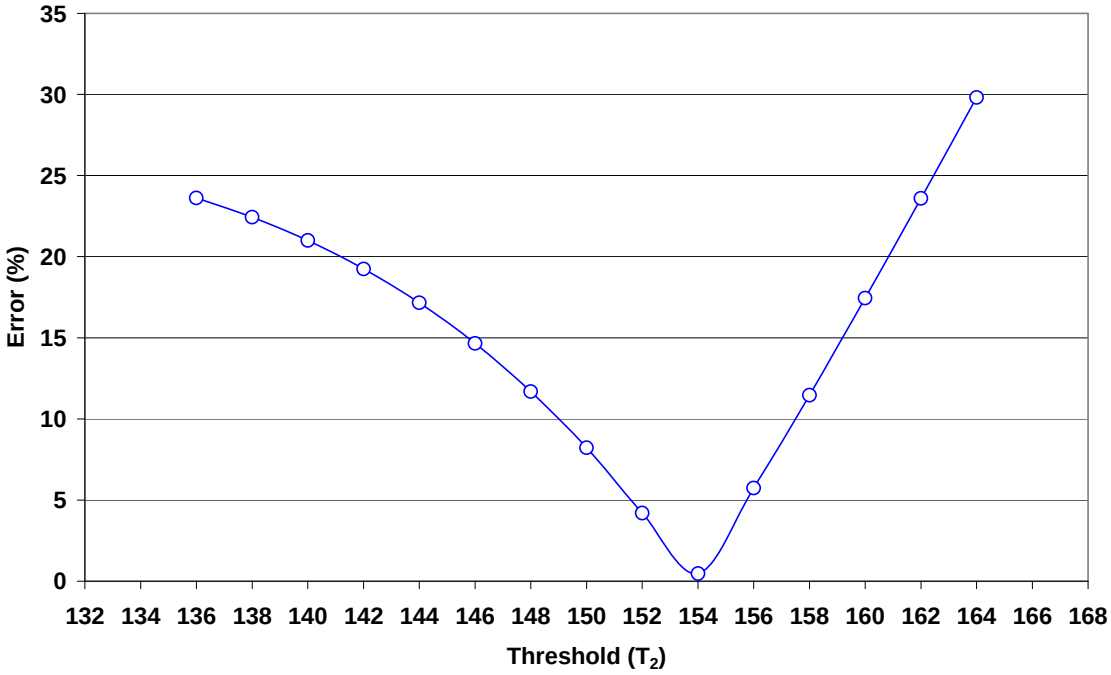

Figure B.12 Mastic-Aggregate Boundary Threshold (T_2 = 154); HL Superpave-C

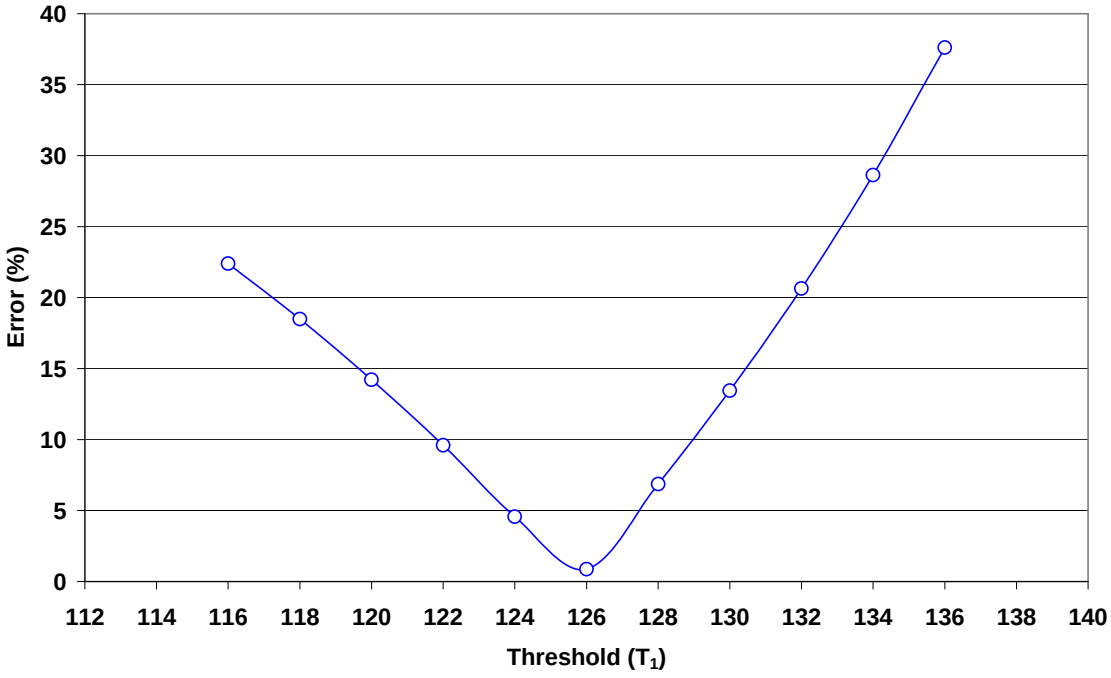

Figure B.13 Air Void-Mastic Boundary Threshold (T_1 = 126); G Superpave-C

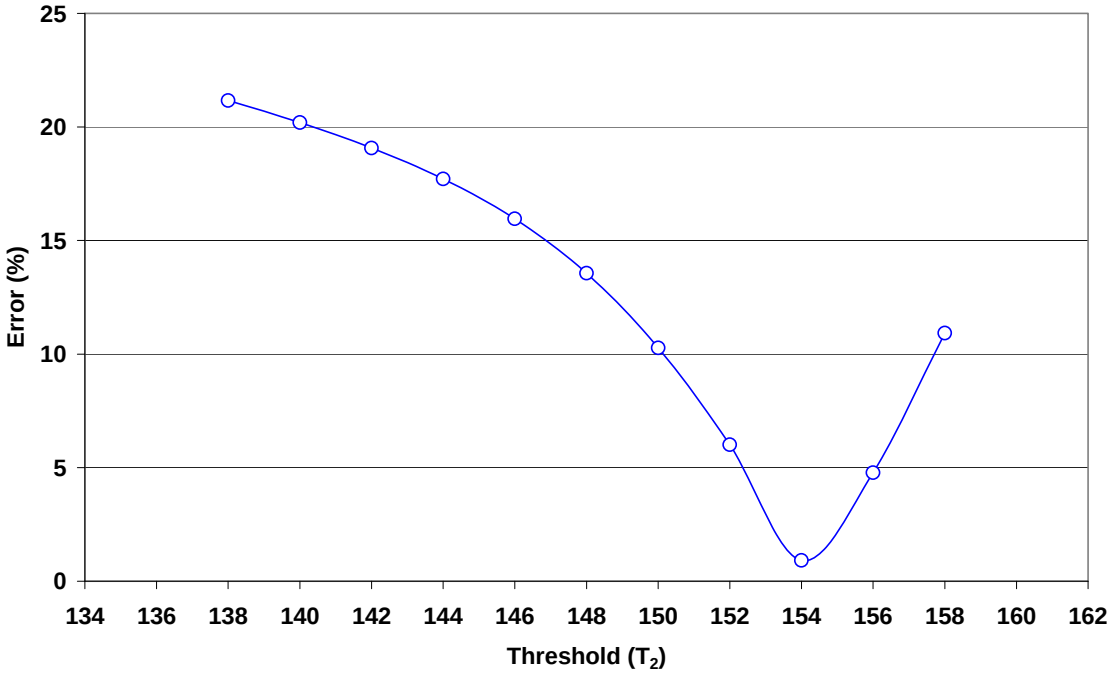

Figure B.14 Mastic-Aggregate Boundary Threshold (T_2 = 154); G Superpave-C

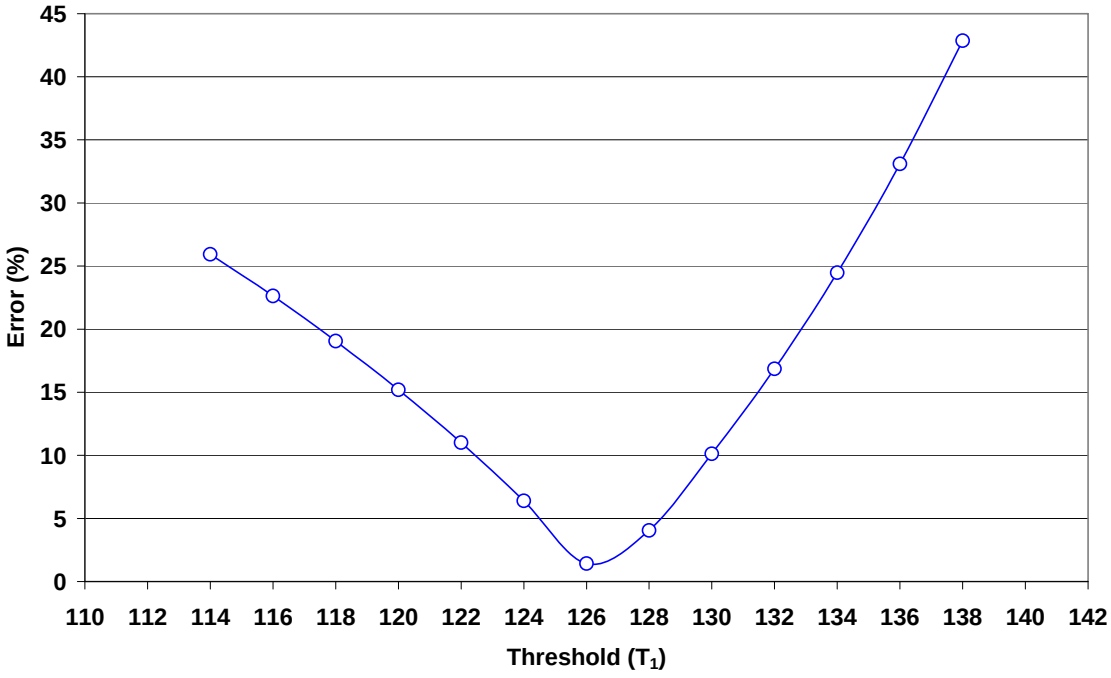

Figure B.15 Air Void-Mastic Boundary Threshold (T_1 = 126); SL Superpave-C

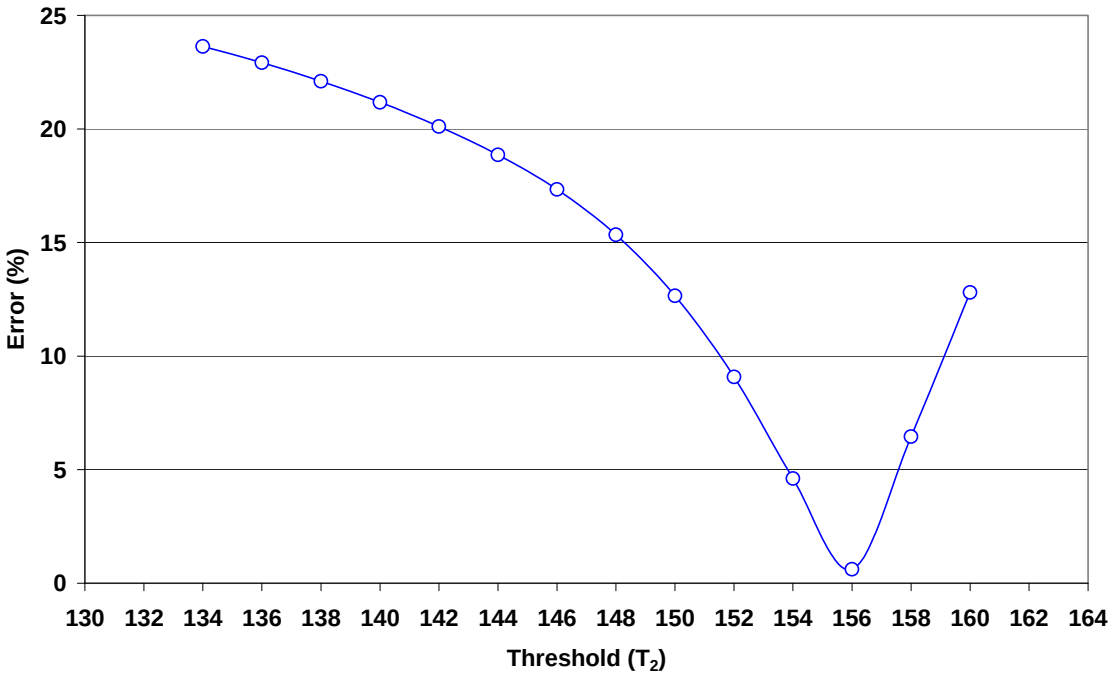

Figure B.16 Mastic-Aggregate Boundary Threshold (T_2 = 156); SL Superpave-C

B.2 Characterization AC Microstructure Distribution

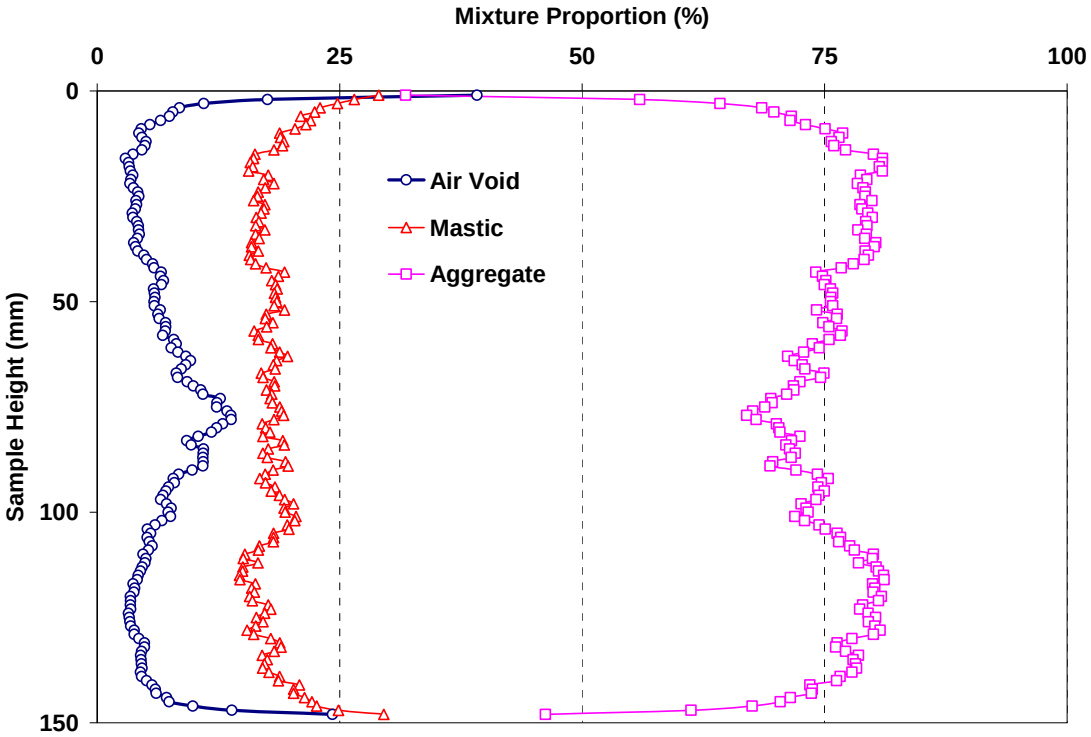

Figure B.17 Distribution of Air Void, Mastic, and Coarse Aggregate; G CMHB-C

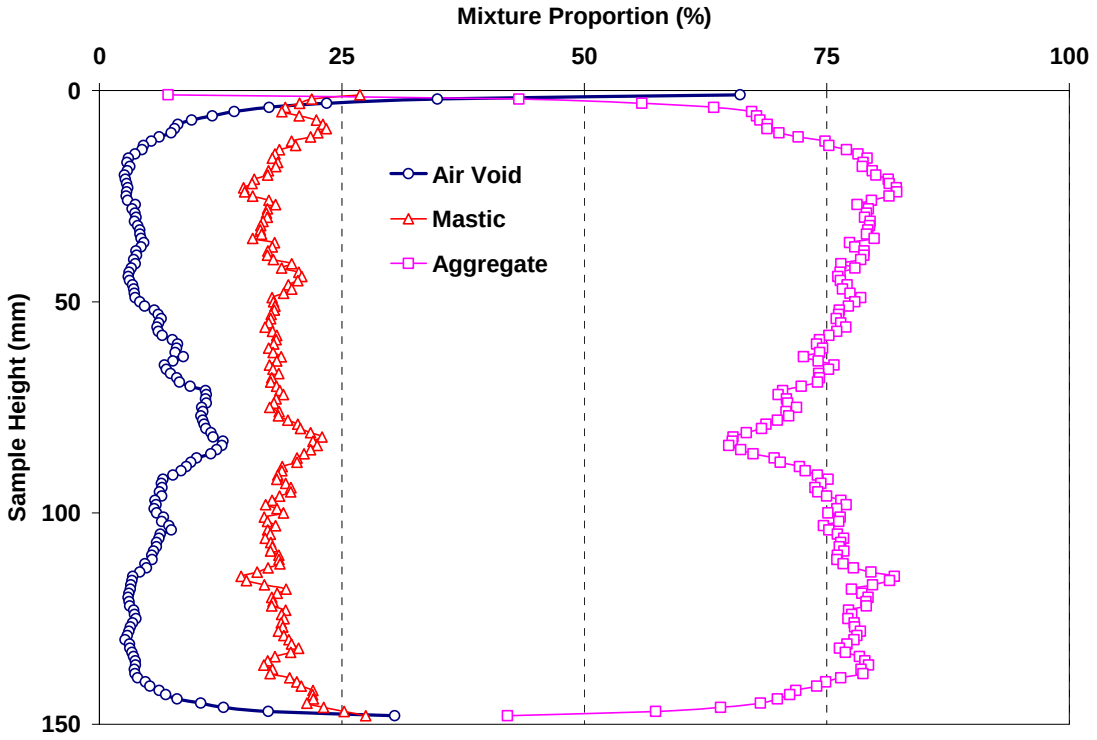

Figure B.18 Distribution of Air Void, Mastic, and Coarse Aggregate; SL CMHB-C

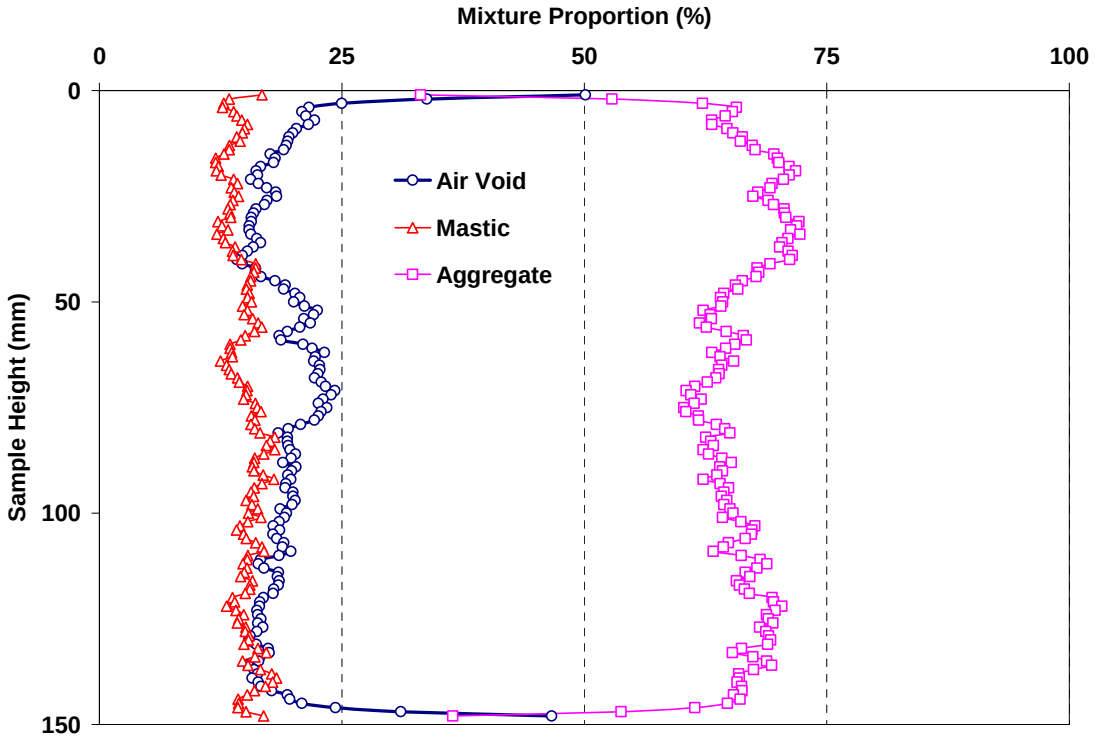

Figure B.19 Distribution of Air Void, Mastic, and Coarse Aggregate; HL PFC

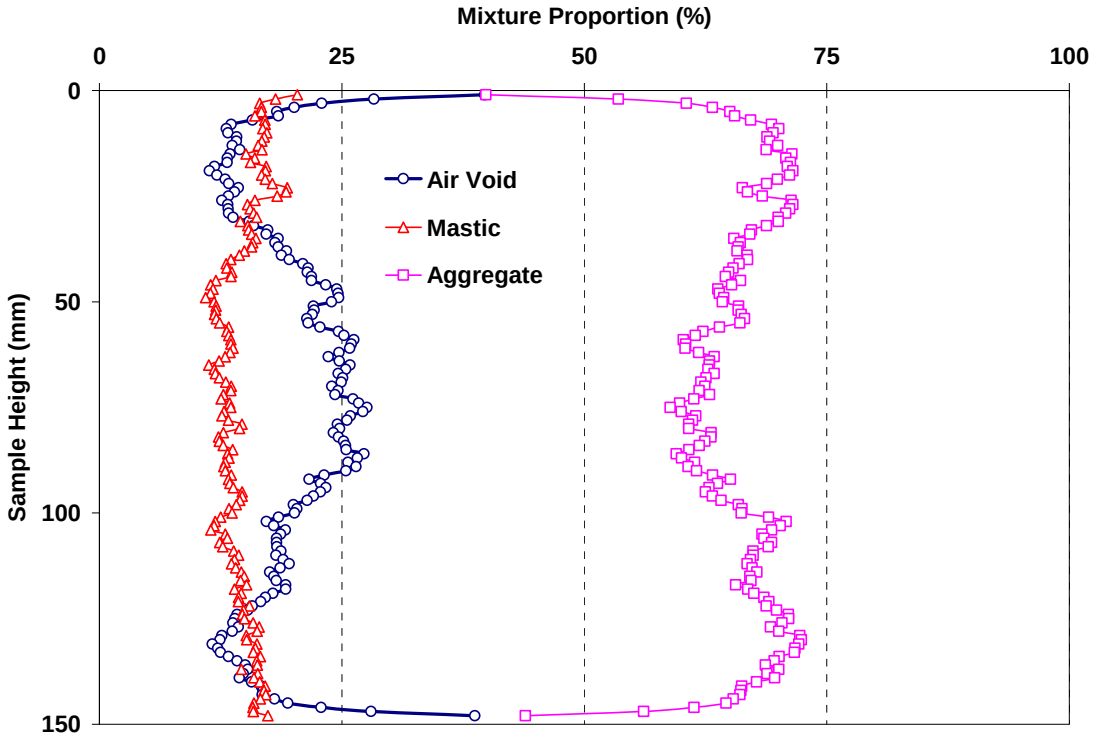

Figure B.20 Distribution of Air Void, Mastic, and Coarse Aggregate; G PFC

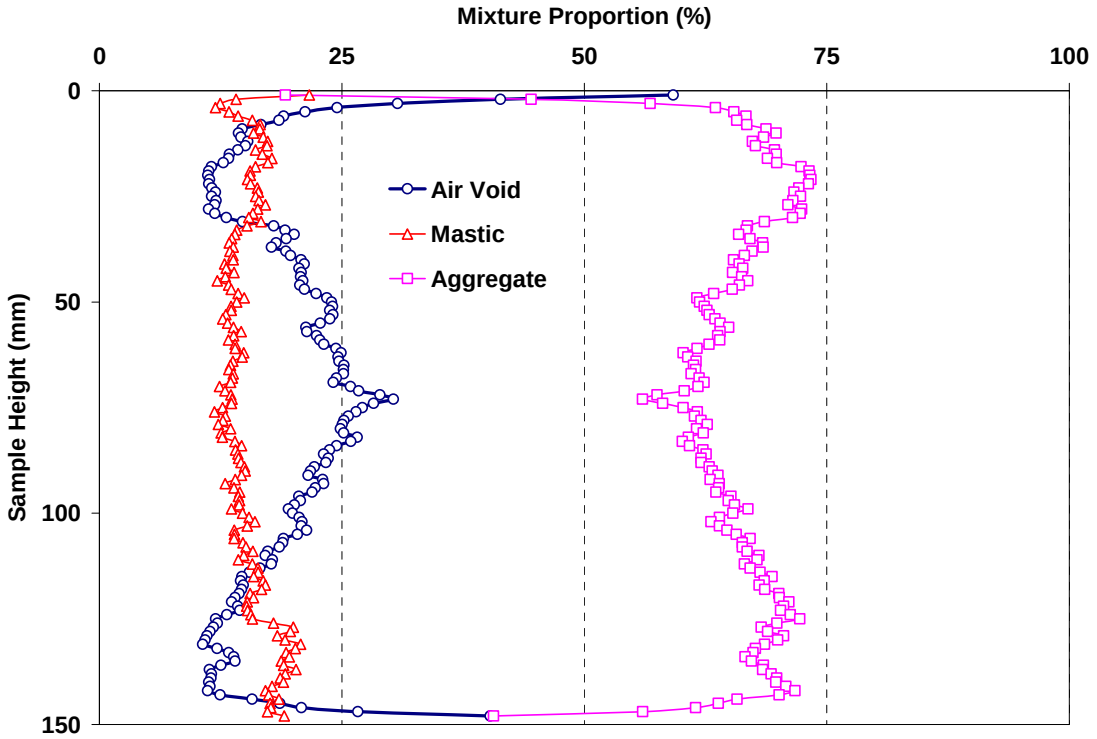

Figure B.21 Distribution of Air Void, Mastic, and Coarse Aggregate; SL PFC

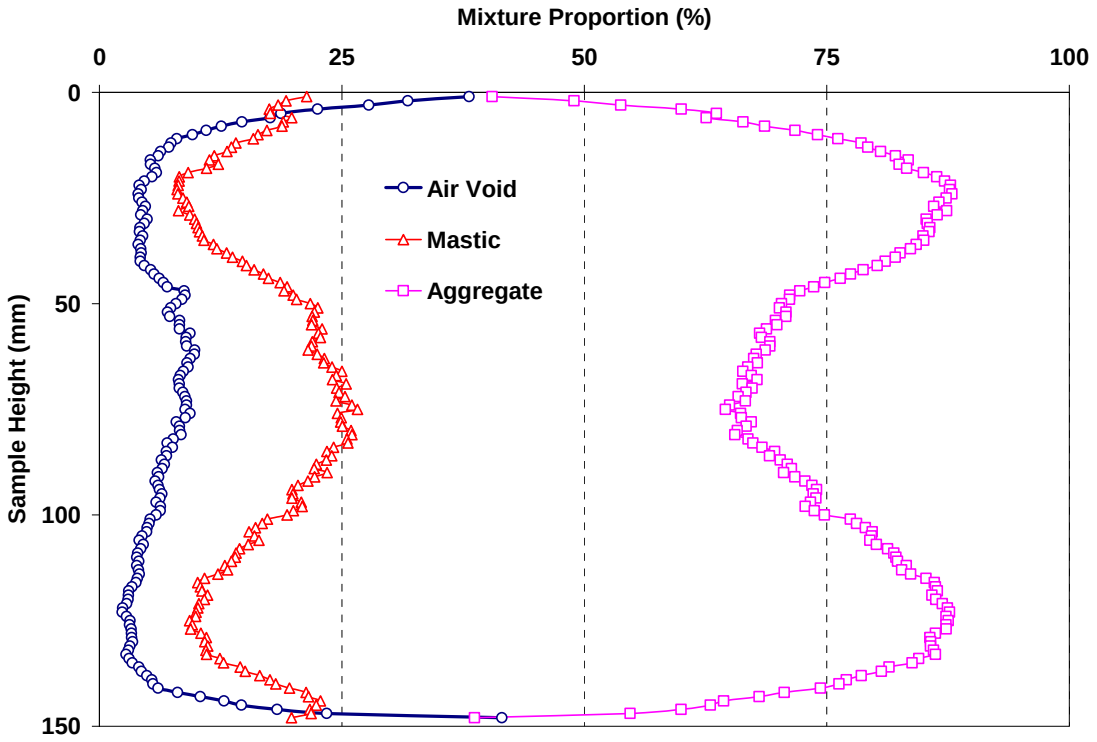

Figure B.22 Distribution of Air Void, Mastic, and Coarse Aggregate; HL Superpave-C

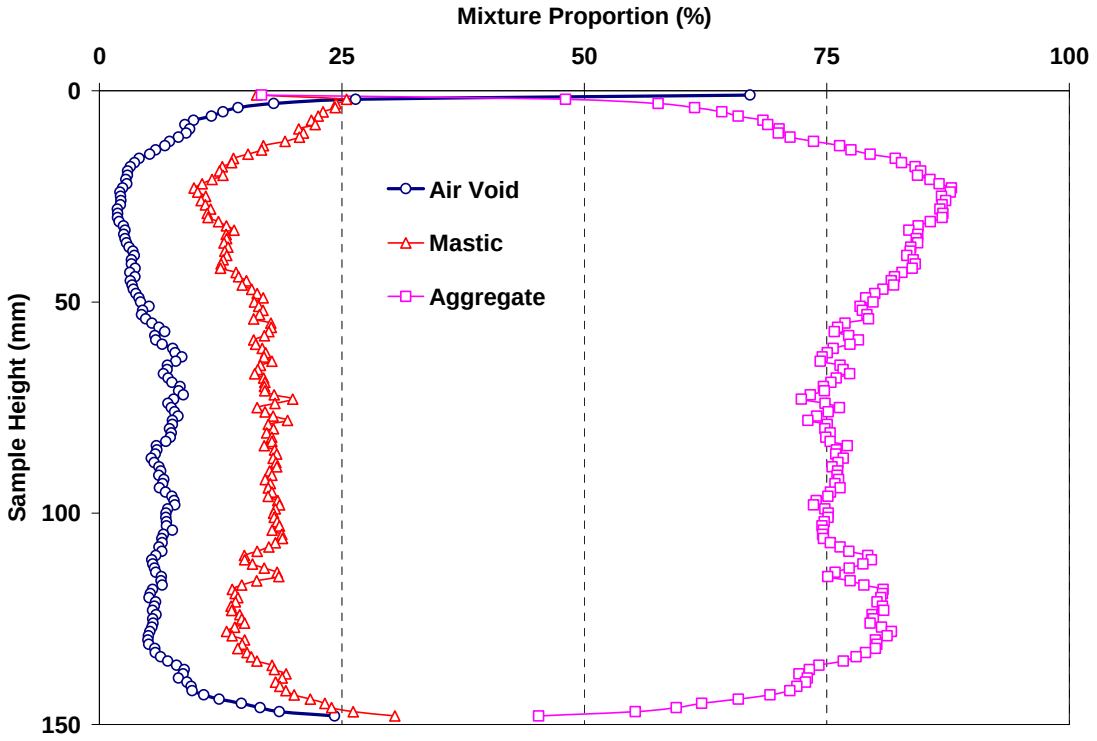

Figure B.23 Distribution of Air Void, Mastic, and Coarse Aggregate; G Superpave-C

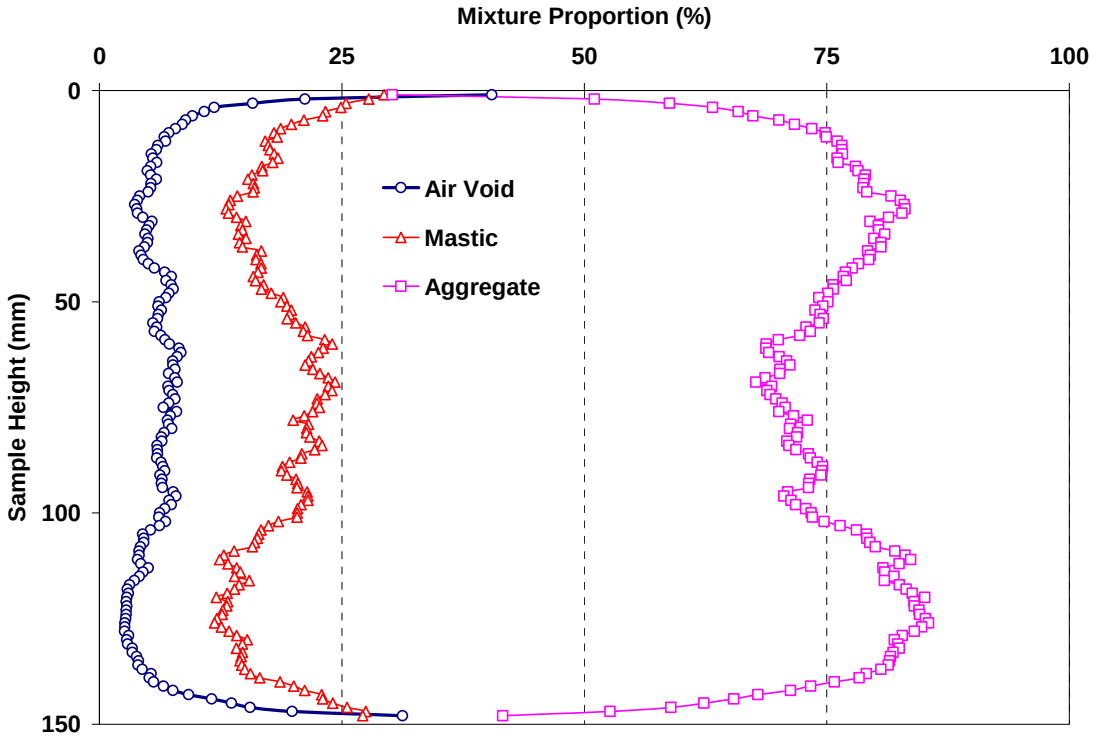

Figure B.24 Distribution of Air Void, Mastic, and Coarse Aggregate; SL Superpave-C

B.3 Two-Dimensional Representation of AC Mixtures

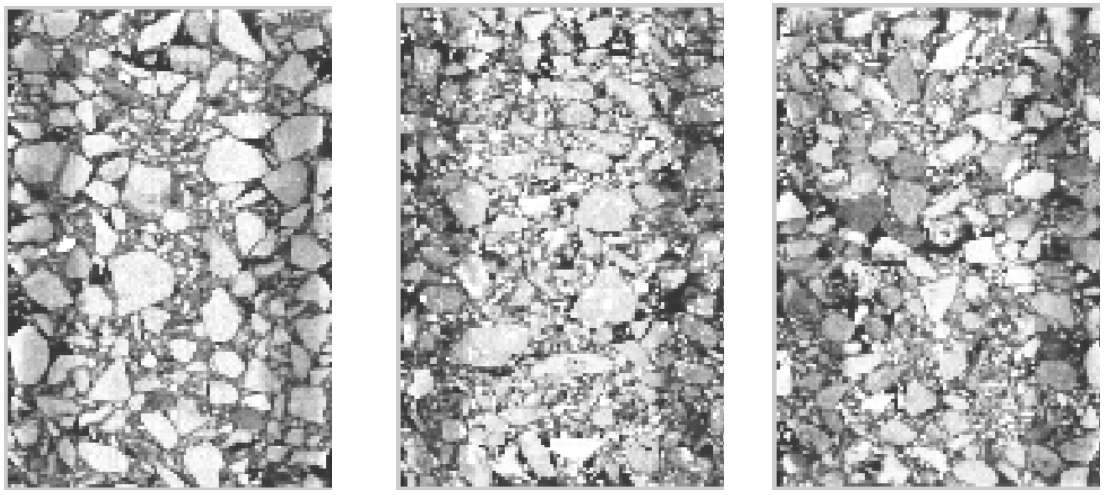

(a) (b) (c)

Figure B.25 Representation of Processed AC Rectangular Sections; (a) HL CMHB-C, (b) G CMHB-C, and (c) SL CMHB-C

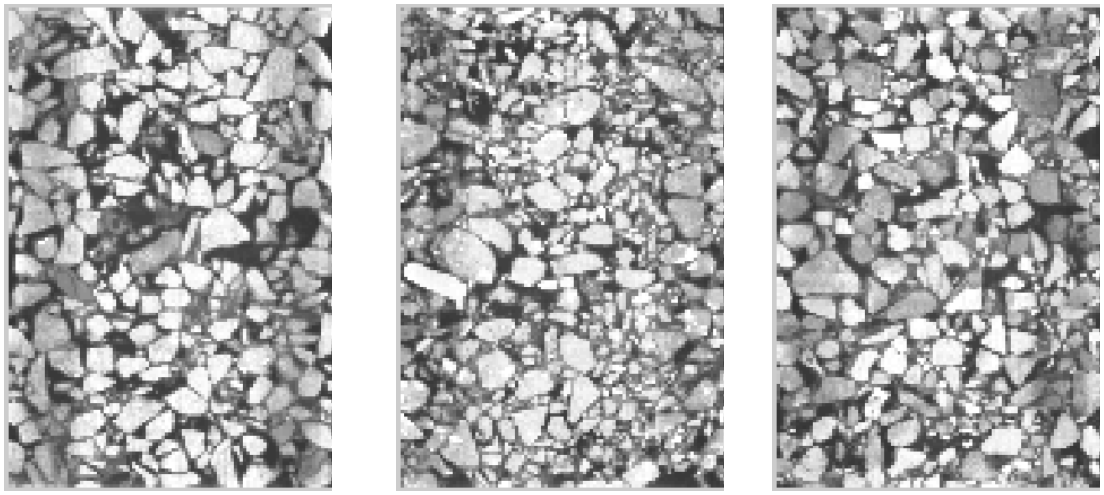

(a) (b) (c)

Figure B.26 Representation of Processed AC Rectangular Sections; (a) HL PFC, (b) G PFC, and (c) SL PFC

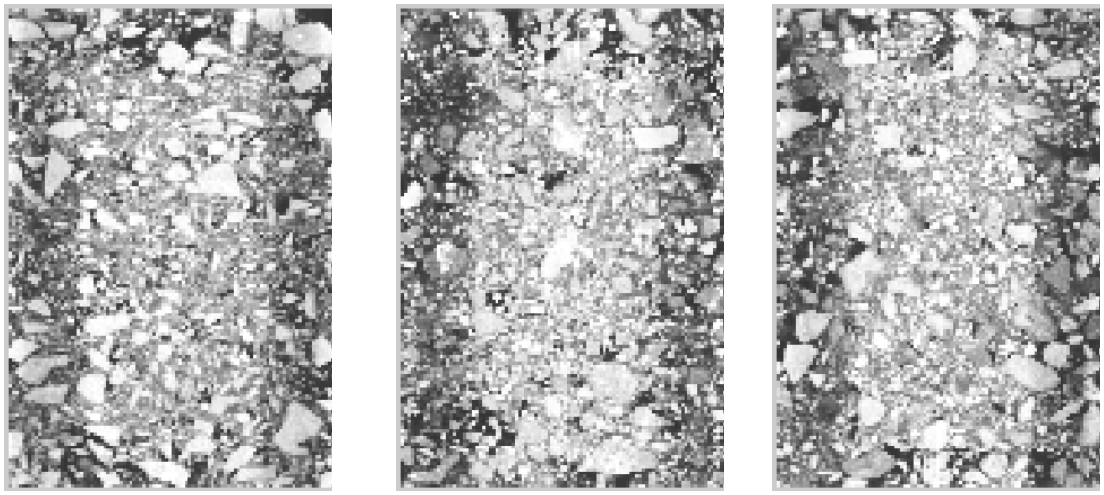

(a) (b) (c)

Figure B.27 Representation of Processed AC Rectangular Sections;

(a) HL Superpave-C, (b) G Superpave-C, and (c) SL Superpave-C

B.4 Processing Two-Dimensional AC Mixtures

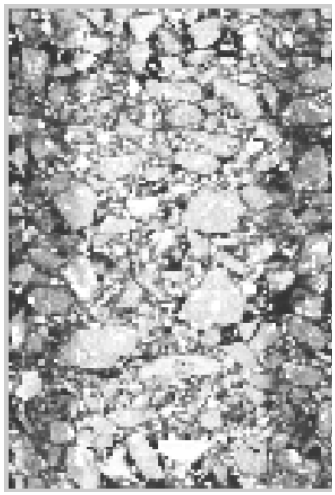
(a)


(b)


(c)

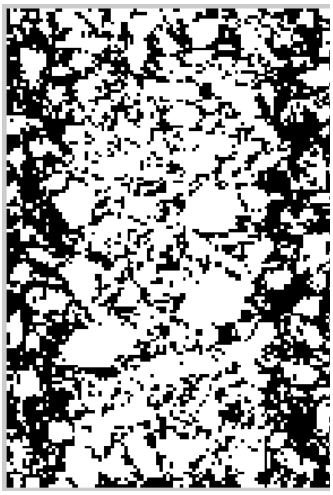
(d)

Figure B.28 Representation of AC Rectangular Sections (a) Processed Image, (b) Air Phase in White, (c) Mastic Phase in White, and (d) Aggregate Phase in White; G CMHB-C


(a)

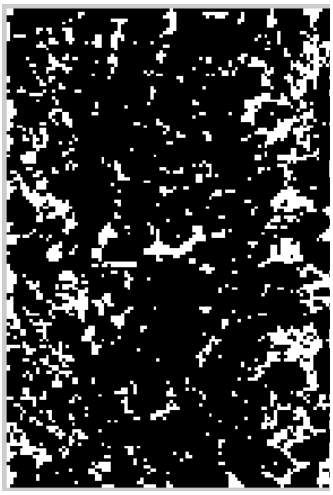
(b)


(c)

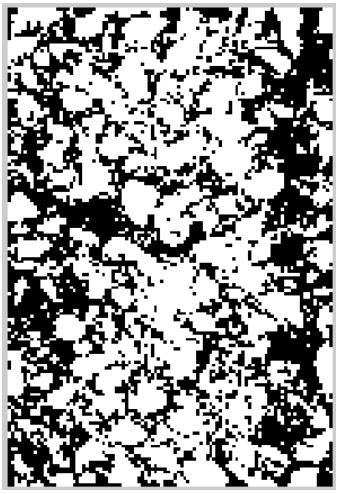
(d)

Figure B.29 Representation of AC Rectangular Sections (a) Processed Image, (b) Air Phase in White, (c) Mastic Phase in White, and (d) Aggregate Phase in White; SL CMHB-C

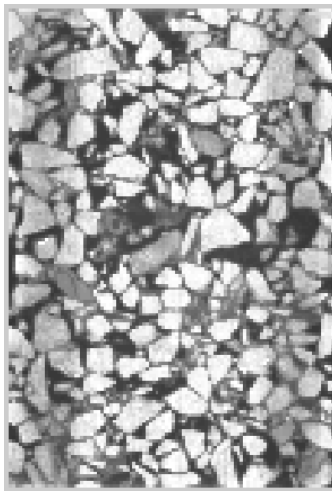
(a)


(b)

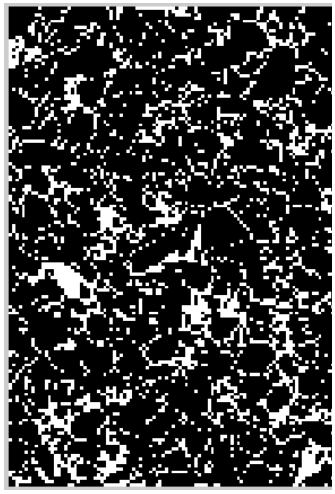
(c)

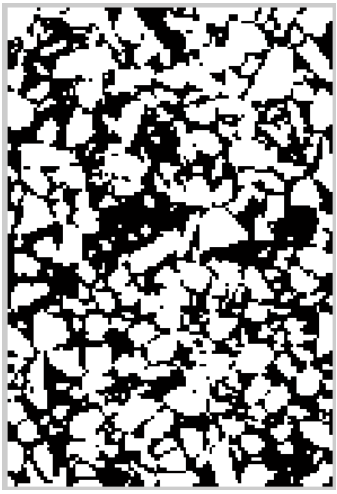
(d)

Figure B.30 Representation of AC Rectangular Sections (a) Processed Image, (b) Air Phase in White, (c) Mastic Phase in White, and (d) Aggregate Phase in White; HL PFC


(a)

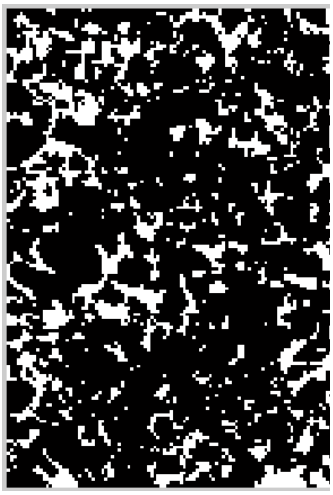
(b)

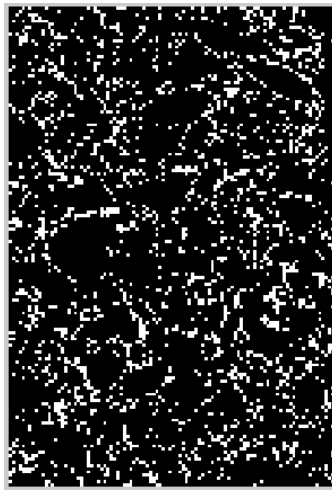
(c)

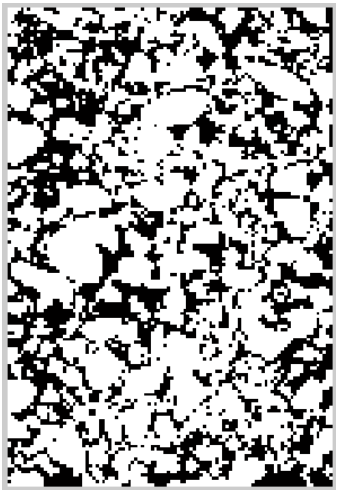
(d)

Figure B.31 Representation of AC Rectangular Sections (a) Processed Image, (b) Air Phase in White, (c) Mastic Phase in White, and (d) Aggregate Phase in White; G PFC

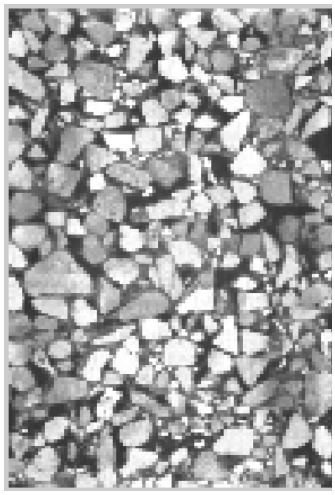
(a)


(b)

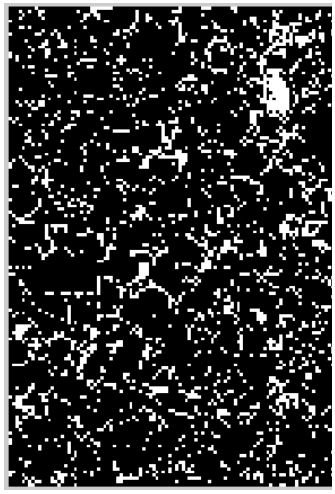
(c)


(d)

Figure B.32 Representation of AC Rectangular Sections (a) Processed Image, (b) Air Phase in White, (c) Mastic Phase in White, and (d) Aggregate Phase in White; SL PFC

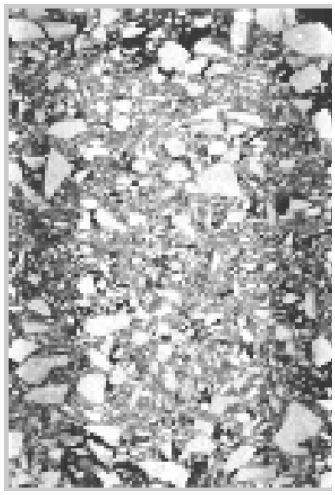
(a)


(b)

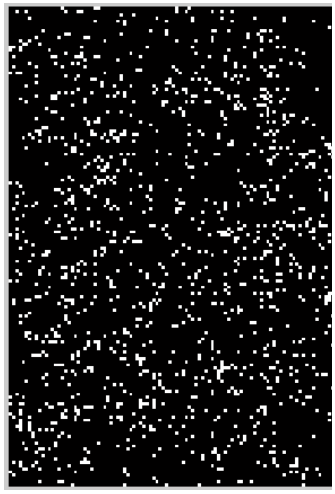
(c)

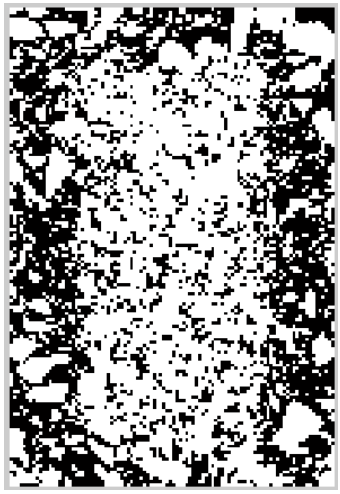
(d)

Figure B.33 Representation of AC Rectangular Sections (a) Processed Image, (b) Air Phase in White, (c) Mastic Phase in White, and (d) Aggregate Phase in White; HL Superpave-C

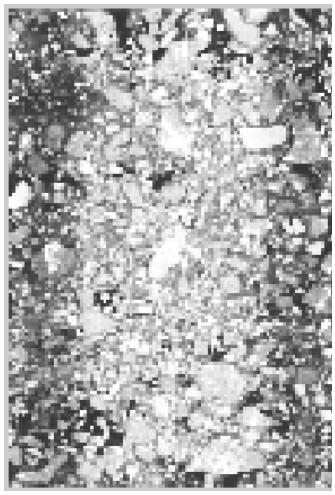
(a)


(b)


(c)


(d)

Figure B.34 Representation of AC Rectangular Sections (a) Processed Image, (b) Air Phase in White, (c) Mastic Phase in White, and (d) Aggregate Phase in White; G Superpave-C


(a)

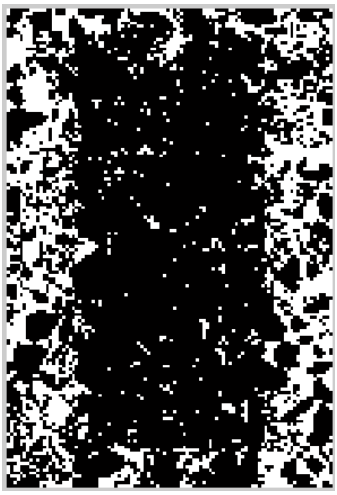
(b)

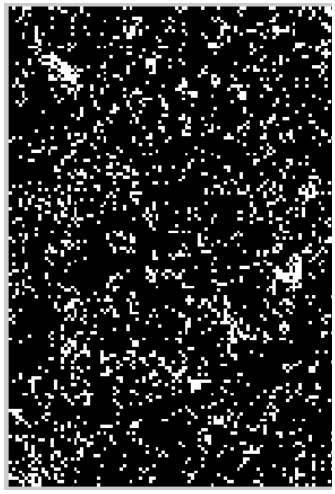
(c)

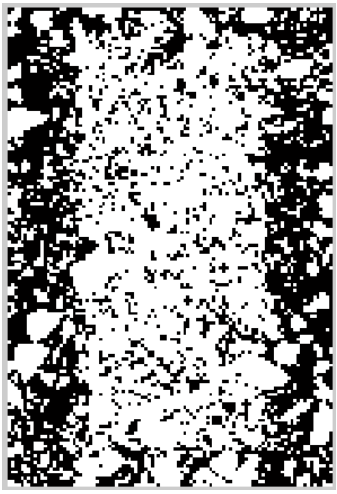
(d)

Figure B.35 Representation of AC Rectangular Sections (a) Processed Image, (b) Air Phase in White, (c) Mastic Phase in White, and (d) Aggregate Phase in White; SL Superpave-C

B.5 Results of Edge Detection and Image Segmentation Techniques

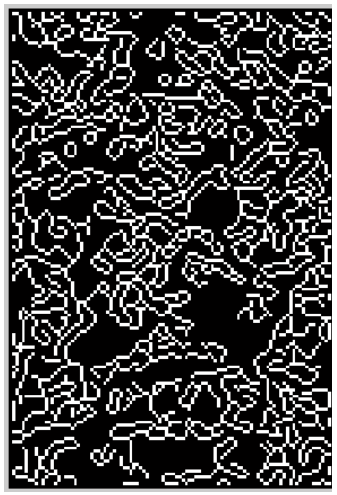
(a)


(b)

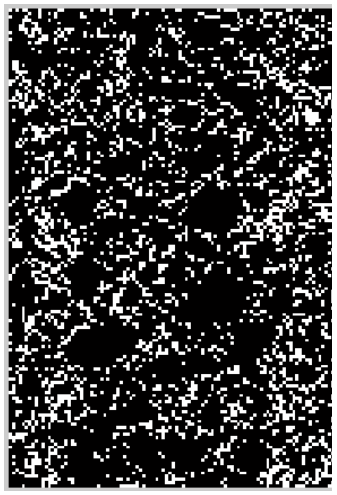
(c)

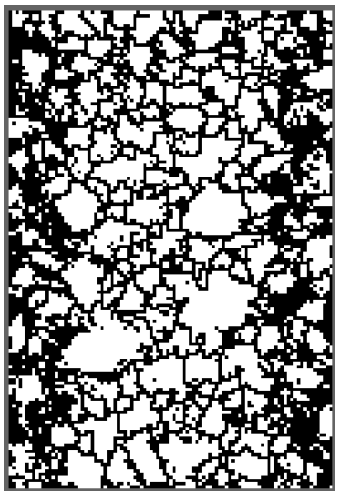
(d)

Figure B.36 Results of Canny Operation (a) Mastic Phase, (b) Aggregate Phase; Results of Watershed Image Segmentation (c) Mastic Phase, (d) Aggregate Phase; G CMHB-C

(a)

(b)

(c)

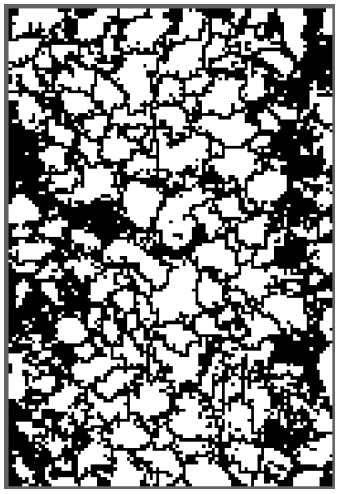

(d)

Figure B.37 Results of Canny Operation (a) Mastic Phase, (b) Aggregate Phase; Results of Watershed Image Segmentation (c) Mastic Phase, (d) Aggregate Phase; SL CMHB-C


(a)


(b)

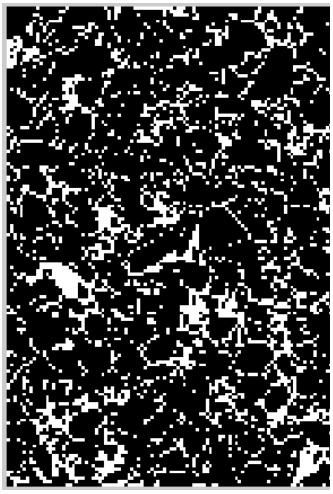
(c)

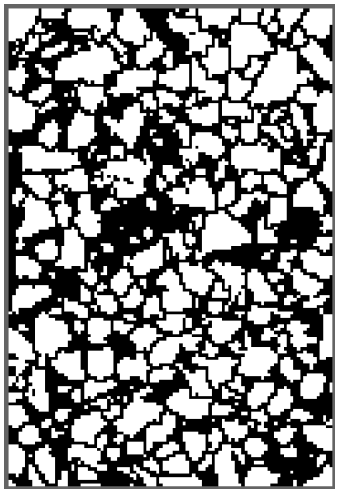
(d)

Figure B.38 Results of Canny Operation (a) Mastic Phase, (b) Aggregate Phase; Results of Watershed Image Segmentation (c) Mastic Phase, (d) Aggregate Phase; HL PFC


(a)

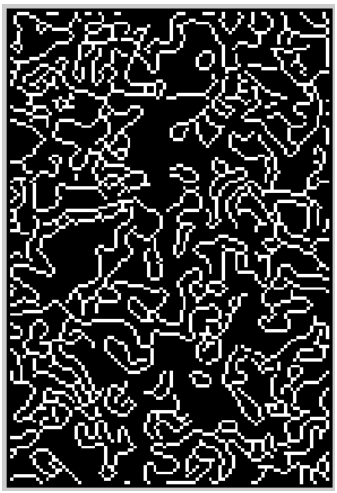
(b)

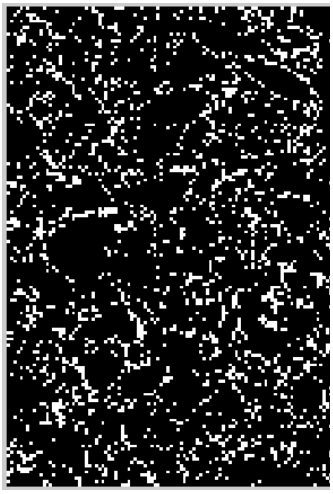
(c)

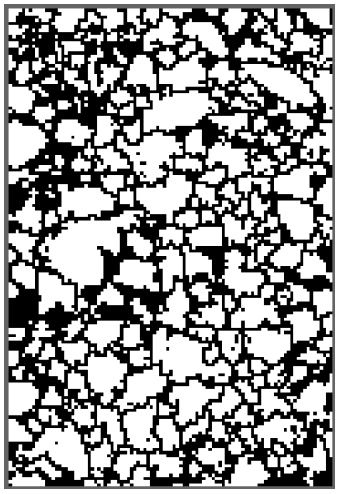
(d)

Figure B.39 Results of Canny Operation (a) Mastic Phase, (b) Aggregate Phase; Results of Watershed Image Segmentation (c) Mastic Phase, (d) Aggregate Phase; G PFC


(a)

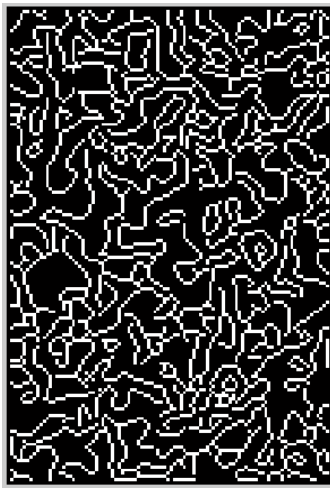
(b)

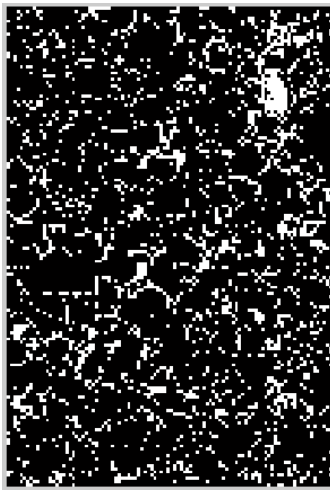
(c)

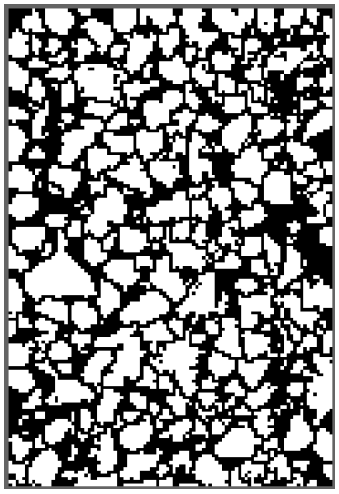
(d)

Figure B.40 Results of Canny Operation (a) Mastic Phase, (b) Aggregate Phase; Results of Watershed Image Segmentation (c) Mastic Phase, (d) Aggregate Phase; SL PFC


(a)


(b)

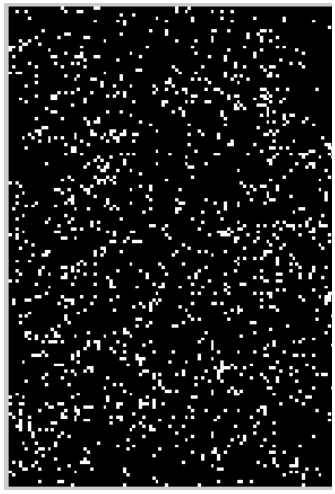
(c)

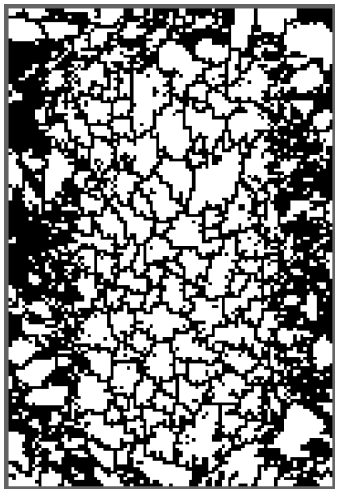
(d)

Figure B.41 Results of Canny Operation (a) Mastic Phase, (b) Aggregate Phase; Results of Watershed Image Segmentation (c) Mastic Phase, (d) Aggregate Phase;
HL Superpave-C

(a)

(b)

(c)

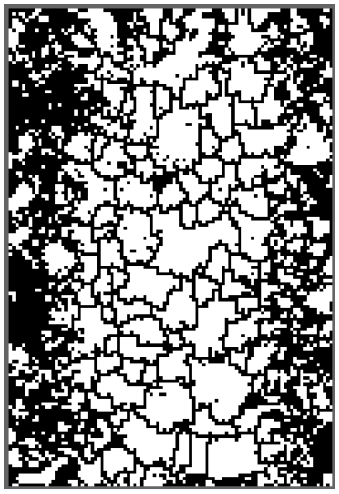

(d)

Figure B.42 Results of Canny Operation (a) Mastic Phase, (b) Aggregate Phase; Results of Watershed Image Segmentation (c) Mastic Phase, (d) Aggregate Phase;
G Superpave-C


(a)


(b)

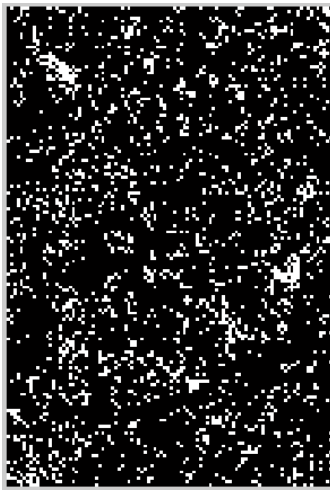
(c)

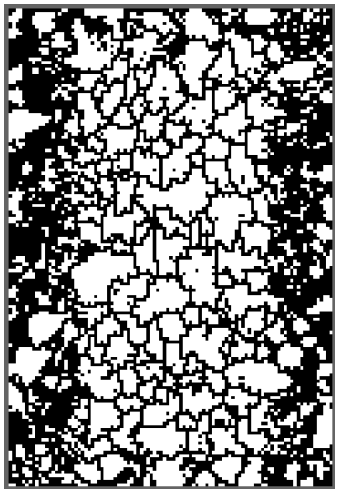
(d)

Figure B.43 Results of Canny Operation (a) Mastic Phase, (b) Aggregate Phase; Results of Watershed Image Segmentation (c) Mastic Phase, (d) Aggregate Phase;
SL Superpave-C

B.6 Realistic Representation of AC Mixtures for DEM Simulation

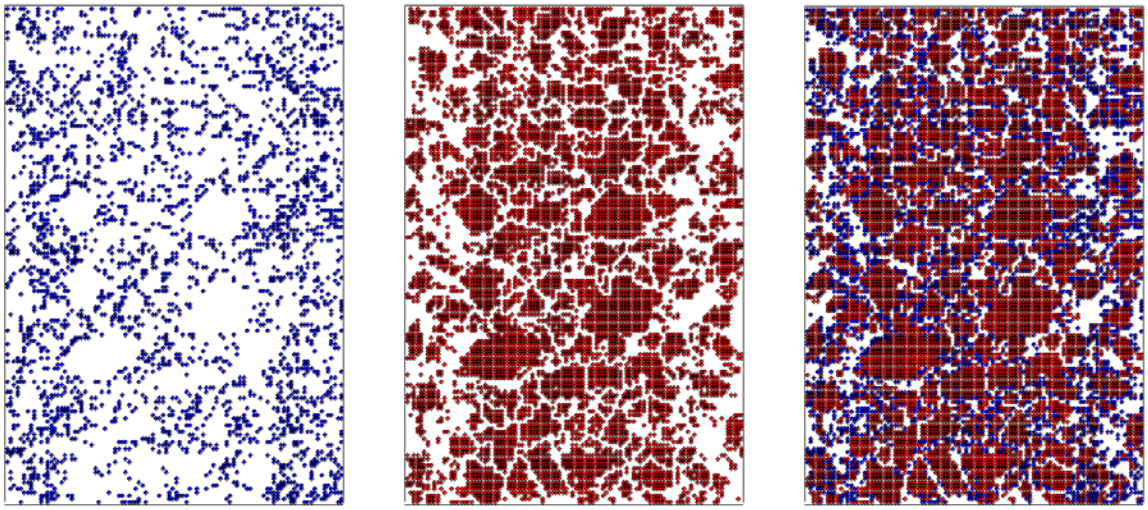

(a) (b) (c)

Figure B.44 Representation AC Rectangular Sections for DEM Simulation, (a) Mastic Phase in Blue, (b) Aggregate Phase in Red, and (c) Mixture; G CMHB-C

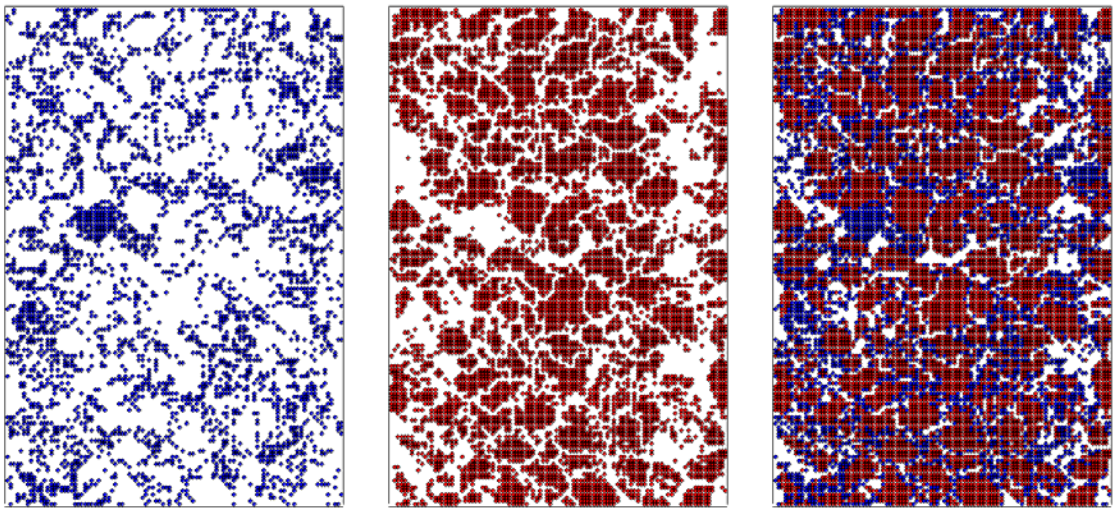

(a) (b) (c)

Figure B.45.Representation AC Rectangular Sections for DEM Simulation, (a) Mastic Phase in Blue, (b) Aggregate Phase in Red, and (c) Mixture; SL CMHB-C

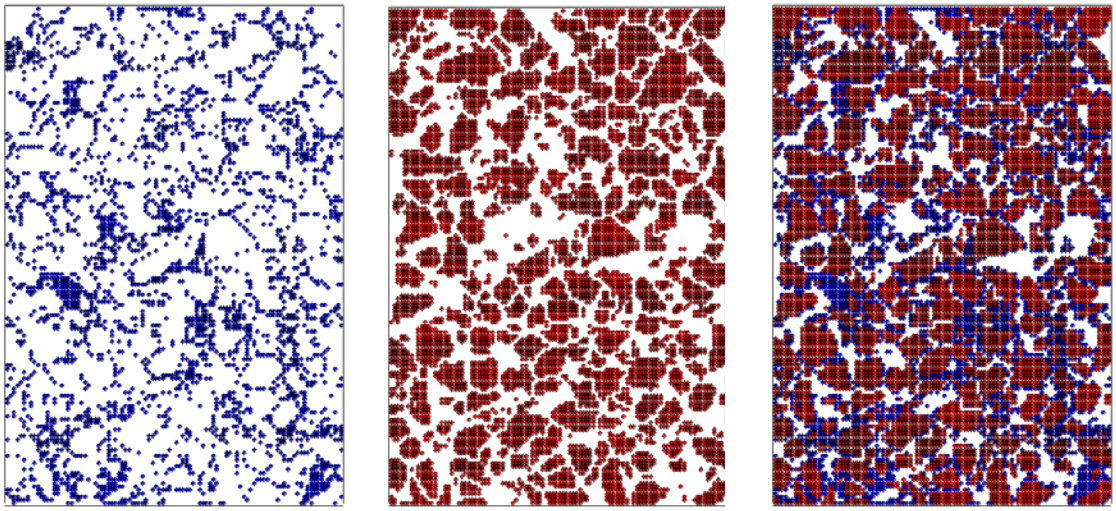

(a) (b) (c)

Figure B.46 Representation AC Rectangular Sections for DEM Simulation, (a) Mastic Phase in Blue, (b) Aggregate Phase in Red, and (c) Mixture; HL PFC

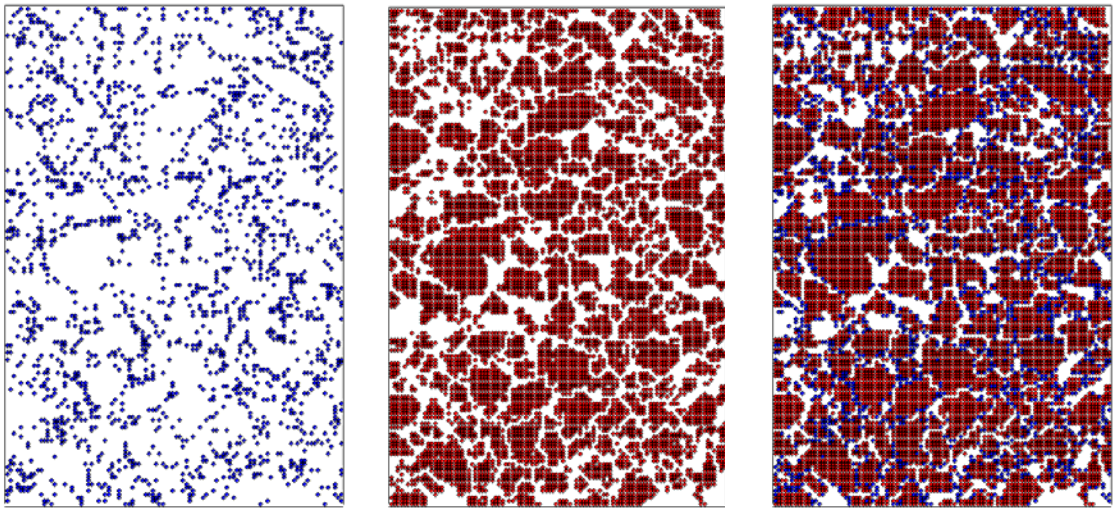

(a) (b) (c)

Figure B.47.Representation AC Rectangular Sections for DEM Simulation, (a) Mastic Phase in Blue, (b) Aggregate Phase in Red, and (c) Mixture; G PFC

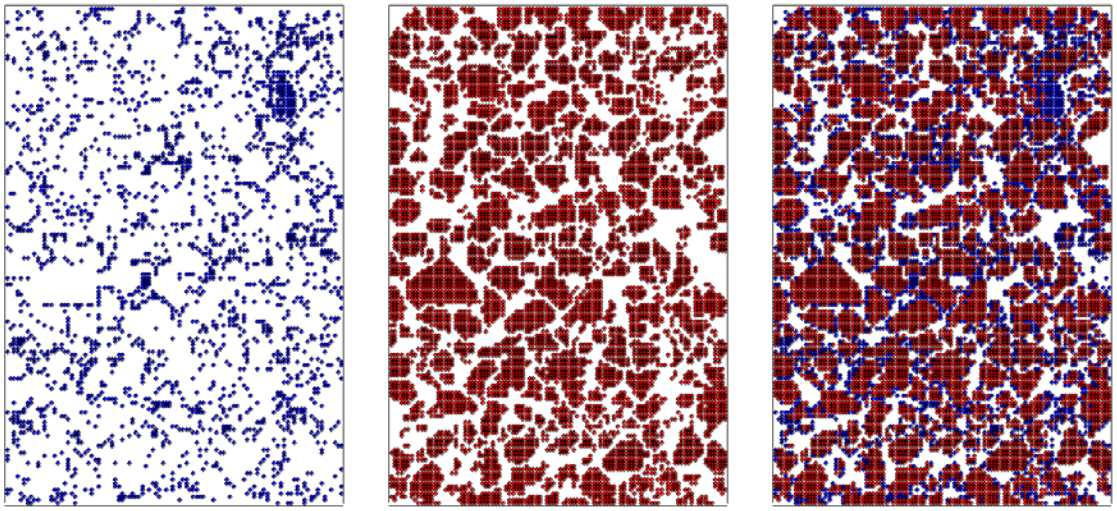

(a) (b) (c)

Figure B.48 Representation AC Rectangular Sections for DEM Simulation, (a) Mastic Phase in Blue, (b) Aggregate Phase in Red, and (c) Mixture; SL PFC

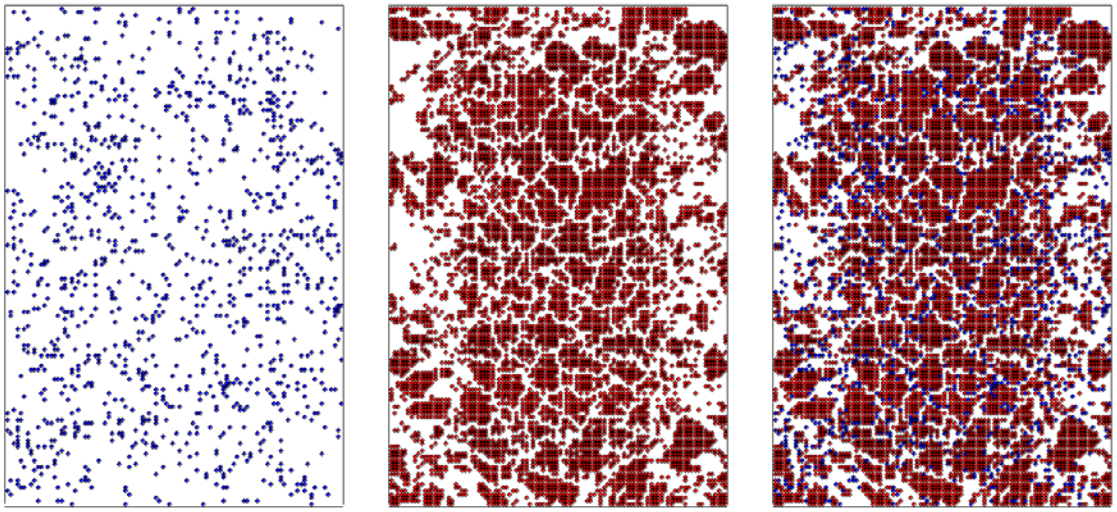

(a) (b) (c)

Figure B.49 Representation AC Rectangular Sections for DEM Simulation, (a) Mastic Phase in Blue, (b) Aggregate Phase in Red, and (c) Mixture; HL Superpave-C

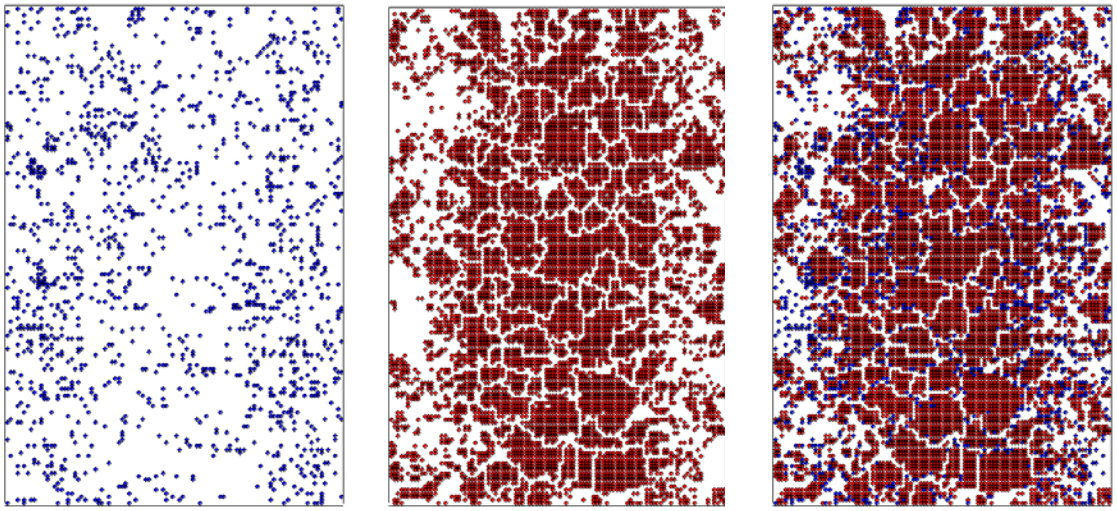

(a) (b) (c)

Figure B.50 Representation AC Rectangular Sections for DEM Simulation, (a) Mastic Phase in Blue, (b) Aggregate Phase in Red, and (c) Mixture; G Superpave-C

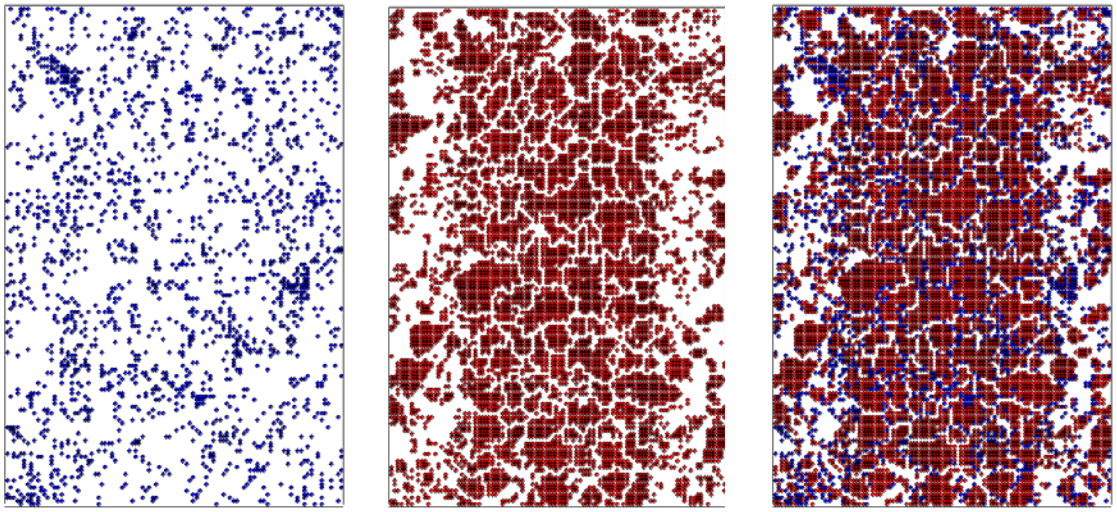

(a) (b) (c)

Figure B.51 Representation AC Rectangular Sections for DEM Simulation, (a) Mastic Phase in Blue, (b) Aggregate Phase in Red, and (c) Mixture; SL Superpave-C

Appendix C

ASPHALT BINDER AND MASTIC RHEOLOGICAL TEST RESULTS

C.1 Amplitude Sweep Test Results

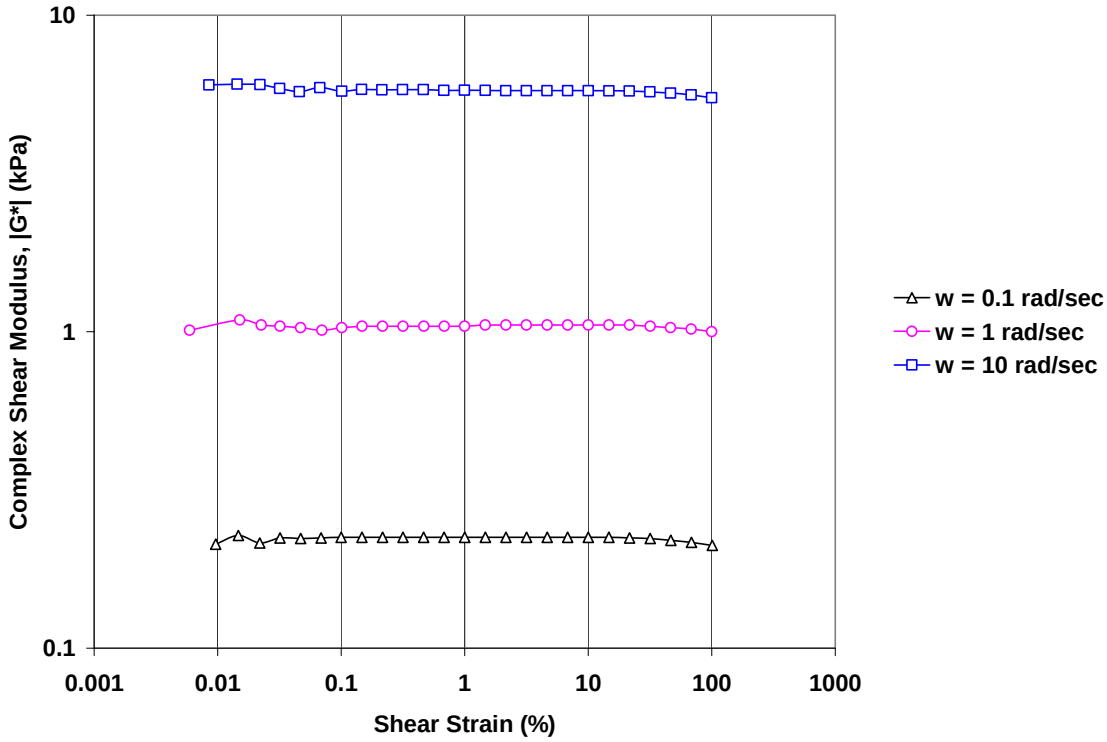

Figure C.1 Amplitude Sweep Test Result; Unaged Binder

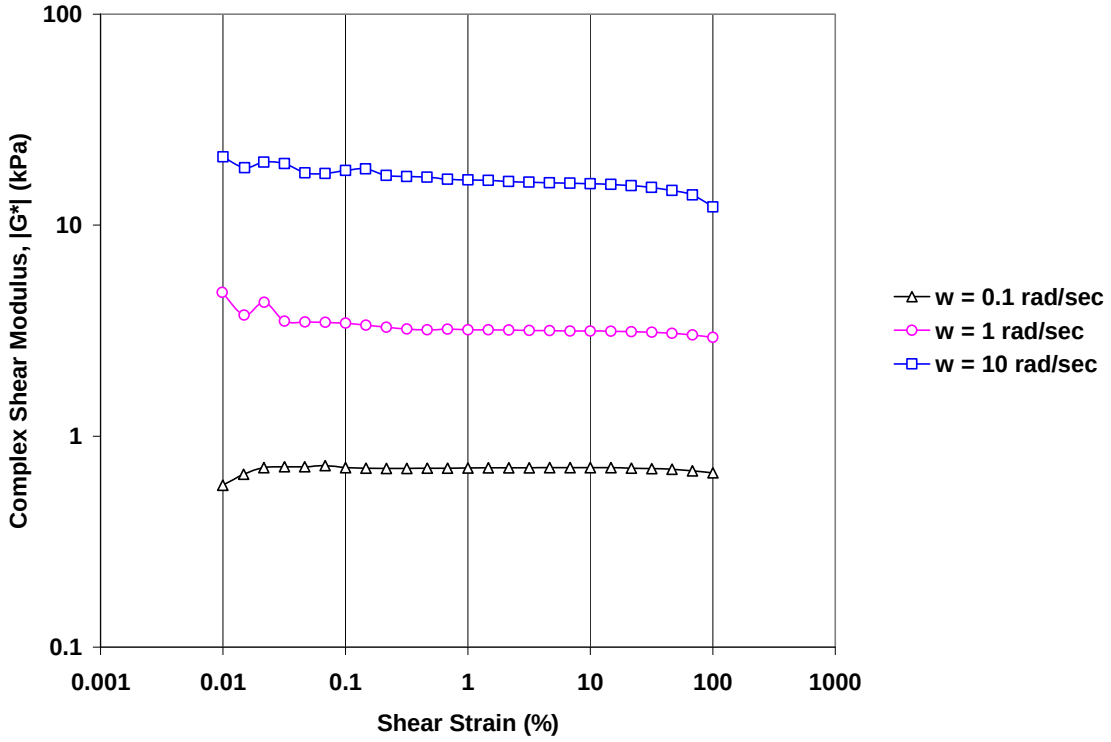

Figure C.2 Amplitude Sweep Test Result; RTFO-aged Binder

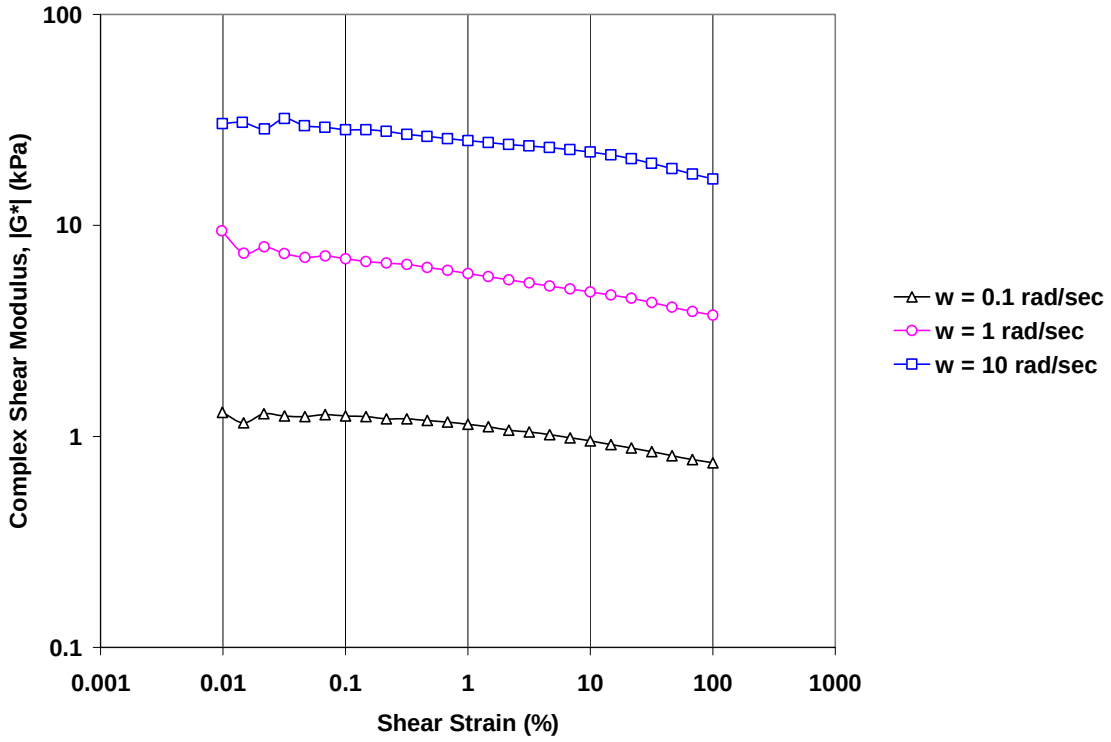

Figure C.3 Amplitude Sweep Test Result; G CMHB Unaged Mastic

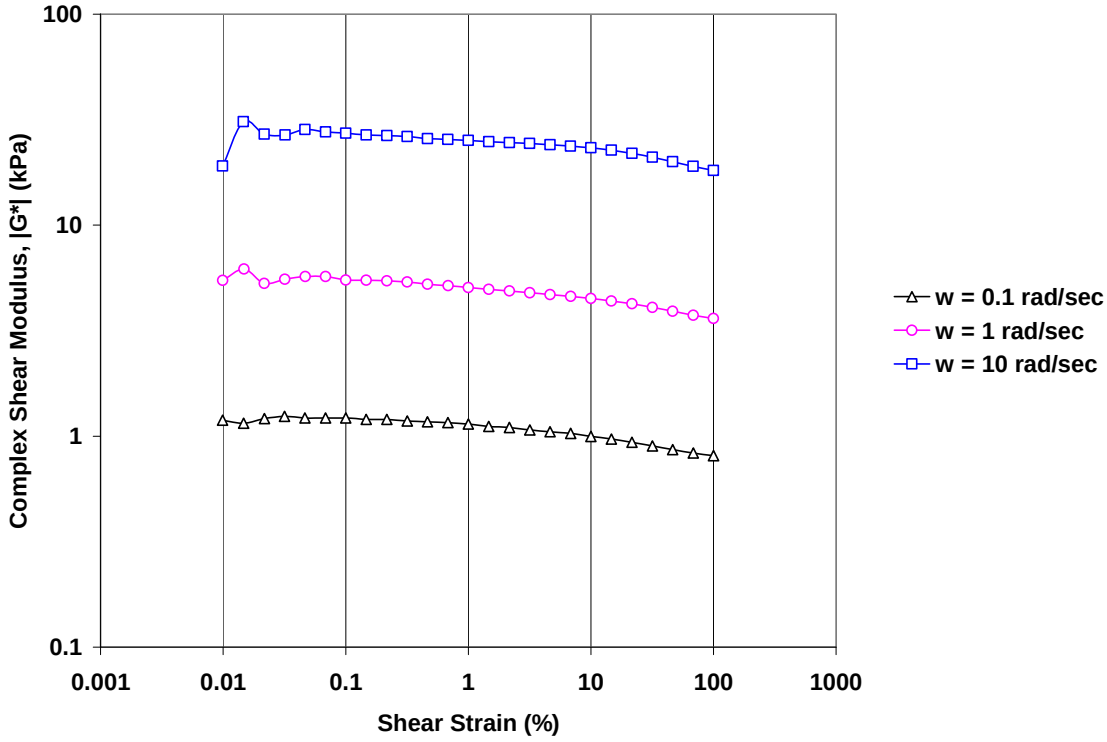

Figure C.4 Amplitude Sweep Test Result; SL CMHB Unaged Mastic

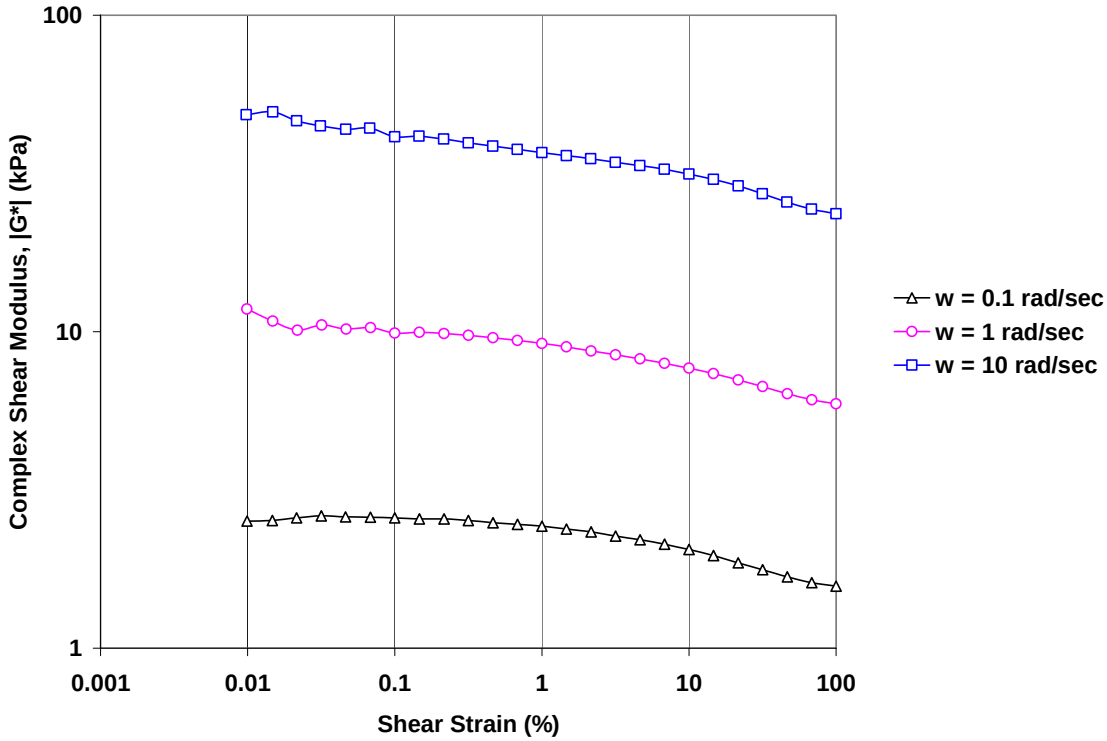

Figure C.5 Amplitude Sweep Test Result; HL PFC Unaged Mastic

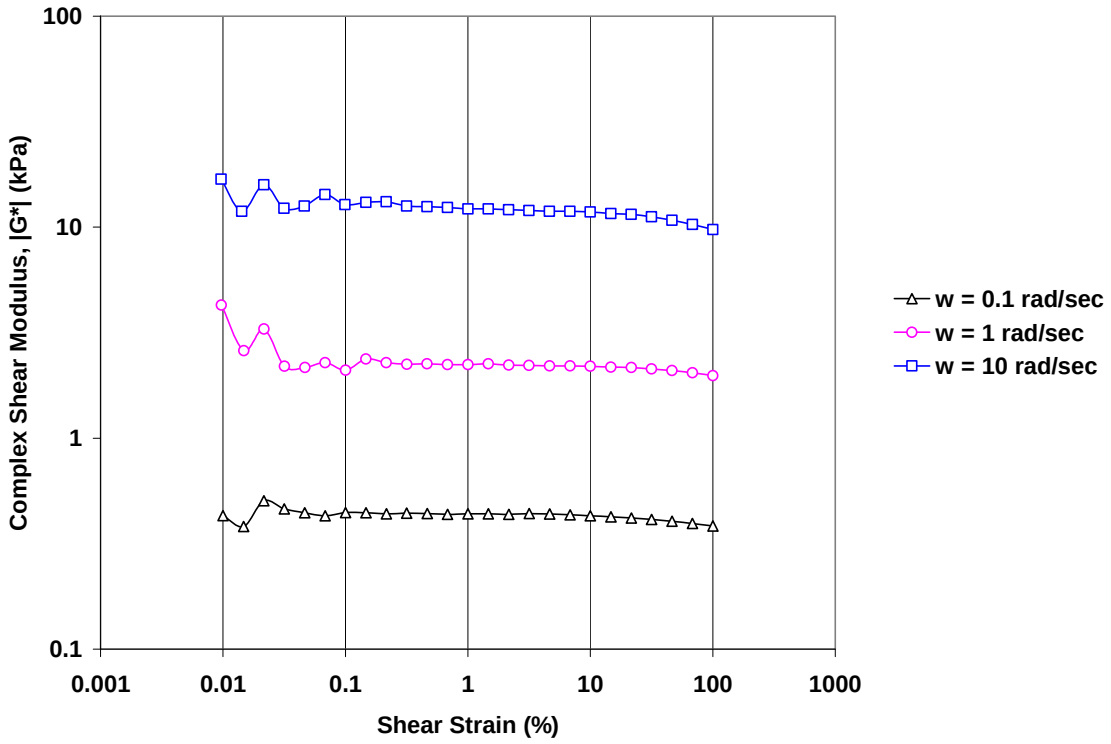

Figure C.6 Amplitude Sweep Test Result; G PFC Unaged Mastic

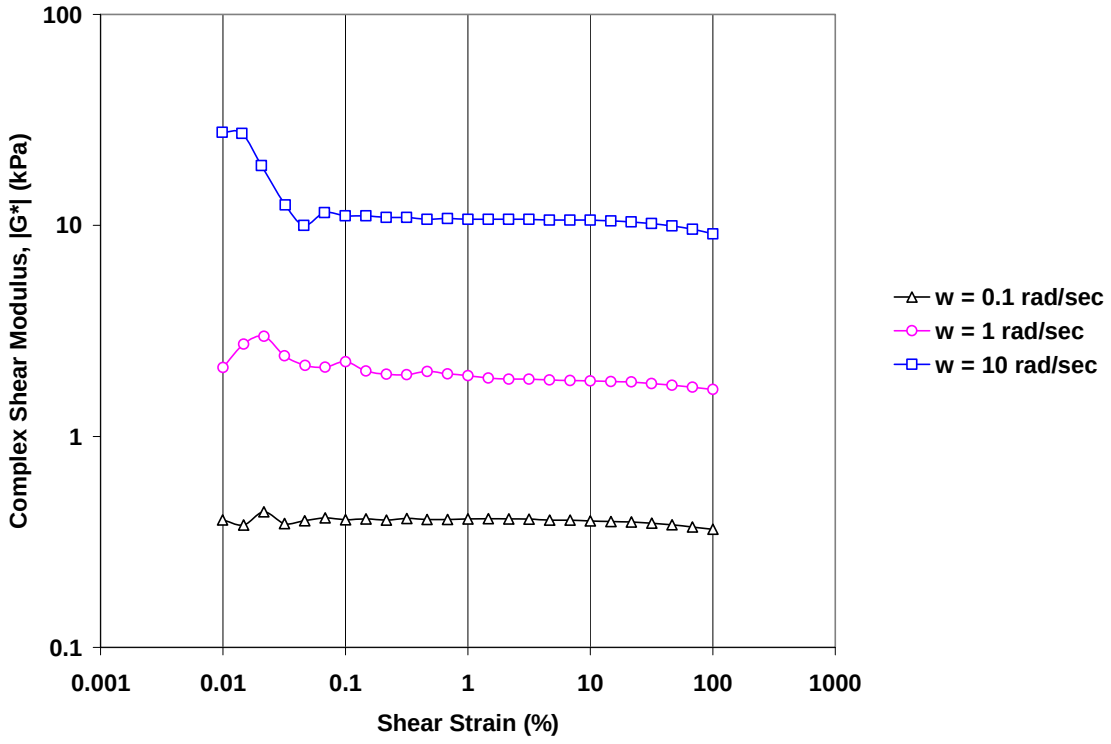

Figure C.7 Amplitude Sweep Test Result; SL PFC Unaged Mastic

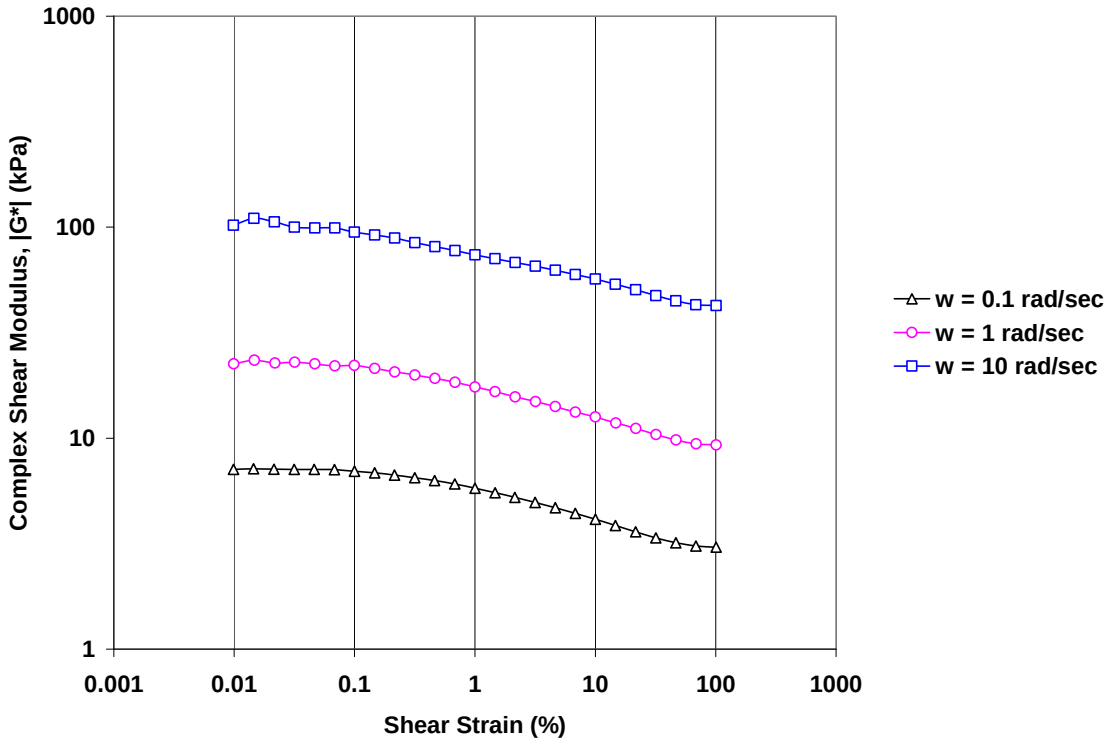

Figure C.8 Amplitude Sweep Test Result; HL Superpave-C Unaged Mastic

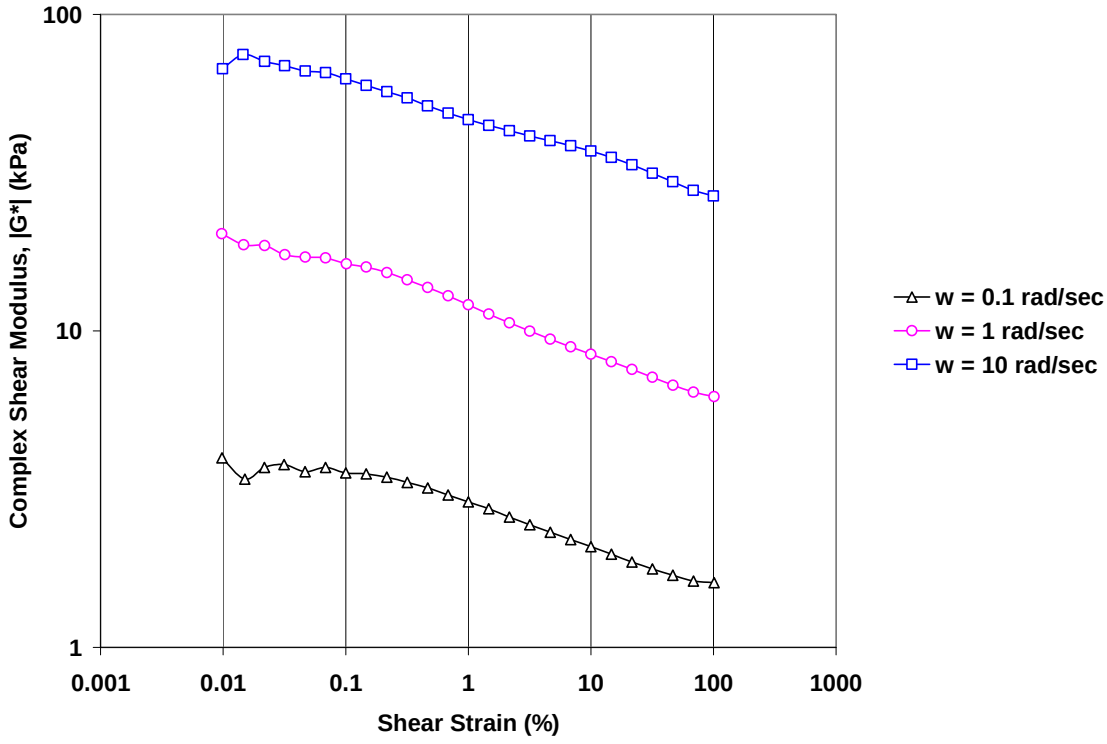

Figure C.9 Amplitude Sweep Test Result; G Superpave-C Unaged Mastic

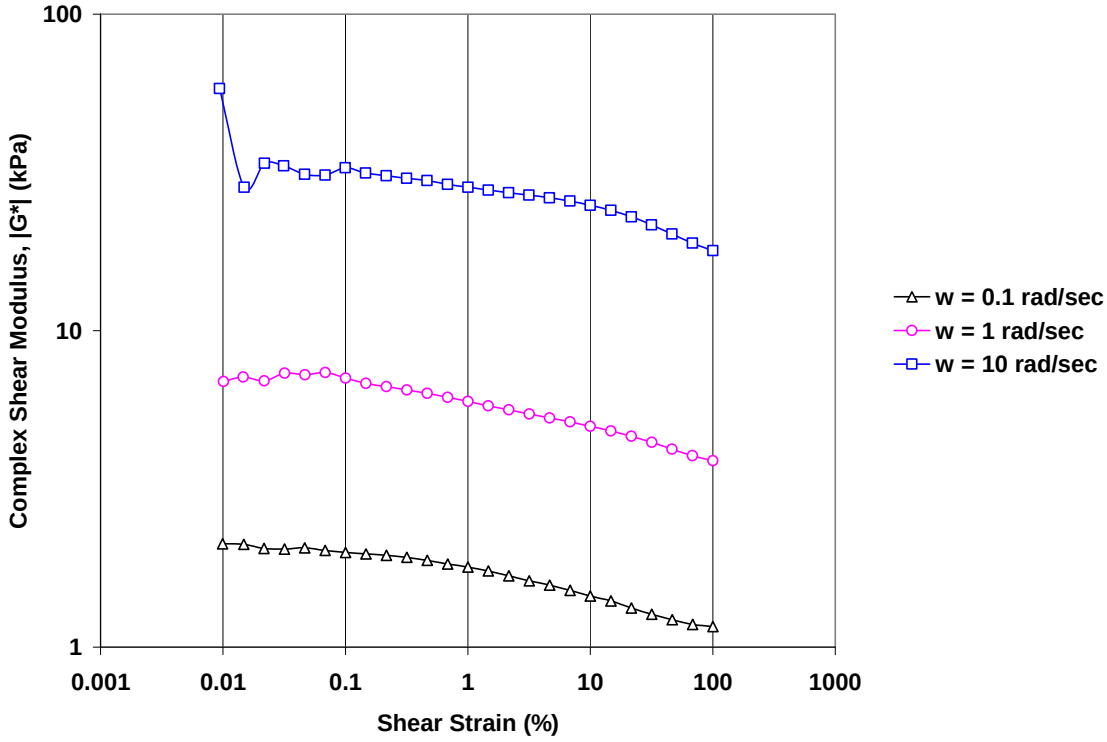

Figure C.10 Amplitude Sweep Test Result; SL Superpave-C Unaged Mastic

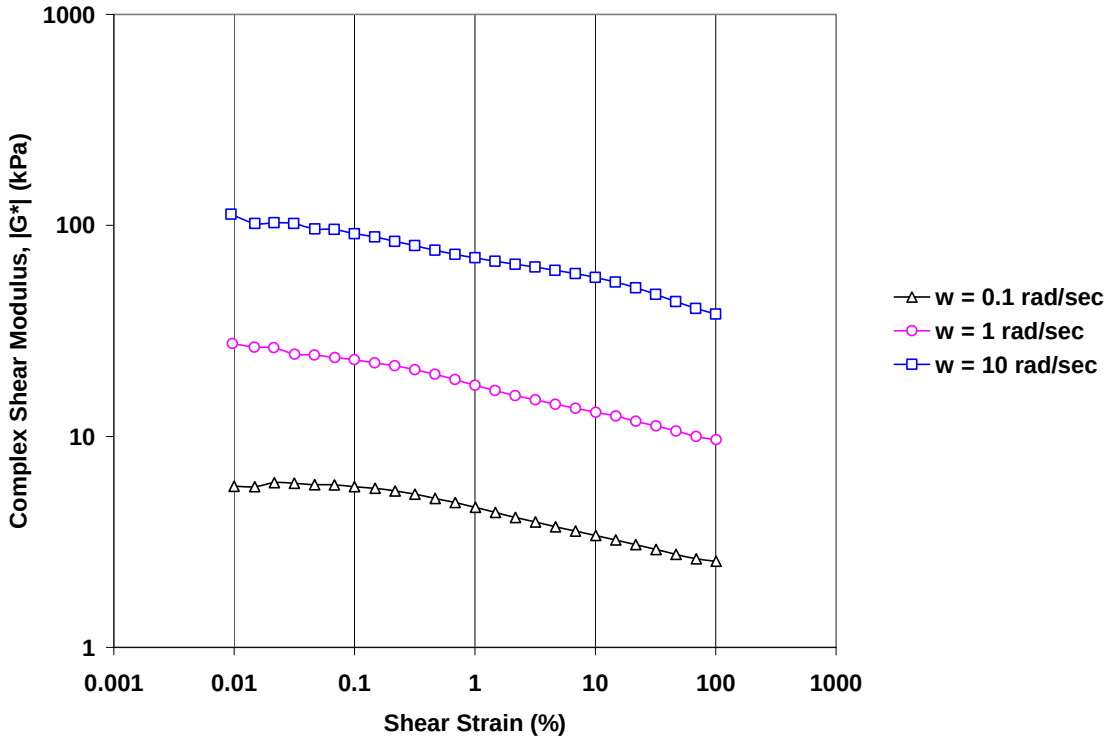

Figure C.11 Amplitude Sweep Test Result; G CMHB RTFO-aged Mastic

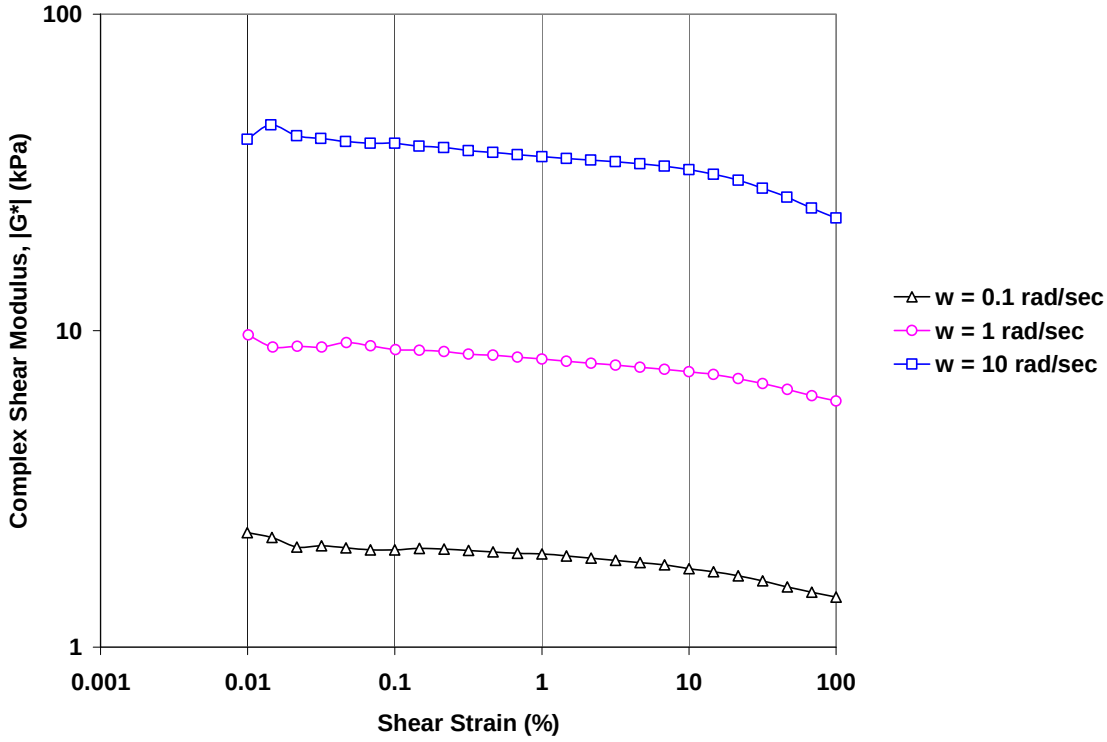

Figure C.12 Amplitude Sweep Test Result; SL CMHB RTFO-aged Mastic

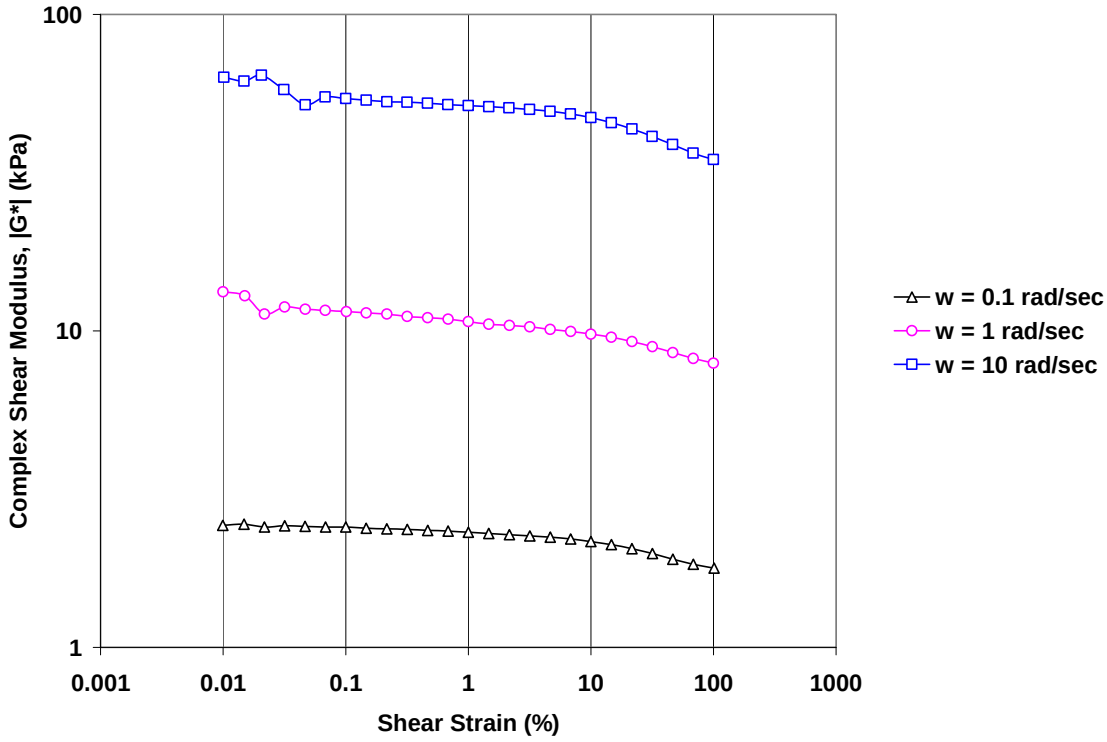

Figure C.13 Amplitude Sweep Test Result; HL PFC RTFO-aged Mastic

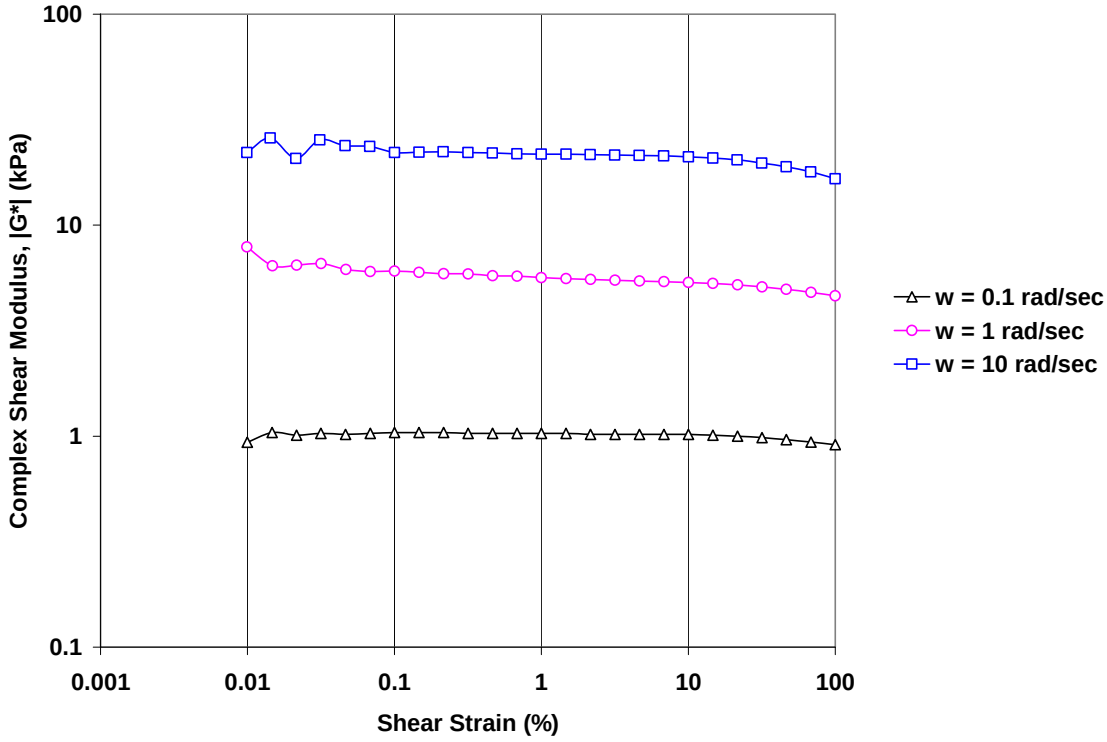

Figure C.14 Amplitude Sweep Test Result; G PFC RTFO-aged Mastic

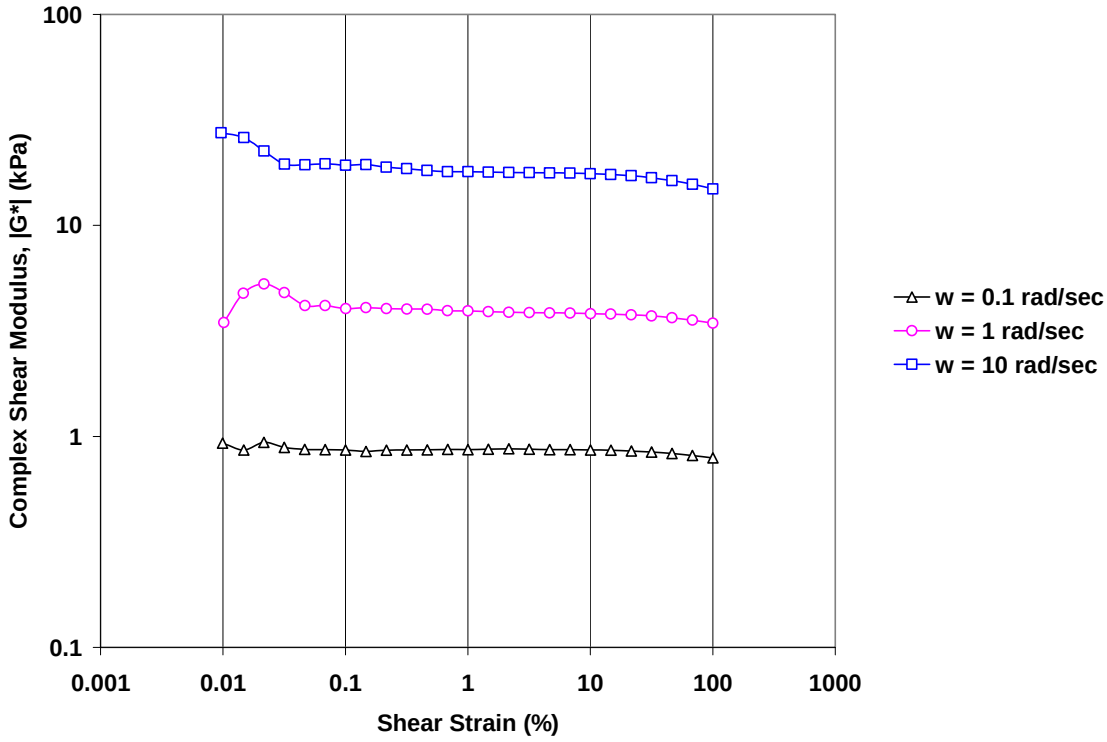

Figure C.15 Amplitude Sweep Test Result; SL PFC RTFO-aged Mastic

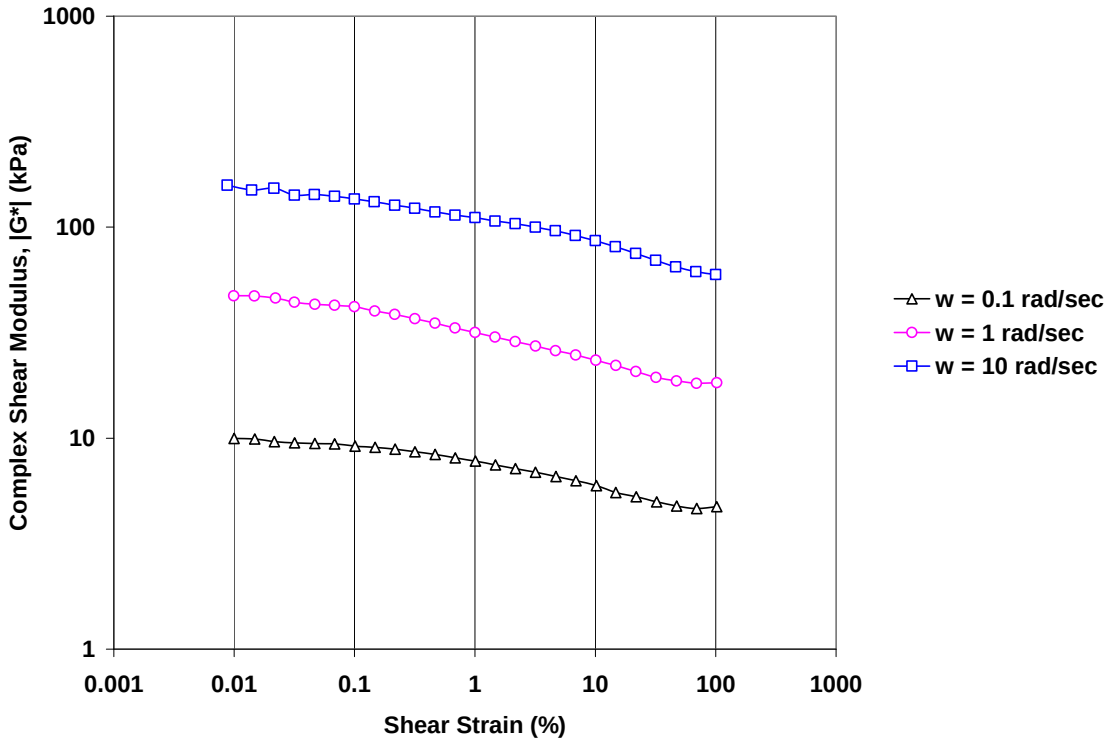

Figure C.16 Amplitude Sweep Test Result; HL Superpave-C RTFO-aged Mastic

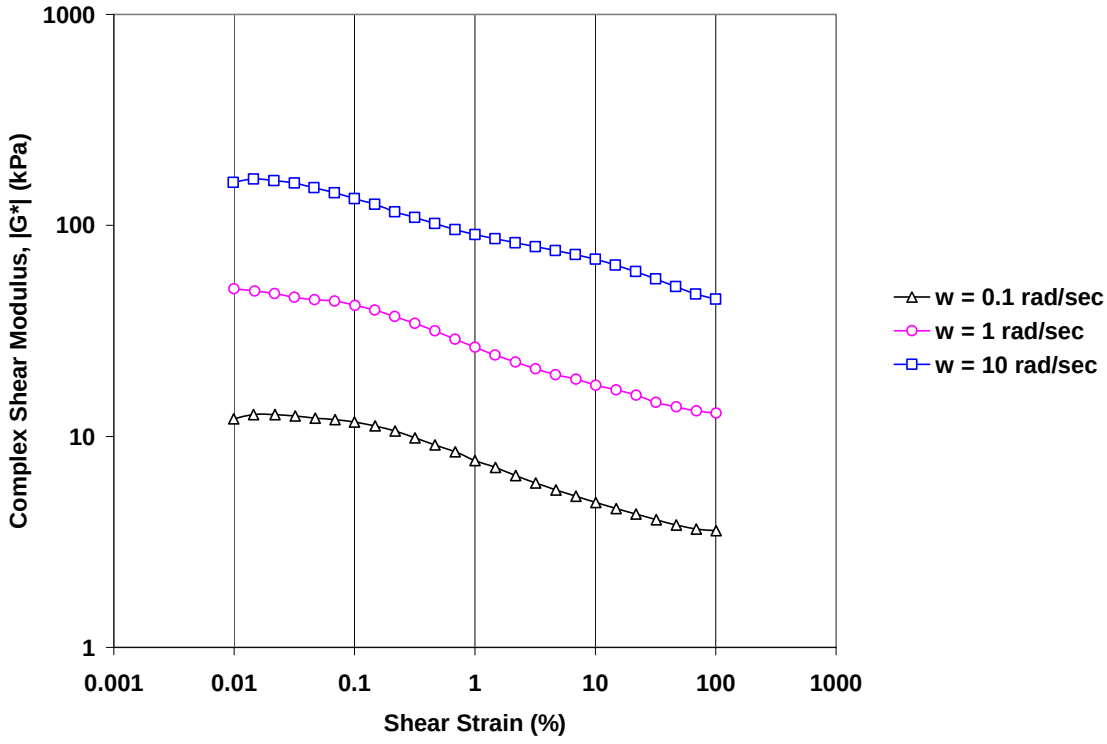

Figure C.17 Amplitude Sweep Test Result; G Superpave-C RTFO-aged Mastic

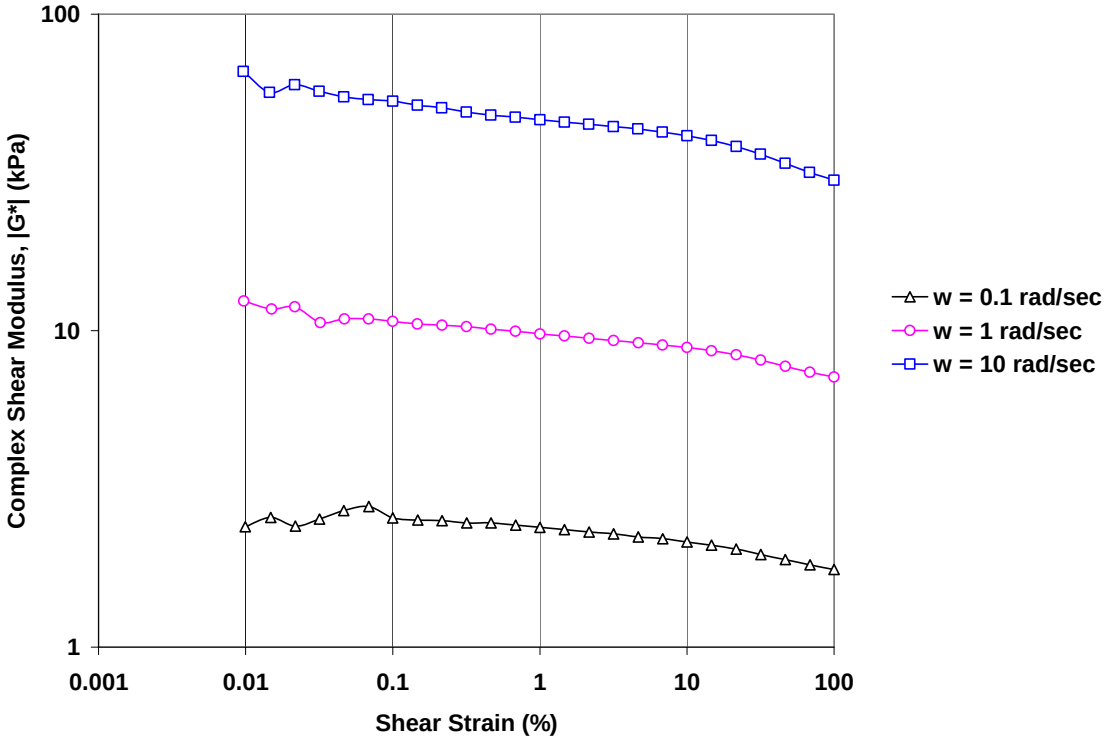

Figure C.18 Amplitude Sweep Test Result; SL Superpave-C RTFO-aged Mastic

C.2 LVE Range at Different Angular Frequencies

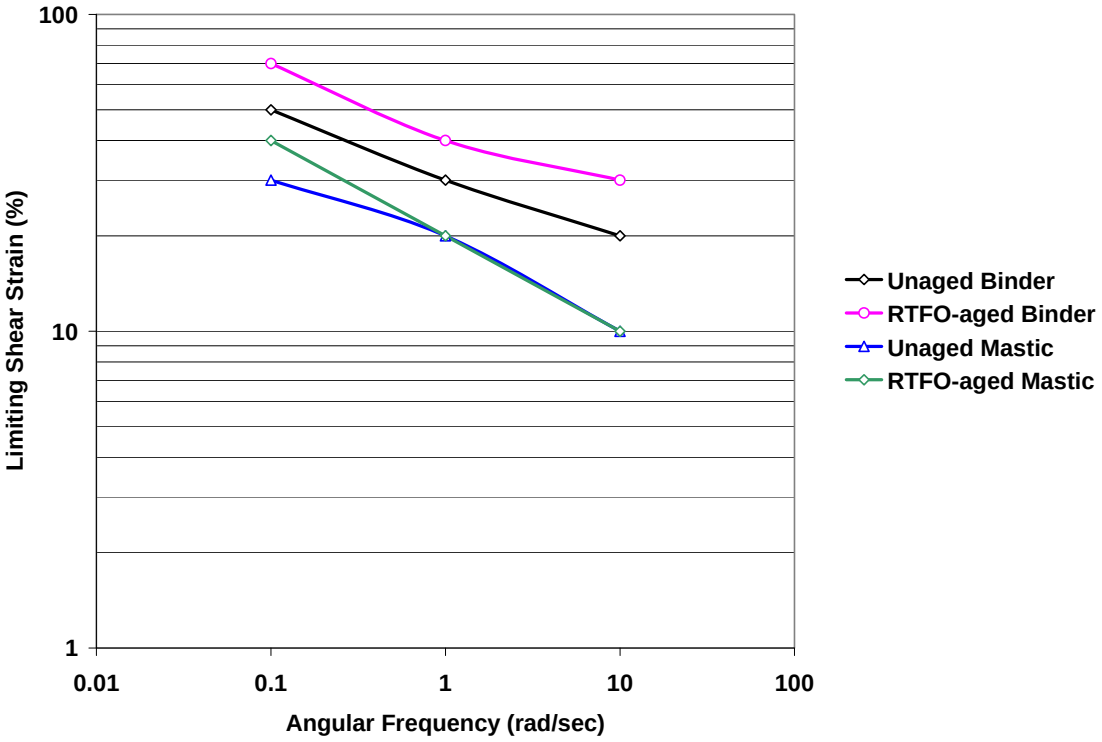

Figure C.19 LVE Range at Different Angular Frequencies; G CMHB-C

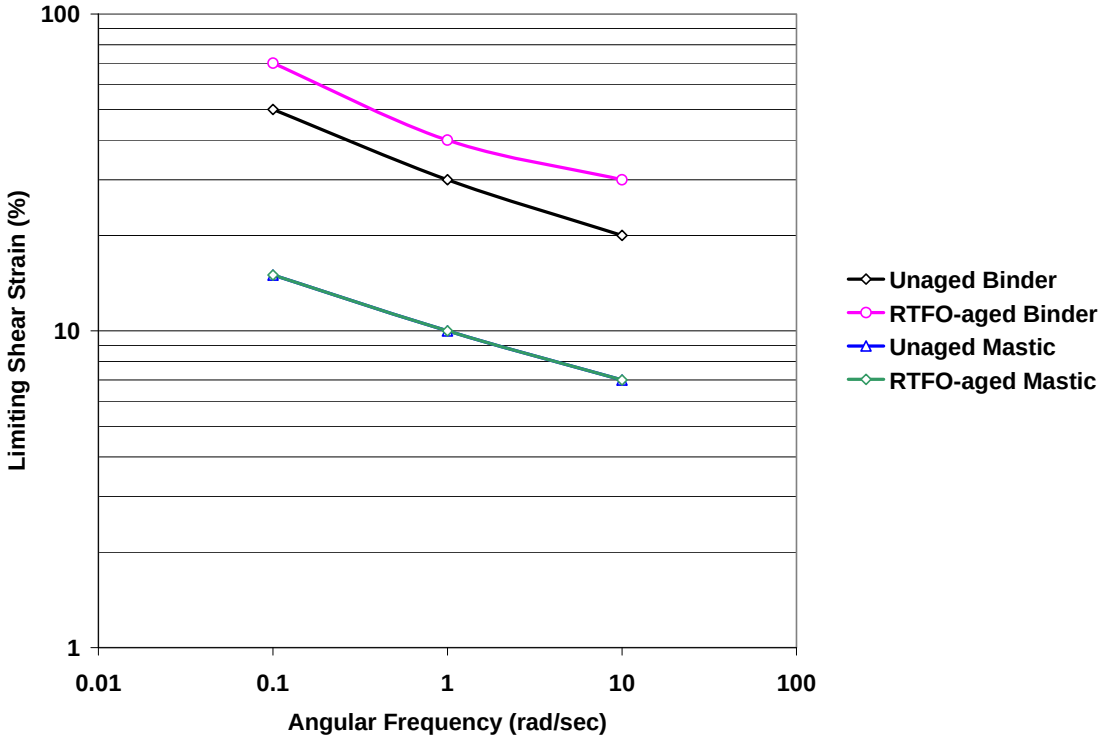

Figure C.20 LVE Range at Different Angular Frequencies; SL CMHB-C

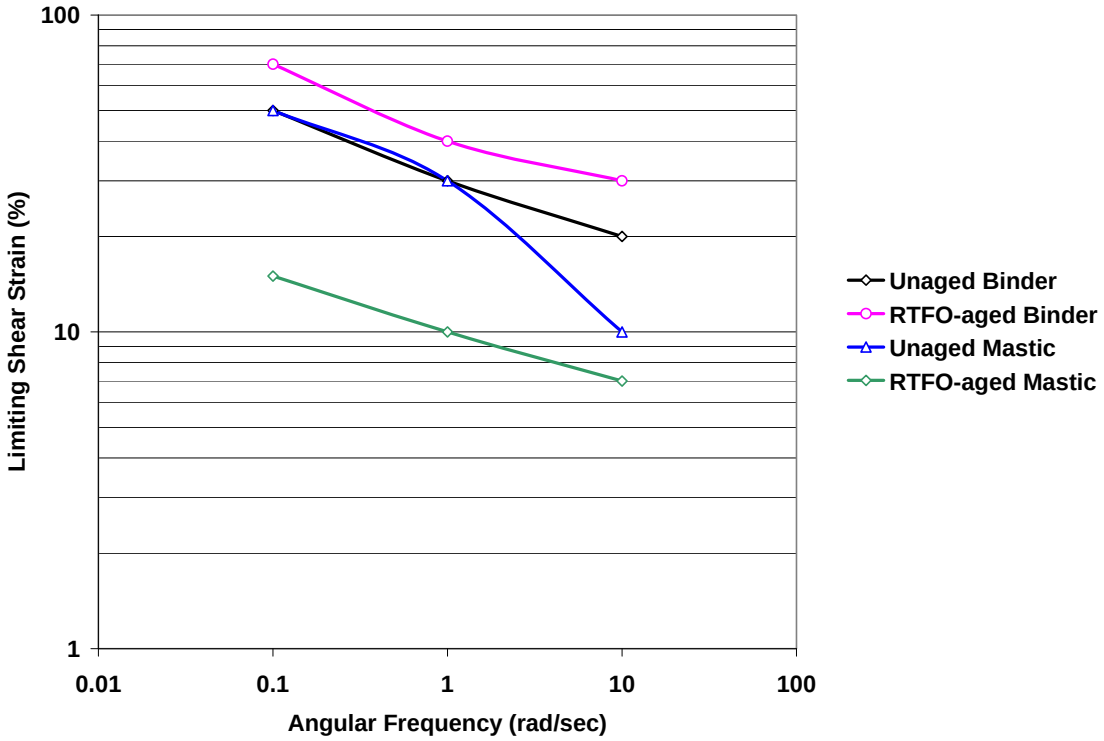

Figure C.21 LVE Range at Different Angular Frequencies; HL PFC

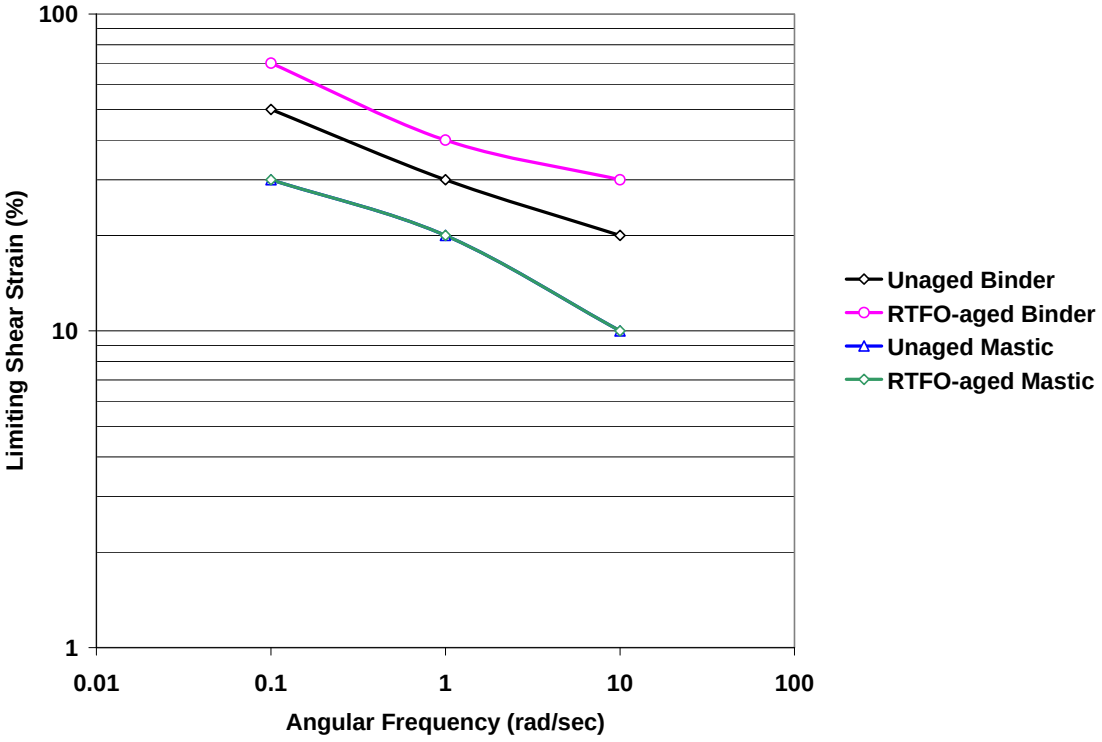

Figure C.22 LVE Range at Different Angular Frequencies; G PFC

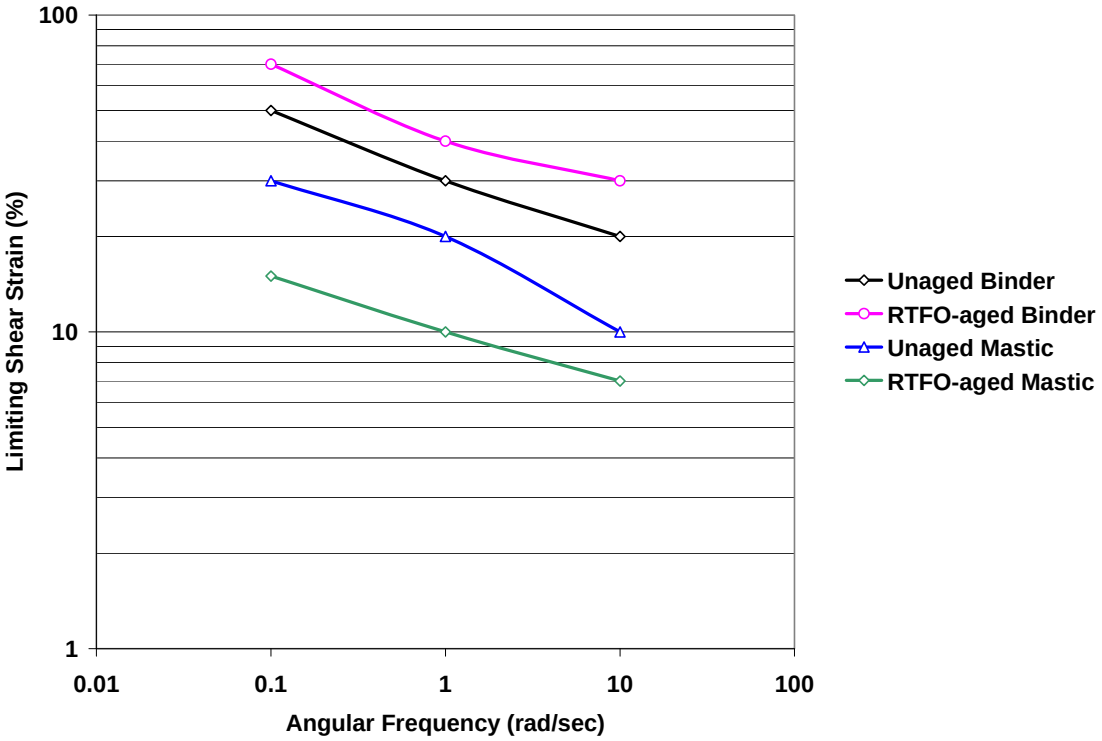

Figure C.23 LVE Range at Different Angular Frequencies; SL PFC

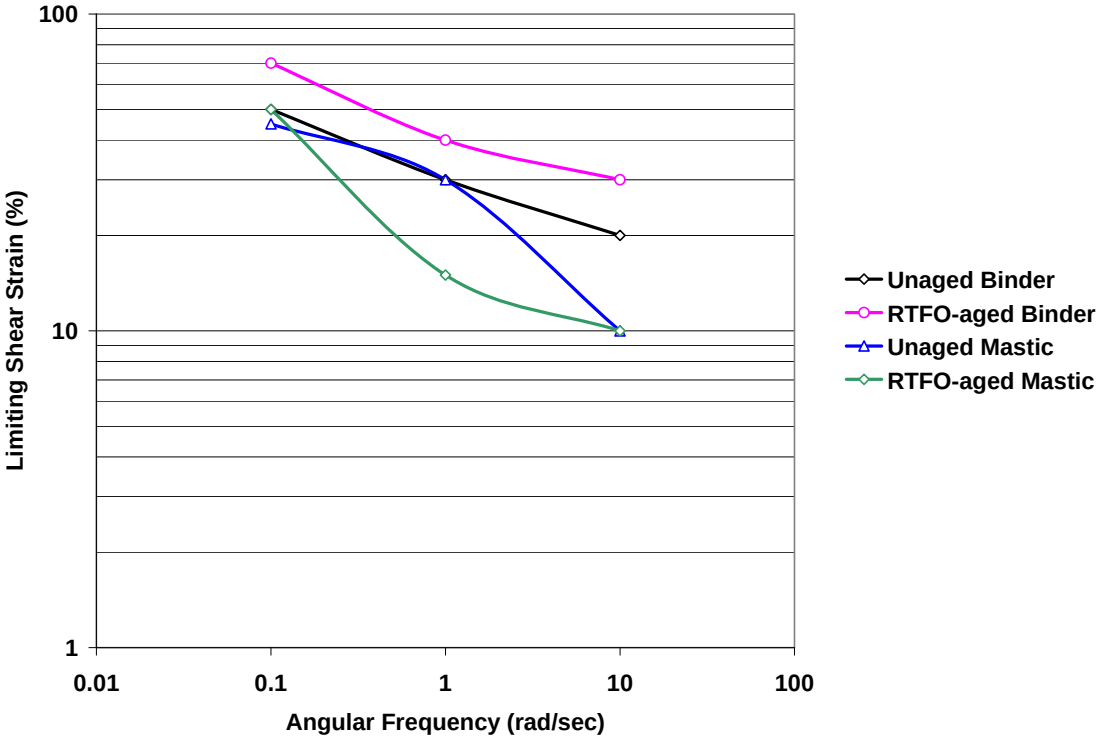

Figure C.24 LVE Range at Different Angular Frequencies; HL Superpave-C

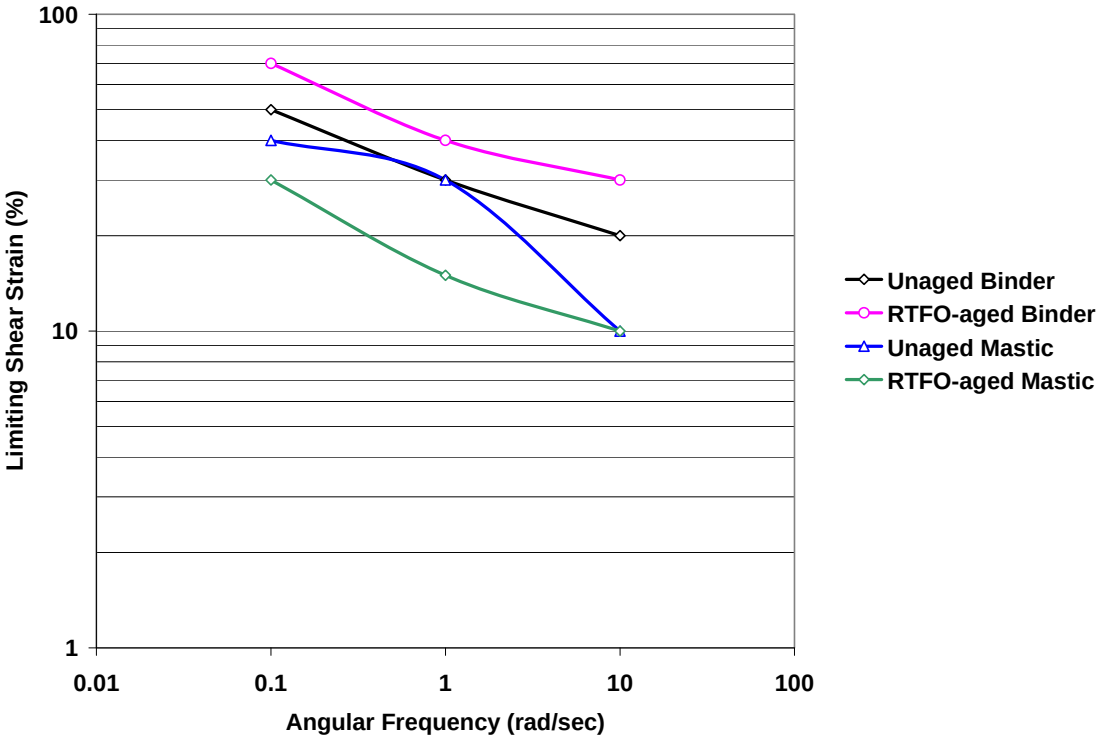

Figure C.25 LVE Range at Different Angular Frequencies; G Superpave-C

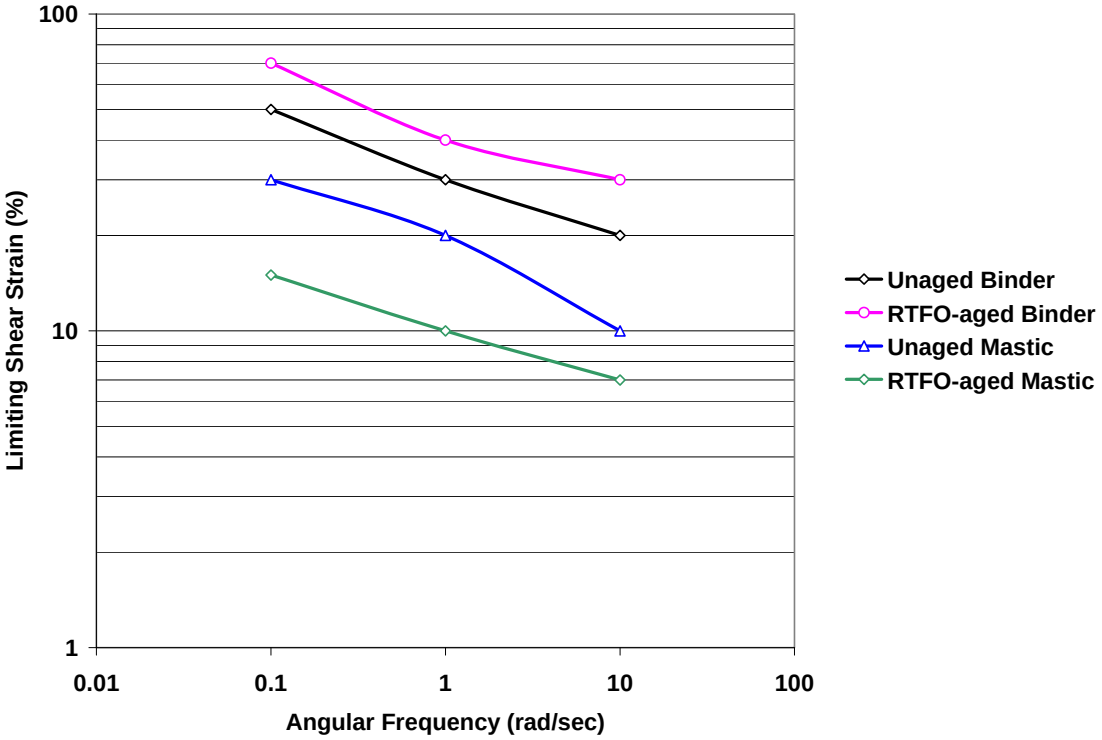

Figure C.26 LVE Range at Different Angular Frequencies; SL Superpave-C

C.3 Frequency Sweep Test Results

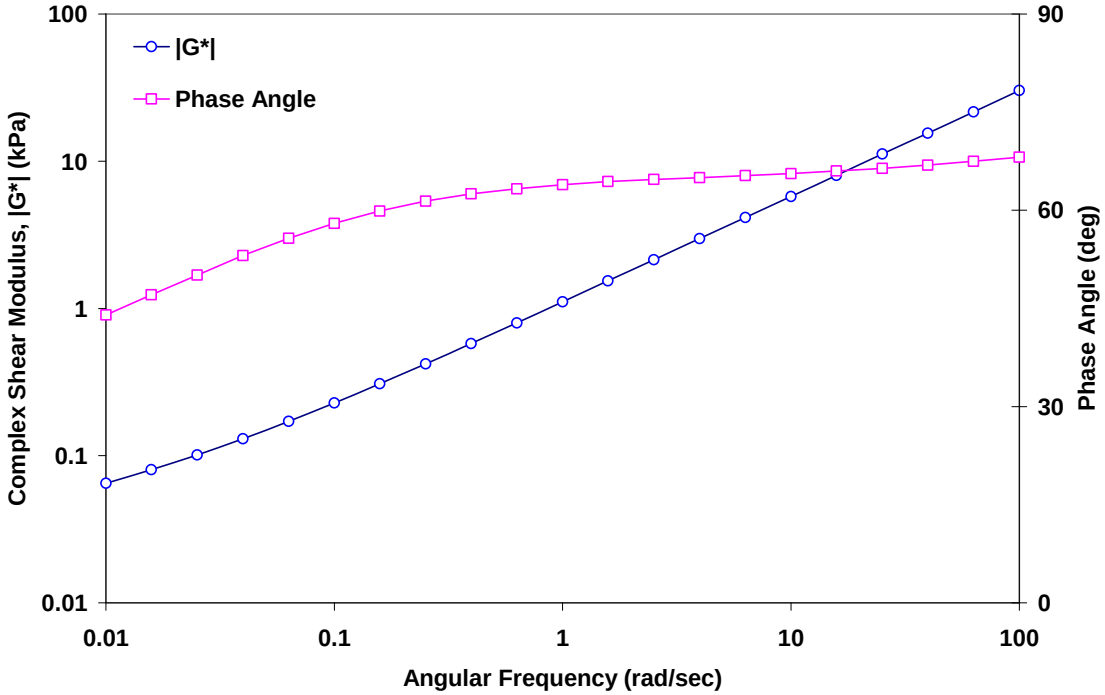

Figure C.27 Frequency Sweep Test Result, γ_A = 52.0%; Unaged Binder

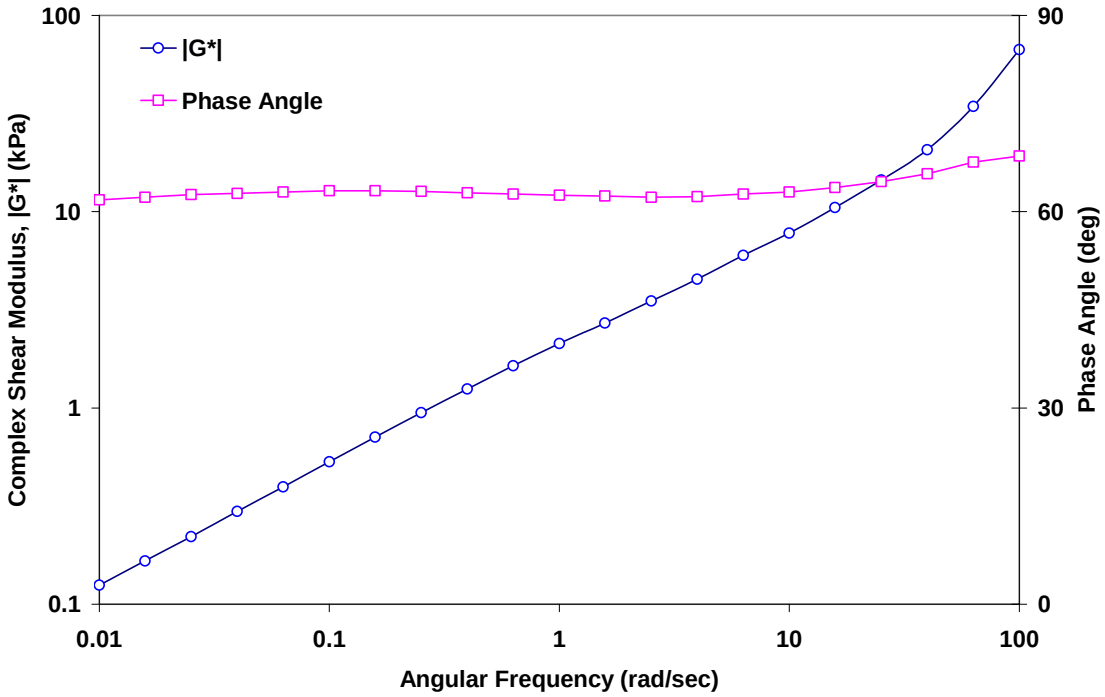

Figure C.28 Frequency Sweep Test Result, γ_A = 73.0%; RTFO-aged Binder

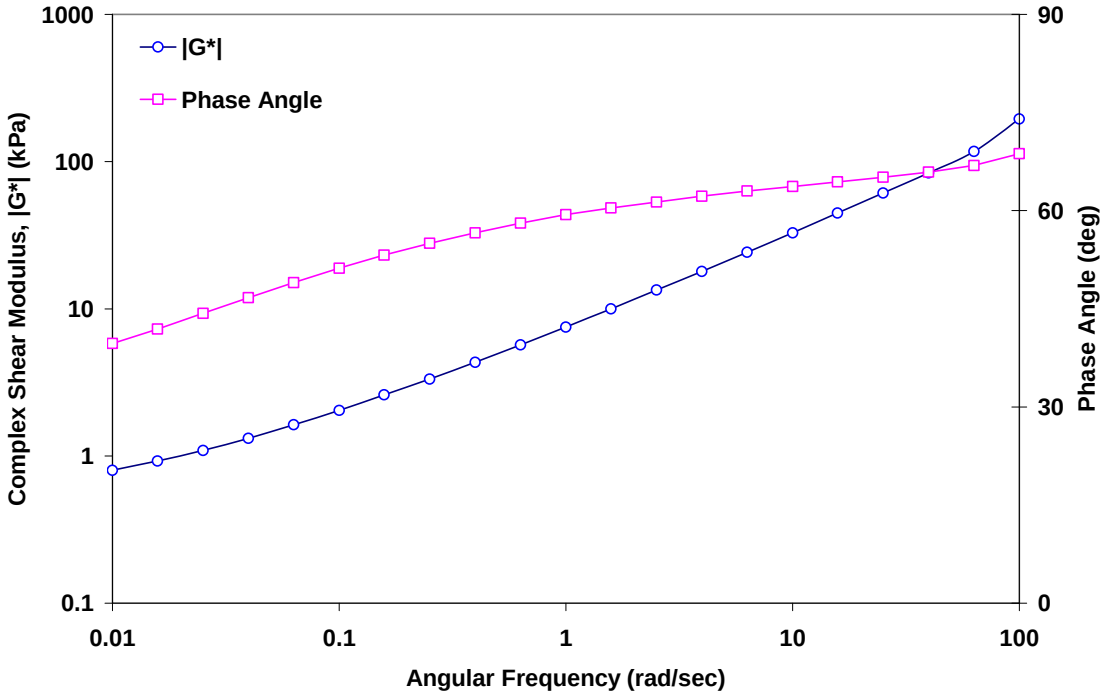

Figure C.29 Frequency Sweep Test Result, γ_A = 52.0%; HL CMHB Unaged Mastic

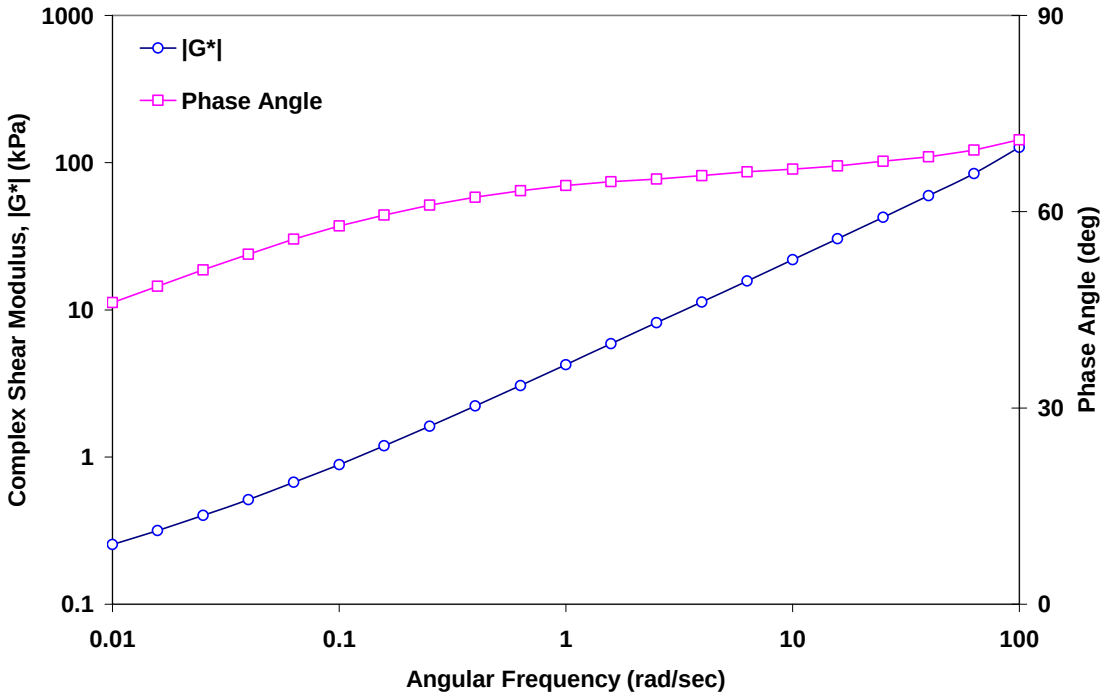

Figure C.30 Frequency Sweep Test Result, γ_A = 31.0%; G CMHB Unaged Mastic

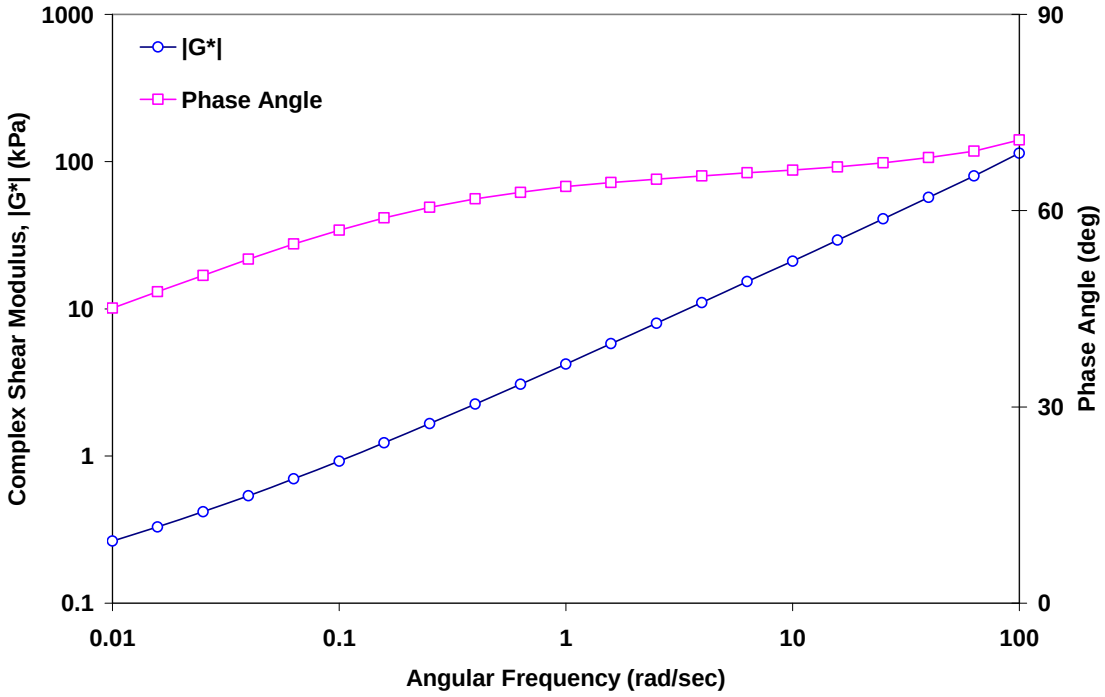

Figure C.31 Frequency Sweep Test Result, γ_A = 15.5%; SL CMHB Unaged Mastic

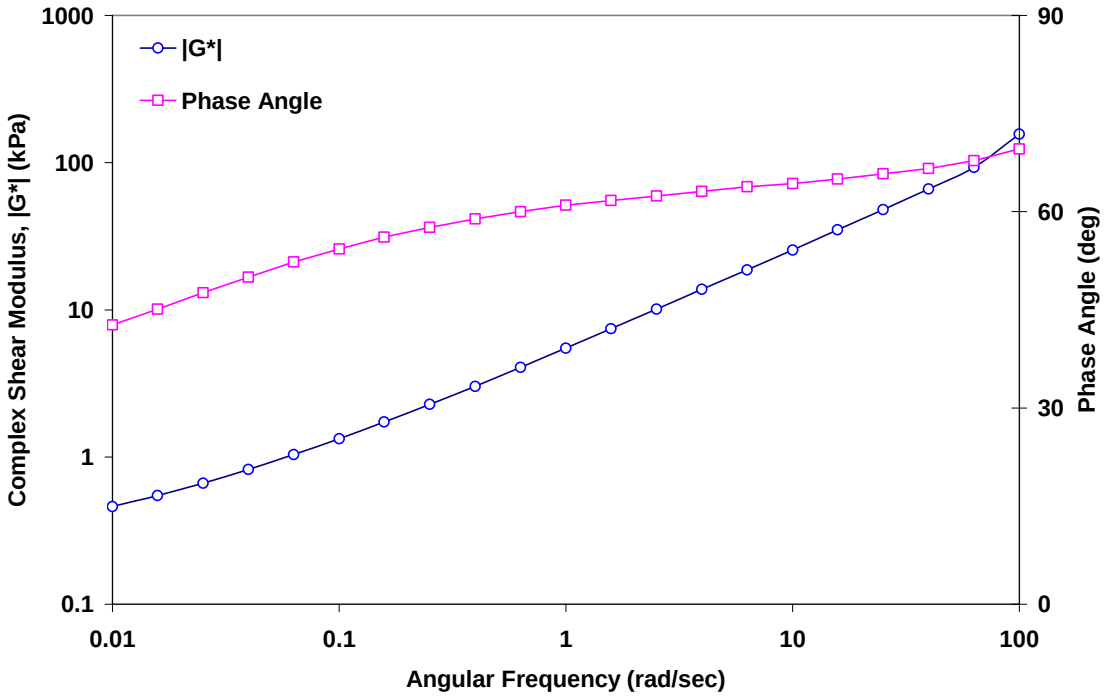

Figure C.32 Frequency Sweep Test Result, γ_A = 52.0%; HL PFC Unaged Mastic

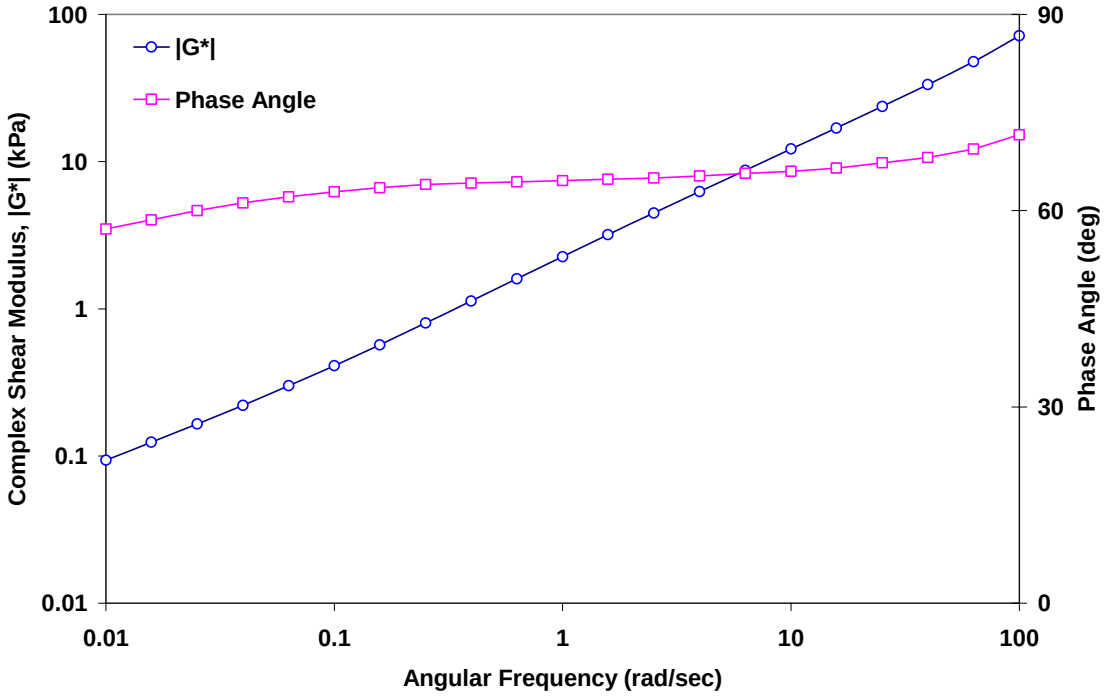

Figure C.33 Frequency Sweep Test Result, γ_A = 31.0%; G PFC Unaged Mastic

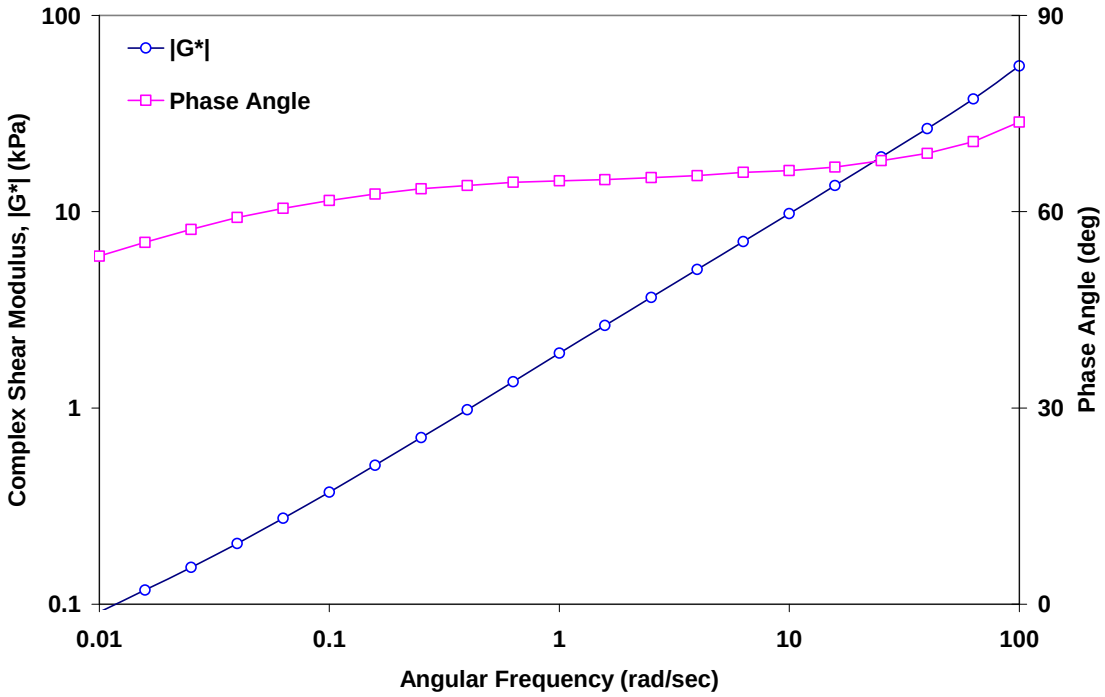

Figure C.34 Frequency Sweep Test Result, γ_A = 31.0%; SL PFC Unaged Mastic

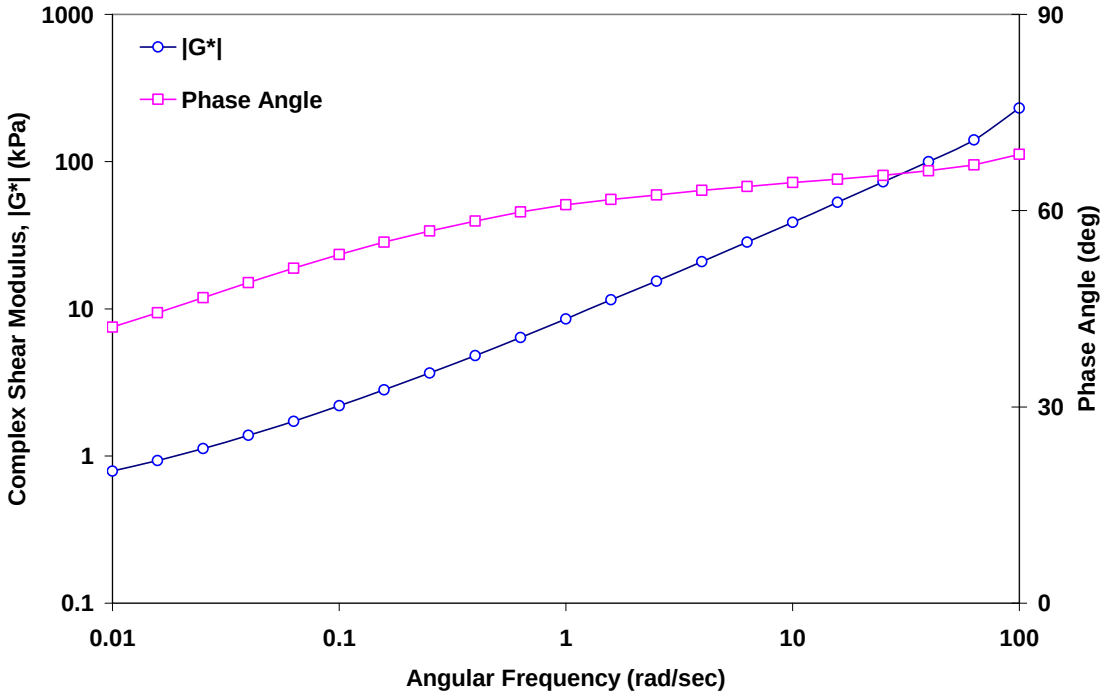

Figure C.35 Frequency Sweep Test Result, γ_A = 46.5%; HL Superpave-C Unaged Mastic

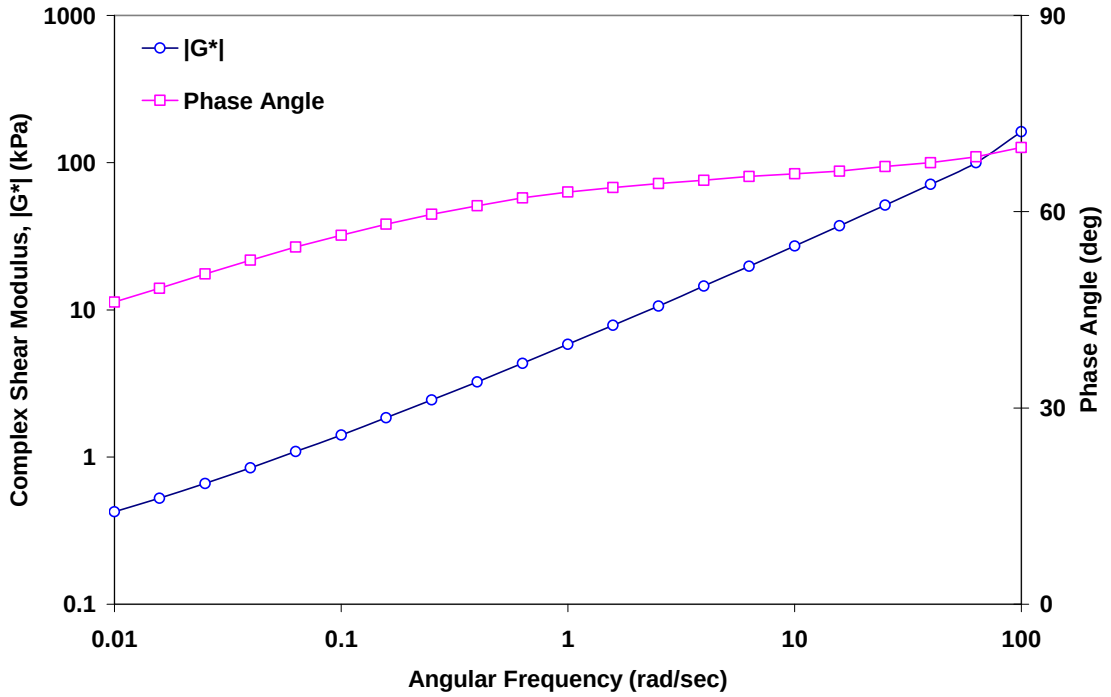

Figure C.36 Frequency Sweep Test Result, γ_A = 41.0%; G Superpave-C Unaged Mastic

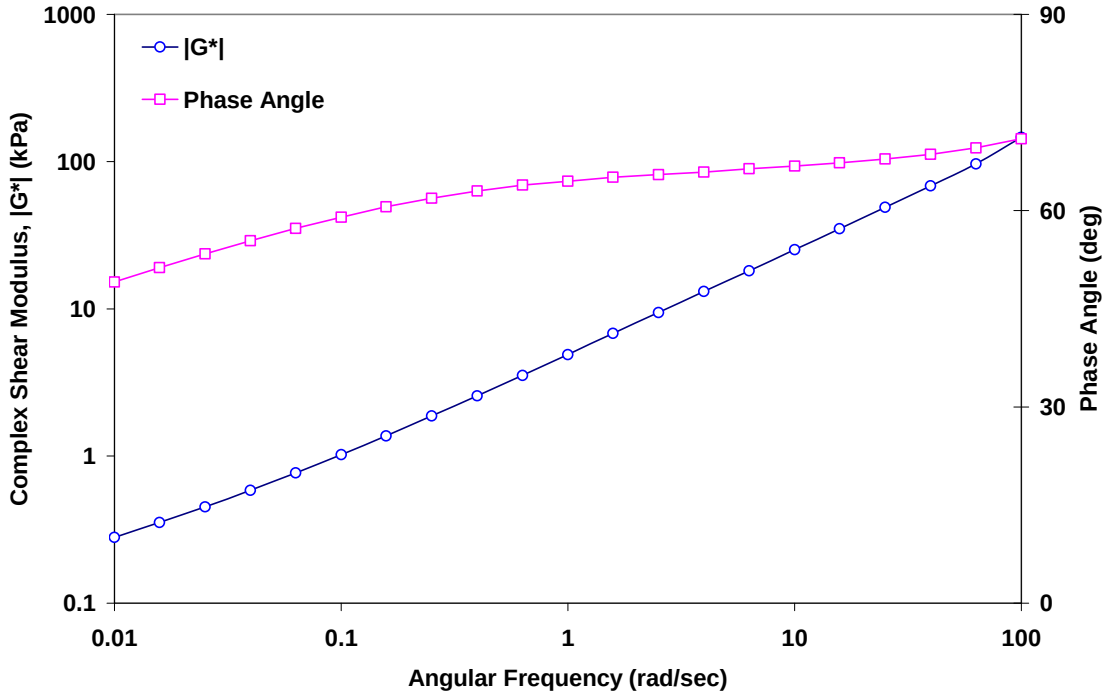

Figure C.37 Frequency Sweep Test Result, γ_A = 31.0%; SL Superpave-C Unaged Mastic

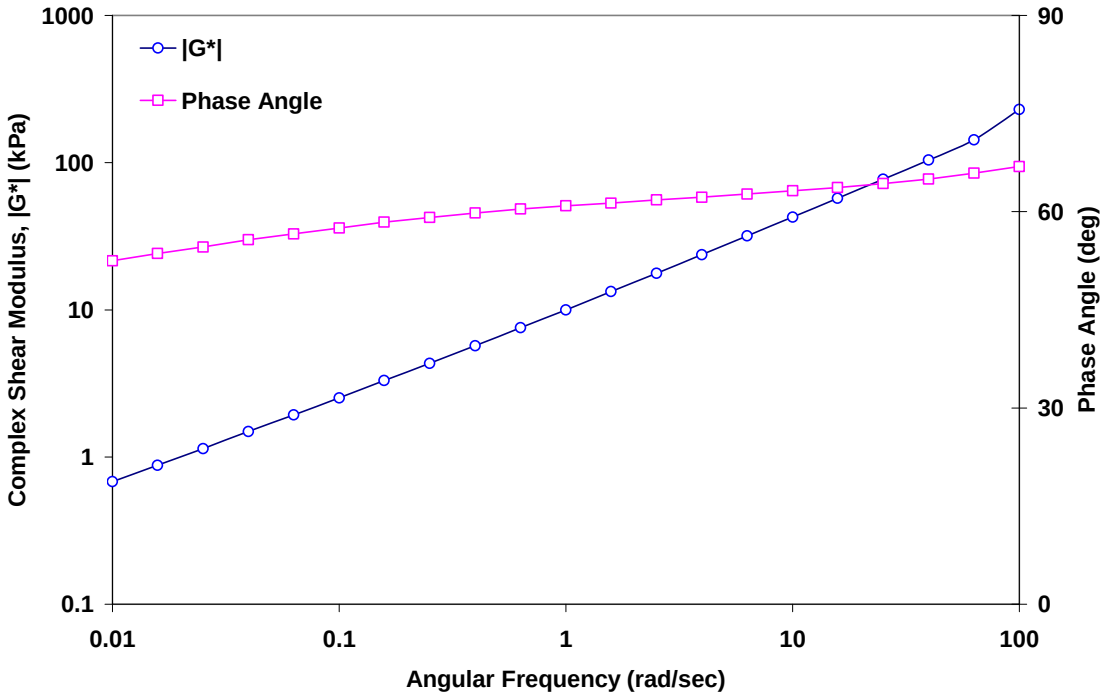

Figure C.38 Frequency Sweep Test Result, γ_A = 42.0%; G CMHB RTFO-aged Mastic

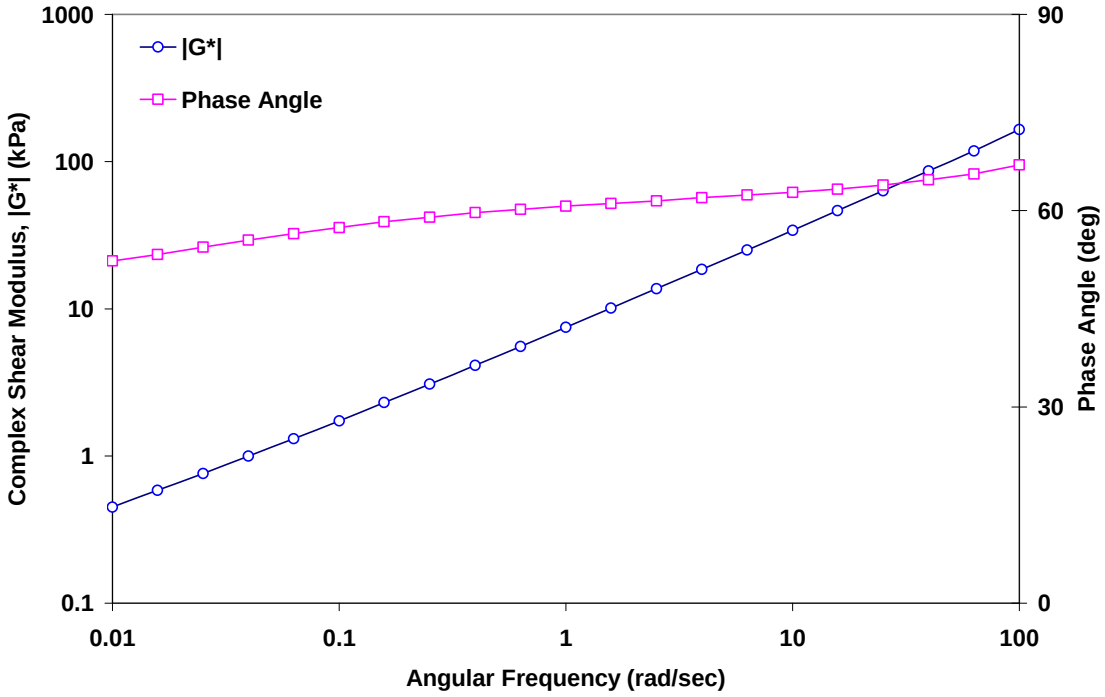

Figure C.39 Frequency Sweep Test Result, γ_A = 15.5%; SL CMHB RTFO-aged Mastic

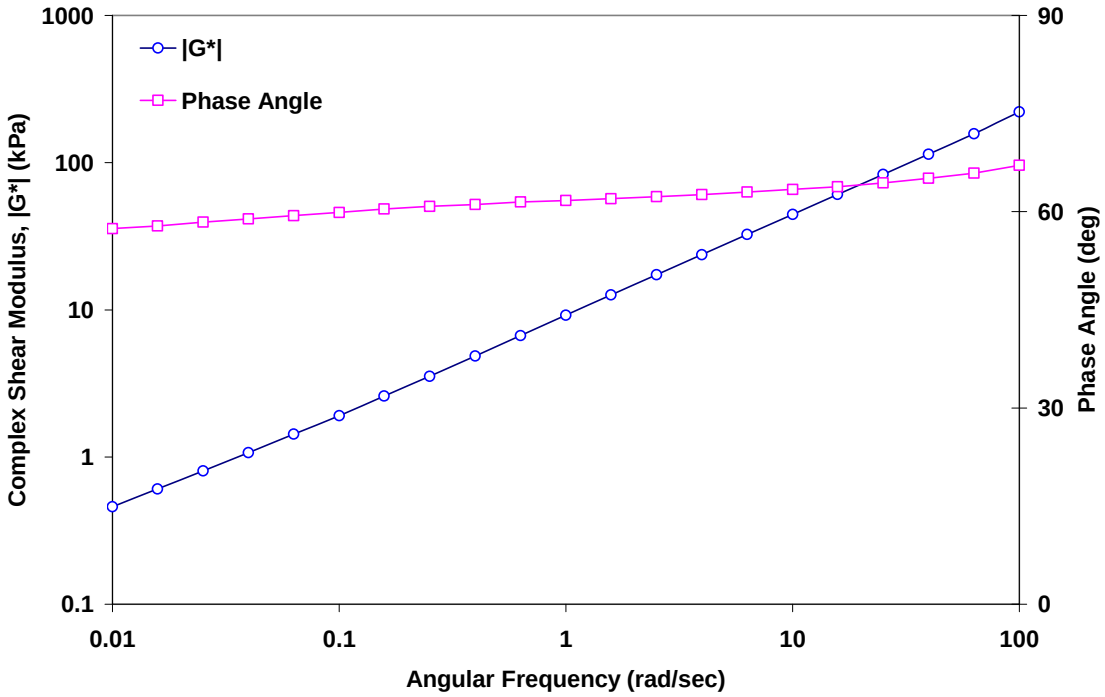

Figure C.40 Frequency Sweep Test Result, γ_A = 15.5%; HL PFC RTFO-aged Mastic

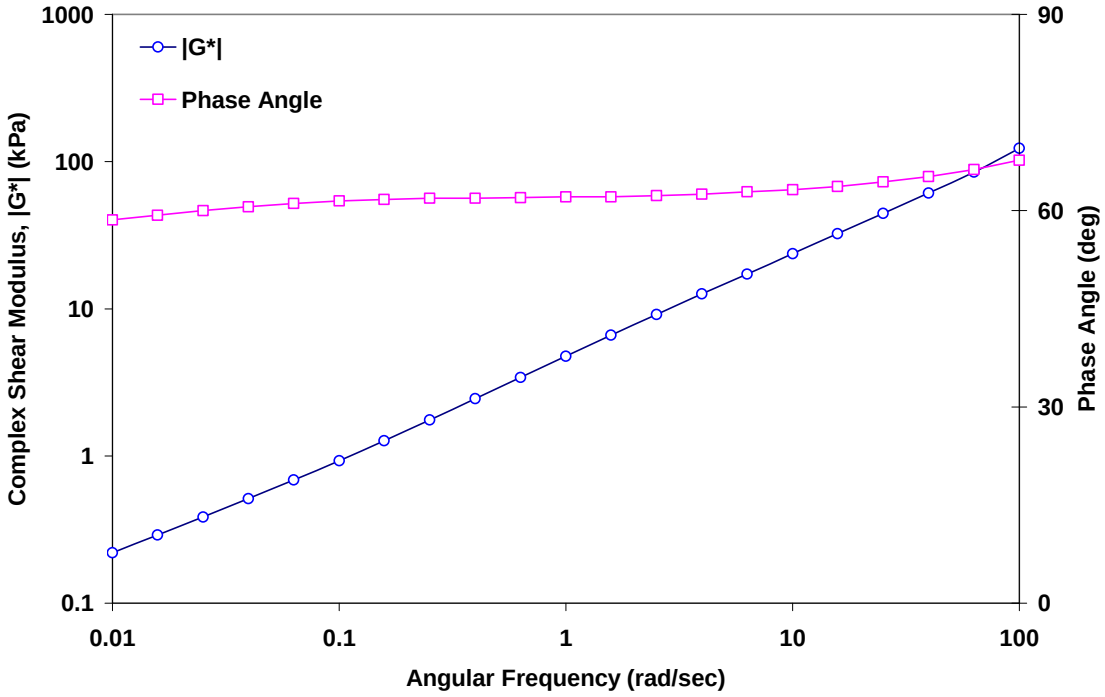

Figure C.41 Frequency Sweep Test Result, γ_A = 31.0%; G PFC RTFO-aged Mastic

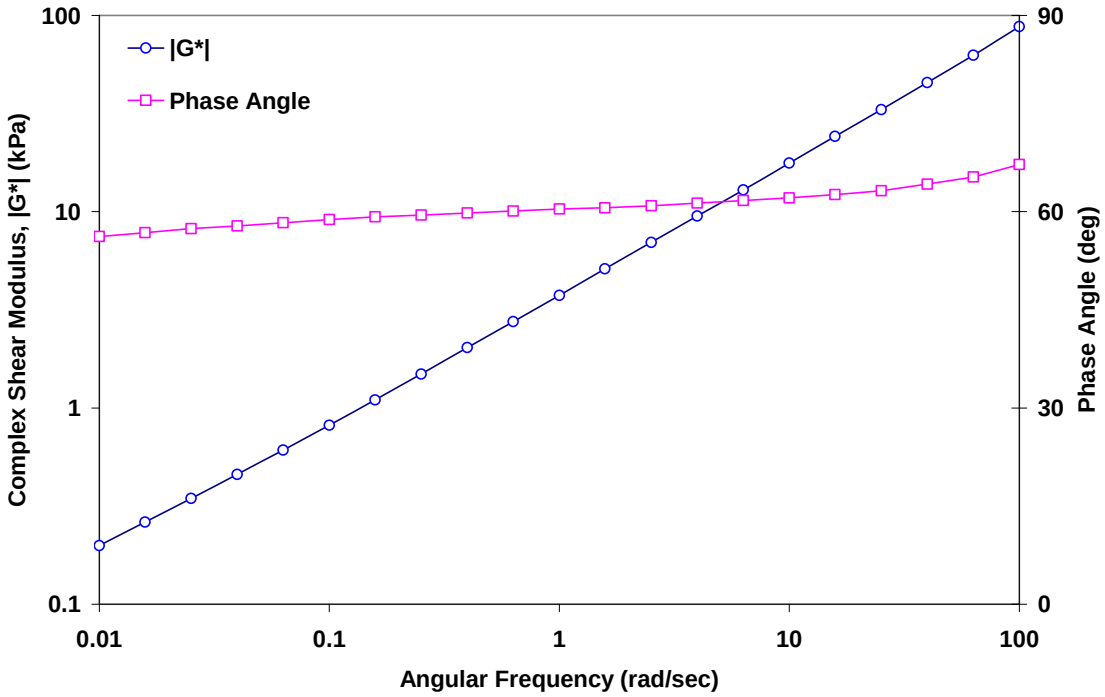

Figure C.42 Frequency Sweep Test Result, γ_A = 15.5%; SL PFC RTFO-aged Mastic

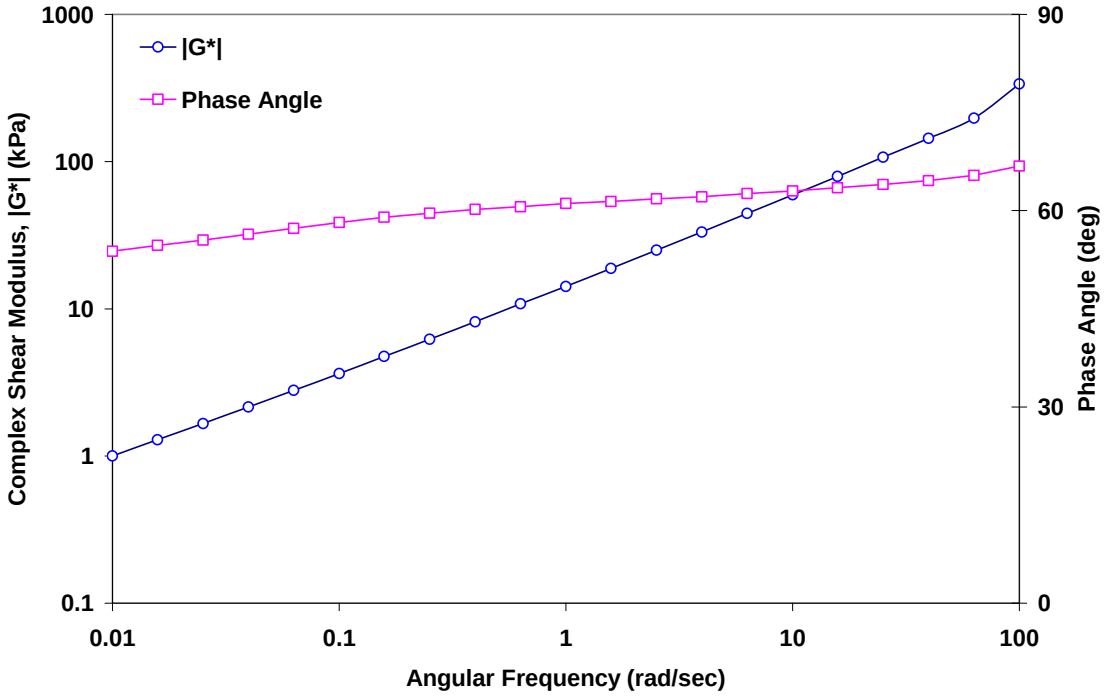

Figure C.43 Frequency Sweep Test Result, γ_A = 53.5%;

HL Superpave-C RTFO-aged Mastic

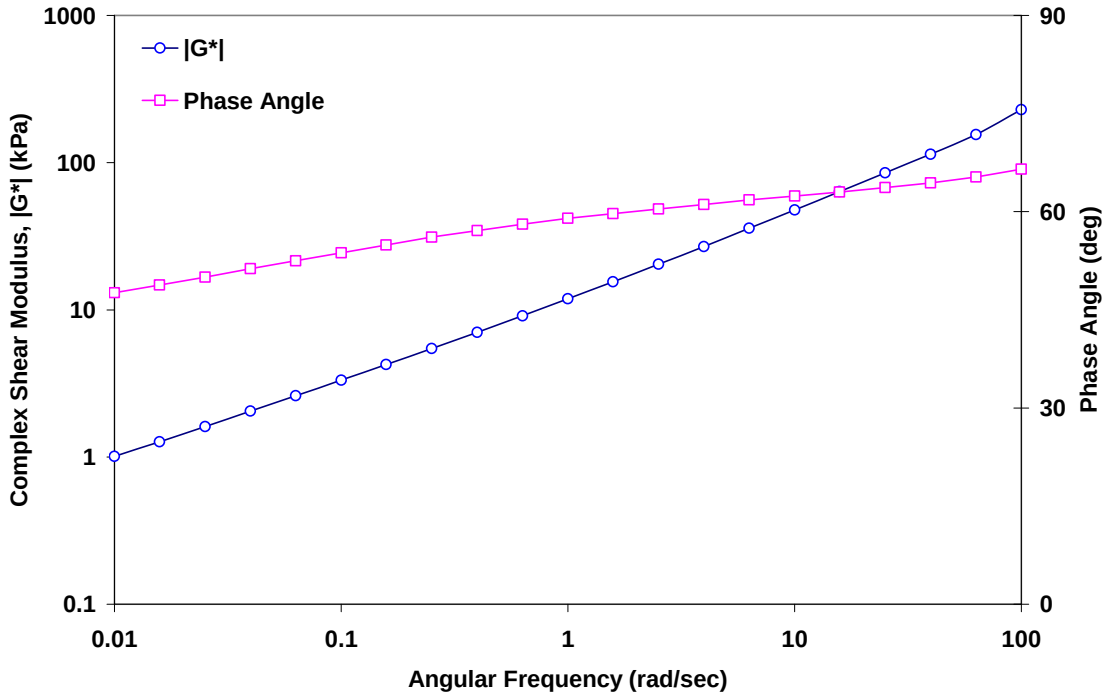

Figure C.44 Frequency Sweep Test Result, γ_A = 31.5%; G Super.-C RTFO-aged Mastic

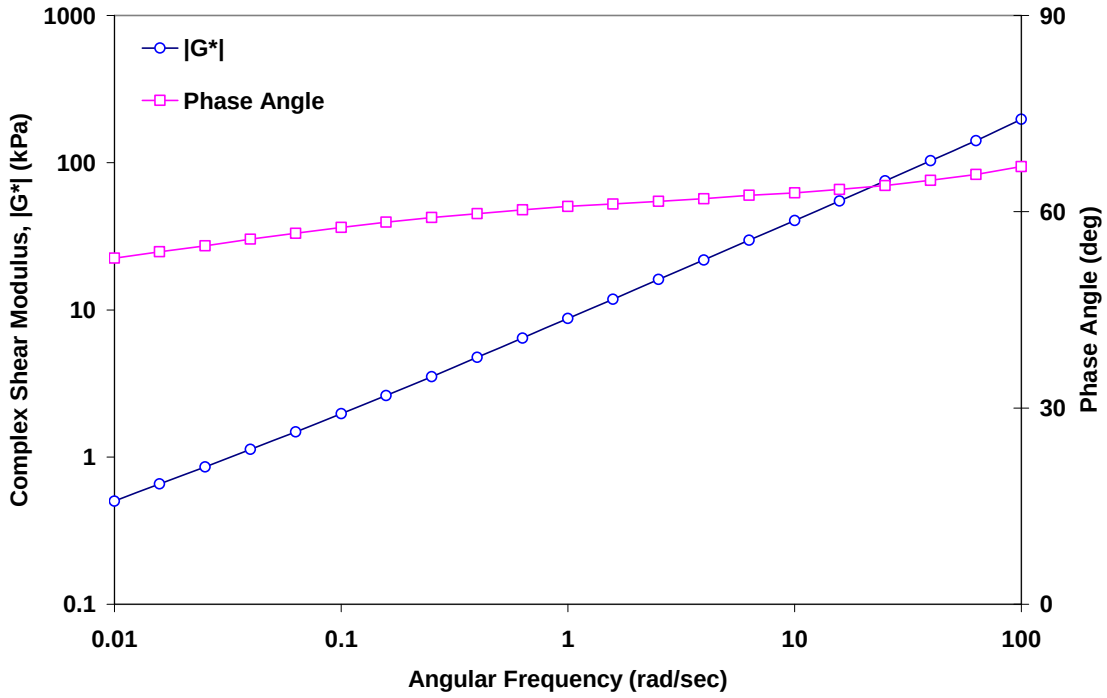

Figure C.45 Frequency Sweep Test Result, γ_A = 15.5%; SL Super.-C RTFO-aged Mastic

C.4 Non-Linear Optimization MATLAB Code

```
%--------------------------------REFERENCE-------------------------------
%-----------------Zelelew[1] H.M. and Papagiannakis[2] A.T.----------------
% [1]   PhD Candidate Civil and Environmental Engineering
%     Washington State University, Pullman, WA 99164-2910
%     (509) 335-2434 e-mail: hzelelew@yahoo.com
% [2]   Professor and Chair, Department of Civil and Environmental
%     Engineering, University of Texas at San Antonio
%     San Antonio TX 78249-0668
%     (210) 458-7517 e-mail: at.papagiannakis@utsa.edu

%--------------------------PURPOSE-------------------------------------
% This program was written to fit the Burger viscoelastic model
% parameters for research purposes only utilizing the non-linear
% optimization MATLAB® built-in function called lsqnonlin
% The files Burg_T.mat and Burg_H.mat must be saved in the same folder.
% First, Run Burg_H.mat and then run Burg_T.mat file to get the Burger
% model parameters. The program also plots the predicted and measured
values of the dynamic complex shear modulus with angular frequency.

%-----------------------FILE NAME “Burg_T.mat”-----------------------
clc
close all
clear
% Experimental Data
% Col_1: Frequency (rad/sec)
% Col_2: Storage Modulus (kPa)
% Col_3: Loss Modulus (kPa)
% Col_4: Dynamic Complex Shear Modulus (kPa)
% Col_5: Phase Angle (degrees)
% Col_6: Phase Angle (radians)
global data;
data=[
100.000     137.000     311.000     340.000     66.300      1.160
63.100      84.400      180.000     199.000     64.900      1.130
39.800      63.900      132.000     146.000     64.100      1.120
25.100      48.800      97.500      109.000     63.400      1.110
15.800      37.100      72.300      81.300      62.800      1.100
10.000      28.300      54.000      61.000      62.300      1.090
6.310       21.600      40.200      45.700      61.800      1.080
3.980       16.400      30.000      34.200      61.300      1.070
2.510       12.500      22.400      25.700      60.900      1.060
1.580       9.500       16.800      19.300      60.600      1.060
1.000       7.220       12.600      14.500      60.200      1.050
0.631       5.500       9.450       10.900      59.800      1.040
0.398       4.200       7.110       8.260       59.400      1.040
0.251       3.240       5.370       6.270       58.900      1.030
0.158       2.520       4.060       4.770       58.200      1.020
0.100       1.970       3.090       3.660       57.500      1.000
0.063       1.550       2.360       2.820       56.700      0.989
0.040       1.220       1.800       2.180       55.800      0.975
0.025       0.971       1.380       1.690       54.900      0.958
0.016       0.772       1.060       1.310       54.000      0.943
0.010       0.617       0.822       1.030       53.100      0.927
]
```

```
% x0 is a vector containing
% x01 = E_M x02 = Mu_M x03 = E_K x04 = Mu_K
% E_M = Maxwell Spring Mu_M =  Maxwell Dashpot
% E_K = Kelvin Spring Mu_K = Kelvin Dashpot

lb=0; ub=9999999;
x0=[225 45 80e-11 100e-9];

% Run the lsqnonlin, non-linear optimization fun. using start value x0,
x=(lsqnonlin('Burg_H',x0,lb,ub))


w=data(:,1);
G1exp=data(:,2);
G2exp=data(:,3);
Gexp=data(:,4);


%--------------Data No. 1-------------
w1=w(1);
G1exp_1=G1exp(1);
G2exp_1=G2exp(1);
Gexp_1=Gexp(1);

A_1= (1/x(1));
B_1= x(3);
C_1=x(4)*x(4);

Jc_1=(w1*w1);
Je_1= w1*x(2);
Jf_1= (w1*x(4));

J1_1= A_1+(B_1/(B_1^2+Jc_1*C_1));
J2_1= (1/(Je_1))+(Jf_1/(B_1^2+Jc_1*C_1));

J1sqr_1=J1_1*J1_1;
J2sqr_1=J2_1*J2_1;

G1pred_1=(J1_1/(J1sqr_1+J2sqr_1));
G2pred_1=(J2_1/(J1sqr_1+J2sqr_1));
Gpred_1=sqrt(G1pred_1^2+G2pred_1^2);

%--------------Data No. 2-------------
w2=w(2);
G1exp_2=G1exp(2);
G2exp_2=G2exp(2);
Gexp_2=Gexp(2);

A_2= (1/x(1));
B_2= x(3);
C_2=x(4)*x(4);

Jc_2=(w2*w2);
Je_2= w2*x(2);
Jf_2= (w2*x(4));

J1_2= A_2+(B_2/(B_2^2+Jc_2*C_2));
```

```
J2_2= (1/(Je_2))+(Jf_2/(B_2^2+Jc_2*C_2));
J1sqr_2=J1_2*J1_2;
J2sqr_2=J2_2*J2_2;

G1pred_2=(J1_2/(J1sqr_2+J2sqr_2));
G2pred_2=(J2_2/(J1sqr_2+J2sqr_2));
Gpred_2=sqrt(G1pred_2^2+G2pred_2^2);
            .
            .
            .
%--------------Data No. 17-------------
w17=w(17);
G1exp_17=G1exp(17);
G2exp_17=G2exp(17);
Gexp_17=Gexp(17);

A_17= (1/x(1));
B_17= x(3);
C_17=x(4)*x(4);

Jc_17=(w17*w17);
Je_17= w17*x(2);
Jf_17= (w17*x(4));
J1_17= A_17+(B_17/(B_17^2+Jc_17*C_17));
J2_17= (1/(Je_17))+(Jf_17/(B_17^2+Jc_17*C_17));
J1sqr_17=J1_17*J1_17;
J2sqr_17=J2_17*J2_17;

G1pred_17=(J1_17/(J1sqr_17+J2sqr_17));
G2pred_17=(J2_17/(J1sqr_17+J2sqr_17));
Gpred_17=sqrt(G1pred_17^2+G2pred_17^2);
            .
            .
            .
%--------------Data No. 21-------------
w21=w(21);
G1exp_21=G1exp(21);
G2exp_21=G2exp(21);
Gexp_21=Gexp(21);

A_21= (1/x(1));
B_21= x(3);
C_21=x(4)*x(4);

Jc_21=(w21*w21);
Je_21= w21*x(2);
Jf_21= (w21*x(4));
J1_21= A_21+(B_21/(B_21^2+Jc_21*C_21));
J2_21= (1/(Je_21))+(Jf_21/(B_21^2+Jc_21*C_21));
J1sqr_21=J1_21*J1_21;
J2sqr_21=J2_21*J2_21;

G1pred_21=(J1_21/(J1sqr_21+J2sqr_21));
G2pred_21=(J2_21/(J1sqr_21+J2sqr_21));
```

```
Gpred_21=sqrt(G1pred_21^2+G2pred_21^2);
Freq=[w1,w2,w3,w4,w5,w6,w7,w8,w9,w10,w11,w12,w13,w14,w15,w16,w17,w18,w1
9,w20,w21];
Gexpt=[Gexp_1,Gexp_2,Gexp_3,Gexp_4,Gexp_5,Gexp_6,Gexp_7,Gexp_8,Gexp_9,G
exp_10,Gexp_11,Gexp_12,Gexp_13,Gexp_14,Gexp_15,Gexp_16,Gexp_17,Gexp_18,
Gexp_19,Gexp_20,Gexp_21];
Gpred=[Gpred_1,Gpred_2,Gpred_3,Gpred_4,Gpred_5,Gpred_6,Gpred_7,Gpred_8,
Gpred_9,Gpred_10,Gpred_11,Gpred_12,Gpred_13,Gpred_14,Gpred_15,Gpred_16,
Gpred_17,Gpred_18,Gpred_19,Gpred_20,Gpred_21];


loglog(Freq,Gexpt,'bo'); hold on
loglog(Freq,Gpred,'r-'); hold on


Gexptpred=[Gexp_1,Gpred_1;Gexp_2,Gpred_2;Gexp_3,Gpred_3;Gexp_4,Gpred_4;
Gexp_5,Gpred_5;Gexp_6,Gpred_6;Gexp_7,Gpred_7;Gexp_8,Gpred_8;Gexp_9,Gpre
d_9;Gexp_10,Gpred_10;Gexp_11,Gpred_11;Gexp_12,Gpred_12;Gexp_13,Gpred_13
;Gexp_14,Gpred_14;Gexp_15,Gpred_15;Gexp_16,Gpred_16;Gexp_17,Gpred_17;Ge
xp_18,Gpred_18;Gexp_19,Gpred_19;Gexp_20,Gpred_20;Gexp_21,Gpred_21]



%------------------------FILE NAME “Burg_H.mat”------------------------
function y=Burg_H(x)
global data;
w=data(:,1);
G1exp=data(:,2);
G2exp=data(:,3);
Gexp=data(:,4);


%--------------Data No. 1-------------
w1=w(1);
G1exp_1=G1exp(1);
G2exp_1=G2exp(1);
Gexp_1=Gexp(1);

A_1= (1/x(1));
B_1= x(3);
C_1=x(4)*x(4);

Jc_1=(w1*w1);
Je_1= w1*x(2);
Jf_1= (w1*x(4));

J1_1= A_1+(B_1/(B_1^2+Jc_1*C_1));
J2_1= (1/(Je_1))+(Jf_1/(B_1^2+Jc_1*C_1));

J1sqr_1=J1_1*J1_1;
J2sqr_1=J2_1*J2_1;

G1pred_1=(J1_1/(J1sqr_1+J2sqr_1));
G2pred_1=(J2_1/(J1sqr_1+J2sqr_1));
Gpred_1=sqrt(G1pred_1^2+G2pred_1^2);
%--------------Data No. 2-------------
w2=w(2);
```

```
G1exp_2=G1exp(2);
G2exp_2=G2exp(2);
Gexp_2=Gexp(2);

A_2= (1/x(1));
B_2= x(3);
C_2=x(4)*x(4);

Jc_2=(w2*w2);
Je_2= w2*x(2);
Jf_2= (w2*x(4));

J1_2= A_2+(B_2/(B_2^2+Jc_2*C_2));
J2_2= (1/(Je_2))+(Jf_2/(B_2^2+Jc_2*C_2));

J1sqr_2=J1_2*J1_2;
J2sqr_2=J2_2*J2_2;

G1pred_2=(J1_2/(J1sqr_2+J2sqr_2));
G2pred_2=(J2_2/(J1sqr_2+J2sqr_2));
Gpred_2=sqrt(G1pred_2^2+G2pred_2^2);
            .
            .
            .
%--------------Data No. 17-------------
w17=w(17);
G1exp_17=G1exp(17);
G2exp_17=G2exp(17);
Gexp_17=Gexp(17);

A_17= (1/x(1));
B_17= x(3);
C_17=x(4)*x(4);

Jc_17=(w17*w17);
Je_17= w17*x(2);
Jf_17= (w17*x(4));
J1_17= A_17+(B_17/(B_17^2+Jc_17*C_17));
J2_17= (1/(Je_17))+(Jf_17/(B_17^2+Jc_17*C_17));
J1sqr_17=J1_17*J1_17;
J2sqr_17=J2_17*J2_17;

G1pred_17=(J1_17/(J1sqr_17+J2sqr_17));
G2pred_17=(J2_17/(J1sqr_17+J2sqr_17));
Gpred_17=sqrt(G1pred_17^2+G2pred_17^2);
            .
            .
            .
%--------------Data No. 21-------------
w21=w(21);
G1exp_21=G1exp(21);
G2exp_21=G2exp(21);
Gexp_21=Gexp(21);
```

```
A_21= (1/x(1));
B_21= x(3);
C_21=x(4)*x(4);

Jc_21=(w21*w21);
Je_21= w21*x(2);
Jf_21= (w21*x(4));
J1_21= A_21+(B_21/(B_21^2+Jc_21*C_21));
J2_21= (1/(Je_21))+(Jf_21/(B_21^2+Jc_21*C_21));
J1sqr_21=J1_21*J1_21;
J2sqr_21=J2_21*J2_21;

G1pred_21=(J1_21/(J1sqr_21+J2sqr_21));
G2pred_21=(J2_21/(J1sqr_21+J2sqr_21));
Gpred_21=sqrt(G1pred_21^2+G2pred_21^2);



y_1=((Gpred_1/Gexp_1)-1);
y_2=((Gpred_2/Gexp_2)-1);
y_3=((Gpred_3/Gexp_3)-1);
y_4=((Gpred_4/Gexp_4)-1);
y_5=((Gpred_5/Gexp_5)-1);
y_6=((Gpred_6/Gexp_6)-1);
y_7=((Gpred_7/Gexp_7)-1);
y_8=((Gpred_8/Gexp_8)-1);
y_9=((Gpred_9/Gexp_9)-1);
y_10=((Gpred_10/Gexp_10)-1);
y_11=((Gpred_11/Gexp_11)-1);
y_12=((Gpred_12/Gexp_12)-1);
y_13=((Gpred_13/Gexp_13)-1);
y_14=((Gpred_14/Gexp_14)-1);
y_15=((Gpred_15/Gexp_15)-1);
y_16=((Gpred_16/Gexp_16)-1);
y_17=((Gpred_17/Gexp_17)-1);
y_18=((Gpred_18/Gexp_18)-1);
y_19=((Gpred_19/Gexp_19)-1);
y_20=((Gpred_20/Gexp_20)-1);
y_21=((Gpred_21/Gexp_21)-1);



y=y_1+y_2+y_3+y_4+y_5+y_6+y_7+y_8+y_9+y_10+y_11+y_12+y_13+y_14+y_15+y_1
6+y_17+y_18+y_19+y_20+y_21;
```

Appendix D

DEM SIMULATION RESULTS

D.1 Effects of Stiffness Ratio (K_n/K_s) on the Permanent Deformation Behavior of AC Mixtures

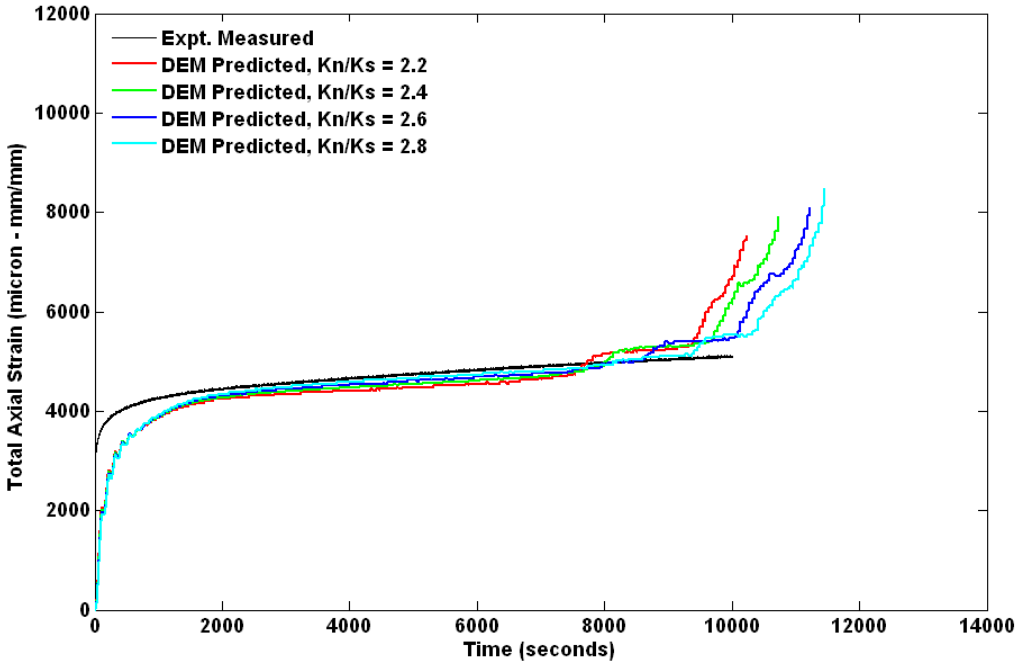

Figure D.1 Effects of Contact Stiffness Ratio on Axial Strain, $\mu = 0.5$; G CMHB-C

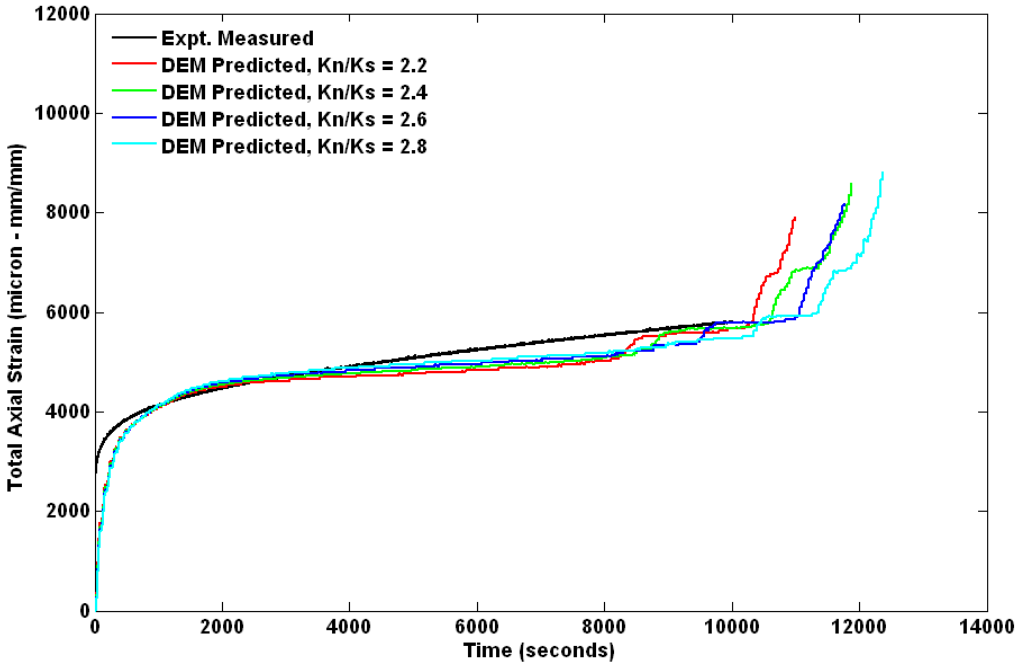

Figure D.2 Effects of Contact Stiffness Ratio on Axial Strain, $\mu = 0.5$; SL CMHB-C

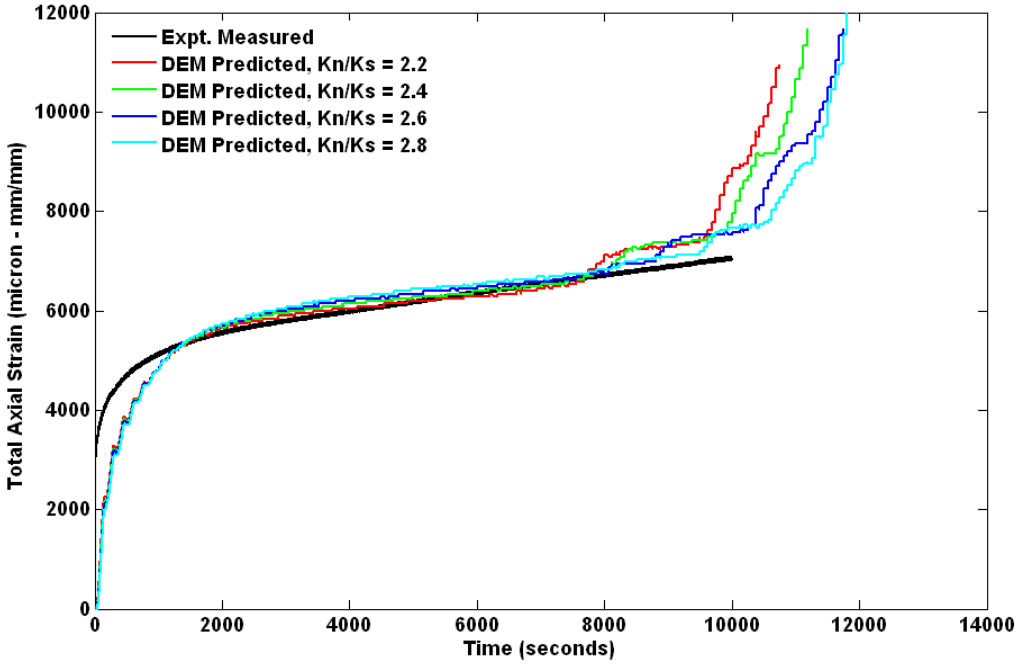

Figure D.3 Effects of Contact Stiffness Ratio on Axial Strain, $\mu = 0.5$; HL PFC

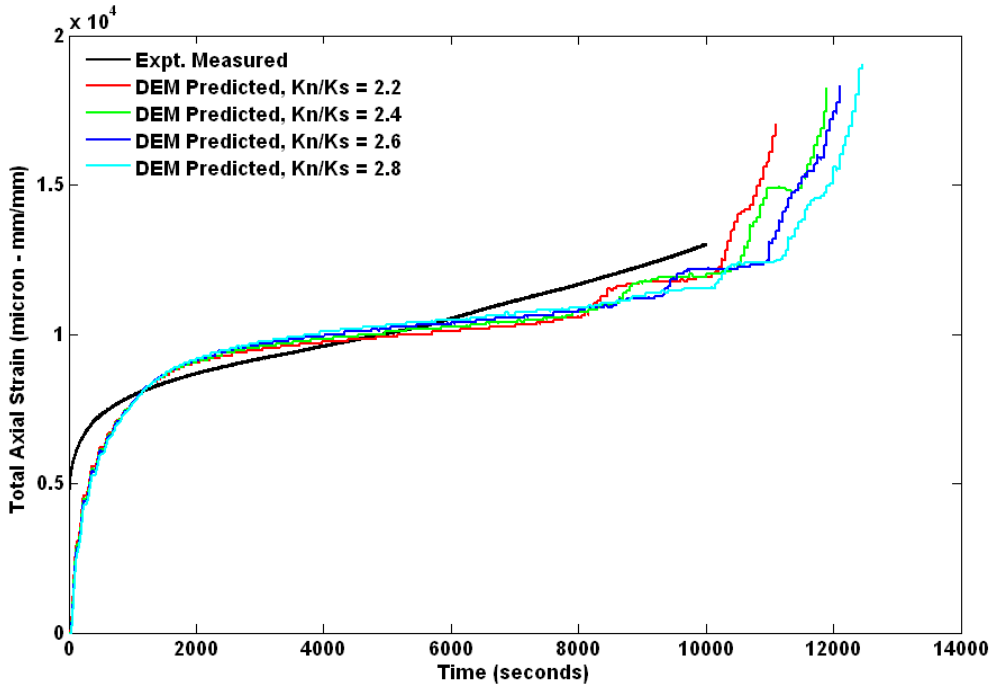

Figure D.4 Effects of Contact Stiffness Ratio on Axial Strain, $\mu = 0.5$; G PFC

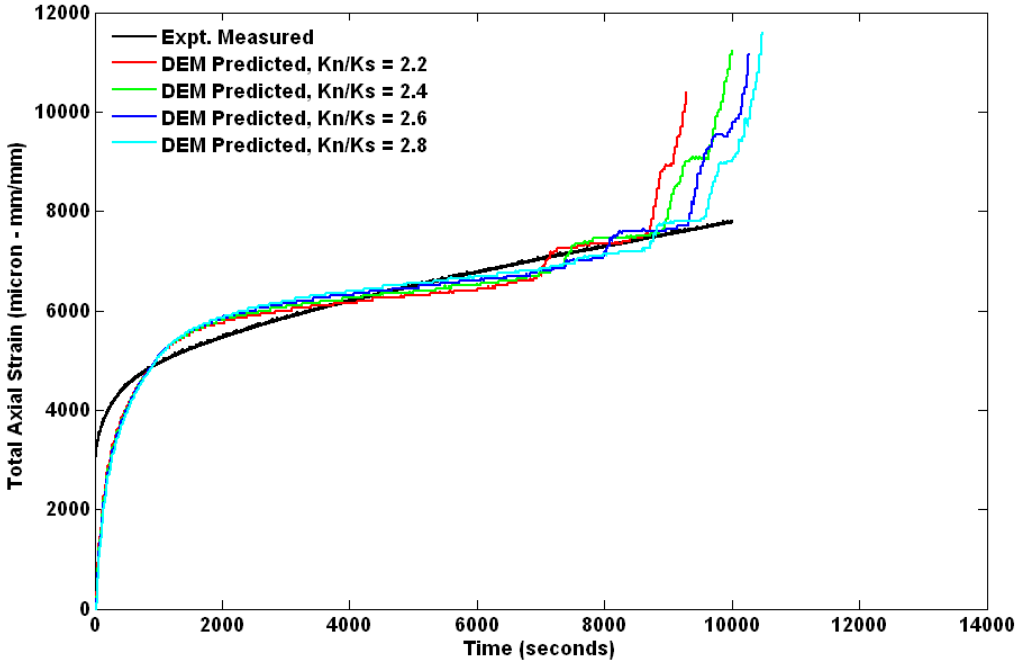

Figure D.5 Effects of Contact Stiffness Ratio on Axial Strain, $\mu = 0.5$; SL PFC

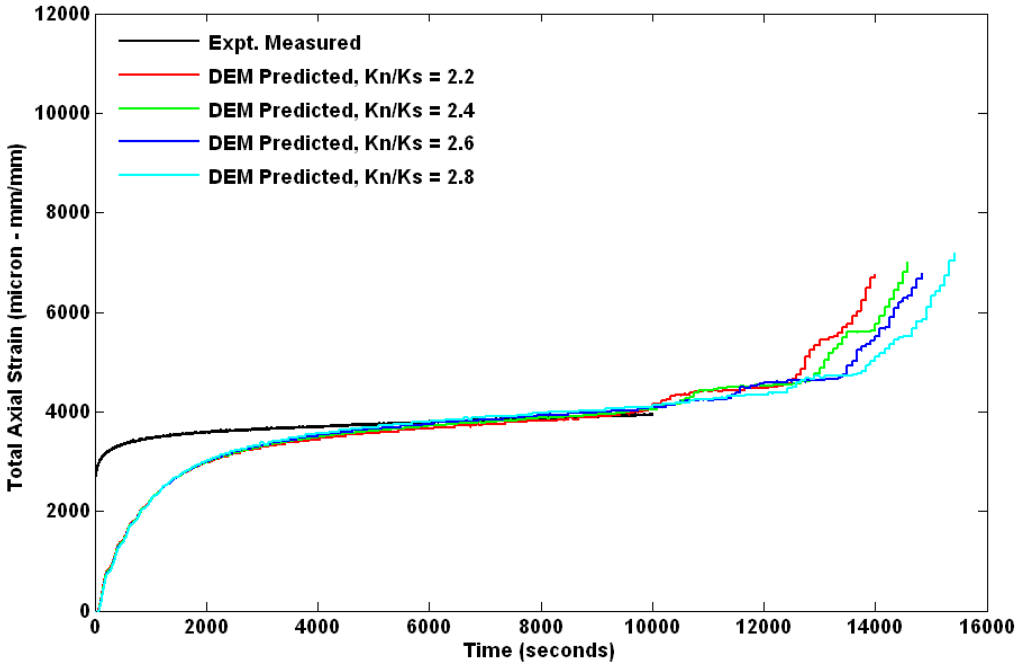

Figure D.6 Effects of Contact Stiffness Ratio on Axial Strain, $\mu = 0.5$; HL Superpave-C

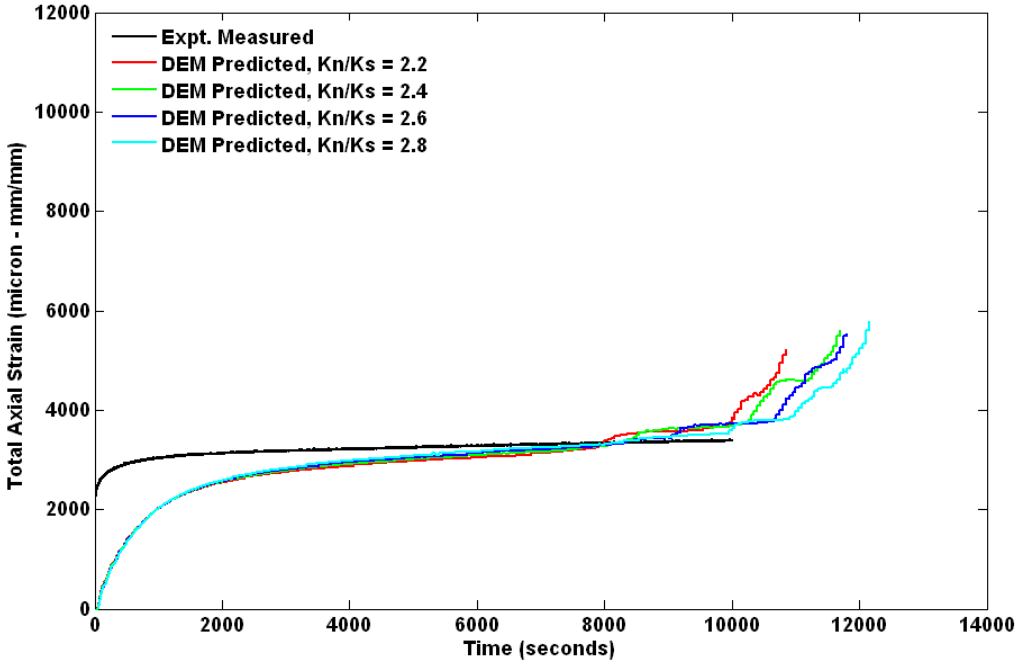

Figure D.7 Effects of Contact Stiffness Ratio on Axial Strain, $\mu = 0.5$; G Superpave-C

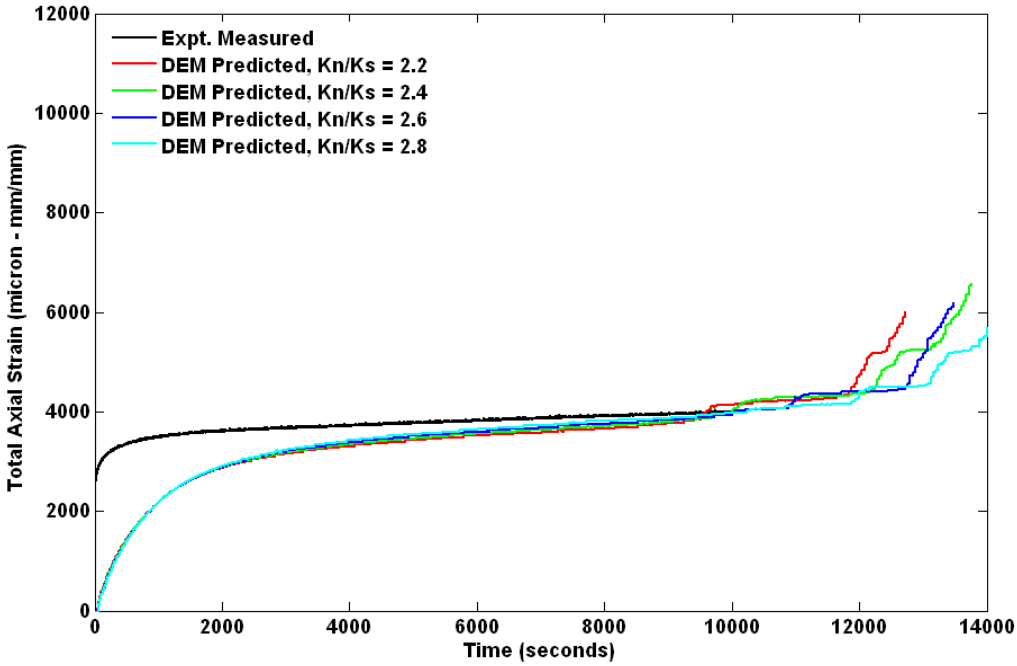

Figure D.8 Effects of Contact Stiffness Ratio on Axial Strain, $\mu = 0.5$; SL Superpave-C

D.2 Effects of Aggregate-to-Aggregate Contact Friction (μ) on the Permanent Deformation Behavior of AC Mixtures

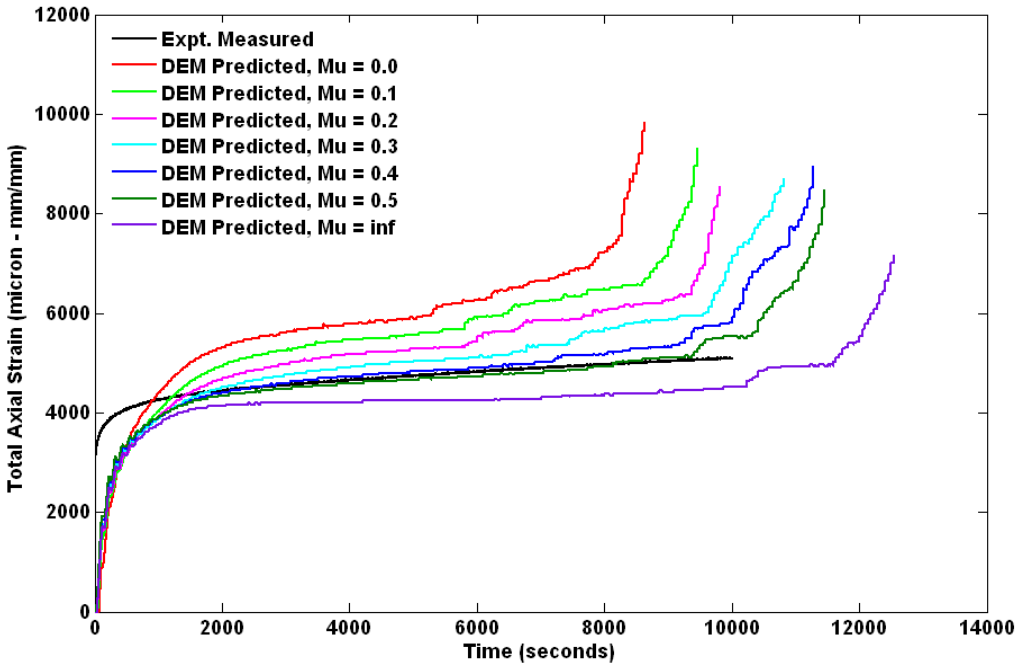

Figure D.9 Effects of Aggregate-to-Aggregate Contact Friction (μ) on Axial Strain, K_n/K_s = 2.8; G CMHB-C

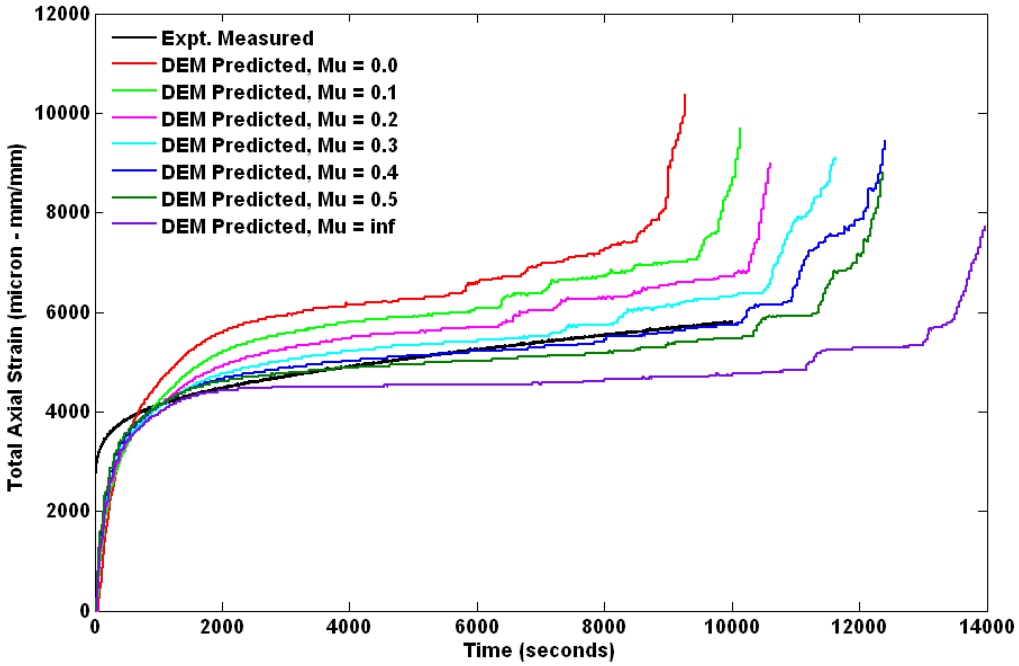

Figure D.10 Effects of Aggregate-to-Aggregate Contact Friction (μ) on Axial Strain, K_n/K_s = 2.8; SL CMHB-C

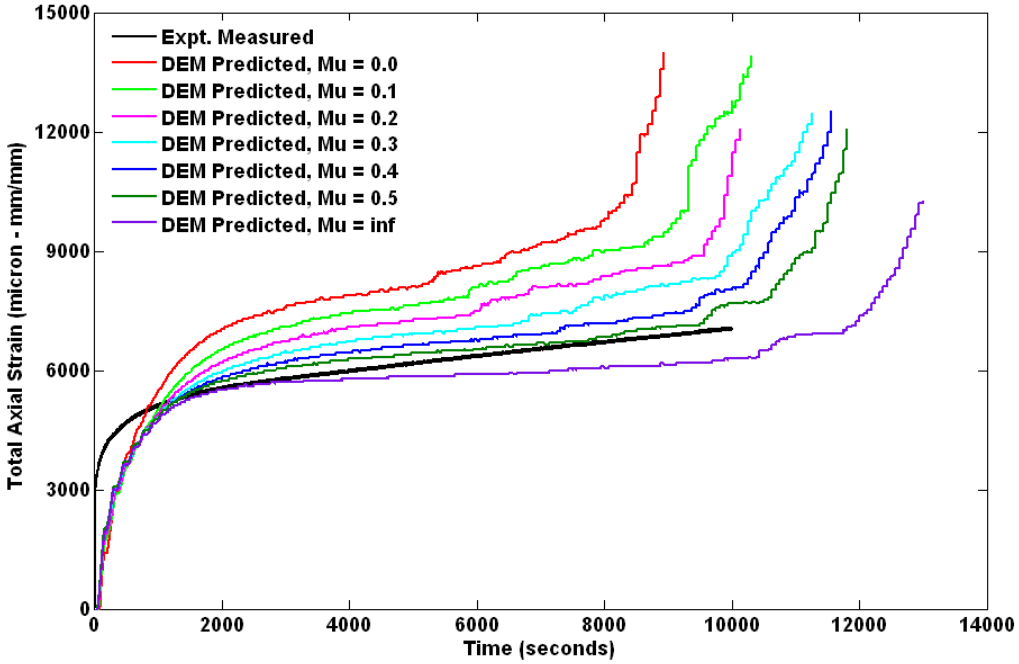

Figure D.11 Effects of Aggregate-to-Aggregate Contact Friction (μ) on Axial Strain, K_n/K_s = 2.8; HL PFC

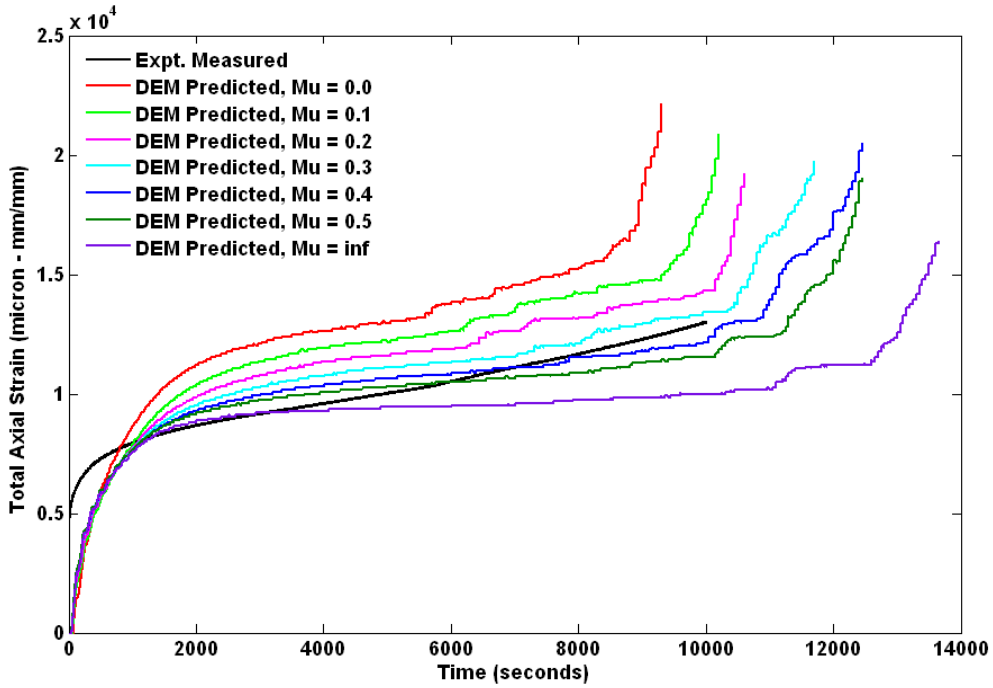

Figure D.12 Effects of Aggregate-to-Aggregate Contact Friction (μ) on Axial Strain, K_n/K_s = 2.8; G PFC

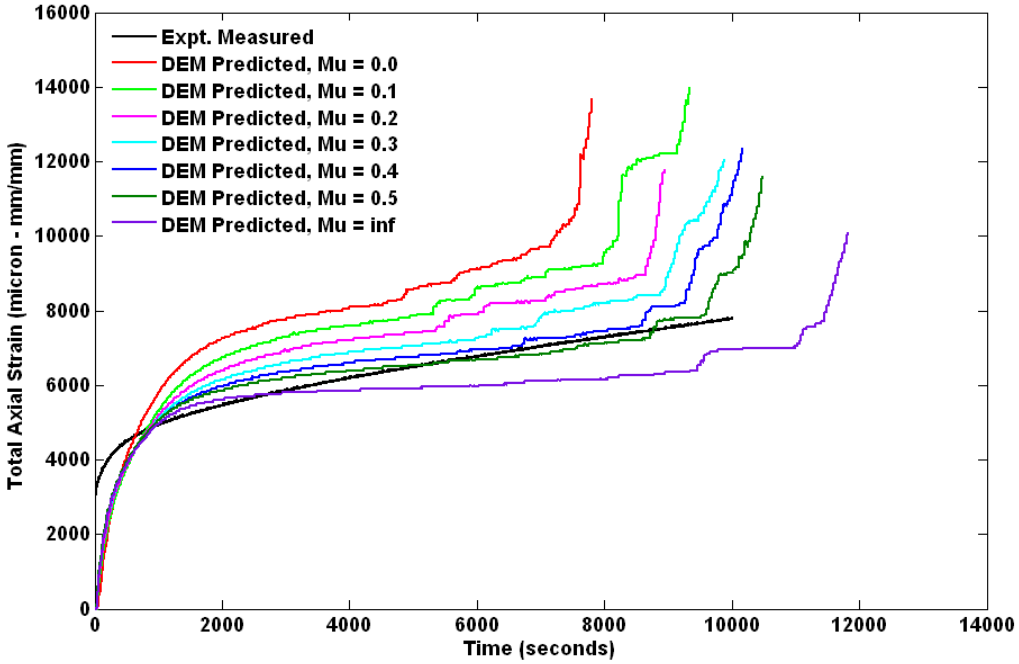

Figure D.13 Effects of Aggregate-to-Aggregate Contact Friction (μ) on Axial Strain, K_n/K_s = 2.8; SL PFC

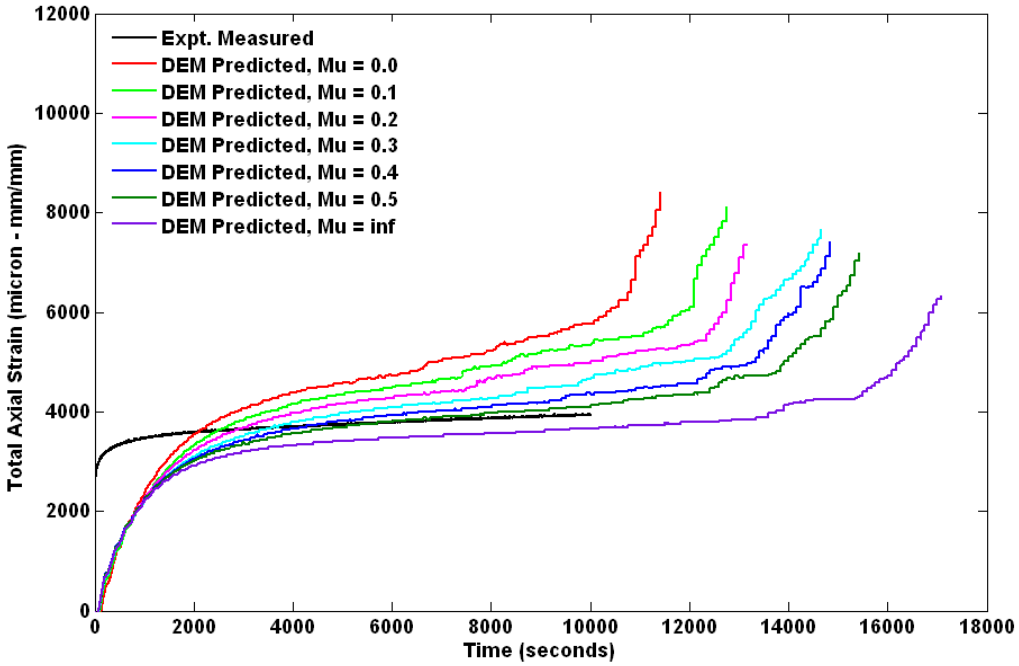

Figure D.14 Effects of Aggregate-to-Aggregate Contact Friction (μ) on Axial Strain, K_n/K_s = 2.8; HL Superpave-C

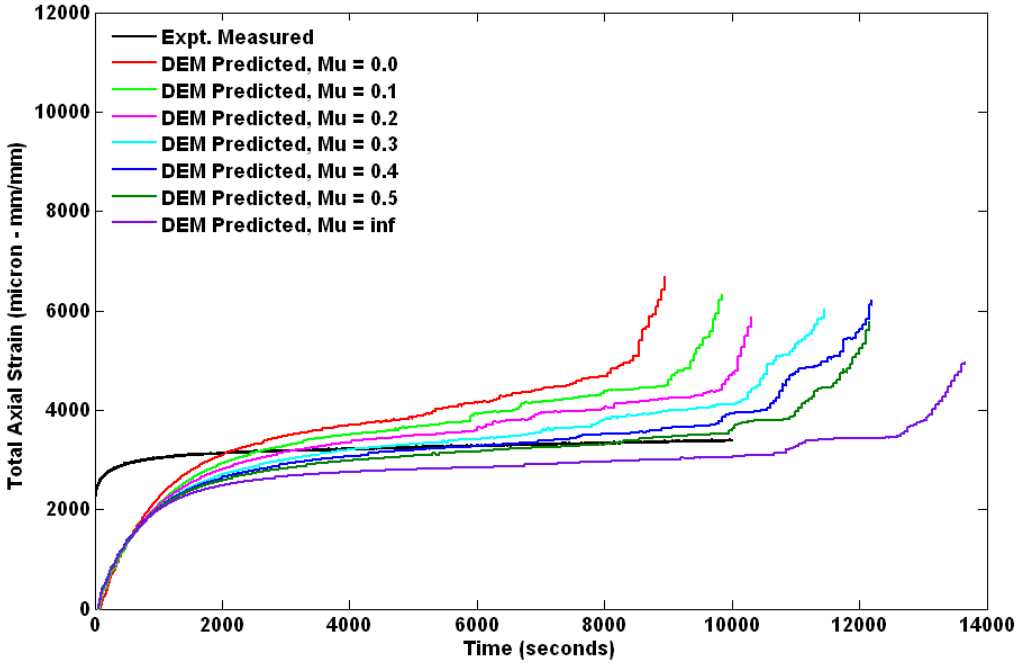

Figure D.15 Effects of Aggregate-to-Aggregate Contact Friction (μ) on Axial Strain, K_n/K_s = 2.8; G Superpave-C

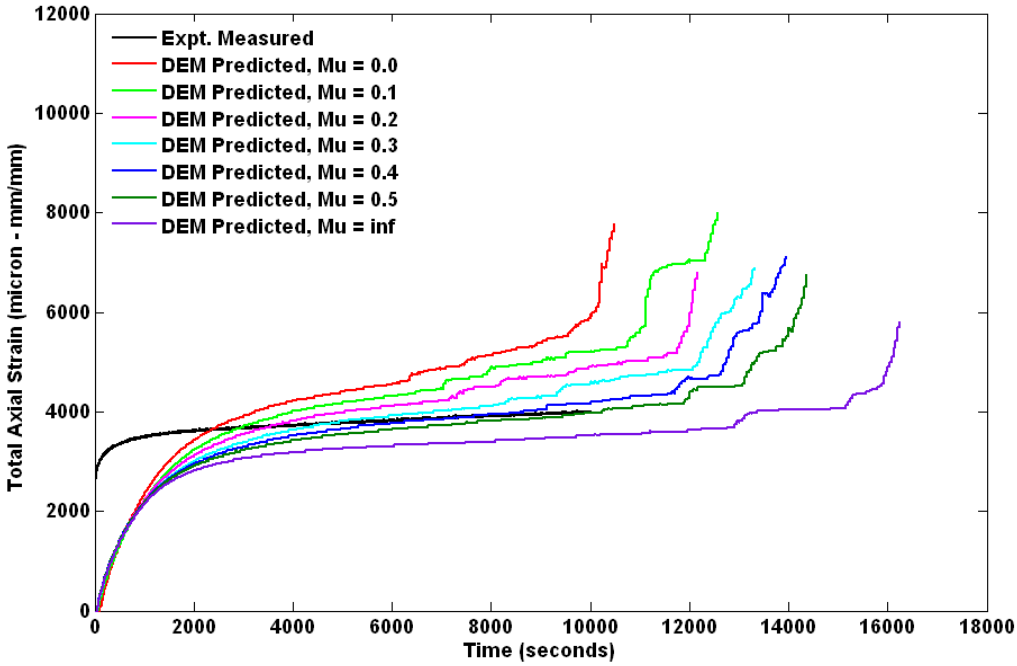

Figure D.16 Effects of Aggregate-to-Aggregate Contact Friction (μ) on Axial Strain, K_n/K_s = 2.8; SL Superpave-C

D.3 Predicted and Measured Axial Creep Compliance of AC Mixtures

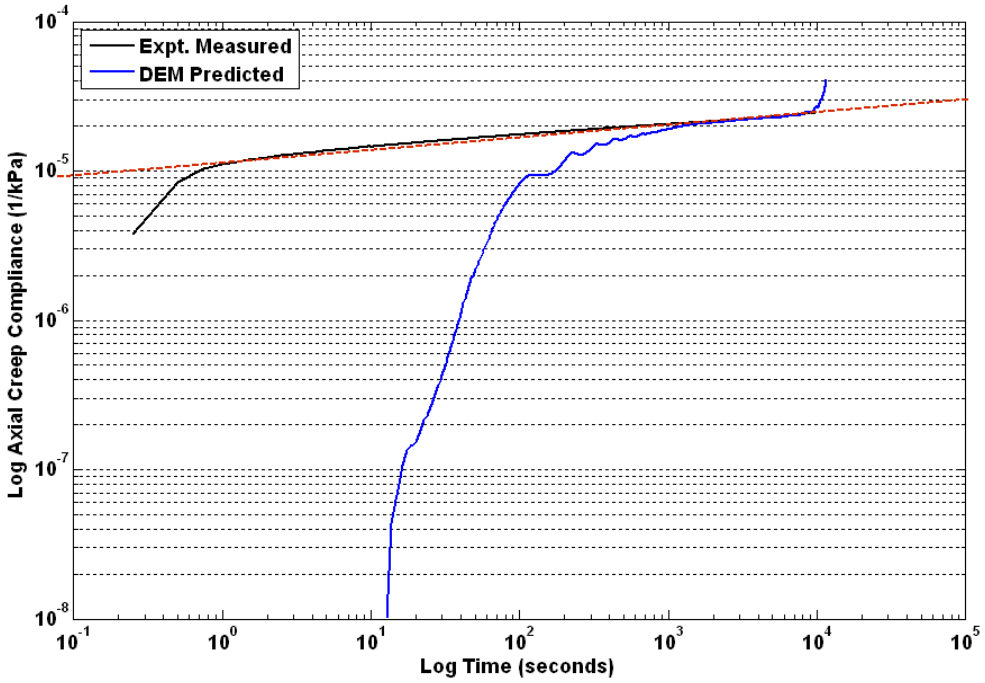

Figure D.17 Measured and Predicted Axial Creep Compliance, K_n/K_s = 2.8 and $\mu = 0.5$; G CMHB-C

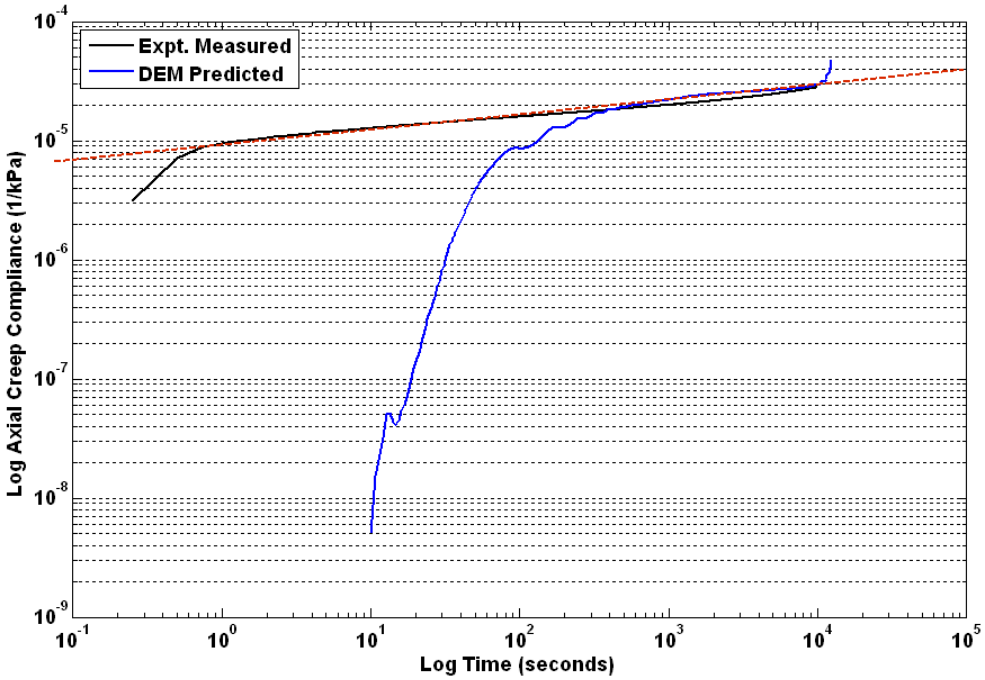

Figure D.18 Measured and Predicted Axial Creep Compliance, K_n/K_s = 2.8 and $\mu = 0.5$; SL CMHB-C

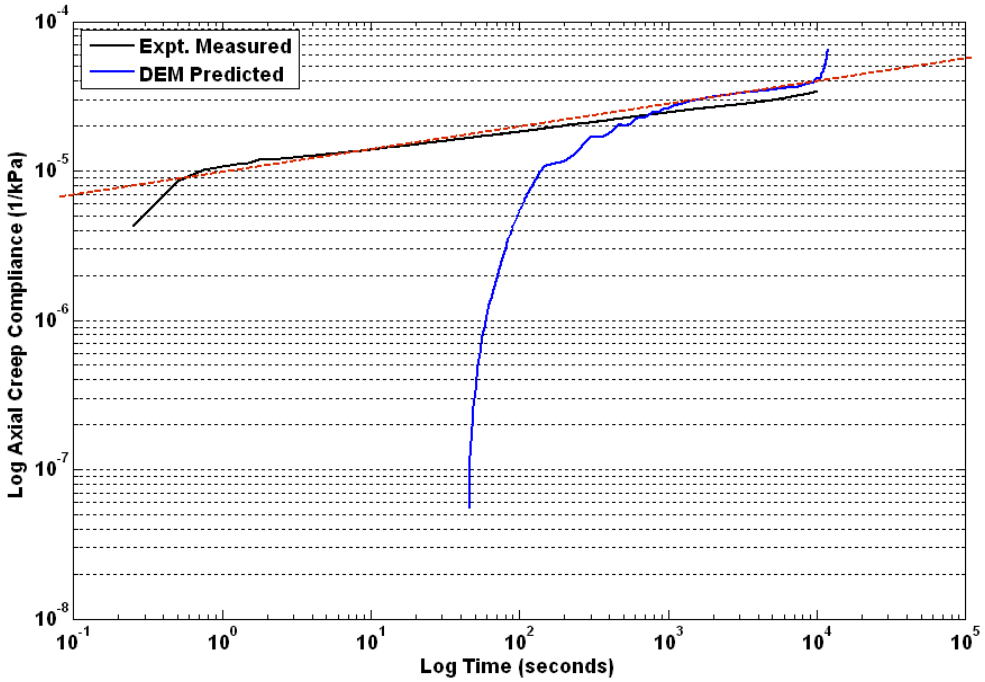

Figure D.19 Measured and Predicted Axial Creep Compliance, K_n/K_s = 2.8 and $\mu = 0.5$; HL PFC

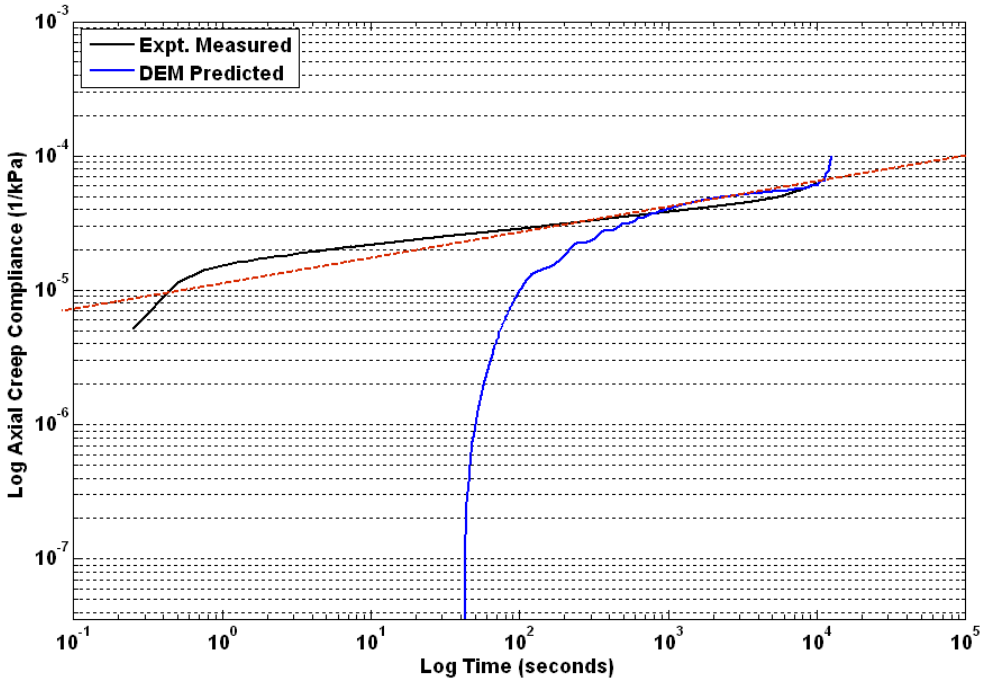

Figure D.20 Measured and Predicted Axial Creep Compliance, K_n/K_s = 2.8 and $\mu = 0.5$; G PFC

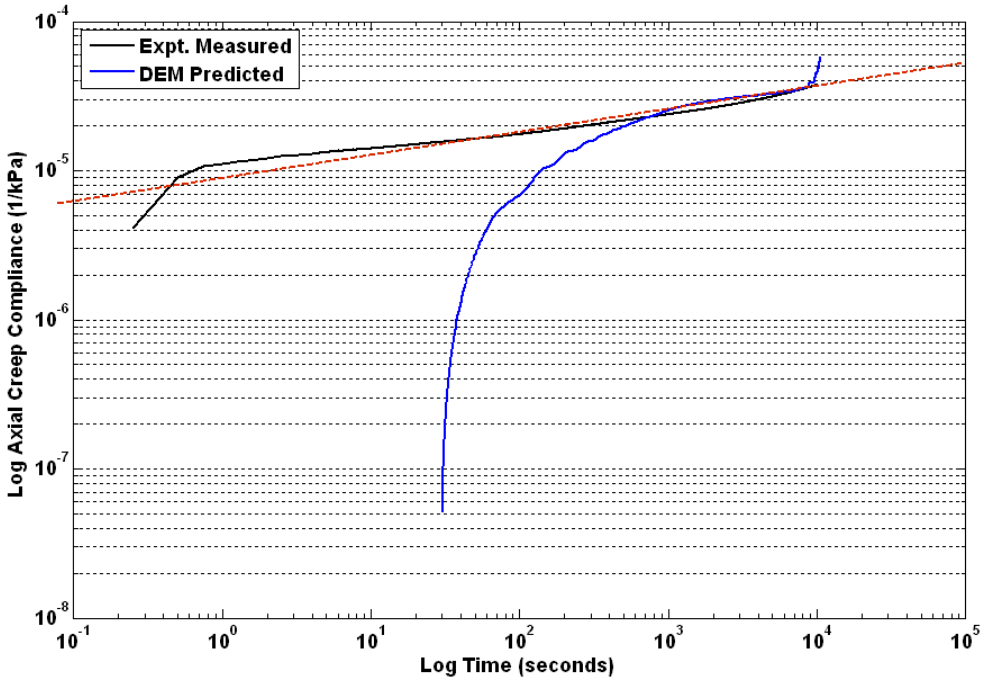

Figure D.21 Measured and Predicted Axial Creep Compliance, K_n/K_s = 2.8 and $\mu = 0.5$; SL PFC

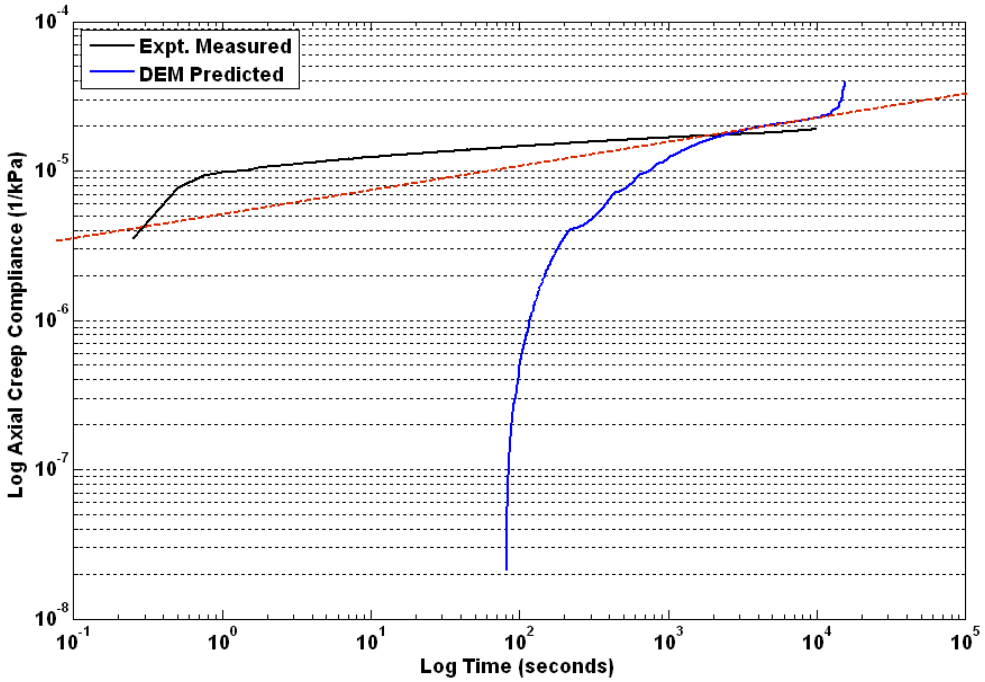

Figure D.22 Measured and Predicted Axial Creep Compliance, K_n/K_s = 2.8 and $\mu = 0.5$; HL Superpave-C

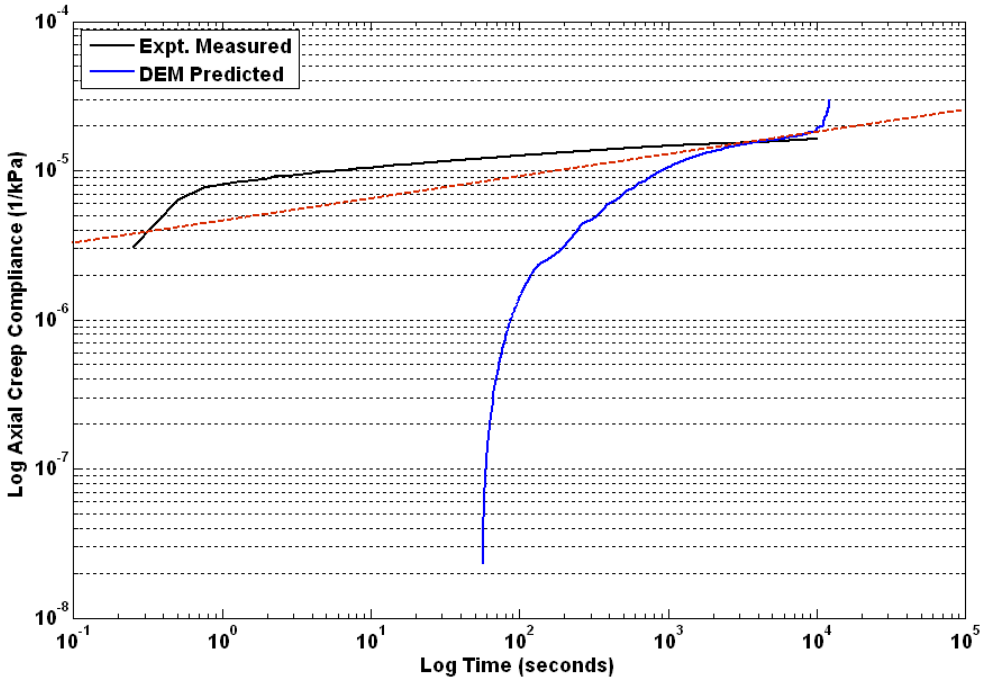

Figure D.23 Measured and Predicted Axial Creep Compliance, K_n/K_s = 2.8 and $\mu = 0.5$; G Superpave-C

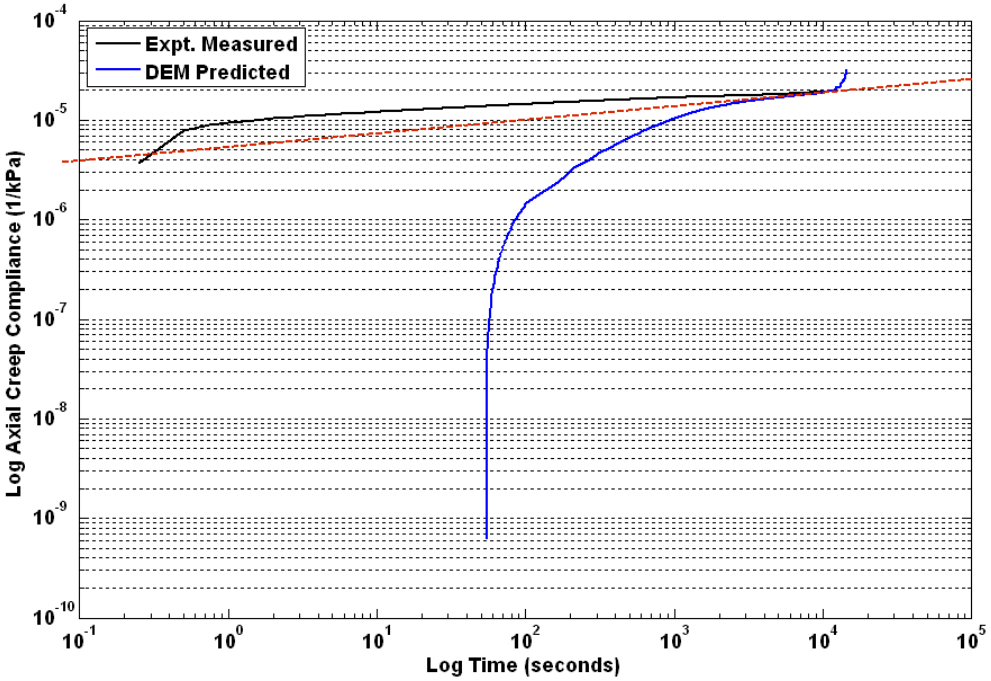

Figure D.24 Measured and Predicted Axial Creep Compliance, K_n/K_s = 2.8 and $\mu = 0.5$; SL Superpave-C